New Frontiers in Organic Polariton Devices: Fluorescent Molecules, Polariton Lasers, and Biological Systems

Richard Theodore Grant

University of Sheffield

A dissertation submitted for the degree of

Doctor of Philosophy

26 September, 2016

Supervised by Professor David G. Lidzey

Declaration

The research described in this thesis was carried out by the author between October 2012 and September 2016. The use of the first person plural is strictly a matter of style in keeping with standard scientific convention. Contributions from collaborators are noted in the text where appropriate. This dissertation has not been submitted in whole or in part for the award of a degree at this, or any other university and does not exceed 60,000 words in length.

Richard Theodore Grant

Dedicated to Grace Conacher, James Andrew Grant, and Edward Francis Grant

Acknowledgements

Over the last four years I have had the great pleasure and privilege of working with many remarkable people who have made my time in Sheffield a joy. Without whom, I could not have hoped to complete this thesis. I would first like to thank my parents for their continued support, and to apologize for all of the grey hairs that I have given them over the years.

I would like to thank the former members of EPMM who welcomed me into group: Nick Scarratt, Charlotte Nicolaou, Jonathan Griffin, Ben Robinson, Darren Watters, David Coles, Adam Green, and Andrew Pearson. The friends with whom I have shared an office that made life entertaining: Christopher Bracher, Mary Snape, Michael Stringer, Benjamin Freestone, Thomas Routledge, Alex Barrows and Nicola Robinson. Finally thanks to the newer members of the group Kyriacos Georgiou, James Bishop, Claire Greenland, Andrew Musser and Rahul Jayaprakash who continue to provide a warm welcoming environment and a wicked sense of humour for future members of the group.

To my collaborators Carlos Silva, Eleonora Vella, and Pascal Gregoire at the Université de Montréal, thank you for the opportunity to work with you and explore your beautiful city. Thank you to Tersilla Virgili, Francesco Galeotti, and Marco Cavazzini at Politecnico di Milano for providing the BODIPY derivatives which have proved to be such a rich vein of research. Sai Kiran Rajedendran at St. Andrews for all of his help with lasing experiments.

Special thanks are due to Thomas Routledge and Lindsey Wherry for their kindness putting a roof over my head for the last two months of my studies; Rahul Jayaprakash for his assistance with modelling and simulations; and David Coles for going above and beyond, spending many hours in the lab teaching me everything I know about optics. Thanks again to my housemates Daniel Griffiths, Liam Hardy, and Thomas Sydney for many hours of entertainment and discussion, I couldn't have wished for better housemates. To Jessica Ren, thank you for putting a smile on my face and providing support and encouragement through difficult times.

Finally I would like to thank my supervisor David Lidzey for providing me with the opportunity to join his research group and work with such an outstanding group of people. His advice and guidance have been invaluable over the last four years. I could not have hoped for a better supervisor.

Abstract

This thesis concerns the manufacture and study of strongly-coupled microcavities containing a series of different organic semiconductors; it is divided into 9 chapters. **Chapter 1** provides a brief historical overview of the field of polaritonics, both organic and inorganic, and lists a timeline of major developments. **Chapters 2** and **3** are theoretical chapters concerning the organic semiconductors, and photonics respectively. **Chapters 4** and **5** describe the techniques used to process and characterize the samples discussed in the subsequent experimental chapters.

In **Chapter 6**, changes to exciton-photon mode detunings in strongly-coupled microcavities containing a fluorescent dye were shown to change the distribution of the polariton population along the lower polariton branch. A simple fitting model was developed to describe these changes in terms of direct radiative pumping of polariton states by weakly-coupled states co-existing within the cavity.

Chapter 7 describes the careful selection and characterisation of a series of molecular dyes to evaluate their likelihood of first entering the strong coupling regime and secondly producing coherent emission. The construction of a polariton laser containing one of these dyes is shown.

By placing a component of light-harvesting complexes harvested from bacteria within a planar microcavity, **Chapter 8** details the first demonstration of strong-coupling in a biological system. The implications upon the modification of energy transfer within the cell are discussed along with the possibility of creating so called "living" polaritons. Additionally, work with carotenoids is discussed in this chapter. By entering the strong coupling regime, and achieving sufficiently large Rabi splitting, the author hopes to place the S_2 state below that of the symmetry-inverted S_1 and enhance emission form a (virtually) non-emissive material. Proof that carotenoids are capable of coupling is demonstrated with β-carotene and alternative materials are suggested for further work.

Publications

Efficient Radiative Pumping of Polaritons in a Strongly-Coupled Microcavity by a Fluorescent Molecular Dye
Advanced Optical Materials, Volume 5, July 2016

Photoluminescent and superparamagnetic reduced graphene oxide–iron oxide quantum dots for dual-modality imaging, drug delivery and photothermal therapy
Carbon, Volume 97, 54-70, February 2016

Biodegradable and conductive chitosan–graphene quantum dot nanocomposite microneedles for delivery of both small and large molecular weight therapeutics
RSC Advances, 5, 51934-51946 June 2015

Vertical stratification and its impact on device performance in polycarbazole based copolymer solar cells
Journal of Materials Chemistry C, March 2015

Strong coupling between chlorosomes of photosynthetic bacteria and a confined optical cavity mode
Nature Communications, Volume 5, November 2014

Imaging the polariton relaxation bottleneck in strongly coupled organic semiconductor microcavities
Physical Review B, Volume 88, Issue 12, September 2013

Water-gated organic nanowire transistors
Organic Electronics, Volume 14, Issue 4, April 2013

Conference Presentations

The Photophysics of BODIPY Dyes in a Strong-Coupled Microcavity
UK Semiconductors – Sheffield, United Kingdom 2016

Characterising Polariton Populations in Microcavities Containing Highly Fluorescent Molecular Dyes
Symposium on Exciton Processes in Molecular Materials – Rank Prize, 2015

Polariton Population Mechanisms in Organic Semiconductor Microcavities
UK Semiconductors – Sheffield, United Kingdom 2015

Strong Coupling in Microcavities Containing a Fluorescent Organic Dye
Advanced Polaritonics and Photonics Workshop – Suzdal, Russia 2015

The Luminescence Quantum Efficiency of Strongly-Coupled Organic Microcavities
European Optical Society Annual Meeting (poster) – Berlin, Germany 2014

Table of Contents

1.

Introduction

Man has manipulated the interactions between light and matter for hundreds of years, most notably in the form of glass optics which allowed the production of lenses to restore vision or construct telescopes and prisms with which to refract light. Advances in processing techniques over the last few decades have allowed the construction of progressively smaller and more complex optical elements. Fabrication techniques have has now reached the point where we can now produce nano-scale devices capable of reproducing the iridescent structural colour observed in nature on butterfly wings and other interesting phenomena. On small enough length-scales, single photons and atoms are able to be confined and their interactions studied[1]. Confinement of photons on small length-scales allows interactions which may not normally be seen in bulk materials to be observed. This is typically achieved by constructing a Fabry-Pérot interferometer; a sandwich-like structure composed of two planar reflective surfaces placed parallel to one another. These two surfaces serve as an optical resonator which allow the wavelength (and thus energy) of the confined photons to be varied simply by changing the separation between the two; a similar feat can be achieved by changing the angle of observation.

Photons have an electric field associated with them that, once confined, can influence the energy levels and density of photonic states within the cavity with respect to their normal free space values. This in turn modifies the properties of an electronic transition of any (semiconducting) material that also shares the same confined volume. A confined photon may interact with an electronic transition in a semiconducting material, causing spontaneous emission rates to be enhanced if the two are resonant, or suppressed if non-resonant; this behaviour is described by Fermi's golden rule and is a characteristic of the so called "weak coupling" regime. If however this interaction is sufficiently strong, it cannot be described by a simple perturbation of the existing energy levels. An oscillatory exchange of energy between the photon and transition dipole occurs which must instead be explained by quantum mechanical means and can be described as a superposition of the individual photon and exciton wavefunctions. This superposition describes the new allowed states within the system and can be treated as a bosonic quasi-particle known as a polariton. Polaritons retain some properties of both of their constituents, namely very low effective masses ($\sim 10^{-4}$ to $\sim 10^{-7}$ that of an electron[2]) and the capacity to scatter off one another. The new allowed energy levels (or eigenvalues) of the system described by this superposition have two solutions; these can be observed experimentally through either photoluminescence or reflectivity measurements as two polariton "branches" that anti-cross around the energy at which the photon and exciton are resonant. The strength of the interaction can be quantified by the magnitude of the anti-crossing, referred to as the Rabi splitting energy, $\hbar\Omega$, where $\hbar$ is the reduced Planck Constant and Ω is the frequency of oscillation.

1.1. A Historical Overview

1.1.1. Strong-Coupling

First considered in 1950[3], polaritons were not experimentally observed until 1965 in (anisotropic) bulk crystals of ZnO[4]. In general however, planar microcavities are preferred to bulk systems for the study of polaritons as bulk-polaritons can only be studied externally and lose their polaritonic nature as they approach the surface of the material[5]. Polaritons in three dimensional systems are limited in their use in functional devices, as within an ideal crystalline material, polaritons can only decay into photons when their energy and momentum are degenerate (due to energy and momentum conservation in all three dimensions). This can be

difficult to achieve as it requires interaction with defects, surfaces or phonons[6,7]. It would be another 27 years before polaritons were observed in conventional Fabry-Pérot microcavities by Weisbuch et al in 1992[8] as the concept of polaritons remained linked to bulk semiconductors for decades[9]. Eventually planar microcavities became the norm for studying interactions due to their anisotropy in one direction which facilitated radiative decay. It is worth noting that microcavities are not used exclusively for the study of polaritons but also in a wide range of applications such as photonic lasing[10], photovoltaics[11,12], and light emitting diodes (LED)[13–15]; indeed microcavities were originally developed in the 1980s for the production of vertical-cavity surface emitting lasers (VCSELs) and resonantly coupled LEDs[16,17].

The first demonstration of polaritons in organic semiconductors came in 1998 when Lidzey et al successfully coupled the exciton of a porphyrin molecule to a confined photon mode[18]. A Rabi splitting ($\hbar\Omega$) of 160meV was observed, which at the time was an order of magnitude greater than those observed in inorganic II-VI quantum microcavities[19], and more than 30 times larger than those seen in III-V quantum well microcavities at room temperature[20,21]. Though Rabi splittings >1eV have since been reported[22], this result served to highlight some of the fundamental differences between excitons produced in organic and inorganic structures.

Inorganic semiconductors are generally characterised by large dielectric constants. Electric field screening in these materials reduces the coulombic interactions between electrons and holes. This results in excitons with large radii, small binding energies (on the order of 1-10 meV), capable of diffusing over relatively large distances; these are termed Wannier-Mott excitons[23]. By contrast, organic semiconductors typically possess smaller dielectric constants. As binding energies are inversely proportional to the dielectric constant of a material, coulombic interactions between charges are stronger. This results in the formation of Frenkel excitons[24]: smaller, more localised excitons whose binding energies are generally in the order of 0.1 to 1eV. The higher binding energies of Frenkel excitons make them more stable and resistant to thermal dissociation; this in turn means that cryogenic temperatures are not required to produce stable systems. This is not to say that room temperature (or higher) systems are not possible with inorganic materials, indeed much success has been had in recent years using GaN[25–27] and CdTe[28] based strongly-coupled structures. Some systems (such as carbon nanotubes) are capable of producing both Frenkel and Wannier-Mott –like excitons[29] which may utilised in interesting systems in the future.

Following the demonstration of strong-coupling in both organic and inorganic semiconductors, the next significant developments came in 2000 in the form of polariton parametric amplification[30,31] and its spontaneous counterpart, parametric photoluminescence[32]. It was found that emission from planar microcavities could greatly be enhanced by changing the incident angle of pump light to directly access critical optical wave vectors. Two polaritons are injected by the pump source with a wave vector k_p. Polaritons scatter off one another, and as energy and momentum are conserved, polariton populations build up at $2k_p$ and $k_{//}=0$. This can be a useful technique for overcoming the "bottleneck" that can form in some systems in which a population of polaritons builds up at some wave vector k due to an inability to migrate to the bottom of the branch ($k_{//}=0$) over the course of a polariton's (short) lifetime. Polaritons at $2k_p$ can then relax through conventional means. Polariton scattering processes become increasingly inefficient as the energy separation from exciton reservoir increases and their photonic fraction increases. There exist other methods of overcoming this bottleneck, the simplest of which is to increase the excitation density whilst the system is still in the strong coupling regime. This has been attributed to increased contributions from exciton-exciton scattering[32]. Shortly after this, the observation of non-equilibrium Bose-Einstein condensation[33] and lasing[34] from strongly coupled systems were discovered in 2002 and 2003 respectively.

1.1.2. Bose-Einstein Condensation

The roots of Bose-Einstein condensation (BEC) lie in 1924 when Bose and Einstein proposed that below a critical temperature, an ideal gas comprised solely of bosons would condense in the lowest quantum state, creating a new phase of matter[35]. A characteristic of BECs is that the de Broglie wavelength of their constituent bosons becomes comparable to their average separation; in this way a large population of particles can exchange information and together demonstrate quantum phenomena on a macroscopic scale[36]. Initially this theory was not widely accepted as it was thought to be impossible to observe a BEC in a finite system[37], but gained credibility with the observation of superfluidity in He-4[38,39] which was attributed to BECs[40]. It is important to note that the threshold temperature required to form a BEC is inversely proportional to the effective mass of the boson undergoing condensation. This proved to be a large barrier to overcome and it would be another 57 years before BEC was observed in dilute atomic gasses of rubidium[41] and sodium[42] which had threshold temperatures of ~6μK. In this interim period the possibility of observing BECs in the solid state was postulated as the excitons

within the system could be considered a dilute Bose gas. The exceedingly low effective mass of excitons (~10^{-4} that of an electron) meant that the critical temperature could be raised by several orders of magnitude. Unfortunately publications claiming to observe BEC in solid state systems proved to be inconclusive. BEC formation in solids was ultimately hindered by short (excited state) lifetimes which prevented excitons from thermalizing and reaching the lattice temperature before electrons and holes underwent recombination. Inorganic systems were further limited by the weak binding energy of the Wannier-Mott excitons which tended to lose excitonic nature and break down into their fermionic components as excitation power increased. Polaritons emerged as a candidate for the formation of BECs in 1992 after the successful demonstration of strong coupling in planar microcavities[8] which eliminated the need to work with troublesome bulk materials.

Polaritons have an advantage over excitons when it comes to forming BECs, namely their ability to change the ratio of their photonic and excitonic components simply by varying the wavevector (or angle) of observation. At $k_\parallel$=0, polaritons in the lower polariton branch are largely photon-like (depending on detuning) and can possess effective masses ranging from four to seven orders of magnitude smaller than that of a bare exciton. This raises the critical temperature considerably (or equivalently, lowers the critical density of bosons by several orders of magnitude). Unlike exciton BECs, polariton BECs are not hindered by local disorder and crystal defects, this is because their photonic component allows them to extend their phase-coherent wavefunctions spatially; excitons are easily localised in a fluctuating potential inside a crystal[43].

The first demonstration of BEC in polaritons came in 2002 when Deng et al placed a series of GaAs quantum-wells within a microcavity[33] followed by Kasprzak et al in 2006[36]. BEC of organic materials was achieved in 2013 by Plumhof et al with a solution-processed conjugated ladder-type polymer[44], shortly followed by a thermally-evaporated molecule by Daskalakis et al[45]; both of these systems showed condensation at room temperature. It is worth nothing that whilst organic polariton lasers can operate at room temperatures (as a result of their high binding energies), the lasing threshold can be further decreased by an order of magnitude when reduced to cryogenic temperatures[46]. Most recently Dietrich et al have demonstrated polariton condensation and lasing in a biologically-produced green fluorescent protein[47].

1.1.3. Polariton Lasing

Shortly after the demonstrations of BECs in microcavities the first (optically pumped) polariton laser was demonstrated in 2003 by Deng et al[34]. BECs and polariton lasers are of great interest to the scientific community as they offer the potential for ultra-low, or even zero, threshold sources of coherent light. In the case of BECs, all participating particles are thermalized, share a macroscopic wave-function, and occupy the same (lowest available) quantum state. This means that all (spontaneous) emission from the BEC is coming from the same state and is monochromatic and coherent. Polariton lasing also produces coherent monochromatic light as emission is occurring from the same position along the lower polariton branch, but differs from BECs in that the lifetime of the polariton state is shorter than the time taken for it to thermalize with its surrounds; polariton lasers are thus non-equilibrium and said to be in the kinetic regime. Polariton lasers and emission from BECs can be distinguished from conventional lasers in that they do not require a population inversion to produce coherent light; it is merely sufficient to form a BEC with the emission being spontaneous rather than stimulated in nature. Early work on VCSELs in 1996[48] appeared to suggest coherent emission from a BEC, but this later transpired to be misleading as the system was neither in thermal equilibrium or the strong-coupling regime.

In the same year as Deng's discovery, a single-atom, zero-threshold polariton laser was observed[49], though it would be another four years before an inorganic semiconductor capable of (polariton) lasing at room temperature was produced[50]. These structures were unusual at the time as they were bulk devices that did not incorporate any quantum well. Work with nitride-based cavities have remained popular as they possess larger exciton binding energies than GaAs based systems with Rabi splittings on the order of 50meV observed[51,52]. The first organic materials capable of polariton lasing at room temperature were melt-grown crystalline anthracene stuctures by Kéna-Cohen et al in 2010[53]. Although these results were initially treated with a degree of scepticism, a more complete temperature-dependent analysis by Slootsky et al later supported these conclusions[46].

1.1.4. Electrical Injection

While the entirety of the work covered in this thesis is based upon the optical pumping of states and fluorescence, electrical injection of carriers and electroluminescence has also been demonstrated in a microcavity and deserves a brief discussion. After the discovery of electroluminescence in 1907[54], it was many years before the first LED was produced in 1927[55]. LEDs proceeded to be largely forgotten about until 1962 when four research groups independently published reports of LED semiconductor lasers based upon GaAs crystals[56–59], three of which were printed in the same volume of Applied Physics Letters. Organic LEDs (OLEDs) followed in the 1970s and 80s[60] and though initially very inefficient (particularly in the blue region), have made themselves ubiquitous in the consumer electronics market thanks to advances in both device efficiency and fabrication techniques.

The metallic electrodes employed by LEDs have long been known to affect exciton recombination rates[61] (and hence device efficiency); they also serve to create microcavity-like confinements which can lead to the modification and enhancement of cavity emission, producing weakly-coupled (O)LEDs[62]. The next significant development was the incorporation of distributed Bragg reflectors (DBRs) into the existing structure to create microcavity-LEDs[63]. The first strongly-coupled electrically injected device was achieved in 2005 by Tischler et al[64]. This was a particularly significant accomplishment as it was achieved with organic materials and was operated at room temperature. This preceded the inorganic field by three years for devices operating at cryogenic temperatures[65–67], and six years for those at room temperature[25]. It was not long however before the more established inorganic field demonstrated the first electrically pumped (cryogenic) polariton laser in 2013 produced by Schneider et al[68] followed by a device capable of operating at room temperature the subsequent year by Bhattacharya[69].

Practical strongly-coupled electrically-injected devices have additional barriers to overcome compared to their optically-pumped counterparts. Increasing the current supplied to the device can cause the system to transition from the strong to the weak coupling regime as an abundance of free carriers screen the exciton resonance[65]. This can be observed by a change in the measured spectrum from the device: as the carrier density increases, the emission peaks corresponding to the upper and lower polariton branches disappear and are replaced by a single line corresponding to the energy of the bare cavity-photon mode. Electrical injection has

the added problem of generating triplet excited states. Triplets possess longer lifetimes than singlets and do not contribute to electroluminescence. Over time (in steady state measurements), a significant population of triplets can be built up and can lead to a significant degree of singlet quenching[70].

1.1.5. Organic Semiconductors

As stated previously, the first demonstration of strong-coupling in organic semiconductors occurred in 1998 when Lidzey et al placed a porphyrin-doped polystyrene film within a DBR-metal microcavity and observed an anticrossing in the reflectivity spectra[18]. Room-temperature polariton photoluminescence followed in the next year in a microcavity containing J-aggregates of cyanine dyes[71]. J-aggregates are formed when planar dye monomers self-assemble into larger structures under the influence of a solvent. By doing so the monomers change their spectral properties, experiencing a narrowing of absorption features which also undergo a bathochromic shift to longer wavelengths[72,73]. J-aggregates have proven to be a very popular system to study in microcavities[74–90] and the underlying physics behind them is covered in more detail in **Chapter 2**.

In 2000 Lidzey et al demonstrated the hybridization of Frenkel excitons[90]. This was achieved by placing two different aggregates of cyanine dyes (both independently capable of strong coupling and energetically separated from one another) within a microcavity. Both excitons coupled to the cavity photon-mode; two distinct anticrossings around the exciton energies were observed forming three distinct polariton branches which possessed properties (in varying proportions corresponding to the angle of observation) of both excitons and the photon mode. Shortly after this, organic polaritons were shown to interact with the vibrational modes of molecular system within the cavity[76] as had previously been observed in inorganic systems[91–93]. Hybridization of both Wannier-Mott and Frenkel excitons would later be achieved in 2006 by Holmes et al by incorporating tetraphenylporphyrin and InGaP quantum wells within the same cavity[94]. Polaritons in these cavities possessed characteristics of both excitons; exciton-exciton and polariton-polariton interaction dynamics were described in detail by Zoubi and La Rocca[95].

2003 and 2004 heralded new device architectures and materials in organic-semiconductor microcavities. Takada showed that strong-coupling was not just limited to small molecules by using a polymer previously employed in OLEDs[96] to produce a strongly-coupled microcavity with a very large Rabi splitting of 430meV[97]. Connolly et al produced the first cavity composed of two dielectric mirrors[98], and in the process attained significantly longer photon confinement times than had previously been seen using metallic mirrors. Cavities containing organic semiconductors utilising two dielectric mirrors have historically proved difficult to manufacture as the harsh conditions (high temperatures) required to deposit layers of materials such as SiO_2 or Si_3N_4 can damage the (relatively) fragile organic layer. This was eventually overcome by thermally evaporating alternating layers of LiF-TeO_2 at low temperatures on top of the organic layer. Around the same time Wenus et al produced a twin-DBR cavity by depositing the mirrors onto separate substrates and laminating the two together at an angle[99]. In the process of doing so, a wedge was formed between the two which allowed variations in cavity detuning to be explored simply by moving the region of interest across the sample. Despite the higher reflectivities of the dielectric mirrors in comparison to their metallic counterparts, photon confinement time in this structure remained low due to large scattering losses at the boundary between the mirror and sample. Other unusual architectures and fabrication have since been demonstrated. Kéna-Cohen formed empty cavities by cold-welding two mirrors together using gold strips separated by ~140nm, liquid anthracene was then allowed to permeate between the two mirrors before cooling to form a single crystal. These structures were later shown to undergo strong coupling with strong vibronic replicas[100], and later room temperature polariton lasing[53].

Building upon the work of Tischler[64], in 2010 Lodden et al optically pumped strongly-coupled tetraphenylporphyrin with electroluminescence from weakly-coupled Alq_3[101]. At a similar time, Bradley et al demonstrated that the polariton "bottleneck" observed in some systems could be overcome by placing an emissive material with spectrally broad features within the cavity[102]. If the cavity is designed such that the luminescence of this material overlaps with the energies of both the exciton and polariton, polariton populations can be optically pumped directly, bypassing the bottleneck that can occur when scattering rates are low. This result played a significant role in the development of the radiative pumping model described in **Chapter 6**[103]. Prior to these studies upon materials with high fluorescence quantum yields, most models of polariton populations in organic structures were based upon (relatively) weakly emissive aggregates in which vibrationally-assisted scattering of excitons and polaritons was the dominant mechanism of populating polariton states[75,77,79,80,82,86,104].

Organic semiconductor microcavities continue to prove themselves as interesting systems with which to study interactions between light and matter. In recent years a number of unconventional materials have proved themselves capable of entering the strong-coupling regime. Perovskites (now ubiquitous in the field of photovoltaics) [105], the light harvesting complexes of bacteria (**Chapter 8**)[106], fluorescent proteins from jellyfish[47], and recently single molecules in plasmonic cavities[107] have all been shown to form polariton states.

Whilst this chapter has provided a brief history of developments in the field, the physics behind atomic bonding, organic semiconductors and electronic transitions are described more rigorously in **Chapter 2**, and microcavities and strong-coupling in **Chapter 3**. **Chapters 4** and **5** discuss the techniques used throughout this thesis to fabricate and characterise films and microcavities, in addition to the fundamental principles behind these methods and the merits and limitations of said techniques. Finally **Chapters 6** through **9** demonstrate the strong coupling of seven different materials and attempt to explain the physics behind them.

1.2. A Timeline of Major Developments

- 1907 – Electroluminescence - Round[54]
- 1924 – Bose-Einsten condensates proposed - Einstein[35]
- 1927 – First LED - Losev[55]
- 1931 – Excitons proposed - Frenkel[24]
- 1938 – Superfluidity in Helium - Kapitza[38], Allen[39]
- 1950 – Polaritons first considered - Tolpygo[3]
- 1953 – First organic electroluminescence - Bernanose[108]
- 1956 – Quantum mechanical approach to polaritons - Fano[109]
- 1962 – First LED lasers - Hall[56], Holonyak[57], Nathan[58], Quist[59]
- 1965 – Polaritons first observed in bulk materials - Hopfield[4]
- 1970-1980 – First OLEDs[60]
- 1992 – First experimental realisation of the strong coupling regime - Weisbuch[8]
- 1995 – Bose-Einstein condensation in atoms - Anderson[41], Davis[42]
- 1998 – First strongly coupled planar microcavities (organic) - Lidzey[18]
- 2000 – Parametric polariton amplification (inorganic) - Baumberg[30,31]
- 2000 – Parametric photoluminescence (inorganic) -Stevenson[32]
- 2000 – Hybridization of Frenkel excitons - Lidzey[90]
- 2002 – BEC (inorganic) - Deng[33]
- 2003 – Polariton Lasing (inorganic) - Deng[34]
- 2003 – One atom, zero threshold laser - McKeever[49]
- 2005 – Polariton LED (room temperature, organic) - Tischler[64]
- 2006 – Polariton BEC (inorganic, second demonstration) - Kasprzak[36]
- 2006 – Hybrid Wannier-Mott-Frenkel polaritons - Holmes[94]
- 2007 – Strong-coupling in Perovskites - Brehier[105]
- 2007 – Polariton laser (room temperature, inorganic) - Christopoulos[50]
- 2008 – Polariton LED (cryogenic, inorganic) - Khalifa[65], Bajoni[66], Tsintzos[67]
- 2010 – Polariton laser (room temperature, organic) - Kéna-Cohen[53]
- 2011 – Polariton LED (room temperature, inorganic) - Lu[25]
- 2013 – BEC (organic) - Plumhof[44]
- 2013 – Ultrastrong coupling (organic) - Kéna-Cohen[22]
- 2013 – Electrically-pumped polariton laser (cryogenic, inorganic) - Schneider[68]
- 2014 – Electrically-pumped polariton laser (room temp. inorganic) - Bhattacharya[69]
- 2014 – First polariton condensate (organic) - Daskalakis[45]
- 2014 – First biological strong coupling - Coles[106]
- 2016 – Single-molecule strong coupling in plasmonic nanocavities - Chikkaraddy[107]
- 2016 – Biological polariton laser - Dietrich[47]

1.3. References

1.	Kim, J., Benson, O., Kan, H. & Yamamoto, Y. A single-photon turnstile device. *Nature* **397,** 500–503 (1999).

2.	Richard, M. *et al.* Experimental evidence for nonequilibrium Bose condensation of exciton polaritons. *Phys. Rev. B - Condens. Matter Mater. Phys.* **72,** 1–4 (2005).

3.	Tolpygo, K. B. PHYSICAL PROPERTIES OF A ROCK SALT LATTICE MADE UP OF DEFORMABLE IONS. *Ukranian J. Phys.* **509,** 93–102 (1950).

4.	Hopfield, J. J. & Thomas, D. Polariton absorption lines. *Phys. Rev. Lett.* **15,** 1–4 (1965).

5.	Skolnick, M. S., Tartakovskii, A. I., Butté, R., Whittaker, D. M. & Stevenson, R. M. High-occupancy effects and stimulation phenomena in semiconductor microcavities. *IEEE J. Sel. Top. Quantum Electron.* **8,** 1060–1071 (2002).

6.	Citrin, D. S. Excitonic radiative dynamics in multiple quantum wells. *Phys. Status Solidi* **188,** 43–55 (1995).

7.	Andreani, L. C., Romand, I. & Numdrique, D. R. Radiative Lifetime of Free Excitons in Quantum Wells. *Solid State Commun.* **77,** 641–645 (1991).

8.	Weisbuch, C., Nishioka, M., Ishikawa, A. & Arakawa, Y. Observation of the Coupled Exciton-Photon Mode Spliting in a Semiconductor Quantum Microcavity. *Phys. Rev. Lett.* **69,** 3314–3317 (1992).

9.	Savona, V. Fifteen years of microcavity polaritons. *Inst. Theor. Phys. - EPFL* (2008).

10.	Field, N. O. & Iga, K. Surface-Emitting Laser — Its Birth and Generation of New Optoelectronics Field. *IEEE* **6,** 1201–1215 (2000).

11.	Jin, Y. *et al.* Matching Photocurrents of Sub-cells in Double-Junction Organic Solar Cells via Coupling Between Surface Plasmon Polaritons and Microcavity Modes. *Adv. Opt. Mater.* **1,** 809–813 (2013).

12.	Lee, Y.-E., Kim, S.-Y., Jeong, W.-I. & Kim, J.-J. Microcavity tandem solar cells with a short circuit current higher than single cells. *Sol. Energy Mater. Sol. Cells* **114,** 59–64 (2013).

13.	Chen, S. & Kwok, H.-S. Alleviate microcavity effects in top-emitting white organic light-emitting diodes for achieving broadband and high color rendition emission spectra. *Org. Electron.* **12,** 2065–2070 (2011).

14.	Mazzeo, M., Mariano, F., Genco, A., Carallo, S. & Gigli, G. High efficiency ITO-free flexible white organic light-emitting diodes based on multi-cavity technology. *Org. Electron.* **14,** 2840–2846 (2013).

15.	Joo, C. W. *et al.* Color temperature tunable white organic light-emitting diodes. *Org. Electron.* **15,** 189–195 (2014).

16.	Soda, H., Iga, K., Kitahara, C. & Suematsu, Y. GaInAsP / InP Surface Emitting Injection Lasers. *Jpn. J. Appl. Phys.* **18,** 2329–2330 (1979).

17.	Koyama, F., Kinoshita, S. & Iga, K. Room-temperature continuous wave lasing characteristics of a GaAs vertical cavity surface-emitting laser. *Appl. Phys. Lett.* **55,** 221–222 (1989).

18.	Lidzey, D. G. *et al.* Strong exciton-photon coupling in an organic semiconductor

microcavity. *Nature* **395,** 53–55 (1998).

19. Kelkar, P. *et al.* Excitons in a II-VI Semiconductor Microcavit in the Strong Coupling Regime. *Phys. Rev. B* **52,** 5491–5494 (1995).

20. Houdré, R., Stanley, R. P., Oesterle, U., Ilegems, M. & Weisbuch, C. Room-Temperature Cavity Polaritons in a Semiconductor Microcavity. *Phys. Rev. B* **49,** 761–764 (1994).

21. Skolnick, M. S., Fisher, T. A. & Whittaker, D. M. Strong coupling phenomena in quantum microcavity structures. *Semicond. Sci. Technol.* **13,** 645–669 (1998).

22. Kéna-Cohen, S., Maier, S. a. & Bradley, D. D. C. Ultrastrongly Coupled Exciton-Polaritons in Metal-Clad Organic Semiconductor Microcavities. *Adv. Opt. Mater.* **1,** 827–833 (2013).

23. Wannier, G. H. The structure of electronic excitation levels in insulating crystals. *Phys. Rev.* **52,** 191–197 (1937).

24. Frenkel, J. On the transformation of light into heat in solids. i. *Phys. Rev.* **37,** 17–44 (1931).

25. Lu, T.-C. *et al.* Room temperature current injection polariton light emitting diode with a hybrid microcavity. *Nano Lett.* **11,** 2791–5 (2011).

26. Christmann, G., Butté, R., Feltin, E., Carlin, J.-F. & Grandjean, N. Room temperature polariton lasing in a GaN/AlGaN multiple quantum well microcavity. *Appl. Phys. Lett.* **93,** 51102 (2008).

27. Butté, R. *et al.* Room-Temperature Polariton Lasing in III-Nitride Microcavities, a Comparison with Blue GaN-Based Vertical Cavity Surface Emitting Lasers. *Proc. Spie* **7216,** 721619-721619–16 (2009).

28. Saba, M., Ciuti, C., Bloch, J. & Andre, R. High-temperature ultrafast polariton parametric amplification in semiconductor microcavities. *Nature* **414,** 731–735 (2001).

29. Lüer, L. *et al.* Size and mobility of excitons in (6, 5) carbon nanotubes. *Nat. Phys.* **5,** 54–58 (2009).

30. Savvidis, P. *et al.* Angle-resonant stimulated polariton amplifier. *Phys. Rev. Lett.* **84,** 1547–50 (2000).

31. Savvidis, P. G. & Baumberg, J. J. Angle-resonant stimulated polariton scattering in semiconductor microcavit ies. *Nonlinear Opt. Mater. Fundam. Appl.* 48–50 (2000).

32. Stevenson, R. *et al.* Continuous wave observation of massive polariton redistribution by stimulated scattering in semiconductor microcavities. *Phys. Rev. Lett.* **85,** 3680–3 (2000).

33. Deng, H., Weihs, G., Santori, C., Bloch, J. & Yamamoto, Y. Condensation of Semiconductor Microcavity Exciton Polaritons. *Science (80-.).* **298,** 199–202 (2002).

34. Deng, H., Weihs, G., Snoke, D., Bloch, J. & Yamamoto, Y. Polariton lasing vs. photon lasing in a semiconductor microcavity. *Proc. Natl. Acad. Sci. U. S. A.* **100,** 15318–23 (2003).

35. Einstein, A. Quantentheorie des einatomigen idealen Gases. *Sitzungs- berichte der Preussischen Akademie der Wissenschaften* **6,** 261–267 (1924).

36. Kasprzak, J. *et al.* Bose-Einstein condensation of exciton polaritons. *Nature* **443,** 409–14 (2006).

37. Uhlenbeck, G. E. Over Statistische Methoden in der Theorie der Quanta. (Gravenhage,

1927).

38.   Kapitza, P. Viscosity of liquid helium below the lambda-point. *Nature* **141,** 74 (1938).

39.   Allen, J. F. & Misener, A. D. Flow of Liquid Helium II. *Nature* (1938).

40.   London, F. On the bose-einstein condensation. *Phys. Rev.* **54,** 947–954 (1938).

41.   Anderson, M. H., Ensher, J. R., Matthews, M. R., Wieman, C. E. & Cornell, E. A. Observation of Bose-Einstein Condensation in a Dilute Atomic Vapor. *Science (80-.).* **269,** 198–201 (1995).

42.   Davis, K. B. *et al.* Bose-Einstein condensation in a gas of sodium atoms. *Phys. Rev. Lett.* **75,** 3969–3973 (1995).

43.   Deng, H., Haug, H. & Yamamoto, Y. Exciton-polariton Bose-Einstein condensation. *Rev. Mod. Phys.* **82,** 1489–1537 (2010).

44.   Plumhof, J. D., Stöferle, T., Mai, L., Scherf, U. & Mahrt, R. F. Room-temperature Bose – Einstein condensation of cavity exciton – polaritons in a polymer. *Nat. Mater.* **13,** 1–6 (2013).

45.   Daskalakis, K. S., Maier, S. A., Murray, R. & Kena-Cohen, S. Nonlinear interactions in an organic polariton condensate. *Nat. Mater.* **13,** 271–278 (2014).

46.   Slootsky, M., Zhang, Y. & Forrest, S. R. Temperature dependence of polariton lasing in a crystalline anthracene microcavity. *Phys. Rev. B* **86,** 45312 (2012).

47.   Dietrich, C. P. *et al.* An exciton-polariton laser based on biologically produced fluorescent protein. *Sci. Adv.* **2,** 1601.06983 (2016).

48.   Imamoglu, A., Ram, R. J., Pau, S. & Yamamoto, Y. Nonequilibrium condensates and lasers without inversion: Exciton-polariton lasers. *Phys. Rev. A* **53,** 4250–4253 (1996).

49.   McKeever, J., Boca, A., Boozer, a D., Buck, J. R. & Kimble, H. J. Experimental realization of a one-atom laser in the regime of strong coupling. *Nature* **425,** 268–71 (2003).

50.   Christopoulos, S. *et al.* Room-Temperature Polariton Lasing in Semiconductor Microcavities. *Phys. Rev. Lett.* **98,** 126405 (2007).

51.   Christmann, G. *et al.* Large vacuum Rabi splitting in a multiple quantum well GaN-based microcavity in the strong-coupling regime. *Phys. Rev. B* **77,** 85310 (2008).

52.   Li, K. *et al.* Vacuum Rabi Splitting of Exciton-Polariton Emission in an AlN Film. *Sci. Rep.* **3,** 3551 (2013).

53.   Kena-Cohen, S. & Forrest, S. R. Room-temperature polariton lasing in an organic single-crystal microcavity. *Nat. Photonics* **8,** 1–5 (2010).

54.   Round, H. A Note on Caborundum. *Electr. World* **309,** 879 (1907).

55.   Zheludev, N. The life and times of the LED — a 100-year history. *Nat. Photonics* **1,** 189–192 (2007).

56.   Hall, R. N., Fenner, G. E., Kingsley, J. D., Soltys, T. J. & Carlson, R. O. Coherent light emission from GaAs junctions. *Phys. Rev. Lett.* **9,** 366–368 (1962).

57.   Holonyak, N. & Bevacqua, S. F. Coherent (visible) light emission from Ga(As1-xPx)

junctions. *Appl. Phys. Lett.* **1,** 82–83 (1962).

58. Nathan, M. I., Dumke, W. P., Burns, G., Dill, F. H. & Lasher, G. Stimulated emission of radiation from GaAs p-n junctions. *Appl. Phys. Lett.* **1,** 62–64 (1962).

59. Keyes, R. J. & Quist, T. M. Injection luminescent pumping of CaF2:U3+ with GaAs diode lasers. *Appl. Phys. Lett.* **4,** 50–52 (1964).

60. Kallmann, H. & Pope, M. Positive hole injection into organic crystals. *J. Chem. Phys.* **32,** 300–301 (1960).

61. Friend, R. H. *et al.* Electroluminescence in conjugated polymers. *Nature* **397,** 121–128 (1999).

62. Bulović, V. *et al.* Weak microcavity effects in organic light-emitting devices. *Phys. Rev. B* **58,** 3730–3740 (1998).

63. Keller, U. *et al.* Microcavity enhanced vertical-cavity light-emitting diodes. *Appl. Phys. Lett.* **62,** 3085–3087 (1993).

64. Tischler, J., Bradley, M. S., Bulović, V., Song, J. & Nurmikko, A. Strong Coupling in a Microcavity LED. *Phys. Rev. Lett.* **95,** 36401 (2005).

65. Khalifa, a. a., Love, a. P. D., Krizhanovskii, D. N., Skolnick, M. S. & Roberts, J. S. Electroluminescence emission from polariton states in GaAs-based semiconductor microcavities. *Appl. Phys. Lett.* **92,** 61107 (2008).

66. Bajoni, D. *et al.* Polariton light-emitting diode in a GaAs-based microcavity. *Phys. Rev. B* **77,** 113303 (2008).

67. Tsintzos, S. I., Pelekanos, N. T., Konstantinidis, G., Hatzopoulos, Z. & Savvidis, P. G. A GaAs polariton light-emitting diode operating near room temperature. *Nature* **453,** 372–5 (2008).

68. Schneider, C. *et al.* An electrically pumped polariton laser. *Nature* **497,** 348–52 (2013).

69. Bhattacharya, P. *et al.* Room Temperature Electrically Injected Polariton Laser. *Phys. Rev. Lett.* **112,** 236802 (2014).

70. Yu, J., Lammi, R., Gesquiere, A. J. & Barbara, P. F. Singlet-triplet and triplet-triplet interactions in conjugated polymer single molecules. *J. Phys. Chem. B* **109,** 10025–34 (2005).

71. Lidzey, D. G. *et al.* Room Temperature Polariton Emission from Strongly Coupled Organic Semiconductor Microcavities. *Phys. Rev. Lett.* **82,** 3316–3319 (1999).

72. Jelley, E. E. Spectral absorption and fluorescence of dyes in the molecular state. *Nature* **138,** 1009 (1936).

73. Scheibe, G. Über die Veränderlichkeit des Absorptionsspektrums einiger Sensibilisierungsfarbstoffe und deren Ursache. *Angew. Chem* **49,** 563 (1936).

74. Lidzey, D. G. *et al.* Observation of strong exciton–photon coupling in semiconductor microcavities containing organic dyes and J-aggregates. *Opt. Mater. (Amst).* **12,** 243–247 (1999).

75. Lidzey, D. ., Tartakovskii, a. ., Emam-Ismail, M., Skolnick, M. . & Walker, S. Enhanced Raman scattering in a strongly coupled microcavity containing J-aggregates. *Synth. Met.*

127, 151–154 (2002).

76. Tartakovskii, a. *et al.* Raman scattering in strongly coupled organic semiconductor microcavities. *Phys. Rev. B* **63,** 121302 (2001).

77. Coles, D. M., Grant, R. T., Lidzey, D. G., Clark, C. & Lagoudakis, P. G. Imaging the polariton relaxation bottleneck in strongly coupled organic semiconductor microcavities. *Phys. Rev. B* **88,** 121303 (2013).

78. Coles, D. M. *et al.* Polariton-mediated energy transfer between organic dyes in a strongly coupled optical microcavity. *Nat. Mater.* **13,** (2014).

79. Somaschi, N. *et al.* Ultrafast polariton population build-up mediated by molecular phonons in organic microcavities. *Appl. Phys. Lett.* **99,** 143303 (2011).

80. Coles, D. M. *et al.* Vibrationally Assisted Polariton-Relaxation Processes in Strongly Coupled Organic-Semiconductor Microcavities. *Adv. Funct. Mater.* **21,** 3691–3696 (2011).

81. Litinskaya, M., Reineker, P. & Agranovich, V. M. Fast polariton relaxation in strongly coupled organic microcavities. *J. Lumin.* **110,** 364–372 (2004).

82. Virgili, T. *et al.* Ultra-fast polariton dynamics in an organic microcavity. *EPJ Web Conf.* **41,** 4015 (2013).

83. Wenus, J. *et al.* Optical strong coupling in microcavities containing J-aggregates absorbing in near-infrared spectral range. *Org. Electron. physics, Mater. Appl.* **8,** 120–126 (2007).

84. Michetti, P. & La Rocca, G. C. Simulation of J-aggregate microcavity photoluminescence. *Phys. Rev. B* **77,** 195301 (2008).

85. Ellenbogen, T. & Crozier, K. B. Exciton-polariton emission from organic semiconductor optical waveguides. *Phys. Rev. B* **84,** 161304 (2011).

86. Lidzey, D. G. *et al.* Experimental study of light emission from strongly coupled organic semiconductor microcavities following nonresonant laser excitation. *Phys. Rev. B* **65,** 195312 (2002).

87. Wenus, J., Connolly, L. G. & Lidzey, D. G. New organic materials and microcavity structures for strong exciton-photon coupling. *Phys. Status Solidi* **2,** 3899–3902 (2005).

88. Coles, D. M. & Lidzey, D. G. A ladder of polariton branches formed by coupling an organic semiconductor exciton to a series of closely spaced cavity-photon modes. *Appl. Phys. Lett.* **104,** 191108 (2014).

89. Wei, H. *et al.* Adjustable exciton-photon coupling with giant Rabi-splitting using layer-by-layer J-aggregate thin films in all-metal mirror microcavities. *Opt. Express* **21,** 21365–21373 (2013).

90. Lidzey, Bradley, Armitage, Walker & Skolnick. Photon-mediated hybridization of frenkel excitons in organic semiconductor microcavities. *Science (80-.).* **288,** 1620–3 (2000).

91. Fainstein, A., Jusserand, B. & ThierryMieg, V. Cavity-polariton mediated resonant Raman scattering. *Phys. Rev. Lett.* **78,** 1576–1579 (1997).

92. Tribe, W. R. *et al.* In- and out-going resonant Raman scattering from the cavity polaritons of semiconductor quantum microcavities. *Phys. Rev. B* **56,** 429–433 (1997).

93. Fainstein, A., Jusserand, B. & Andre, R. Polariton effects on first-order Raman scattering in

II-VI microcavities. *Phys. Rev. B* **57,** 9439–9442 (1998).

94.   Holmes, R. J., Kena-Cohen, S., Menon, V. M. & Forrest, S. R. Hybridization of Frenkel and Wannier-Mott excitons in an optical microcavity. *Phys. Rev. B* **74,** 235211 (2006).

95.   Zoubi, H. & La Rocca, G. C. Microscopic theory of nonlinear polariton interactions in strongly coupled hybrid organic-inorganic microcavities. *Phys. Rev. B - Condens. Matter Mater. Phys.* **76,** 1–9 (2007).

96.   Yuan, C. H. *et al.* Room-temperature near-ultraviolet electroluminescence from a linear silicon chain. *Appl. Phys. Lett.* **71,** 3326–3328 (1997).

97.   Takada, N., Kamata, T. & Bradley, D. D. C. Polariton emission from polysilane-based organic microcavities. *Appl. Phys. Lett.* **1812,** 22–25 (2003).

98.   Connolly, L. G. *et al.* Strong coupling in high-finesse organic semiconductor microcavities. *Appl. Phys. Lett.* **83,** 5377 (2003).

99.   Wenus, J., Connolly, L. G., Whittaker, D. M., Skolnick, M. S. & Lidzey, D. G. Tuning the exciton-photon coupling in a strongly coupled organic microcavity containing an optical wedge. *Appl. Phys. Lett.* **85,** 5848–5850 (2004).

100.   Kéna-Cohen, S., Davanço, M. & Forrest, S. Strong Exciton-Photon Coupling in an Organic Single Crystal Microcavity. *Phys. Rev. Lett.* **101,** 1–4 (2008).

101.   Lodden, G. H. & Holmes, R. J. Electrical excitation of microcavity polaritons by radiative pumping from a weakly coupled organic semiconductor. *Phys. Rev. B - Condens. Matter Mater. Phys.* **82,** 1–5 (2010).

102.   Bradley, M. S. & Bulović, V. Intracavity optical pumping of J-aggregate microcavity exciton polaritons. *Phys. Rev. B* **82,** 33305 (2010).

103.   Grant, R. T. *et al.* Efficient Radiative Pumping of Polaritons in a Strongly Coupled Microcavity by a Fluorescent Molecular Dye. *Adv. Opt. Mater.* 1–9 (2016). doi:10.1002/adom.201600337

104.   Mazza, L., Kéna-Cohen, S., Michetti, P. & La Rocca, G. C. Microscopic theory of polariton lasing via vibronically assisted scattering. *Phys. Rev. B* **88,** 75321 (2013).

105.   Bréhier, a. *et al.* Perovskite organic semiconductor: a way to hybrid microcavities. *AIP Conf. Proc.* **893,** 353–354 (2007).

106.   Coles, D. M. *et al.* Strong coupling between chlorosomes of photosynthetic bacteria and a confined optical cavity mode. *Nat. Commun.* **5,** 5561 (2014).

107.   Chikkaraddy, R. *et al.* Single-molecule strong coupling at room temperature in plasmonic nanocavities. *Nature* **535,** 127–130 (2016).

108.   Bernanose, A., Comte, M. & Vouaux, P. A New Method of Light Emission by Certain Organic Compounds. *J. Chim. Phys* **50,** 64 (1953).

109.   Fano, U. Atomic theory of electromagnetic interactions in dense materials. *Phys. Rev.* **103,** 1202–1218 (1956).

2.

Theory:
Organic Semiconductors

Organic materials can be loosely defined as compounds containing (though not exclusively) carbon and hydrogen atoms. These can be categorised into small molecules, monomers, and repeat units of monomers known as oligomers or polymers. Within these categories, an infinite number of permutations of atoms and bonds are possible allowing the electronic properties of organic materials to be tuned as desired. By changing the number and configuration of carbon atoms and the bonds between them, semiconducting behaviour can be achieved throughout the electromagnetic spectrum. They can also be designed with little to no conjugation creating a "band-gap" of >4eV causing them to act as insulators in practical applications. By careful selection of appropriate solvents, organic materials can be induced to undergo self-assembly to form larger scale structures or aggregates permitting further changes of optical and electronic properties. As the majority of fabrication techniques used with organic materials are "bottom-up", waste material and processing costs can be kept low compared to conventional "top-down" methods.

Compared to its more mature inorganic equivalent, the organic opto-electronics field is in its infancy but is a rapidly expanding field. Whilst the industry required to process silicon in large quantities is well established and has been incorporated into many facets of modern life, the energy cost of such refinement is significant and renders it unsuitable for low-cost or "disposable" electronics. Here the low-cost solution processing of organic materials has the potential to meet this demand. The technology is also being used in niche roles and high-end electronic applications, particularly in display technology where OLEDs are fast becoming the industry standard. Organic electronics can be produced in large quantities via a vast number of methods: spin coating, evaporation, blade coating, and even screen printing and have already proved their versatility by successfully being fabricated on flexible substrates[1–5].

2.1. Atomic Bonding

In 1913, Niels Bohr proposed a simple model of electrons orbiting around atomic nuclei in a circular fashion using coulombic rather than gravitational forces to keep the two bound. As charged particles cannot continue to accelerate without emitting photons, losing energy and thus spiral inwards, he proposed that there must be discrete energy levels at which stable orbits could exist. This model was corroborated by the narrow emission lines observed in hydrogen emission spectra which corresponded well with solutions to the Rydberg formula[6]. While this model accurately and quantitatively predicts the energy levels of one electron atoms (hydrogen, singly ionised helium, doubly ionised lithium, …), it fails to recognise that electrons do not orbit the nucleus in well-defined circular orbits and further breaks down when forced to describe multi-electron atoms.

Electrons are bound to atoms in discrete energy levels called orbitals (or shells) which correspond to solutions of the Schrödinger equation. The orbitals are governed by several quantum numbers which are described in **Table 2.1**. Heisenberg's uncertainty principle states that "*the more precisely the position of a particle is determined, the less precisely its momentum can be known, and vice versa*"[7]; a consequence of this is that the position of the electron within an orbital cannot be precisely known. The energy states in an atom are labelled via a number of quantum numbers. The principal quantum number n determines the size of the orbital, the shape of the orbital is determined by the orbital angular momentum quantum number l, and the orientation of the orbital is given by the magnetic quantum number m_l.

Orbital angular momentum (Azimuthal, *l*) can take any non-negative integer value and is often referred to by a letter instead of a value, a hangover from early measurements of the fine structure of atomic lines. *s*=0 "sharp", *p*=1 "principle", *d*=2 "diffuse", *f*=3 "fundamental" (or "fine"). After "*f*" the sequence continues alphabetically "*g*", "*h*", "*i*" skipping "*j*". Due to the size of these orbitals these letters are rarely encountered.

Quantum Number	Symbol	Electronic Property	Values
Principal	n	Potential energy	$n \geq 1$
Azimuthal	l	Magnitude of angular momentum	$0 \leq l \leq n-1$
Magnetic	m_l	Direction of angular momentum	$-l \leq m_l \leq l$
Spin	m_s	Direction of spin	$m_s = \pm \frac{1}{2}$

Table 2.1. *Quantum numbers defining atomic orbitals. The values for n, l and m_1 must be integers.*

As the magnetic quantum number can only take integer values between –*l* and +*l*, the *s* shell (*l*=0) is only permitted one orbital (0), the *p* (*l*=1) is permitted three (-1, 0, 1) with perpendicular orientations, and *d* (*l*=2) is permitted five (-2, -1, 0, 1, 2) etc. The two most abundant sets of orbitals are *s* and *p*, which have spherical and dumbbell shapes respectively. Pauli's exclusion principle states that "*two identical fermions (particles with half integer spin) cannot occupy the same quantum state simultaneously*"[8]; thus if two electrons are to be placed in the same orbital they already share the same quantum values for *n*, *l*, and m_l so m_s must differ. As m_s can only have one of two values (±1/2), this limits the number of electrons that can be placed in any given quantum state to a maximum of two. Thus the *s* orbitals can hold a maximum of 2 electrons, *p*≤6, *d*≤10 etc. Lower energy orbitals are filled preferentially before filling higher energy levels (e.g. 1s before 2s) as described by the Aufbau principle[9], as is depicted in **Figure 2.1 (a)**. Hund's rule of maximum multiplicity states that "*for a given electron configuration, the lowest energy term is the one with the greatest value of spin multiplicity*"[10], in practice this means that atoms will seek to place electrons singly in equal energy orbitals before placing them in pairs, **Figure 2.1 (b)**.
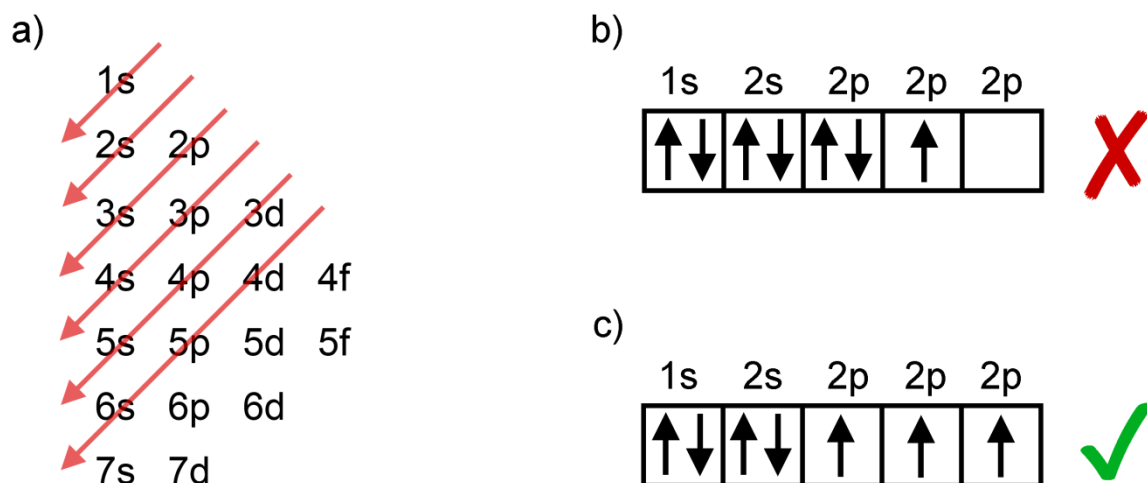
Figure 2.1. (a) *The order in which orbitals are preferentially filled according to the Aufbau principle: 1s, 2s, 2p, 3s, 3p, 4s, 3d, 4p, 5s, etc. Note that the s orbitals can contain 2 electrons, p – 6, d – 10, and f – 14.* **(b)** *Incorrect and,* **(c)** *correct orbital occupancy as governed by Hund's rule of maximum multiplicity.*

Atoms further seek to lower their total energy by filling their outermost incomplete shells; this can be achieved by sharing electrons with other atoms to form covalent bonds. Noble gasses such as helium neon and argon are often considered inert for this reason as their outermost orbits are full and are thus unlikely to participate in chemical reactions, making them commonly used in the synthesis or processing of air-sensitive compounds. Bonding occurs when orbitals from adjacent atoms overlap; if they are of the same phase, the sharing of electrons can occur and the total energy of the system is lowered. If the orbitals are of opposing phases, the two wavefunctions cancel each other out, raise the total energy of the system, and cause the atoms to repel each other. When two atomic orbitals combine, two molecular orbitals are formed, one bonding and one antibonding. If an equal or greater number of electrons are present in the antibonding orbitals compared to that of the bonding orbitals then the molecule will be unstable and will not remain bound.
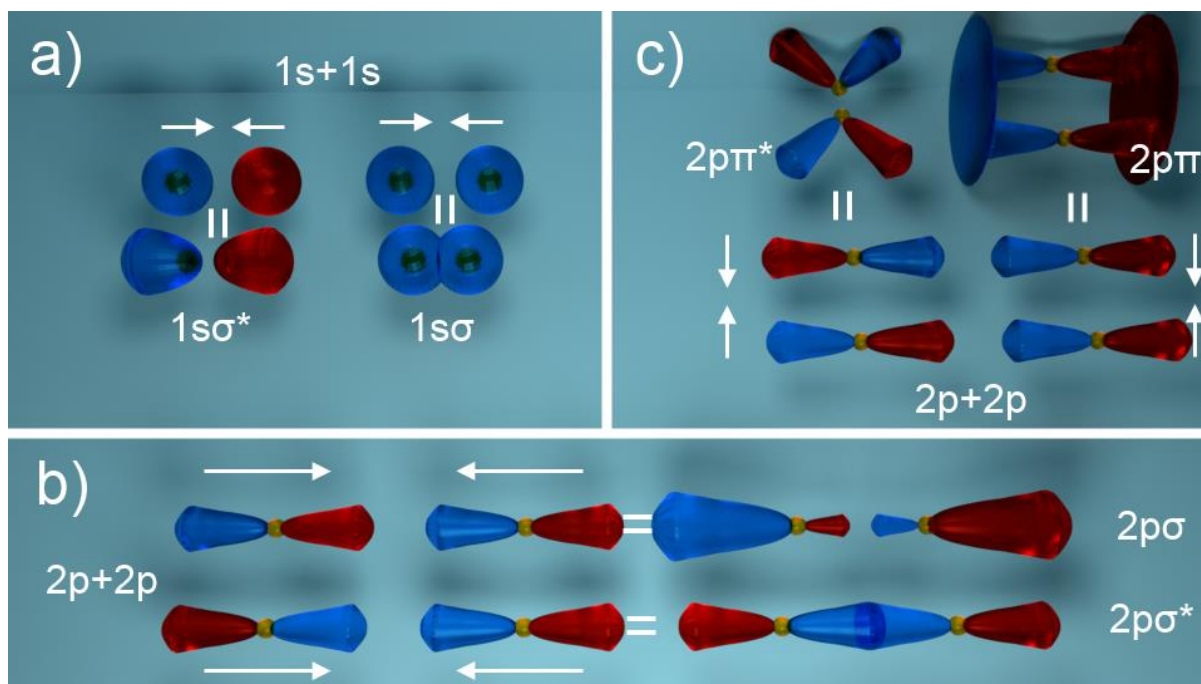
Figure 2.2. *σ and σ* bonds formed by (a) two 1s orbitals or, (b) two 2p orbitals. (c) the π and π* bonds formed by two 2p orbitals. Red and blue represent opposing phases, yellow spheres represent the nucleus position.*

Bonds can be further be categorised by the geometry of the wavefunction overlaps. If the (anti-) bonds are located along (or parallel to) the vector between the two nuclei they are known as $σ$ bonds (or $σ*$ antibonds). If the overlap between the bonds occurs perpendicular to this vector, then they are referred to as $π$ bonds (or $π*$ antibonds). Both (anti-)bonding configurations are depicted in **Figure 2.2**. It is worth nothing that $π$ bonds cannot exist when combining $1s$ atomic orbitals due to their spherical symmetry. For more complex processes it is often necessary to use the hybrid orbital approach.

2.2. Hybrid Orbitals and Conjugation

The carbon atom contains six electrons which in the neutral state adopt the configuration $1s^2 2s^2 2p^2$, of which, only the outer four ($2s^2 2p^2$) participate in chemical bonding. Before the carbon atom can bond with another atom, an electron must move from the $2s$ to the $2p$ orbital so the atom adopts the electronic configuration $1s^2 2s^1 2p^3$. Following this, the remaining 2s electron will "hybridize" with the other orbitals in one of three configurations as depicted in **Table 2.2**.
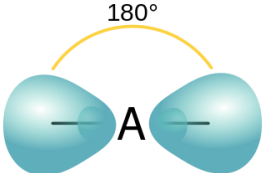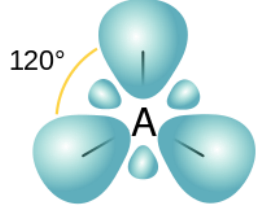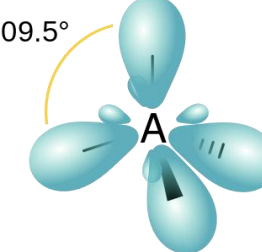
Carbon Configuration	Orbital Occupancy					Bond Angle	Bond Shape
Neutral	↑↓ 1s	↑↓ 2s	↑ 2p	↑ 2p		N/A	N/A
Promoted	↑↓ 1s	↑ 2s	↑ 2p	↑ 2p	↑ 2p	Tetragonal	N/A
sp hybrids	↑↓ 1s	↑ *sp*	↑ *sp*	↑ 2p	↑ 2p	Linear 180°	
sp² hybrids	↑↓ 1s	↑ *sp²*	↑ *sp²*	↑ *sp²*	↑ 2p	Trigonal Planar 120°	
sp³ hybrids	↑↓ 1s	↑ *sp³*	↑ *sp³*	↑ *sp³*	↑ *sp³*	Tetrahedral 109.5°	

Table 2.2. Possible hybridization pathways of carbon, spin orientations, and their resulting orbital configurations

Hybrid orbitals form strong σ-bonds between adjacent atomic nuclei. Unhybridized $2p$ orbitals are orthogonal to the hybridized bonds in the *sp* and *sp²* configurations but do not exist at all in the *sp³* configuration. They may form either σ or π bonds depending on the separation and orientation of other atomic orbitals. In plane orbitals directly between nuclei are known as σ bonds; out of plane (spatially separate) orbitals with an orientation parallel to σ bonds are known as π bonds. π bonds are weaker than σ bond and can be delocalized over a number of atoms or molecules. The nature of the bonding in molecules determines their optical and electronic properties. Three organic materials depicting three different behaviours are shown in **Figure 2.3**.
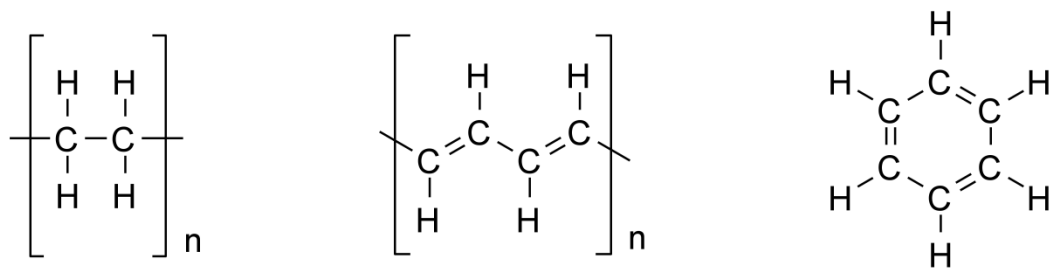
Figure 2.3. *From left to right: the chemical structure of **(a)** polyethylene: bond lengths of 0.154Å(C-C) and 0.110Å (C-H), **(b)** polyacetylene: bond lengths of ~0.135Å to 1.45 Å (C-C), and **(c)** benzene*

One of the simplest polymers to adopt the *sp³* hybridization configuration is polyethylene. It is an insulating material as all of the bonds in the outermost orbitals are saturated with hydrogen or other carbon atoms. It forms a planar structure with ~110° between each carbon atom. All bonds in this polymer are highly localised σ bonds.

Polyacetylene is very similar polymer to polyethylene except that it has undergone *sp²* hybridization and the σ bond between a carbon and hydrogen atom has been replaced with a 2*p* π bond between carbon atoms spatially separated from, but parallel to, the plane of the polymer. If a material contains a backbone of alternating single and double carbon bonds, it is said to be conjugated. π bonds are not restricted to a single atom and can be delocalised along the length of the (conjugated) chain. It is these orbitals that determine the size of the bandgap of a material.

Theoretically if all of the carbon bonds in a polyacetylene chain were of equal length, π electrons would be able to delocalize across the length of the chain and the polymer would act as a one-dimensional metal. In practice however this is not the case as polyacetylene behaves as a semiconductor. This is because π-π bonds alternate between relatively weak and strong which cause the length of the bonds to vary (~0.135Å to 1.45 Å), a phenomena known as Peierls' instability which states that "*a one-dimensional equally spaced chain with on electron per ion is unstable*"[12]. The displacement of atoms from their ideal unit spacing opens up an energy gap at the Fermi level; the greater this displacement is, the larger the gap between levels.

In benzene six hybridized sp^2 σ bonds form a planar hexagonal structure two with two sp^2 σ remaining to bond with additional carbons. The remaining six unhybridized 2p orbitals form delocalised π bonds above and below the atom. These create aromatic rings on opposing sides of the plane of atomic nuclei, three bonding above and three antibonding below, see **Figure 2.2**. The lowest energy configuration of this system exists when the three lowest energy orbitals are filled and the three highest energy orbitals remain empty. The highest occupied molecular orbital (**HOMO**) and lowest unoccupied molecular orbital (**LUMO**) define the bandgap of the material and can be thought of as analogous to the valence and conduction bands in inorganic semiconductors. While there are six π orbitals in benzene, they only occupy four energy levels. Two π orbitals have unique energies (the highest energy antibonding and lowest energy bonding) and the remaining four are split into two pairs with each pair having a different energy. The electrons within each pair share the same energy level are said to be degenerate[13].

Whilst these are relatively simple materials, complex organic structures can be designed using the same principles through the linear combination of atomic orbitals (**LCAO**) approach to describe the properties of far more complex materials.

2.3. Optical Absorption and Electronic Transitions

Absorption can be defined as the transfer of energy from a photon to an atom by the promotion of a bound electron to a higher energy state. The photon must be resonant with (or close to) the energy separation between the LUMO and HOMO levels, as defined by **Equation 2.1**. Here E_γ is the photon energy, h represents Planck's constant, c the speed of light, v the photon frequency and λ is the photon wavelength.

$$E_\gamma = hv = \frac{hc}{\lambda} = E_{LUMO} - E_{HOMO} \qquad \textbf{(2.1)}$$

The likelihood of a photon being absorbed by a molecule (2D cross section) is given by the absorption cross section, $\sigma(\lambda)$, which is the product of the number of potential absorbers, n_1, and their individual absorption coefficients, $\alpha(\lambda)$, which have a wavelength dependence.
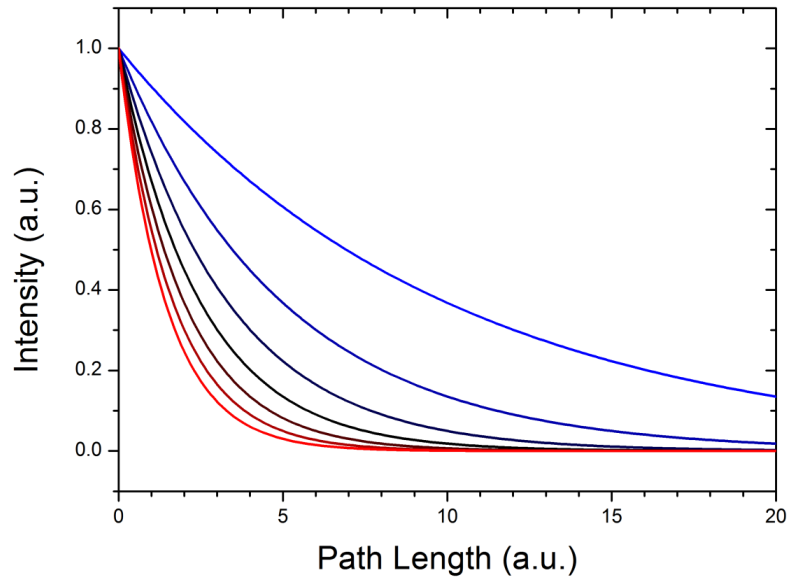
Figure 2.4. *The attenuation of light passing through an absorbing medium as a function of path length for a series of otherwise identical materials with absorption cross-sections ranging from 0.1 (blue) to 0.7 (red).*

The greater the volume of material through which light travels (i.e. the longer the path length l), the more it will be attenuated, as described by the Beer-Lambert law[14]. The intensity of a beam at a given distance into an absorbing medium is given by **Equation 2.3**, and shown in **Figure 2.4**. Here I_0 represents the initial intensity of the beam and I_l the intensity of the beam after passing through a material of path length l.

$$\alpha(\lambda) = n_1 \sigma(\lambda) \tag{2.2}$$

$$I_l = I_0 e^{-\alpha(\lambda)l} \tag{2.3}$$

By taking transmission measurements of films or solutions of known path length, the total absorption of a material and hence its extinction coefficient κ can be determined, **Equations 2.4** and **2.5**. A 0.43 scaling factor is applied to correct for the fact that logarithms of base 10 are used rather than natural logarithms.

$$\frac{I_{l,\lambda}}{I_{0,\lambda}} = e^{-\alpha(\lambda)l} = T(\lambda) \tag{2.4}$$

$$A(\lambda) = 0.43\alpha(\lambda)l = -log_{10}\left[\frac{I_{l,\lambda}}{I_{0,\lambda}}\right] = -log_{10}T(\lambda) \tag{2.5}$$

From κ, both the imaginary and complete refractive index of a material can be worked out (**Equations 2.6** and **2.7**). It is an important value when modelling the optical properties of photonic structures and other molecular materials. Using the Kramers-Kronig relations, the real part of the refractive index n, can be separated from the imaginary.

$$\alpha(\lambda) = \frac{4\pi\kappa(\lambda)}{\lambda} \tag{2.6}$$

$$\bar{n} = n + i\kappa \tag{2.7}$$

The HOMO and LUMO levels of a molecule are analogous to the ground (S_0) and first excited (S_1) states and can be represented (crudely) by the energy curves in **Figure 2.5**. If an incident photon encounters a semiconductor and satisfies the requirements of **Equation 2.1** such that $E_\gamma = E_{LUMO} - E_{HOMO}$, it may be absorbed by the material and its energy used to promote an electron from the ground state to the first excited state. When an electron is promoted to a higher energy state, it leaves behind a vacancy in its shell known as a hole. The negatively charged electron experiences a coulombic attraction with the positively charged hole (and repulsion from other electrons) to form an electrically neutral quasiparticle called an exciton; the bound exciton has a lower energy than the unbound electron and hole.
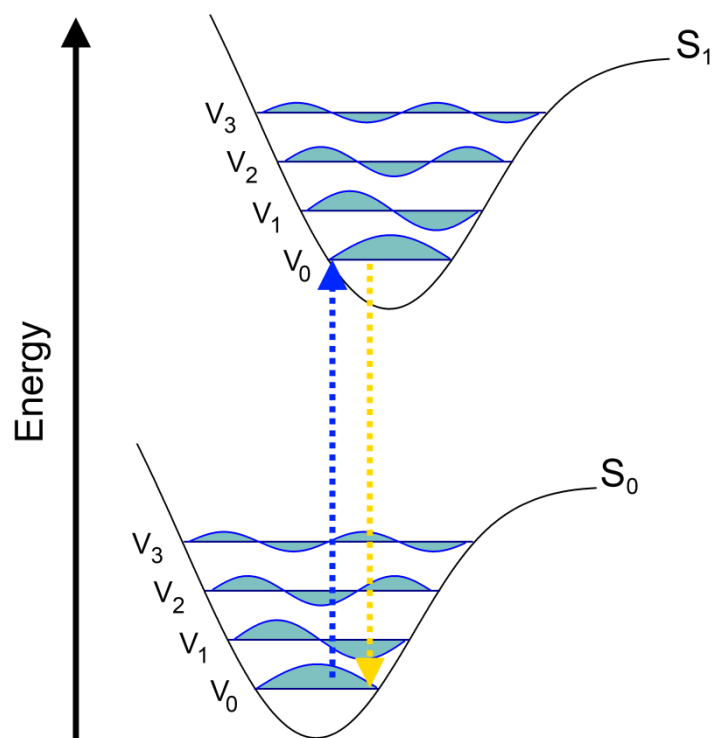
Figure 2.5. *The ground state, S_0, and first excited singlet state S_1. The lowest sublevel within each state is depicted with a solid line, and each vibrational level above it is depicted with a sinusoidal line and marked with V_0, V_1, ..., V_n. Blue arrows denote the promotion of electrons via optical absorption, yellow arrows denote the return of an electron to the ground state via the spontaneous emission of a photon.*

Inorganic semiconductors typically have large dielectric constants which result in high electric field screening of the coulombic interaction between electrons and holes. A consequence of this is that the two are much less tightly bound, have a larger radius and are much likely to be thermally disassociated. This kind of exciton is referred to as a Wannier-Mott exciton and typically has a binding energy in the order of 1-10meV. By contrast organic materials generally have very small dielectric constants. They experience much less electric field screening so the excitons present are much more tightly bound. These are known as Frenkel excitons and typically have binding energies tens or hundreds of times higher than those of Wannier-Mott excitons. Frenkel excitons are very highly localised and it is not unusual for them to be entirely located on one molecule (e.g. fullerenes).
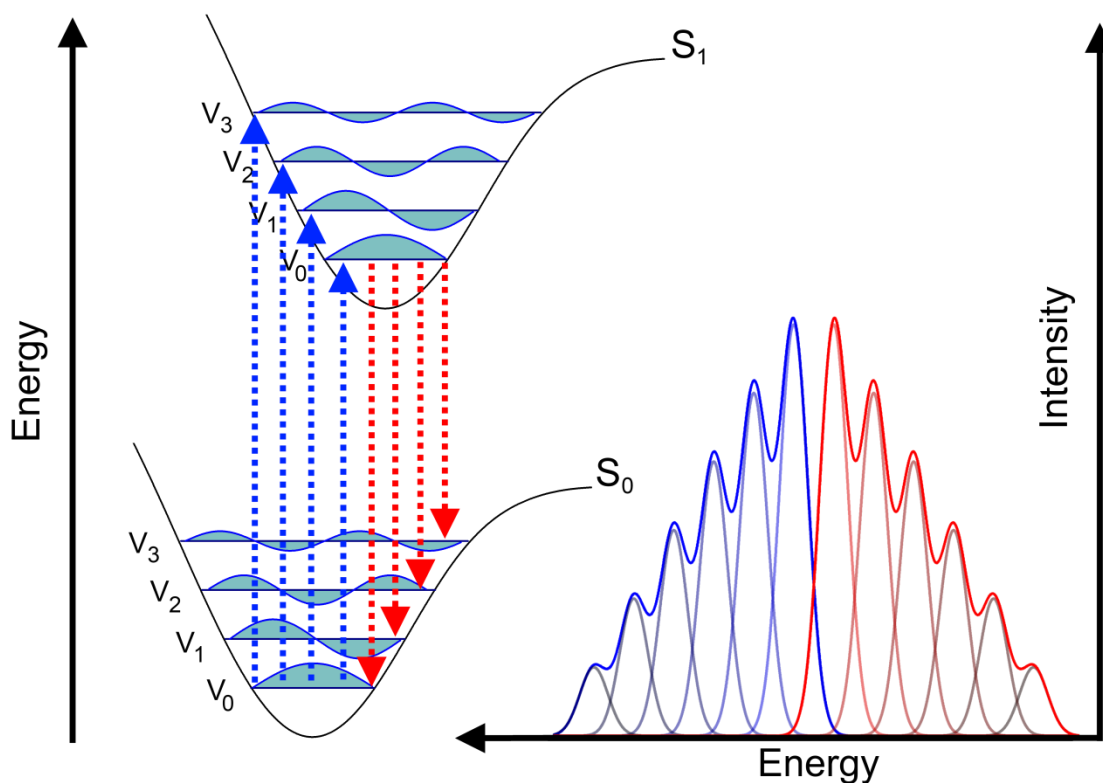
Figure 2.6. *Electronic transitions between different vibrational sublevels of the S_0 and S_1 states. Absorption is marked by blue lines and emission, red. A consequence of the Franck-Condon principle is that the two spectra are (typically) mirror images of one another.*

If a photon of greater energy than the minimum separation between the HOMO and LUMO levels is absorbed, the excess energy allows it to jump into one of the higher energy vibrational modes; likewise if the electron is located in one of the ground state vibrational levels (possibly due to thermal assistance), the energy required to promote the electron is lower and a longer wavelength photon can be used. Vibrational sublevels within each state are represented with sinusoidal lines in **Figures 2.5** and **2.6**. At room temperature, the thermal energy of the system is generally such that the electrons will reside in the lowest vibrational energy level v_0.

Excited states in organic semiconductors typically have lifetimes on the order of 1-10ns before experiencing recombination. Vibronic relaxation to the lowest energy level within an excited state after photo-excitation occurs on timescales of ≤1ps. After this relaxation occurs, the exciton has a chance to return to the ground state (or one of its vibronic sublevels) through the emission of a photon; a process called fluorescence. Fluoresence occurs at equal or lower energies to absorption; the energy separation between the peak absorption and fluorescence energy is referred to as the Stokes shift.

If an electron returns to the one of the ground-state vibronic levels, the energy separation between states is smaller and thus the photon emitted is of longer wavelength. This is evidenced by vibronic replicas in measured fluorescence spectra and their corresponding partners in absorption. The likelihood of a transition to or from a vibronic energy level to another is proportional to the degree of overlap between the two vibrational wavefunctions. This is known as the Franck-Condon principle, it assumes that there is no nuclear motion during the absorption process due to its speed (on the order of femtoseconds), and thus can be considered stationary throughout the transition. It is valid for all excitonic transitions.

Excitons can be further classified into singlet and triplet states. Singlet excitons are defined as a molecular electronic state in which all electron spins are paired i.e. the electron in the excited state is of opposing spin to the remaining electron in the lower energy state. Electrons possess a spin of ½ and may combine with another carrier (electron or hole) to give a total angular momentum S of 0 or 1.

$$\psi_{S_1} = |0,0\rangle = \frac{(\uparrow\downarrow - \downarrow\uparrow)}{\sqrt{2}} \Bigg\} \; s = 0 \; (singlet) \tag{2.8}$$

$$\psi_{S_1} = \begin{matrix} |1,1\rangle & = & (\uparrow\uparrow) \\ |1,0\rangle & = & \dfrac{(\uparrow\downarrow + \downarrow\uparrow)}{\sqrt{2}} \\ |1,-1\rangle & = & (\downarrow\downarrow) \end{matrix} \Bigg\} \; s = 1 \; (triplet) \tag{2.9}$$

When two spin ½ particles combine with matching orientations ($\uparrow\uparrow$ or $\downarrow\downarrow$), three symmetric configurations are possible, and these are known as triplet states. The Pauli exclusion principle forbids two fermions with identical spin orientation to be in the same orbital, thus it is not (typically) possible to have S_0 triplets and the ground state is always a (spatially antisymmetric) singlet state.
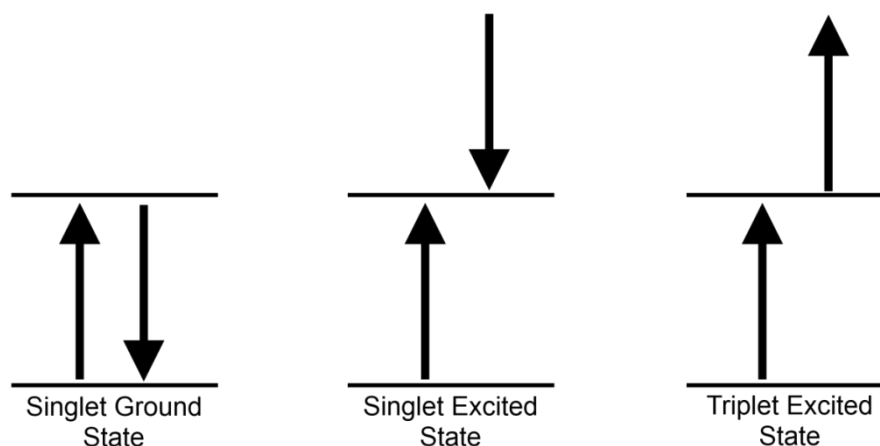
Figure 2.7. *Spin orientations of singlet and triplet states. Triplet states possess two unpaired parallel electronic spins and are generated through internal conversion from higher energy singlet states. In singlet states, no net spin angular momentum exists (m_s=0) because all electronic spins are paired.*

These transitions are determined by selection rules which state that parity must be conserved when an electronic transition occurs. For an optical transition to occur, the total spatial angular momentum ΔL must change by 1. From the S_0 to S_1 transition ΔL=1, but from S_1 to T_1, or S_0 to T_0, ΔL=0. It is for this reason that all exciton states created through photo-excitation are singlet states as the formation of triplet states is spin forbidden. By contrast, electrical injection of carriers results in a mere 25% of singlet states with the remaining 75% of excitons being triplets. This is shown more clearly by **Equations 2.8** and **2.9** which reveal that there is only one possible singlet electron configuration, but three triplet configurations.

It is possible for a transition between the S_1 and T_1 states, but one particle must undergo a spin flip, this is known as intersystem crossing. This happens via spin-orbit coupling in which the spin and spatial components of a particle's angular momentum can interact with one another and exchange energy. The spontaneous emission of a photon from a triplet state is spin forbidden. This does not mean that emission from triplet states is impossible, but that it is selection rule forbidden and thus the triplet states are generally much longer lived than their singlet counterparts. The process is called phosphorescence and timescales are on the order of milliseconds to hours. The exciton may also undergo a second spin flip before this happens and return to a singlet state before decaying via delayed fluorescence. All possible electronic transitions can be depicted are shown in **Figure 2.8**.
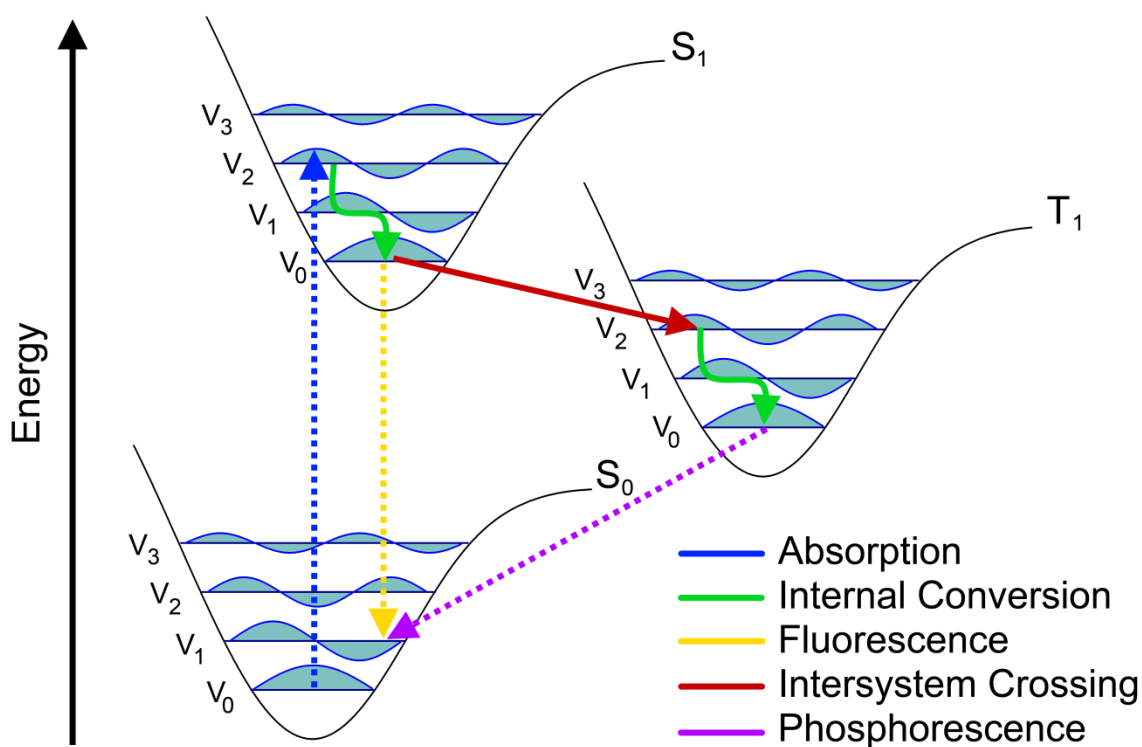
Figure 2.8. *All possible electronic transitions within a system. It is worth nothing that due to electron repulsion, excited triplet states are lower energy and spatially asymmetric Transitions marked by dotted lines involve the absorption or emission of a photon.*

Triplet states are often useful in certain structures such as organic light emitting diodes. The increased lifetime increases the chance of the exciton undergoing a spin flip. This interaction is enhanced in materials containing more massive atoms with larger angular momenta. In systems where this is desired it is not unusual for materials to contain heavy metal complexes such as rubidium or more recently thermally activated delayed fluorescence (**TDAF**) materials. Triplet states are lower energy than their singlet counterparts. Whilst they are spin symmetric, the totality of the wavefunction must be antisymmetric, thus their orbitals are spatially anti-symmetric. This means that there is a node in the middle of the molecule so the electrons are further apart, experience less electron-electron exchange energy repulsion, and hence the triplet state has lower energy.

The energy levels of a molecule can be influenced by an external electric field, an effect called the electrochromic or Stark effect. The molecule can be treated similarly to a coupled oscillator system. Atoms can be considered as point masses, and bonds as springs which preferentially

exist at their equilibrium length. Any distortion of the springs (extension or compression) increases the energy of the system. Atomic nuclei and bonds can oscillate at discrete frequencies which appear as vibronic sublevels in Jablonski diagrams and features in the absorption and emission spectra.

Some materials possess very high energy vibrational levels in the ground state (particularly at high temperatures), which may overlap with the lowest energy vibrational levels of the excited state. If this is the case, the system can vibronically relax directly into the S_{0v0} state. Other non-radiative decay pathways include: collisional deactivation - the transfer of energy to neighbouring molecules through physical collision (gaseous or liquid phase); Phonon emission - the emission of a lattice or molecular vibration (solid crystalline phases); or Forster resonant energy transfer (**FRET**) – the coupling of two physically near dipoles which allows the excited state of a donor dipole to transfer to an acceptor dipole in the ground state.

2.4. Molecular Aggregation

In certain circumstances, molecules may alter their electronic properties by assembling into larger structures, these are referred to as aggregates. This generally occurs when hydrophobic molecules are placed into polar solvents; strong intermolecular van der Waals-like attractive forces draw the individual molecules to one another. In these cases, the electronic excited state may be delocalised over some or all of the aggregate instead of being localised to a single molecule.

One form of aggregation causes the absorption band to (bathochromically) shift to longer wavelengths and reduce the absorption bandwidth (with respect to the original spectrum of the unaggregated monomer). This type of aggregation is referred to as "J-aggregation" after the scientist E.E. Jelley who discovered the phenomemon in 1936[15,16]. This kind of aggregation is commonly found in cyanine and squarine dyes and an example of which is shown in **Figure 2.9**. If the aggregate absorption spectrum is shifted to shorter wavelengths, it is said to have undergone a hypsochromic shift and is referred to as a "H-aggregate". H-aggregates exhibit little to no fluorescence.
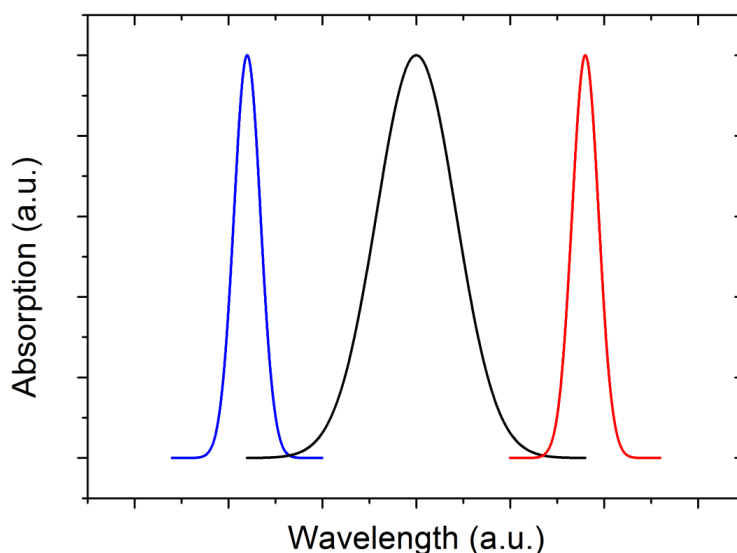
Figure 2.9. *The absorption spectra of a monomer (black) undergoing a hypsochromic shift to form a H-aggregate (blue) or bathochromic shift to form a J-aggregate (red)*

Molecules in J- and H- aggregates typically form one of several patterns, all of which can be treated as a one-dimensional assembly and modelled using only nearest neighbour interactions. They can take the form of several patterns shown in **Figure 2.10**. "Brickwork" pattern: individual units are stacked linearly in parallel with one another with each row/column offset by one half unit length. "Staircase" pattern: individual units are stacked vertically but offset by one half unit length in the same perpendicular direction. "Ladder" pattern: individual units are stacked vertically and offset by one half unit length in alternating directions. H-aggregates are stacked plane-to-plane; J-aggregates are stacked end to end with a slight angular offset from one another.

Figure 2.10. (a) *Ladder-type, **(b)** Staircase-type, and **(c)** brickwork-Type stacking arrangements for J- and H- aggregates.*

The number of interacting molecules (n) that form the aggregate provides an upper limit to the number of excitons (X_n) states that can exist on the aggregate. Each excited electronic state is split into $\binom{n}{i}$ sub-states in which i is the i-exciton state and can take any quantum number k. The simplest system is one in which there is only one exciton (X_1), which is split into n energy levels (k_1, k_2, ..., k_n) centred around the monomer energy, E_{mon}, the energy of which is given by **Equation 2.10**, in which V is the interaction potential.

$$E_k = E_{mon} + 2V\cos\left(\pi\frac{k}{n+1}\right) \tag{2.10}$$

In J-aggregates the dipoles are aligned parallel to one another but possess an angular offset between adjacent dipoles. V is thus negative and k_1 is the lowest energy state. In H-aggregates, dipoles are parallel to each other, but there is no angular displacement between adjacent dipoles. Here V is positive and the highest possible excited energy state is k_1.

The oscillator strength F, of any given transition from the ground state to a specific energy level is given by **Equation 2.11** in which μ_{mon} is the monomer dipole moment. F is a dimensionless quantity that determines the likelihood of an electronic transition between two levels. Transitions with high oscillator strengths are evidenced in absorption and emission spectra as having higher intensities than transitions with low oscillator strengths. From **Equation 2.11**, it can be seen that only transitions for which k is odd have any oscillator strength, and that the greatest total oscillator strength is found in the k=1 transition; in the case where $n\to\infty$ (an infinitely large aggregate) ~81% of the oscillator strength of all transitions is found in k=1.

$$F_k = \left[\mu_{mon}\sqrt{\frac{2}{n+1}}\frac{1-(-1)^k}{2}\cot\left(\frac{\pi k}{2(n+1)}\right)\right]^2 \tag{2.11}$$

In the case where two excitations are located on the aggregate (X_2), two quantum numbers are required in order to describe the sub levels a and b, in the format $k_{1,b}$. The Pauli exclusion principle means that a and b cannot be equal otherwise they would occupy the same quantum state simultaneously, thus a can range from 2→n and b from 1→n-1, subject to the constraint that $a>b$. The X_2 state is split into $\frac{n(n-1)}{2}$ energy levels, centred around an energy twice that of the monomer exciton energy; each of these sublevels can be described by (as in the X_1 case) by averaging the solutions determined using values of k_a and k_b individually[17,18].
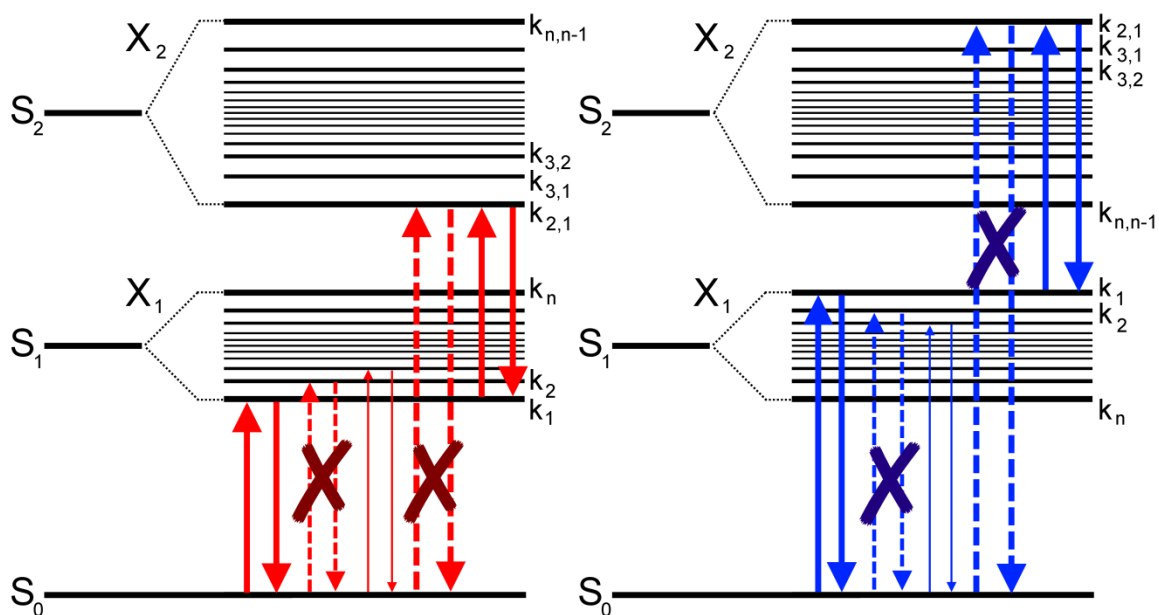
Figure 2.11. *The allowed (solid) and forbidden (dashed) optical transitions in J-aggregated (left, red) and H-aggregated (right, blue) systems. The relative oscillator strengths of transitions is indicated by linewidth of the transition.*

As direct transitions can only occur between adjacent energy levels, transfers from the ground state to the X_2 transition are forbidden and cannot be observed in steady state measurements. The X_1 state must be used as an intermediary transition between the two; X_2 (and higher) states can only be probed using non-linear techniques. The allowed energy levels and transitions for both forms of aggregates are depicted in **Figure 2.11**. The oscillator strengths for these higher transitions are given by references[17,18] which reveal that ~70% of the total oscillator strength is located in the $X_1k_1 \rightarrow X_2k_{2,1}$ transition in J-aggregates.

It is important to note that the size of the vibrational or electronic aggregate need not correspond with the spatial dimensions of the physical aggregate.

2.5. Carotenoids, Polyenes, and Biological Systems

Polyenes are defined as polymer chains that contain a minimum of three alternating single and double conjugated carbon bonds. Carotenoids are pigments with strong absorption features produced in nature by a variety of (predominantly photosynthetic) organisms. Carotenoids are often terminated with functional groups though they also possess a "backbone" of conjugated carbon atoms and are thus a subset of polyenes.

Whilst the models used in the previous sections can accurately describe the energy levels of a multitude of polymers and aggregates, they tend to break down when describing carotenoids and polyenes in general. This is because the model tends to neglect the electronic correlation of the system which can be defined as the interaction between electrons in the electronic structure of a quantum system; this can result in slight deviations from exact solutions of the Schrödinger equation and becomes more significant in materials with high degrees of spatial (thus rotational) symmetry.

From here it is beneficial to adopt spectroscopic notation for materials with the C_{2h} point group symmetry[19]: Labels A and B refer to the symmetry or antisymmetry upon 180° rotation; subscripts g and u denote symmetry or antisymmetry with respect to spatial inversion (from the german, *gerade* and *ungerade*); the superscripts "+" and "-" designate pseudoparity elements derived from orbital pairing relationships[20,21]. In order for any photon-facilitated transition to occur, the only transitions that are allowed are ones with opposing symmetry in all three parameters e.g. $1A_g^- \rightarrow 1B_u^+$ or $2A_g^- \rightarrow nB_u^+$. For all materials with a centre of inversion, the lowest lying (ground) state is the $1A_g^-$.

If electron-electron correlation is ignored, the symmetry of electronic states simply alternates between A&B, +&-, and g&u as energy increases as depicted in **Figure 2.12 (b)**; this is the case for most polymers (and polyenes with short conjugation lengths)[20,22,23]. If however this correlation is accounted for in long-chain polyenes, the excited states adopt a different configuration (**Figure 2.12 (c)**) and the $2A_g^-$ state replaces the $1B_u^+$ state as the lowest-lying excited state[21,24–26]. As this state is dipole-forbidden due to equivalent symmetries, it cannot be directly accessed from the ground state and must be reached through relaxation from the higher

energy $1B_u^+$ energy state which is dipole-permitted. This relaxation occurs on much smaller timescales than immediate radiative decay ($1B_u^+$ [S_2] → $1A_g^-$ [S_0]) to the ground state, leaving the exciton in a "dark" inaccessible state from which it is not permitted to radiatively decay ($2A_g^-$ [S_1] → $1A_g^-$ [S_0])[27].
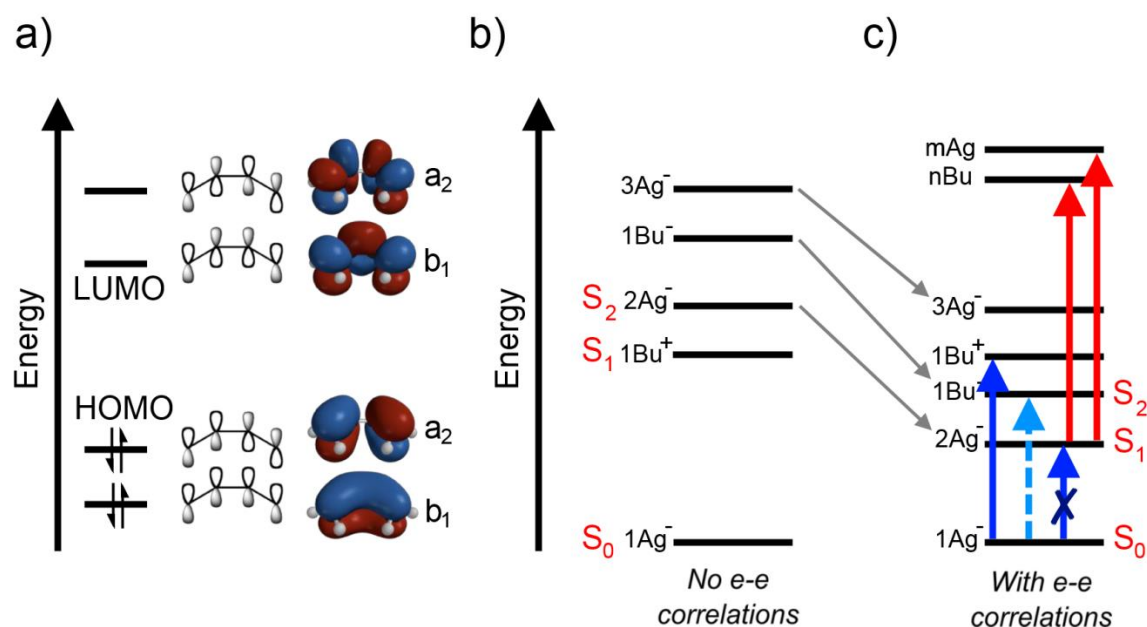

Figure 2.12. (a) *Relative energy of bonding and anti-bonding molecular orbitals of butadiene (C_{2v} symmetry due to cis conformation of central bond) and how they arise from atomic orbitals. The energy of each orbital increases with the number of nodes present (orbital symmetry labels are lower case to distinguish them from electronic state symmetry labels). Orbital and spatial symmetry alternate as energy is increased.* **(b)** *Alternating symmetry and energy levels of excited states without accounting for electron-electron correlation.* **(c)** *Symmetry states of different excited states accounting for electron-electron correlation. The $1B_u^-$ state is rarely seen or discussed in the literature. Image adapted from Musser[19]. Blue arrows indicate transitions capable of being observed in steady state measurements, red arrows require two-photon techniques.*

The energy separation, relative positions, and excited state lifetimes of the S_1 and S_2 states are determined primarily by the conjugation length along the polyene backbone; the degree of planarity, aromaticity, and presence (or lack thereof) of electron withdrawing/releasing substitutions also contribute to the shape and size of the optical bandgap, but to a lesser extent. In shorter chain (where the number of conjugated double bonds, N, is less than 5) polyenes, conventional A→B→A symmetry is preserved and direct transitions between the S_0 and S_1 states are permitted. In longer (N>5) chain polyenes electron-electron correlation becomes more significant and the A→A→B configuration is adopted.

Carotenoids possessing eight or fewer conjugated double bonds exhibit (very weak) features in emission spectra corresponding to the S_1 to S_0 transitions. However this fluorescence becomes steadily weaker as chain length increases, and in longer-chromophore carotenoids comes predominantly from the S_2 to S_0 transition. In dilute solutions at low temperatures it is possible to observe direct emission from the S_1 ($2^1A_g^-$) to S_0 ($1^1A_g^-$) transition in octatetraene with a quantum yield of almost 1. As chain length increases, the ratio of $[S_2{\rightarrow}S_0]{:}[S_1{\rightarrow}S_0]$ emission increases and the fluorescence quantum yield diminishes. For carotenoids such as lycopene and beta carotene, the S_1 to S_0 emission yields are effectively non-existent ($<10^{-5}$), and it is for this reason that longer-chain polyenes are considered to be virtually non-emissive.[28]

The changeover from S_1 to S_2 emission can be explained by the increase in non-radiative decay rates between the S_1 and S_0 states; a consequence of both the reduced S_1 to S_0 energy gaps in longer chains (the bandgap diminishes in energy as conjugation length increases, causing the material to take on a "redder" appearance) and the increased density of S_0 accepting modes[28]. Transitions in carotenoid absorption and emission spectra tend to be very broad and are dominated by vibronic features. This can make it difficult to determine which transition emitted light originated from in the case where there is emission from both excited states; this is only the case for one or two values of N, otherwise the nature of the emission is generally unambiguous.

The behaviour of these transitions can be explained with either molecular orbital theory or the free electron "particle in a box" model[29]. Both of which predict that the energy of the S_0 to S_2 transition can be estimated by **Equation 2.12**[28]. Here N refers to the number of conjugated double carbon bonds in a carotenoid or polyene, the presence of additional side-groups or functional at the end of the molecule does not significantly alter this relationship. If there is a double bond to the functional group or an oxygen atom at the end of the carotenoid, this adds an additional 0.5 to the value of N. A and B refer to the energies of the S_1 and S_2 transitions in wavenumbers.

$$\Delta E = A + \frac{B}{N} \qquad\qquad (2.12)$$

There exists experimental data which suggests that there is an asymptotic limit of ~700nm for the $S_0 \rightarrow S_2$ transition in infinitely long polyenes and carotenoids. In this case $A \approx 14,000$ cm^{-1}, which is in contrast to cyanine dyes and other linearly conjugated systems which do not possess alternating carbon bond lengths and have a value of $A \approx 0$. In carotenoids phosphorescence from triplet states is almost entirely absent and cannot compete with the rapid relaxation that occurs between the T_1 and S_0 states.

It is worth noting that the selection rules which govern these transitions are based upon idealised geometries that obey group theory symmetry and as such are only approximate descriptions of real molecules. A consequence of this is that some transitions are not outright forbidden but weakly allowed, particularly particle-hole symmetry ("+" and "-" superscripts) allowing $1A_g^-$ [S_0] $\rightarrow 1B_u^-$ [S_2] transitions to occur[21].

Whilst we cannot probe the S_1 state directly using steady-state techniques, they can be studied using pump-probe or two photon-techniques. Femtosecond lasers are used to excite carotenoids from the ground state to the S_2 level, from here they relax to the lowest vibrational level of the S_1 state. The S_1 state is then probed using an infrared laser. Subtracting the energies of the $S_1 \rightarrow S_2$ transition from the $S_0 \rightarrow S_2$ transition reveals the energy of the S_1 state.
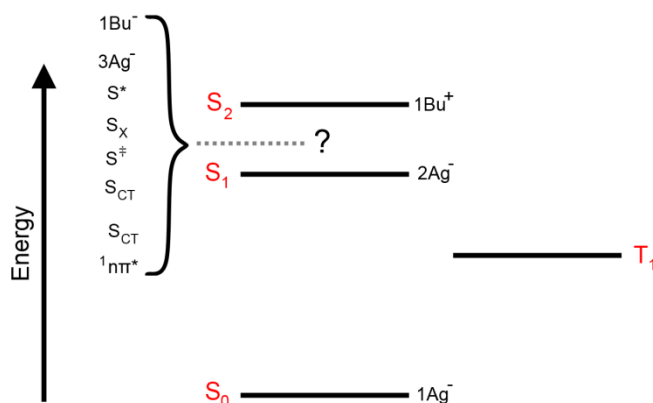

Figure 2.13. *Energy levels of other potential forbidden excited states in the vicinity of S_1 ($^1A_g^-$ and $^1B_u^-$ symmetry).*

Slight variations upon this technique in conjunction with semi-empirical and *ab-initio* quantum calculations[24,30–32] have suggested that there may be additional excited singlet states close to the energy of the S_1 state. These are depicted in **Figure 2.13**, but unfortunately lie beyond the scope of this thesis. *Ab-initio* calculations for intermediate length chains ($5 \leq N \leq 15$) are now feasible, but remain cost-prohibitive for longer carotenoids.

2.6. Summary

Organic semiconductors, and aggregates thereof, are used throughout this thesis as the active layers in strongly-coupled microcavities. In order to determine which materials are most appropriate for this purpose, it is first necessary to understand the optical and electronic properties that define them.

In this chapter we have discussed the nature of atomic bonding between single atoms. From this we have expanded into the hybridization of carbon orbitals and described the characteristics of larger conjugated systems and how their bandgaps are formed. The creation and properties of singlet and triplet states and the rules that govern transitions between the two are explored.

Following this we discussed how the spectral properties of monomers change as they undergo hypso- or batho-chromic shifts to form H- and J-Aggregates. Finally we present the special case of carotenoids, materials with a high degree of spatial symmetry that possess inverted electronic symmetry.

It is important to note that many of the materials explored in this thesis are generally quite disordered or amorphous in nature and as such transitions between bands are broader and less well defined.

2.7. References

1.   Krebs, F. C. Fabrication and processing of polymer solar cells: A review of printing and coating techniques. *Sol. Energy Mater. Sol. Cells* **93,** 394–412 (2009).

2.   Sondergaard, R. R., Hosel, M. & Krebs, F. C. Roll-to-Roll fabrication of large area functional organic materials. *J. Polym. Sci. Part B Polym. Phys.* **51,** 16–34 (2013).

3.   Eggenhuisen, T. M. *et al.* Organic photovoltaic cells with all inkjet printed layers and freedom of form. *2014 IEEE 40th Photovolt. Spec. Conf. PVSC 2014* **2,** 2842–2845 (2014).

4.   Hösel, M., Søndergaard, R. R., Jørgensen, M. & Krebs, F. C. Fast Inline Roll-to-Roll Printing for Indium-Tin-Oxide-Free Polymer Solar Cells Using Automatic Registration. *Energy Technol.* **1,** 102–107 (2013).

5.   Carlé, J. E. *et al.* Upscaling from single cells to modules – fabrication of vacuum- and ITO-free polymer solar cells on flexible substrates with long lifetime. *J. Mater. Chem. C* **2,** 1290 (2014).

6.   Bohr, N. Rydberg's discovery of the spectral laws. in *Rydb. Centen. Conf.* (Lund University, 1954).

7.   Heisenberg, W. Uber den anschaulichen Inhalt der quantentheoretischen Kinematik und Mechanik. *Zeitschrift Phys.* **43,** 172–198 (1927).

8.   Pauli, W. On the connexion between the completion of electron groups in an atom with the complex structure of spectra. *Zeitschrift Phys.* 1–13 (1925).

9.   Richards, P. I. & Goudsmit, S. A. The Order of Electron Shells in Ionized Atoms. in *Proc. Natl. Acad. Sci.* **51,** (1964).

10.   Engel, T. & Reid, P. in *Phys. Chem.* 447–479 (2006).

11.   Coles, D. Polaritons in Strongly-Coupled Organic Microcavities - Thesis. *Univ. Sheff.* (2011).

12.   Coleman, L. B. *et al.* Superconducting Fluctuations and The Peierls Instability in an Organic Solid. *Solid State Commun.* **12,** 1125–1132 (1973).

13.   Soderberg, T. *Organic Chemistry with a Biological Emphasis Volume I. Univ. Minnesota Morris Digit. Well* **I,** (2010).

14.   Beer, A. Bestimmung der Absorption des rothen Lichts in farbigen Flussgkeiten (Determination of the absorption of red light in colored liquids). *Ann. der Phys. und Chemie* **86,** 78–88 (1852).

15.   Jelley, E. E. Spectral absorption and fluorescence of dyes in the molecular state. *Nature* **138,** 1009 (1936).

16.   Scheibe, G. Über die Veränderlichkeit des Absorptionsspektrums einiger Sensibilisierungsfarbstoffe und deren Ursache. *Angew. Chem* **49,** 563 (1936).

17.   Bednarz, M. Dynamics of Frenkel excitons in J-aggregates. (2003).

18.   van Burgel, M. The Ultrafast Dynamics of Aggregate Excitons in Water. *Adv. Sci.* (1999).

19.   Musser, A. J. Singlet Exciton Fission in Unconventional Systems. (2013). doi:10.1038/nchem.1801

20. Barford, W. *Electronic and Optical Properties of Conjugated Polymers*. (Oxford University Press, 2005).

21. Schmidt, M. & Tavan, P. Electronic excitations in long polyenes revisited. *J. Chem. Phys.* **136,** 0–13 (2012).

22. Pope, M. & Swenberg, C. E. *Electronic Processes in Organic Crystals and Polymers*. (Oxford University Press, 1999).

23. Barford, W. & Paiboonvorachat, N. Excitons in conjugated polymers: Wavefunctions, symmetries, and quantum numbers. *J. Chem. Phys.* **129,** (2008).

24. Tavan, P. & Schulten, K. Electronic excitations in finite and infinite polyenes. *Phys. Rev. Lett.* **36,** 4337–4358 (1987).

25. Schulten, K. & Karplus, M. On the origin of a low-lying forbidden transition in polyenes and related molecules. *Chem. Phys. Lett.* **14,** 305–309 (1972).

26. Schulten, K., Ohmine, I. & Karplus, M. Correlation effects in the spectra of polyenes. *J. Chem. Phys.* **64,** 4422 (1976).

27. Polívka, T. & Sundström, V. Ultrafast dynamics of carotenoid excited states-from solution to natural and artificial systems. *Chem. Rev.* **104,** 2021–2071 (2004).

28. Frank, H. A. & Christensen, R. L. in *Carotenoids, Vol. 4 Nat. Funct.* 167–188 (2008). doi:10.1007/978-3-7643-7499-0_9

29. *The Photochemistry of Carotenoids*. (Kluwer Academic Publishers, 1999).

30. Tavan, P. & Schulten, K. The low lying electronic excitations in long polyenes: A PPP-MRD-CI study. *J. Chem. Phys.* **85,** 6602–6609 (1986).

31. Tavan, P. & Schulten, K. The 2Ag-1Bu energy gap in the polyenes: An extended configuration interaction study. *J. Chem. Phys.* **70,** 5407–5413 (1979).

32. Dreuw, A. Influence of geometry relaxation on the energies of the S1 and S2 states of violaxanthin, zeaxanthin, and lutein. *J. Phys. Chem. A* **110,** 4592–4599 (2006).

3.

Theory:
Microcavities and Strong Coupling

3.1. Introduction to Microcavities

A microcavity is a structure comprised of two (typically) planar highly reflective surfaces parallel to one another separated by a distance generally on the order of 100s of nanometers. The structure acts as an optical resonator that confines light in the form of standing waves, and is known as a Fabry-Pérot resonator. Wavelengths of light that experience no phase shift upon reflection from the mirrors are said to be resonant and undergo constructive interference. Wavelengths of light which do experience a phase shift experience destructive interference over the course of several round-trips of the cavity and their intensity is diminished towards zero. The separation of the two mirrors determines which wavelengths (λ_c) are allowed within a planar microcavity and is expressed by **Equation 3.1** in which n represents the refractive index of the media between the two mirrors, L_c is the separation between the mirrors (or cavity length), m is an integer which can take any positive value, and θ_{int} is the angle of propagation within the cavity relative to the normal plane of the mirror surface.
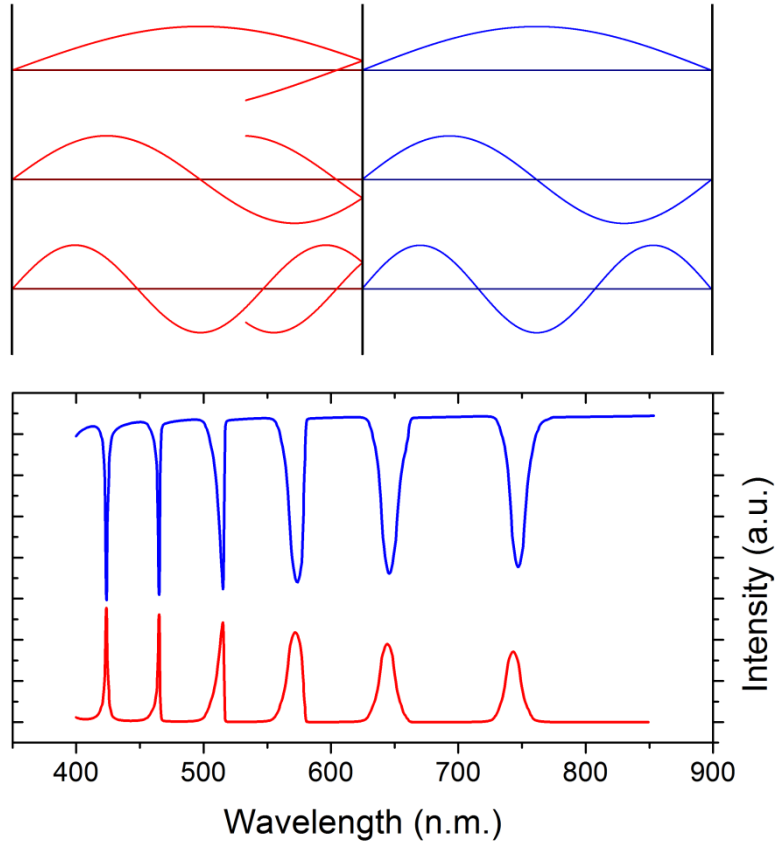
Figure 3.1. (a) *Allowed modes for confined photons which form standing waves for the first three values of m as described by Equation 3.1,* **(b)** *short lived non-resonant photon modes which experience destructive interference,* **(c)** *Reflectivity (blue) and transmission (red) of the first six modes of a microcavity containing a 1.5μm layer with a refractive index of 1.5.*

$$\lambda_c = \frac{2nL_c}{m}cos\theta_{int} \qquad (3.1)$$

These allowed modes can be probed with either reflectivity or transmission measurements as can be observed in **Figure 3.1**.

The wavenumber of light can be expressed as the number of radians (or wavelengths) per unit distance k, and can be expressed by **Equation 3.2**, or resolved into its perpendicular $k_{\gamma\perp}$ and parallel $k_{\gamma\parallel}$ components by **Equations 3.3** and **3.4** respectively.

$$k_\gamma = \frac{2\pi}{\lambda_c} = \frac{\pi m}{nL_c}\frac{1}{cos\theta_{int}} \qquad (3.2)$$

$$k_{\gamma,\perp} = \frac{\pi m}{nL_c} \tag{3.3}$$

$$k_{\gamma,\parallel} = \frac{\pi m}{nL_c} tan\theta_{int} \tag{3.4}$$

It can be seen that the perpendicular component is fixed primarily by the cavity length, whilst the parallel component increases with angle (though refractive index and mode number also contribute to both terms). Experimentally, it is found that the wavelength of light confined within the cavity appears to decrease with angle. These formulae can be also expressed in terms of energy as given by **Equation 3.5**.

$$E_\gamma = \frac{hck}{2\pi} = \frac{hcm}{2nL_c}\frac{1}{cos\theta_{int}} = E_0(1 - sin^2\theta_{int})^{-\frac{1}{2}} \tag{3.5}$$

As the system cannot be observed from within, all measurements on a cavity are made from an external frame of reference that has a different refractive index to that of the cavity (most organic polymers have refractive indices of ~1.5). Snell's law (**Equation 3.6**) is used to calculate the angle of refraction of light passing the interface between two materials of differing refractive index.

$$n_1 sin\theta_1 = n_2 sin\theta_2 \tag{3.6}$$

If the microcavity is surrounded by air (n=1), and the interior region within has a larger refractive index, then **Equation 3.6** can be reduced to **3.7**.

$$\theta_{int} = arcsin\left(\frac{sin\theta_{ext}}{n}\right) \tag{3.7}$$

By substituting **Equations 3.5** and **3.7**, the photon energy of a given cavity mode can be expressed as a function of external viewing angle as described by **Equation 3.8**.

$$E_\gamma = E_0\left(1 - \frac{sin^2\theta_{ext}}{n^2}\right)^{-\frac{1}{2}} \tag{3.8}$$
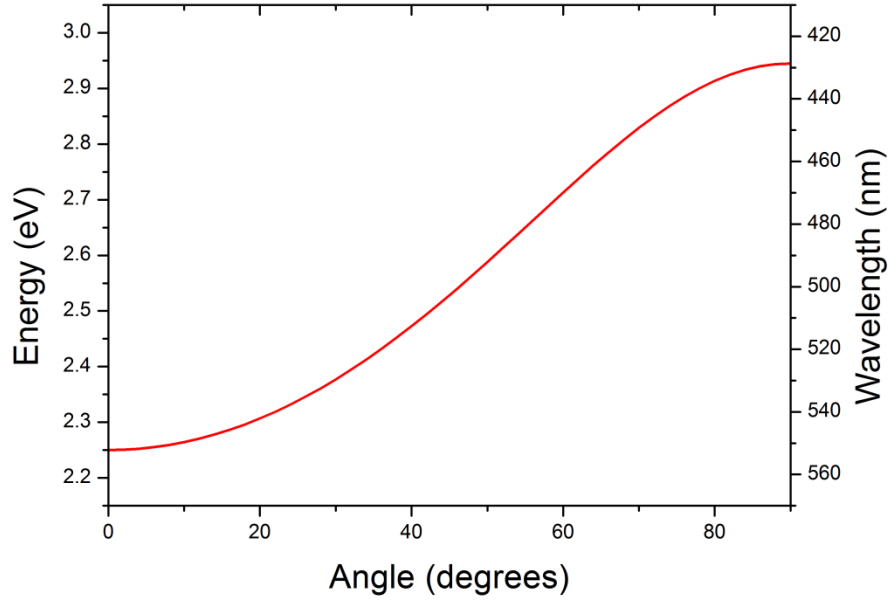
Figure 3.2. *Variations in confined photon mode energy as a function of external viewing angle*

The length of time that a photon can be confined within a microcavity, τ_{cav}, before it escapes is primarily determined by the reflectivity of the mirrors used to confine. Two major loss mechanisms which can affect this time are scattering due to rough surfaces, and absorption from the mirror itself. Uneven mirror surfaces result in slight variations in the effective cavity length. This causes several slightly different energy photons to coexist within the cavity; over time these photons will destructively interfere with one another, causing the linewidth of the photon mode as measured through transmission (or reflection) to increase. These modes constructively interfere with one another, causing the τ_{cav} to decrease. A measure of the "Quality" or Q-Factor of a cavity can be derived from the measured linewidth of the mode at a given wavelength, as expressed by **Equation 3.9**. Here λ_c represents the central wavelength of the mode, and $\Delta\lambda_c$ represents the FWHM of the mode; this can also be expressed in terms of energy E, or angular frequency ω.

$$Q = \frac{\lambda_c}{\Delta\lambda_c} = \frac{\omega}{\Delta\omega} = \frac{E}{\Delta E} \tag{3.9}$$

3.2. Metallic Mirrors vs. Distributed Bragg Reflectors

For an ideal microcavity, one which is limited solely by the reflectivity of the mirrors, R_1 and R_2, another metric can be used to measure how well a photon can be confined is finesse, $\mathcal{F}$ as described by **Equation 3.10**. It can also be obtained by dividing the width of the stopband by the width of the optical mode.

$$\mathcal{F} = \frac{\pi(R_1 R_2)^{1/4}}{1 - (R_1 R_2)^{1/2}} \qquad \text{(3.10)}$$

The photon confinement time is limited by the mirror with the lowest reflectivity. Metallic mirrors typically have a reflectivity of ~95% (though evaporated silver can achieve reflectivities as high as 97% at certain wavelengths[1]). This reflectivity is caused by the abundance of free charge carriers in the conduction band of the metal at its surface. As these free carriers are very loosely bound, they can be readily induced to vibrate by the incident electromagnetic field of the photons; this causes them to oscillate and in re-radiate energy. If the surface is planar, these re-radiated photons are symmetric in terms of phase and angle to the incident photons. Metallic mirrors can however suffer absorption losses from these free carriers which provide a virtual continuum of energy levels which can form excited states and place an upper limit on the reflectivity of the material.
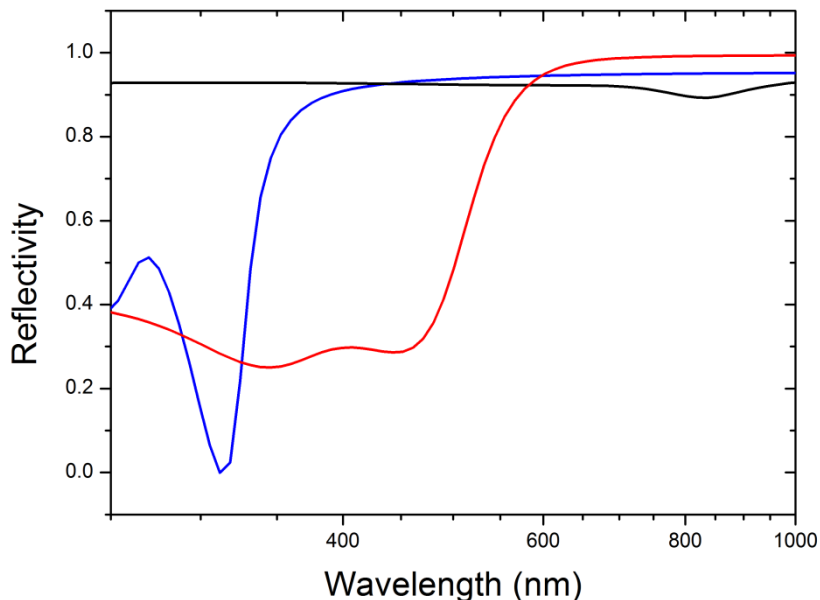

Figure 3.3. *Calculated reflectivity of thin films of metal as a function of wavelength. The blue line denotes silver, black – aluminium, and red – gold.*

For this reason, distributed Bragg reflectors, **DBR**s, are often employed as they can combine very high reflectivity with very low losses. DBRs are structures comprised pairs of materials with different refractive indices. In contrast to conducting materials (metals), reflectivity results from constructive and destructive interference of light at the interface of layers of very specific lengths. By selecting dielectric materials (bandgaps of>4eV), absorption losses can be negated and reflectivities of ≫99% are achievable. The thickness, *l*, of any individual layer is determined by the desired wavelength for maximal reflectivity and its refractive index as given by **Equation 3.11**; it is chosen so that the reflected light from each successive interface is in phase.

$$l = \frac{\lambda}{4n}$$

(3.11)

The peak reflectivity of DBR stopband at its central wavelength can be quantified using **Equation 3.12**. Here n_1 and n_2 represent the refractive indices of the two layers within the stack, n_i and n_f represent the refractive indices of the initial and final media that the light passes through, N is the total number of pairs within the structure[2].

$$R = \left[\frac{n_i(n_2)^{2N} - n_f(n_1)^{2N}}{n_i(n_2)^{2N} + n_f(n_1)^{2N}}\right]^2$$

(3.12)

The frequency bandwidth Δf_0 of the DBR stopband is described by **Equation 3.13**, in which f_0 is the central frequency of the stopband.

$$\frac{\Delta f_0}{f_0} = \frac{4}{\pi} arcsin\left(\frac{n_2 - n_1}{n_2 + n_1}\right)$$
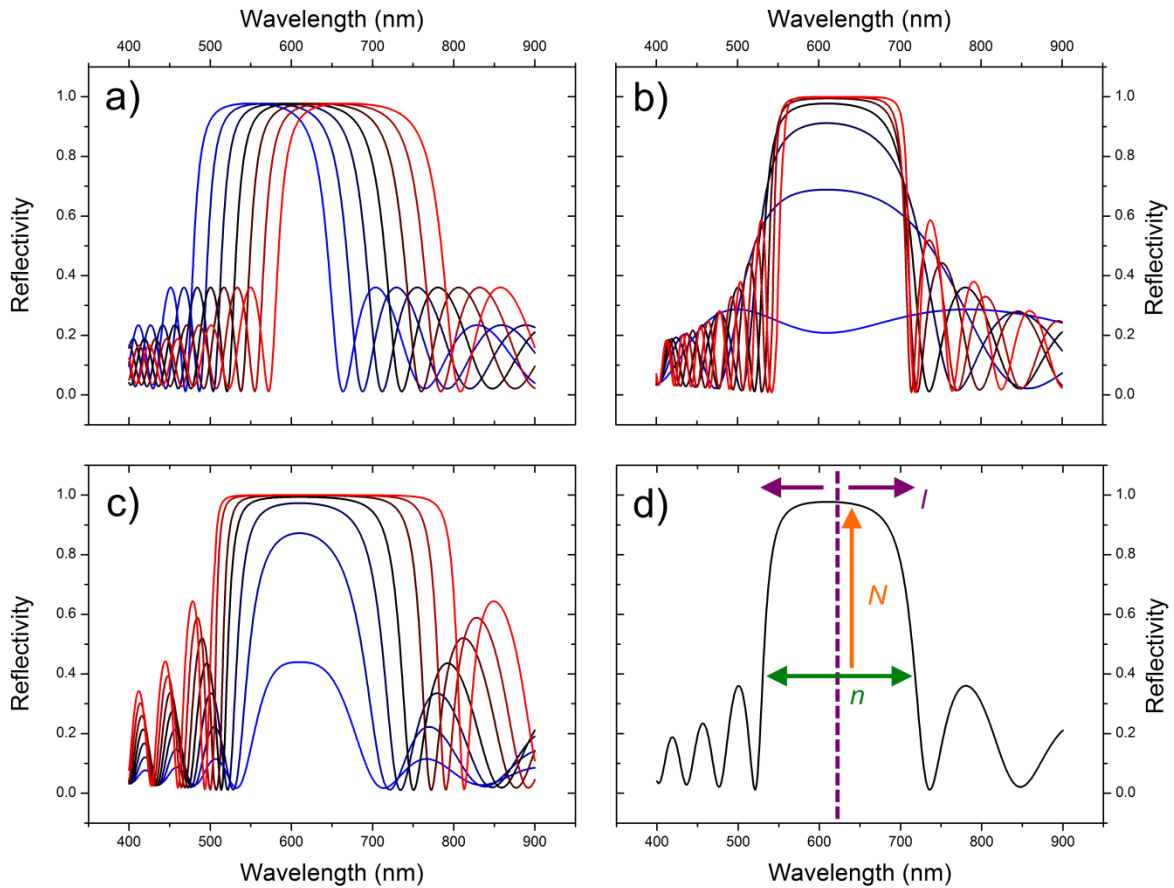
(3.13)

Figure 3.4. (a) *Shifts in central stopband wavelength caused by varying the thickness of individual layers from thin (blue) to thick (red).* **(b)** *Changes in absolute reflectivity at the central stopband wavelength caused by increasing the number of pairs within the stack from 2 (blue) to 14 (red).* **(c)** *changing the FWHM of the DBR by increasing the refractive index contrast between layers from Δn = 0.2 (blue) to 1.4 (red).* **(d)** *A guide to how the stopband of a DBR can be changed by changing a single parameter.*

This means that the peak reflectivity of the cavity can be increased with the addition of more mirror pairs; the width of the stopband can be extended by increasing the refractive index contrast between the two materials, and the stopband position can be shifted to higher or lower energies by adjusting the thickness of the individual layers. This is evidenced more clearly in **Figure 3.4**.
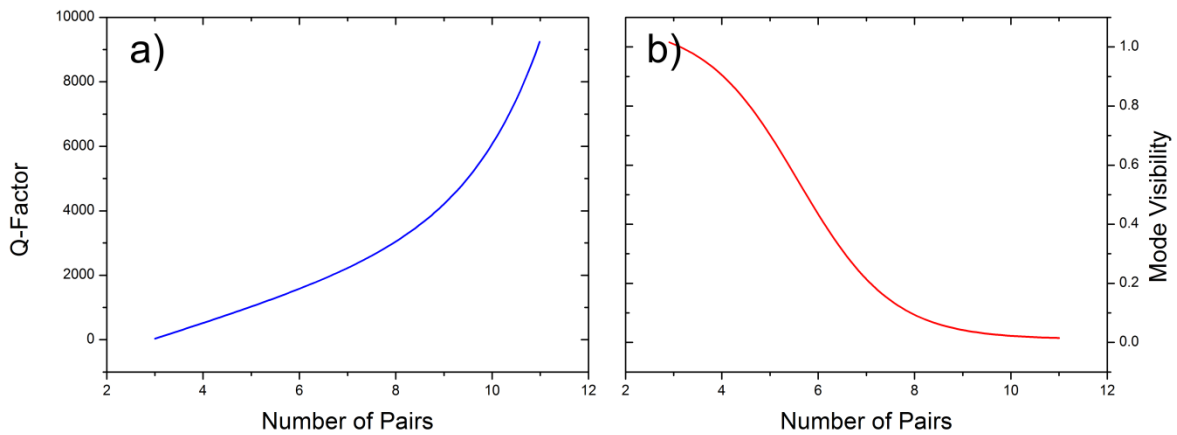
Figure 3.5. (a) *Narrowing of cavity-mode linewidths and increasing Q-factors as number of pairs is increased,* **(b)** *Reduced visibility of said features as number of pairs increases.*

Whilst the number of DBR pairs can be increased to achieve the narrowest cavity-mode linewidths and hence longest photon confinement times possible, **Figure 3.5(a)**, the visibility (defined by the magnitude of the dip in the stopband) of said modes reduces with each additional pair; see **Figure 3.5(b)**. These additional mirror pairs reduce the number of photons that can enter or leave the microcavity and can make it difficult to distinguish features within the cavity. A careful balance must therefore be struck.

To describe light passing across a single interface, the angle with which light propagates can be modelled using Snell's law (**Equation 3.6**) but for multi-layer structures with many interfaces, it is simpler to use a transfer matrix modelling method (**TMM**). This modelling method is based upon the Fresnel Equations and accounts for the multiple internal reflections and interference effects that occur within the different media. A more rigorous derivation of this can be found in Optics by Hecht[1], but will be briefly covered here. **Figure 3.6** depicts the path that the magnetic, H, and electric, E, fields for s polarised light must take when propagating through three media with different refractive indices (A, B, and C); it is assumed that A and C are semi-infinite (i.e. substrate and air). This is described by **Equation 3.14**, which describes the transition between media A and B.
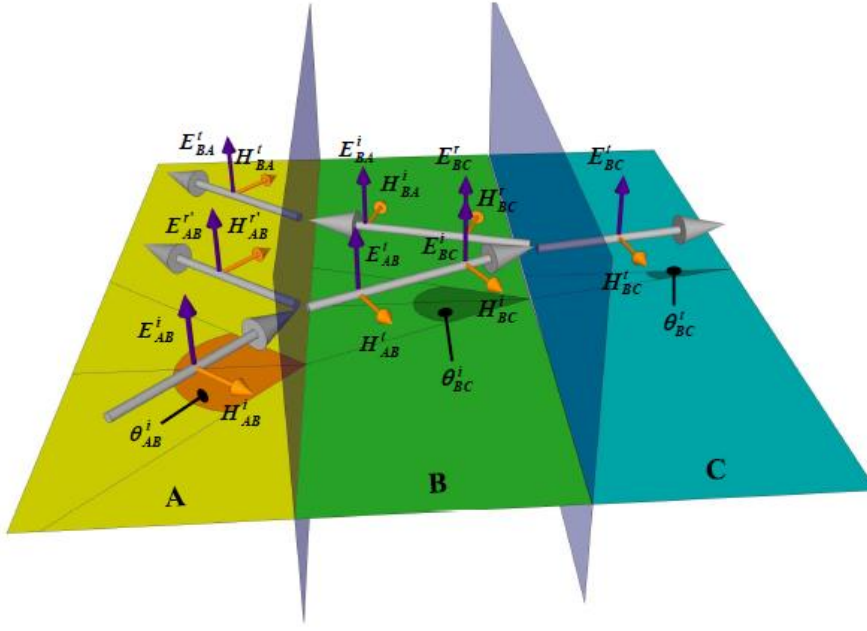
Figure 3.6. *The propagation paths that magnetic (H) and electric (E) fields of s-polarised light take as they pass through materials with varying refractive indices as determined by the Fresnel equations. Image adapted from Coles[3].*

$$\begin{bmatrix} E_{AB} \\ H_{AB} \end{bmatrix} = \begin{bmatrix} cos(\varphi_B d_B) & \dfrac{i}{\Gamma_B} sin(\varphi_B d_B) \\ \Gamma_B i\, sin(\varphi_B d_B) & cos(\varphi_B d_B) \end{bmatrix} \begin{bmatrix} E_{BC} \\ H_{BC} \end{bmatrix} = \mathbb{M}_B \begin{bmatrix} E_{BC} \\ H_{BC} \end{bmatrix} \tag{3.14}$$

Here $\varphi_B d_B$ represents the phase difference of the E-field as it enters and leaves the medium B (**Equation 3.15**), Γ_B is given by **Equation 3.16**, and the characteristic matrix that relates the field boundaries at either side of medium B is given by $\mathbb{M}_B$.

$$\varphi_B d_B = \frac{2\pi}{\lambda_0} d_B n_B cos\theta_{BC}^i \tag{3.15}$$

$$\Gamma_B = \sqrt{\frac{\epsilon_0}{\mu_0}} n_B cos\theta_{BC}^i \tag{3.16}$$

Here ϵ_0 and μ_0 are the permittivity and permeability of free space. The same formulae apply to medium C to give the characteristic matrix $\mathbb{M}_C$; this can be multiplied by the characteristic matrix of medium B to give **Equation 3.17**.

$$\begin{bmatrix} E_{AB} \\ H_{AB} \end{bmatrix} = \mathbb{M}_B \mathbb{M}_C \begin{bmatrix} E_{CD} \\ H_{CD} \end{bmatrix} \tag{3.17}$$

This matrix multiplication can be repeated indefinitely for an arbitrarily large number of layers, Z, to give the characteristic matrix in **Equations 3.18** or **3.19**. Here m_{xy} denotes individual matrix elements.

$$\begin{bmatrix} E_{AB} \\ H_{AB} \end{bmatrix} = \mathbb{M}_B \mathbb{M}_C \ldots \mathbb{M}_Z \begin{bmatrix} E_{Z(Z+1)} \\ H_{Z(Z+1)} \end{bmatrix} \tag{3.18}$$

$$\mathbb{M} = \mathbb{M}_B \mathbb{M}_C \ldots \mathbb{M}_Z = \begin{bmatrix} m_{11} & m_{12} \\ m_{21} & m_{22} \end{bmatrix} \tag{3.19}$$

These can be expanded to give the reflectivity, R, and transmission, T, for the whole structure (**Equations 3.20** and **3.21**).

$$R = \frac{\Gamma_A m_{11} + \Gamma_A \Gamma_C m_{12} - m_{21} - \Gamma_C m_{22}}{\Gamma_A m_{11} + \Gamma_A \Gamma_C m_{12} + m_{21} + \Gamma_C m_{22}} \tag{3.20}$$

$$T = \frac{2\Gamma_A}{\Gamma_A m_{11} + \Gamma_A \Gamma_C m_{12} + m_{21} + \Gamma_C m_{22}} \tag{3.21}$$

Whilst it may seem that DBRs are preferable to metallic mirrors in general due to their potentially higher reflectivities and the tunability of central stopband wavelength, it is worth noting that metallic mirrors do have a number of advantages. Metallic mirrors confine EM fields to a much higher degree than their dielectric counterparts. This means the EM field penetrates into the DBR structure by a distance L_{DBR}; a microcavity comprised of two DBRs thus has an effective cavity length L_{eff} as described by **Equation 3.22**.

$$L_{eff} = L_C + 2L_{DBR} \tag{3.22}$$

$$L_{DBR} \approx \frac{\lambda_C}{16 n_1 n_2} \frac{(n_1 + n_2)^2}{(n_1 - n_2)} \tag{3.23}$$

For a microcavity designed to confine light of ≈ 600nm with mirror refractive indices $n_1 \approx 2$ and $n_2 \approx 1.5$ (corresponding to those of silicon nitride and silicon dioxide), it can be seen that $L_{eff} \approx 2L_C$. Panzarini et al[4] show that the cavity mode wavelength $\lambda_m(\theta)$, at any given angle can be described by a weighted average of the central wavelength of the DBR stopband $\lambda_0(\theta)$, and that of the cavity length $\lambda_C(\theta)$; this is given by **Equation 3.24**.

$$\lambda_m(\theta) = \frac{L_C \lambda_C(\theta) + 2L_{DBR}\lambda_0(\theta)}{L_{eff}} \tag{3.24}$$

In the ideal case where $\lambda_0 = \lambda_c$ then $\lambda_m = \lambda_c$ and there is no polarization dependence on the cavity mode energy. However if $\lambda_c \neq \lambda_0$ it means that $\lambda_m(\theta)$ has a polarization dependence. As the external viewing angle is increased, this can lead to large separations between the confined TE and TM polarisations. It is worth noting that transverse electric (**TE**) polarizations of light are used exclusively in the microcavity work in this thesis as transverse magnetic (**TM**) can cause the stopband of a DBR to vary and narrow as a function of angle, **Figure 3.7**. DBRs can be considered one-dimensional photonic crystals in that they have a complete TE bandgap (in one dimension), but only a partial TM bandgap.

This is a powerful method for modelling multilayer structures as the only parameters needed to describe a complex structure are the refractive indices and thicknesses of individual layers, the angle the beam of incident light, and the polarization of said light. It does however assume a transparent medium with no attenuation from any of the layers. This can be accounted for by replacing the real component of the refractive index n, with the complex refractive index $\vec{n} = n + i\kappa$, in which κ is the extinction coefficient. As n and κ are both wavelength dependent, calculations of R and T must be repeated at each wavelength of interest.
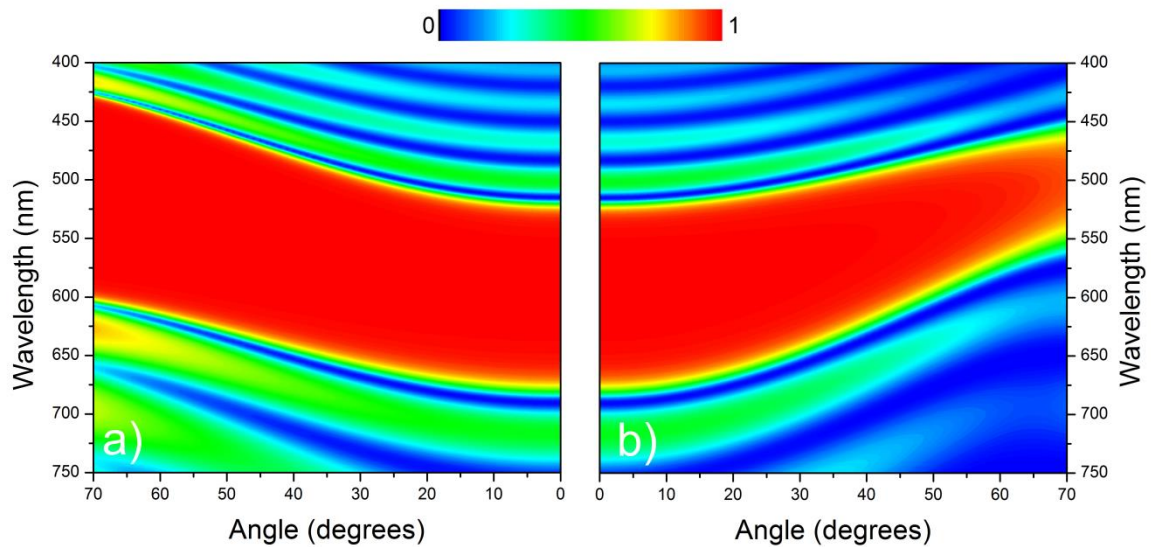
Figure 3.7. *The stopband of a DBR as a function of external viewing angle for **(a)** TE, and **(b)** TM polarisations of light. Whilst both the cavity mode and DBR stopband move to shorter wavelengths as angle is increased, the reflectivity of TE-polarised light is maintained as the incident angle is increased but falls for TM-polarisations. The reflectivity of TM polarisations continues to fall as the angle increases before reaching zero at the Brewster angle; due in part to the non-continuous phase shift of TM-polarizations of light.*
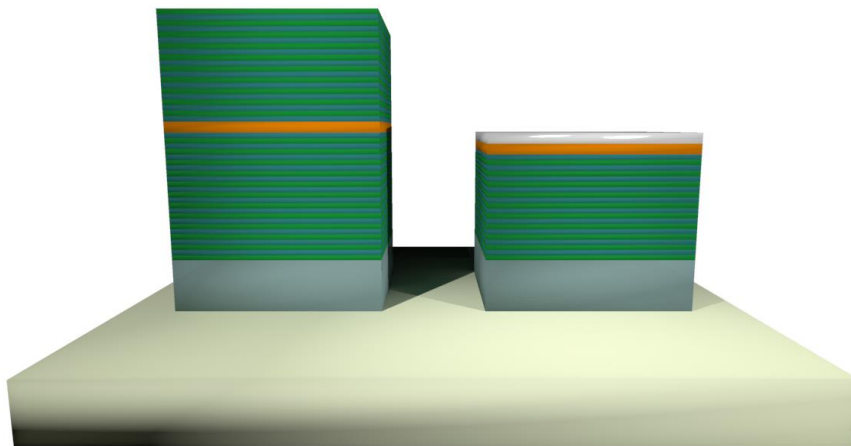
Figure 3.8. *Structures of two microcavities employing: (left) two dielectric mirrors and (right) one DBR and one metallic mirror. Images are not drawn to scale. The (grey) bottom layer is a glass substrate, the (orange) middle layer is an organic semiconductor, (green/blue) striped structures are dielectric mirrors, and the thin (white) layer is a metallic mirror.*

3.3. Light-Matter Coupling within a Microcavity

If a semiconducting material is placed within a microcavity, the EM field of the confined photons can interact with the dipole of the electronic transition[5]. The strength of this interaction is determined by the absorption of the material (derived from the oscillator strength of a given electronic transition and number of interacting particles as described in **Chapter 2**). If this coupling strength cannot overcome the loss mechanisms of the microcavity and semiconductor, the system is said to be in the weak coupling regime.

3.3.1. Weak Coupling

Confinement within a cavity modifies the local photonic density of states, each of which has an associated electromagnetic field, this causes a change in their distribution with respect to their normal free space values. Fermi's golden rule[6] describes the spontaneous emission rate, W, for a dipole as affected by a perturbation, **Equation 3.25**. If the energy of the confined photons/EM field is resonant with that of the dipole transition energy, the optical density of states at said energy can be increased; in this case the optical density of states at other energies is suppressed.

$$W = \frac{2\pi}{\hbar}|M|^2 g(\omega) \qquad (3.25)$$

Here M is the transition matrix element, $\hbar$ is the reduced Planck constant, and $g(\omega)$ is the optical density of states as a function of angular frequency ω as described by **Equations 3.26** and **3.27**

$$\omega = \frac{2\pi c n}{\lambda} \qquad (3.26)$$

$$M^2 = \xi^2 \mu^2 \varepsilon_{vacuum}^2 \qquad (3.27)$$

It is worth noting that the coupling strength has an orientation dependence. If a dipole is aligned with the EM field, the coupling strength can be greatly enhanced. This can be described by **Equations 3.27** and **3.28**. Here ξ^2 is he dipole orientation factor. A dipole in free space with a random orientation has a value of $\xi^2=1/3$; a dipole within a microcavity aligned with the confined field has a value of $\xi^2=1$.

$$\varepsilon_{vacuum} = \frac{\hbar\omega}{2\epsilon_0 V} \tag{3.28}$$

Here V refers to the mode volume, μ, the dipole matrix element, ϵ_0, permittivity of free space, and ε_{vacuum}, the vacuum field magnitude. In the case where the energy of the transition is resonant with that of the cavity mode, **Equation 3.30** simplifies to **3.31**.

$$g(\omega)_{free\ space} = \frac{\omega^2 V}{\pi^2 c^3} \tag{3.29}$$

$$g(\omega)_{cavity} = \frac{2}{\pi} \frac{\Delta\omega_c}{4(\omega - \omega_C)^2 + \Delta\omega_C{}^2} \tag{3.30}$$

$$g(\omega)_{cavity} = \frac{2Q}{\pi\omega} \tag{3.31}$$

Taking the ratio of the spontaneous emission rates within the cavity and in free space gives the Purcell enhancement effect[7] as described by **Equation 3.32** in which Q and V refer to the quality factor and mode volume of the cavity respectively. The Purcell effect provides an upper limit to the degree that the spontaneous emission within a cavity can be enhanced; it assumes that all dipoles within the cavity are aligned, the transition and cavity mode are exactly resonant with one another, and all non-resonant transitions are suppressed. It is worth noting that the in the original publication refractive index n was not included, but is a modern addition.

$$F = \frac{W_{cavity}}{W_{free\ space}} = \frac{3}{4\pi^2}\left(\frac{\lambda}{n}\right)^3 \frac{Q}{V} \tag{3.32}$$

3.3.2. Strong Coupling

If the loss mechanisms associated with the microcavity and semiconductor can be overcome and the coupling strength between exciton and cavity mode is sufficiently strong, the system is said to be in the strong coupling regime.

Upon entering the strong coupling regime, perturbation theory is no longer sufficient to describe the interaction between the electronic transition and the cavity mode. An oscillatory exchange of energy between the two occurs, the frequency of which is known as the Rabi frequency, Ω_{Rabi}. The wavefunctions of the two possible states can no longer be individually distinguished and the system is described as a superposition of the two; this superposition can be treated as a quasi-particle named a cavity-polariton which possesses some properties of both of its constituent components.

To facilitate entry into the strong coupling regime, the system must meet a number of criteria. The primary concern is selecting an appropriate semiconductor, ideally one possessing a narrow, high-oscillator strength electronic transition. While it is possible to couple to broad transitions if the interaction strength is larger than the linewidth of the transition, achieving sufficiently high oscillator strengths can be difficult. The narrower this transition is, the more emission into forbidden (non-resonant with the cavity) modes can be minimized. Likewise the cavity is designed to confine the photon for as long as possible, as the maximum polariton lifetime ($\tau_{polariton}$) is determined by the lifetimes of the exciton and photon used to form it and their respective fractions (α and β), this is given by **Equation 3.33**.

$$\tau_{polariton} = \alpha \tau_X + \beta \tau_\gamma \qquad \textbf{(3.33)}$$

Though polaritons and the mixing of states which form them are quantum mechanical in nature, they can be modelled classically as a pair of coupled oscillators, allowing the energies of the polariton states which correspond to the new eigenmodes of the system to be determined. The interaction of two coupled classical oscillators is given by **Equation 3.34**, in which Λ is the interaction potential.

$$A = \begin{bmatrix} E_\gamma & \Lambda \\ \Lambda & E_X \end{bmatrix} \qquad \textbf{(3.34)}$$

The characteristic polynomial of this matrix reveals a quadratic energy term which can be solved using **Equations 3.35** and **3.36**, in which I is a 2x2 identity matrix.

$$det(A - EI) = \begin{bmatrix} E_\gamma - E & \Lambda \\ \Lambda & E_X - E \end{bmatrix} = (E_\gamma - E)(E_X - E) - \Lambda^2 = 0 \qquad \textbf{(3.35)}$$

$$E = \frac{E_\gamma + E_X}{2} \pm \frac{1}{2}\sqrt{(E_\gamma - E_X)^2 + 4\Lambda^2} \qquad \textbf{(3.36)}$$

As can be seen in **Equation 3.36**, there are two possible solutions for the polariton energy, both of which are dependent upon the energy of the photon mode. The two solutions for polariton energies are termed as "branches", hereafter referred to as the upper and lower polariton branches, **UPB** and **LPB**.

If the cavity is designed with negative photon-mode detuning (i.e. at normal incidence, the photon mode energy is lower than that of the electronic transition), then at some angle θ_{res}, the energies of the photon and exciton modes E_γ and E_X are degenerate. Here the energy separation between the UPB and LPB is at its smallest possible value, known as the Rabi splitting energy $\hbar\Omega_{rabi}$, which is equal to twice that of the interaction potential Λ, this is given by **Equation 3.37**. It is possible however to design a cavity such that the energy of the confined photon mode is always at a higher energy than that of the exciton, such microcavities are said to be positively detuned.
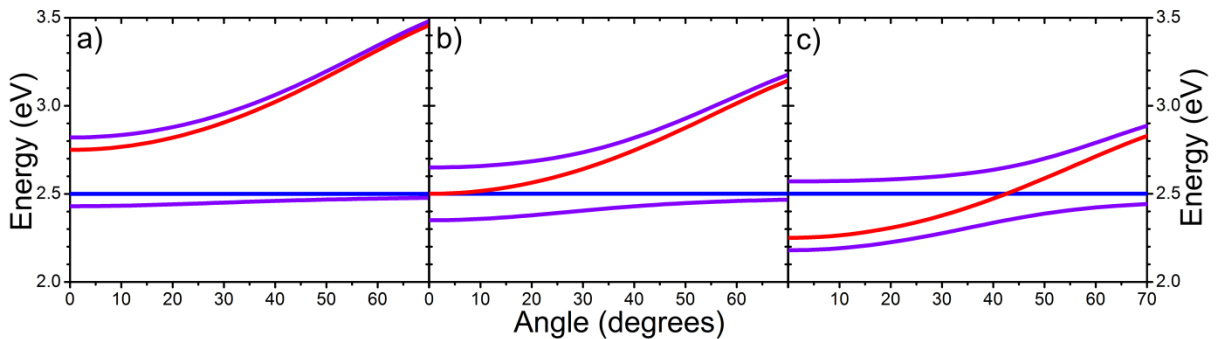
$$\hbar\Omega_{Rabi} = 2\Lambda \qquad \textbf{(3.37)}$$

Figure 3.9. *Polariton branch positions for (a) positive, (b) resonant, and (c) negative photon mode detunings. The exciton is marked with a blue line, photon – red, and polariton branches with purple lines.*

It is worth noting that the photonic and excitonic components of the polariton vary along each polariton branch. This is described by two mixing coefficients α and β which are the eigenvector of matrix A and correspond to the fraction of exciton and photon in the coupled polariton modes. This is given by **Equation 3.38**, which can be solved for either α or β, subject to the constraints of **Equation 3.39**.

$$\begin{bmatrix} E_\gamma & \Lambda \\ \Lambda & E_X \end{bmatrix} \begin{bmatrix} \alpha \\ \beta \end{bmatrix} = E \begin{bmatrix} \alpha \\ \beta \end{bmatrix} \tag{3.38}$$

$$\alpha^2 + \beta^2 = 1 \tag{3.39}$$

This yields the **Equations 3.40** and **3.41**, which can further be simplified by eliminating the interaction potential term Λ by using **Equation 3.36**. From this the photonic (or excitonic) fraction of the polaritons in the LPB (or UPB) can be calculated.

$$\alpha E_\gamma + \beta \Lambda = \alpha E \tag{3.40}$$

$$\alpha \Lambda + \beta E_X = \beta E \tag{3.41}$$

$$\alpha^2 = \frac{E_\gamma - E}{E_X + E_\gamma - 2E} \tag{3.42}$$
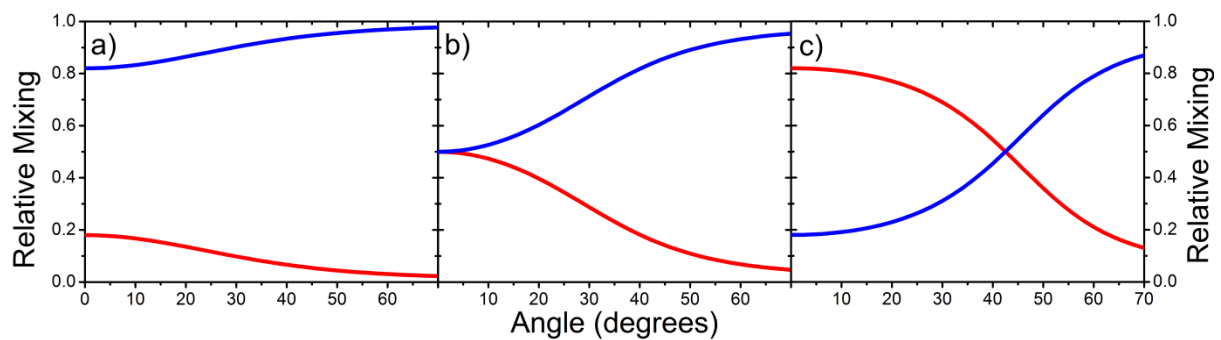

Figure 3.10. *Proportion of photonic, red (blue), and excitonic, blue (red), components of the upper (lower) polariton branch as a function of angle for a cavity with **(a)** positive, **(b)** resonant, and **(c)** negative photon mode detuning.*

Once one component has been calculated, the second can quickly be calculated by subtracting the first from unit, **Equation 3.39**. Note, that as these mixing coefficients are derived from the energy of the confined photon mode, they too carry an angular dependence; this is depicted in **Figure 3.10**. At resonance, the photonic and excitonic components for both the UPB and LPB are equal.

Whilst strong-coupling of a confined photon mode with that of an electronic excitation requires a more complete quantum mechanical description of cavity polaritons, this can also be described using a classical approach as described by Zhu et al[8]. This is because the characteristic anticrossing of states around the degenerate photon and exciton energies can be predicted in linear spectroscopy if a Lorentzian oscillator is placed within the cavity as a consequence of Linear-Dispersion theory. This allows the transfer matrix approach described previously to be used to calculate the reflectivity and transmission spectra of strongly coupled microcavities.

Using this approach, the cavity exciton is modelled as a Lorentzian oscillator. This proves to be an accurate approximation for many molecular dyes dispersed within a transparent matrix. The real and imaginary components needed in the calculations can be measured experimentally through ellipsometry, or estimated using the Lorentz oscillator approximation given by **Equation 3.44**[9]. Here n_{bg} is the refractive index far from the absorption region, $\aleph$ is a value related to the total oscillator strength of the absorbing medium, γ is the FWHM of the absorption, e and m_e correspond to the charge and mass of an electron, and ω_0 is the angular frequency at the absorption maximum. In most cases, n_{bg} is virtually identical to refractive index of the matrix polymer material as it is present in much greater quantities than the dye dispersed within it; $\aleph$ requires an estimate to its value.

$$\bar{n} = n + i\kappa \tag{3.43}$$

$$\bar{n} = n_{bg}^2 + \frac{\aleph e^2(\omega_0^2 - \omega^2)}{(\omega_0^2 - \omega^2)^2 \epsilon_0 m_e \left[(\omega_0 - \omega)^2 + \left(\frac{\gamma}{2}\right)^2\right]} + i\frac{\aleph e^2 \gamma \omega}{(\omega_0^2 - \omega^2)^2 \epsilon_0 m_e \left[(\omega_0 - \omega)^2 + \left(\frac{\gamma}{2}\right)^2\right]}$$

$$\tag{3.44}$$

Note, this is only valid when the absorption profile of the material can be approximated by a Lorentzian lineshape. More complex absorption profiles, or ones containing more than one feature (e.g. blends of two different materials within the same cavity) can also be approximated (roughly) by averaging the real component and summing the imaginary components of multiple transitions. This approximation becomes increasingly accurate as more transitions are included.
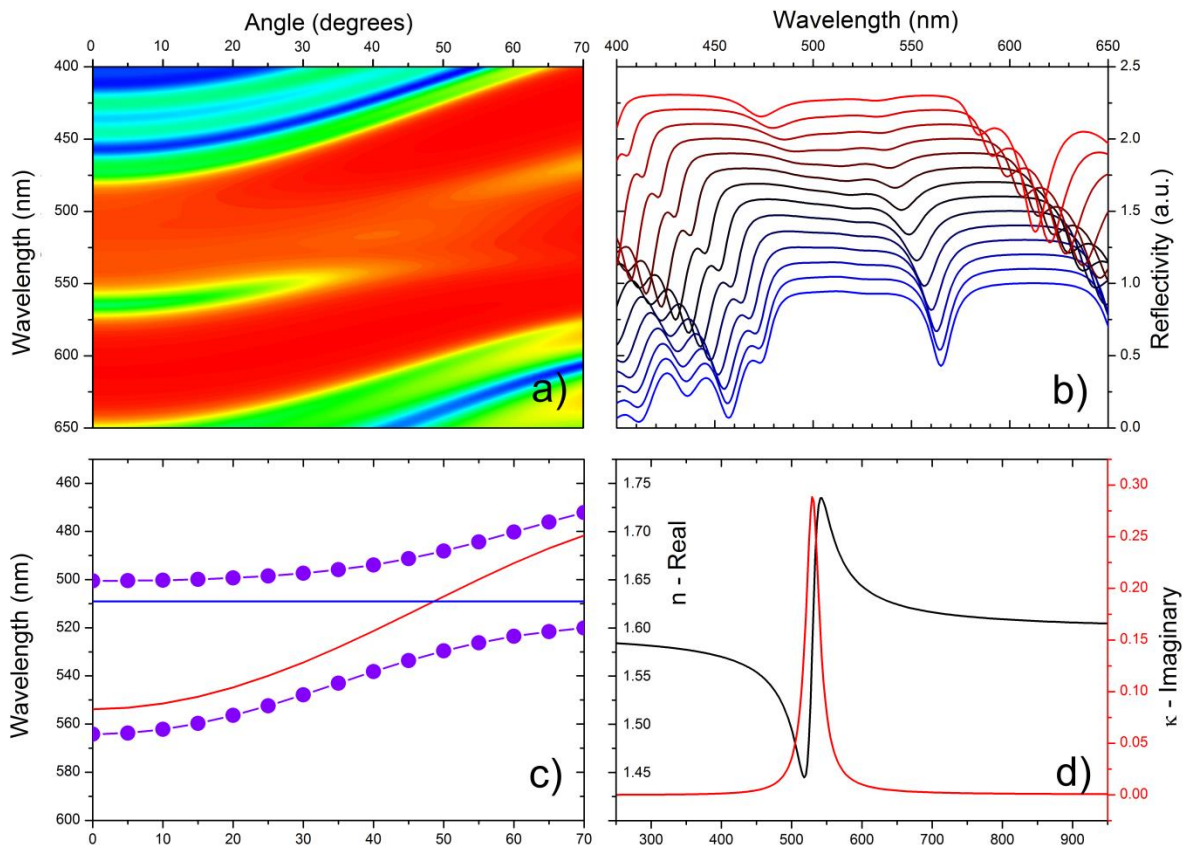

Figure 3.11. (a) Dips in reflectivity spectra corresponding to the UPB and LPB either side of the exciton energy. *(b)* A waterfall plot of individual angular slices from 0 degrees (blue) to 70 degrees (red). *(c)* Dip positions as a function of angle and corresponding fit using a Lorentzian oscillator. *(d)* Real (black) and imaginary (red) absorption components for a single electronic transition.

3.4. Photonic vs. Polaritonic Lasing

3.4.1. Photonic Lasing

Certain semiconducting materials can undergo a process known as stimulated emission. Stimulated emission occurs when a photon resonant with an electronic transition interacts with an electron in an excited state causing the electron to drop to a lower energy level; the energy released in this decay in the form of a photon. The photon produced as a result of stimulated emission propagates along the same path as the initial incident photon and possesses identical energy, phase, and polarization. This differs from spontaneous emission which occurs at random intervals and is not influenced by the surrounding electromagnetic field; this means that both the phase and direction of emission is random, rendering such light incoherent. Technically this is an oversimplification, and spontaneous emission occurs due to random vacuum field fluctuations which 'stimulate' the emission of a photon from an excited state, a consequence of 2nd quantization in quantum field theory.
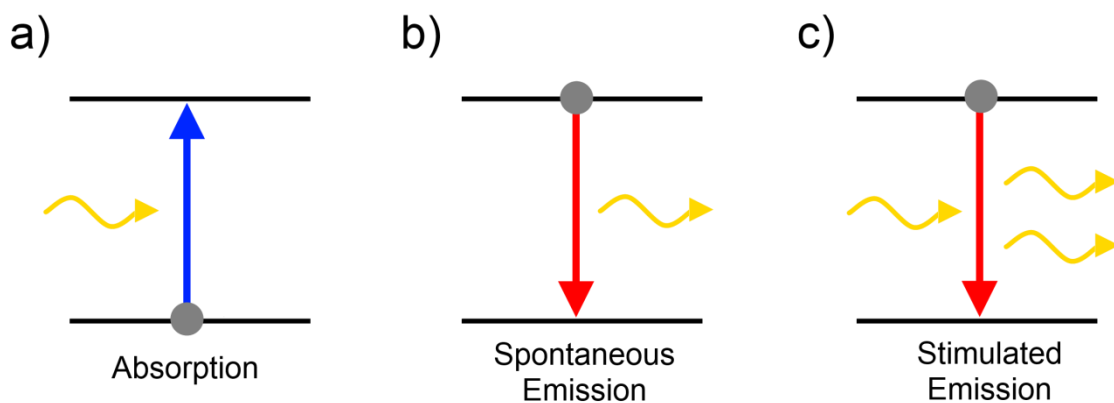

Figure 3.12. *Three possible pathways through which light can interact with matter:* **(a)** *The absorption of a photon and promotion of electron to an excited state.* **(b)** *The spontaneous emission of a photon as an electron decays from the excited state to the ground state (as perturbed by vacuum field fluctuations), this does not require a population inversion.* **(c)** *The stimulated emission of a photon from an excited state (as perturbed by the field of another photon).*

Stimulated emission does not occur at low photon densities as in most media at thermal equilibrium, the majority of electrons are in lower energy "ground" states than in higher energy excited states; in this case incident photons possessing energies resonant with the electronic transition are typically absorbed. If however the majority of electrons are in excited states, the population is said to be inverted, and the rate of stimulated emission exceeds that of absorption. This is a prerequisite for lasing in optical gain medium.

The fraction of electrons in either state is given by n (**Equations 3.45** and **3.46**). Here N_1 represents the number of electrons in the ground state, N_2 the number in excited states, and N_T the total number of electrons in the system.

$$n_1 = \frac{N_1}{N_T} \tag{3.45}$$

$$n_2 = \frac{N_2}{N_T} \tag{3.46}$$

These can also be expressed as competing rate equations, here W represents the rate of transitions from one to another.

$$n_1 = \frac{W_{2 \to 1}}{W_{1 \to 2} + W_{2 \to 1}} \tag{3.47}$$

$$n_2 = \frac{W_{1 \to 2}}{W_{1 \to 2} + W_{2 \to 1}} \tag{3.48}$$

The optical amplification, or gain (G), which a one-dimensional beam of photons experiences as it passes through a medium with a population inversion is given by **Equation 3.49**, in which the power of the beam is given by P and z is the coordinate in the direction of beam propagation.

$$G = \frac{d}{dz} ln(P) = \frac{dP/dz}{P} \tag{3.49}$$

To create a low threshold laser, it is necessary to maximise gain. This can be done by ensuring the greatest possible path length through the gain medium is taken. This is achieved by placing the gain medium within an optical cavity so that it must complete several round trips before escaping. Lasing occurs when the optical gain of a laser medium crosses a threshold ($G_{threshold}$) value large enough that it completely nullifies all of the losses experienced by beam during one round trip of a cavity, this is given by **Equation 3.50**. Here R_1 and R_2 represent the reflectivities of the mirrors used to define the length of the cavity, l the cavity length, and α represents the

optical losses of the system; this possesses a value > 0 and is nearly constant for any particular layer so is often simplified by treating it as a fixed value, α_0. This can also be rearranged for clarity as shown in **Equation 3.51**.

$$R_1 R_2 e^{(2G_{threshold}l)} e^{(-2\alpha l)} = 1 \tag{3.50}$$

$$G_{threshold} = \alpha_0 - \frac{1}{2l} ln(R_1 R_2) \tag{3.51}$$

Below threshold, the light output of a medium scales linearly with the intensity of the pump source and emission is spontaneous in nature. Above this threshold, population inversion occurs and stimulated emission dominates over spontaneous emission. The output of light increases dramatically and linewidths narrow considerably as the majority of photons emitted are coherent with one another; this is shown in **Figure 3.12**.
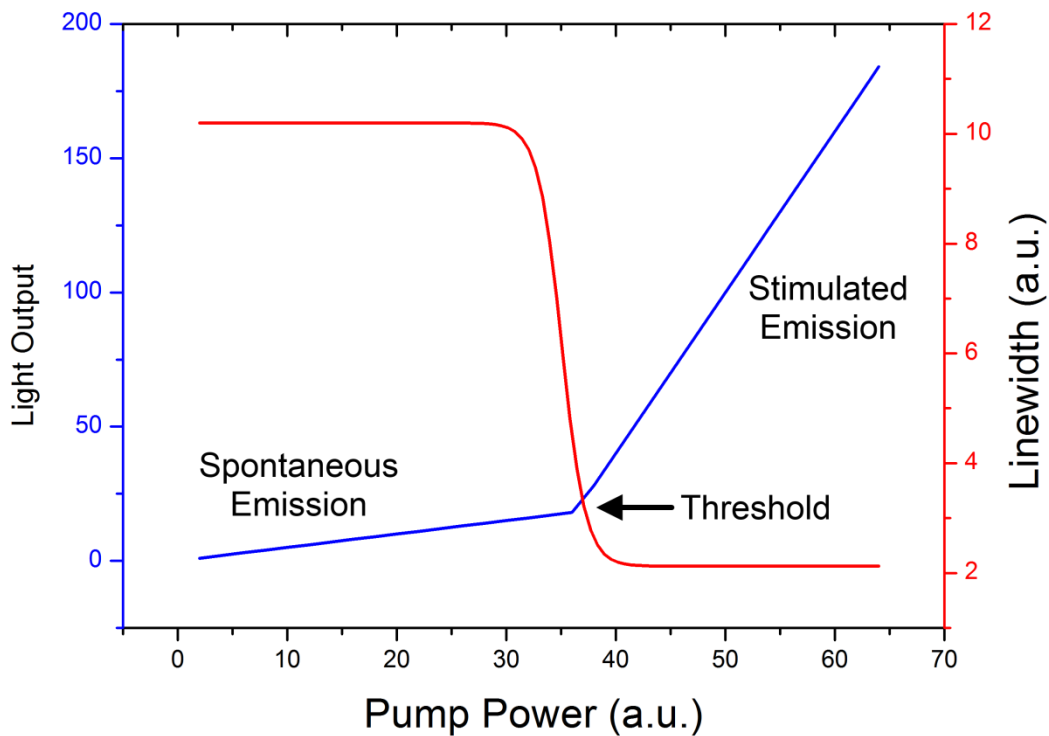
Figure 3.13. Emission of a semiconductor as a function of pump power above and below the lasing threshold $G_{threshold}$. (blue) and linewidth of emission profile above and below threshold (red).

As emission occurs, the excited state population is depleted and more energy must be introduced to the system in order to maintain the population inversion. For a simple two-level system (the ground state and one excited state), it is not possible to form or maintain population inversion through optical pumping. This is because absorption of, and stimulated emission caused by, incident photons are competitive processes. At low excited state populations, absorption will dominate and the proportion of electrons in excited states will grow. As soon as the excited state population exceeds 50%, stimulated emission becomes the dominant process and serves to deplete this population; eventually equilibrium is reached with 50% of the population in the ground state and 50% in the excited state. A two-level system thus experiences no net optical gain, though it may achieve optical transparency if $N_1=N_2$.

To overcome the limitations of the two level system, three- or four-level systems are used which use methods other than direct optical pumping to form population inversions. In three level systems, electrons are pumped to a third higher energy level ($E_1{\rightarrow}E_3$), before undergoing a rapid, non-radiative transfer to a metastable energy level below ($E_3{\rightarrow}E_2$). It is from this meta-stable energy level that lasing occurs ($E_2{\rightarrow}E_1$), on a longer timescale than the initial non-radiative decay. The third level allows electrons to be continually pumped into an excited (E_3) state without immediately undergoing stimulated emission and an inverted population to be created.

The rapid transfer of electrons from $E_3{\rightarrow}E_2$ means both that N_3 is rapidly depleted so there available states for direct absorption from E_1, and that a large excited state population can be built at E_2 ($N_2{>}0$). Three level systems are uncommon as >50% of the atoms must be in excited states and can require a significant amount of pumping.

In four level systems, the $E_2{\rightarrow}E_1$ transition is also a fast non-radiative transition. This means that in order for lasing to occur, population inversion must occur between the third and second energy levels ($N_3{>}N_2$ not $N_3{>}N_1$). As the decay time from the $E_2{\rightarrow}E_1$ is very rapid, no substantial population can be built up in the E_2 level. This means that a much smaller fraction of the total population must be in excited states. This drastically decreases the pumping energy requirements and lowers the threshold for lasing. Two-, three-, and four-level systems are depicted in **Figure 3.13**.
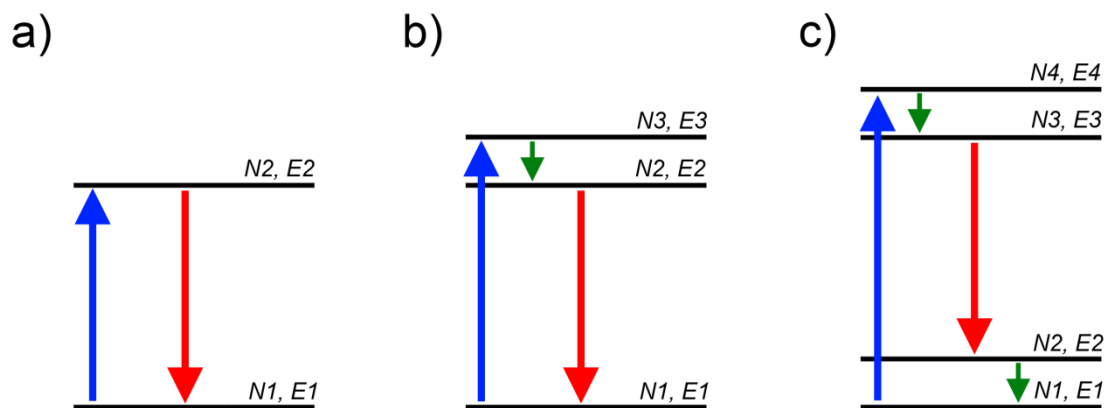
Figure 3.14. *The possible transitions for:* **(a)** *a two level system,* **(b)** *a three level system, and* **(c)** *a four level system. Blue arrows denote absorption from the pump source, red – "slow" radiative decay, and green "fast" radiationless transitions not governed by selection rules. (b) and (c) can both experience population inversions and optical gain, (a) cannot.*

3.4.2. Polaritonic Lasing

Whilst the measured photons from photonic and polaritonic lasing are indistinguishable from one another (both produce coherent photons), the mechanisms behind them are fundamentally different. There are two possible mechanisms for polaritonic lasing which are differentiated by the polariton lifetime in relation to the time it takes for a polariton to relax to the bottom of the branch. In the case where $\tau_{polariton} \gg \tau_{relaxation}$ the polariton states have sufficient time to scatter off one another and dissipate excess energy to form a thermalized population at the bottom of the lower polariton branch. Albert Einstein speculated that below a critical temperature, an ideal gas comprised of non-interacting bosonic particles would condense into the lowest available quantum state. This phenomenon is known as Bose-Einstein condensation (**BEC**); BECs are a state of matter in which a large proportion of a boson population occupy the lowest possible quantum state.

The entirety of the condensate can be treated as one macroscopic expression of quantum phenomena and described using a single wavefunction. A consequence of this is that a population inversion is not required to produce coherent light as all of the particles in the system are in the same state; this can reduce the lasing threshold for a given material by several orders of magnitude.

The primary criterion as to whether a BEC can form is given by **Equation 3.52**, in which T_C is the critical temperature below which condensates can form, n is the particle density, m is the mass per boson, $\hbar$ is the reduced Planck constant, k_B is the Boltzmann constant, and ζ is the Riemann zeta function (ζ (3/2)≈2.6124). This applies to a uniform three-dimensional gas comprised of non-interacting particles with no apparent internal degrees of freedom.

$$T_C = \left(\frac{n}{\zeta\left(^3/_2\right)}\right)^{^2/_3} \frac{2\pi\hbar^2}{mk_B} \approx 3.3125 \frac{\hbar^2 n^{^2/_3}}{mk_B} \tag{3.52}$$

To produce a BEC, polariton states of various energies must first be created and then must migrate from different positions along the LPB to the lowest available quantum state. In inorganic systems, this energy is typically dissipated through scattering from the crystal lattice and the emission of phonons; the further along the LPB the polariton travels, the more photon like it becomes thus reducing the probability of additional scattering events[10] (they are also limited by the polariton lifetime). This forms a "bottleneck" in the polariton population and if it is sufficiently dense, a second cooling mechanism, polariton-polariton scattering, takes over.

Polaritons are excellent candidates for the formation of BECs as their exceedingly low effective mass ($\sim10^{-4}$ that of the mass of an electron) means that the critical temperature, below which condensates can form is remarkably high (of the order of 100s of Kelvin) and can even be observed at room temperature. It is worth noting that as the polariton lifetime is determined their constituent components, and typically decay on faster timescales that are necessary for the population to adopt a thermalized distribution. This means that they require continual pumping to sustain a population and are inherently non-equilibrium in nature, nevertheless they display many of the characteristics expected of equilibrium BECs.

Like photonic lasers, above the BEC threshold temperature the population of polariton states at $k=0$ (normal incidence) increases linearly with the excitation pump power and there exists a broad distribution of polariton energies (thus broader linewidths). Below threshold, the polariton population at $k=0$ increases nonlinearly and emission linewidths narrow. These attributes alone are not sufficient to state that BEC has occurred as they are present in photonic lasing systems too. A second pathway towards polaritonic lasing exists if $\tau_{polariton} \ll \tau_{relaxation}$. In this case, the polaritons do not have time to thermalize, they form non-equilibrium states and are said to be in the kinetic regime. A more in-depth checklist of properties that each system must possess is contained in **Table 3.1**.

Property	Polariton BEC	Polaritonic laser	Photonic Laser
Thermal equilibrium below threshold	✔	✗	✗
Bose distribution above threshold	✔	✗	✗
Threshold corresponds to onset of degeneracy	✔	✔	✗
Linewidth narrowing	✔	✔	✔
Increase of temporal coherence	✔	✔	✔
Spontaneous polarization	✔	?	✗
Long-range spatial coherence	✔	✔	✔
Polaritons are the particles that accumulate coherence (strong coupling)	✔	✔	✗
Heisenberg-limited position and momentum uncertainty product	✔	✔	✗

Table 3.1. *Experimentally observed differences between exciton-polaritons BECs , Exciton-polariton lasers, and vertical-cavity surface-emitting lasers (**VCSEL**) as provided by Byrnes et al.[10]*

3.5. Summary

To summarise, complex multilevel structures can be modelled using a transfer matrix approach. This allows the polariton energies of the upper and lower polariton branches can be predicted using a classical two level model. Experimentally measured data can be fitted using these models to extract key system parameters such as Rabi splitting and cavity mode lifetimes which can be used to characterise polariton populations.

Strong coupling has been shown in seven different materials in the experimental chapters 6 to 9. Changes in polariton population as a function of exciton-photon mode detuning are explored in **Chapter 6** and a model based upon radiative pumping of polariton states is developed. Microcavities containing the fluorescent dye BODIPY-Br in **Chapter 7** have successfully demonstrated polariton lasing, experiments are ongoing with collaborators at the University of Southampton to determine whether or not condensation has occurred. **Chapter 8** details the first reported example of strong coupling in a biological system, and **Chapter 9** details efforts to modify the spectral properties of carotenoids via optical confinement.

3.6. References

1. Hecht, E. *Optics, 4th Edition*. (Addison-Wesley, 2002).

2. Sheppard, C. J. R. Approximate calculation of the reflection coefficient from a stratified medium. *Pure Appl. Opt. J. Eur. Opt. Soc. Part A* **4,** 665–669 (1995).

3. Coles, D. Polaritons in Strongly-Coupled Organic Microcavities - Thesis. *Univ. Sheff.* (2011).

4. Panzarini, G. *et al.* Exciton-light coupling in single and coupled semiconductor microcavities: Polariton dispersion and polarization splitting. *Phys. Rev. B* **59,** 5082–5089 (1999).

5. Fox, M. Quantum Optics. *Univ. Oxford* **53,** 1689–1699 (2013).

6. Fermi, E. *Nuclear Physics*. (University of Chicago Press, 1950).

7. Purcell, E. M. Spontaneous Emission Probabilities at Radio Frequencies. *Phys. Rev.* **69,** 681 (1946).

8. Zhu, Y. *et al.* Vacuum Rabi splitting as a feature of linear-dispersion theory: Analysis and experimental observations. *Phys. Rev. Lett.* **64,** 2499–2502 (1990).

9. Fox, M. *Optical Properties of Solids*. (Oxxford University Press, 2013).

10. Byrnes, T., Kim, N. Y. & Yamamoto, Y. Exciton–polariton condensates. *Nat. Phys.* **10,** 803–813 (2014).

4.

Experimental Methods: Fabrication

This chapter describes the techniques and equipment that were employed in order to fabricate samples and the inherent advantages and limitations of each method. It is divided into three sections, the first of which briefly deals with the solution processing of organic semiconductors which may be studied in a control film or placed within a cavity. It includes a list of the materials employed, and the experimental chapters in which they can be found. The second part concerns the deposition of mirrors, both metallic and dielectric, and the obstacles that must be overcome in order to produce satisfactory mirrors within the constraints of time, money, and the robustness of the organic layer they are to be deposited upon. The third and final section of this chapter details the growth conditions and extraction processes used to remove biological structures and pigments from their host cells.

4.1. Active Layer Preparation

4.1.1. Solution Processing of Films

To position a dye within a planar microcavity, it must first be fixed into a solid form; this is most commonly achieved by dispersing it within a compatible solvent and polymer matrix. The criteria for a suitable matrix are threefold: it must be soluble within the same solvent as the dye, it must not disrupt the formation of aggregates (if so desired), and it must be optically transparent (i.e. not contain any significant any absorption or emission features that may interfere/contribute within the desired spectral range). Aggregation can be induced to a greater or lesser extent by increasing the quantity of dye within a solution, or by changing the solvent used; the introduction of a polar solvent will cause hydrophobic dyes to minimise the amount of surface area they present and form aggregates. Insoluble matter or aggregates over a certain size are filtered out using porous PTFE or PVDF filters.

If the semiconductor being explored is not a small molecule but a polymer, a host matrix is not necessary; One may be added however in order to achieve sufficient solution viscosity for thicker films or to reduce self-quenching, though this runs the risk of phase separation and increasing scattering.

Once dye-doped solutions have been prepared, films are deposited onto substrates via spin-coating. Solutions are deposited onto a rotating substrate which is accelerated to a high velocity. Centrifugal forces drive the solution outwards, evenly coating the substrate causing the solvent to evaporate leaving only a uniform polymer layer. Film thicknesses typically vary by <1% over large areas (>cm^2). The thickness T, of the layer deposited can be described simply by **Equation 4.1**, in which c is the solution concentration, η viscosity, and ω spin speed.

$$T \propto \frac{c\eta}{\sqrt{\omega}} \qquad\qquad \textbf{(4.1)}$$

Whilst coarse adjustment of film thickness can be done by varying the concentration of the material within the solution, fine tuning must be done by adjusting the spin speed. This is because the relationship between concentration and viscosity (and hence film thickness) is not completely linear and can depend upon the molecular weight of the polymer.

A solution can be dispensed upon a substrate in one of two ways: static or dynamic. Static dispense occurs when the substrate is not moving to ensure that complete coverage of the substrate is achieved and is typically employed when working with high-volatility solvents. Dynamic dispense occurs when the substrate is already moving at low speeds (typically <1000RPM) before being increased to higher speed. This method is used when there is a limited supply of the solution as it is less wasteful or if the solution has poor surface wetting properties as this can prevent the formation of voids in the film. **Table 4.1** demonstrates some common film aberrations that can occur and describes their likely causes.

A number of simplifying assumptions can be made in order to model spin-coating simply with **Equation 4.1**. Firstly it is assumed the rotating plane is infinite and horizontal so that there is no radial gravitational component to account for, and secondly that the radial velocity across the entirety of the plane is small enough that Coriolis forces can be neglected. The liquid layer being dispensed is assumed to be radially symmetric, Newtonian in nature, perfectly wet the surface, and experience shear resistance in horizontal planes. A more complete discussion of the solution processing of films and their evaporation dynamics is discussed by Bonn et al[1].

Unfortunately, spin-coating is wasteful of material as a large quantity of solution is thrown from the substrate by the spinning. Despite this, it reliably produces films of consistent thicknesses over large areas, the equipment required is inexpensive, and thus is widely utilised in device development.
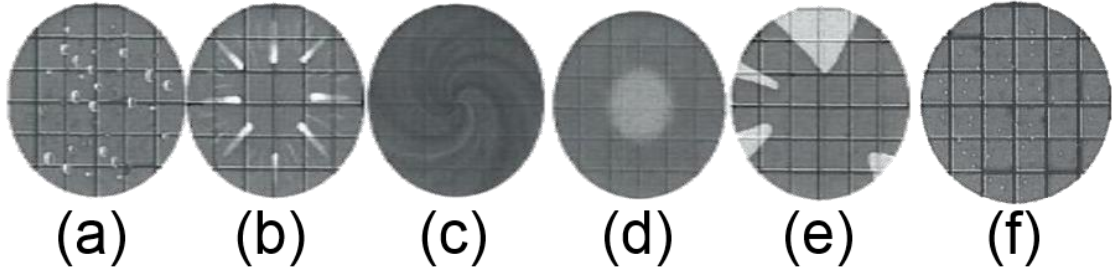
Table 4.1	Problem	Causes	Solutions
(a)	Air bubbles in film	• Air bubbles present in dispersed solution	• Use magnetic stir bar at low RPM
(b)	Streaks	• Fluid velocity (dispense rate) is too high • Spin bowl exhaust rate is too high • Solution rests on wafer too long before spin initiates • Spin speed/acceleration is too high • Particulate matter on substrate surface before spinning • Fluid is not being dispensed at the centre of the substrate	• Slower dispense • Lower volatility solvent • Dynamic dispense • Lower speed/acceleration • Clean substrate more thoroughly • Use static dispense
(c)	Swirl Pattern	• Solvent evaporation too high • Off-centre solution disperse • Spin speed/acceleration is too high • Insufficient spin time	• Lower volatility solvent • Static dispense • Lower spin speed/acceleration • Longer duration
(d)	Centre Circle (Chuck Mark)	• Residue on other side of substrate from prior spins	• Clean the reverse of substrate
(e)	Uncoated Areas	• Insufficient solution dispensed • Imperfect substrate wetting	• Use larger quantity of solution • Modify surface energy of substrate: usually via plasma cleaning or washing with an acid/base • Low RPM dynamic dispense
(f)	Pinholes	• Air bubbles present in solution • Particulate or undissolved matter in fluid • Particulate matter on substrate surface before spinning	• Use magnetic stir bar at low RPM • Use porous filter • Clean Substrate

Table 4.1. *Common spin-coating defects and their causes, information courtesy of MNTC[2,3] and Bonn et al[1]. Image adapted from Micro/Nano Technology Centre[2].*

4.1.2. Materials and Matrices

A number of microcavities containing highly fluorescent small molecules based on derivatives of boron-dipyrromethene (**BODIPY**) were constructed, materials known for their large fluorescence quantum yields and long exciton lifetimes. In certain derivatives it is not uncommon to achieve quantum yields approaching 100% and lifetimes on the order of nanoseconds. This is in contrast with J-aggregates of cyanine dyes which have proved popular in strong-coupling studies[4–7]. J-aggregates experience the phenomenon of superradiance and possess lifetimes of <5ps in the solid phase. Quantum yields are typically lower in aggregated systems in which exciton diffusion is very fast and efficient, providing more opportunities to be quenched by non-radiative defects and limiting quantum yields to <3%[8]. The bromine substituted variant of BODIPY (**BODIPY-Br**) depicted in **Table 4.2 (a)** was synthesized by Francesco Galeotti at CNR-ISMAC, the Institute for Macromolecular Studies. BODIPY-Br proved to have high solubility in toluene and dispersed well within polystyrene matrices to produce films with a low degree of surface roughness. Strongly-coupled microcavities containing BODIPY-Br can be found in **Chapter 6**, exploring changes to the polariton population distribution, and **Chapter 7**, in devices producing polaritonic lasing.

The oligofluorene substituted BODIPY variants depicted in **Table 4.2 (b)** were synthesized by Neil Findlay at the University of Strathclyde and are referred to as meso-terfluorene BODIPY and meso-quaterfluorene BODIPY (**meso-TFBOD** and **meso-QFBOD**). The perylene derivative shown in **Table 4.2 (c)** is known as LUMOGEN ® F Orange 240 (**LFO**), and was purchased from the BASF corporation; similar perylene derivatives have found use as laser dyes. Much like BODIPY-Br, all three of these materials possess high quantum yields (approaching unity at low concentrations) and long exciton lifetimes, unlike BODIPY-Br they have very different spectral profiles. The photophysics of films and microcavities containing these dyes are covered in more detail in **Chapter 7**, which details both amplified spontaneous emission in control films and the formation of polariton states once confined within microcavities. All three materials were dissolved in toluene and dispersed into a polystyrene matrix purchased from Sigma Aldrich with a molecular weight of ~192,000.
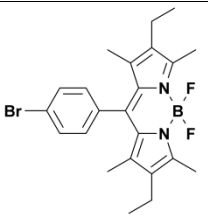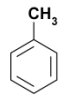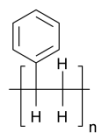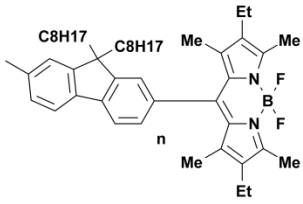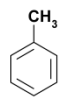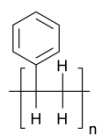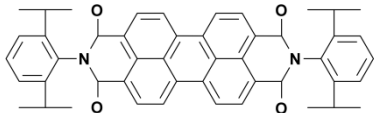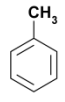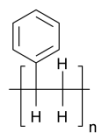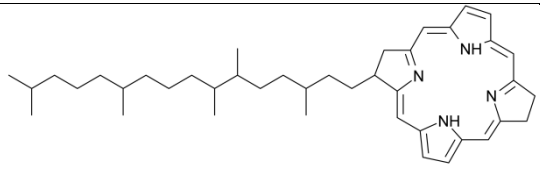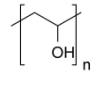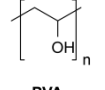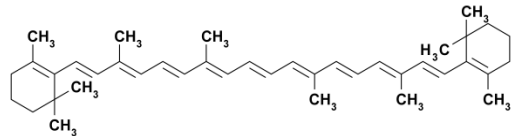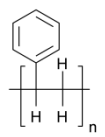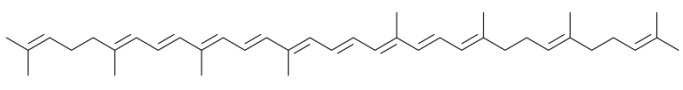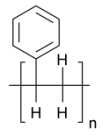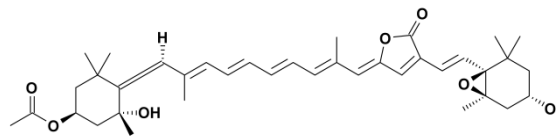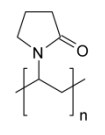
	Material	Solvent	Matrix
(a)	BODIPY-Br	Toluene	Polystyrene
(b)	meso-TFBOD, n=3 / meso-QFBOD, n=4	Toluene	Polystyrene
(c)	Lumogen	Toluene	Polystyrene
(d)	Bacteriochlorophyll	Water	PVA
(e)		Water	PVA
(f)	Beta Carotene	THF	Polystyrene
(g)	Neurosporene	THF	Polystyrene
(h)	Peridinin	Methanol	PVP

Table 4.2. *A list of the organic semiconductors studied in this thesis including both their host material and solvent from which they were cast.*

Biological systems were the next class of materials to be investigated. Chlorosomes, a component of the light harvesting complexes of the *Chlorobium tepidum* green sulphur bacteria were extracted and suspended in water before being dispersed within a polyvinyl alcohol (**PVA**) matrix. *C. tepidum* are a photosynthetic species of bacteria that live deep underwater where they are exposed to extremely limited quantities of light (on the order of 100s of photons per second[9]) and thus have evolved very efficient apparatus to harvest all available photons. The chlorosomes shown in **Table 4.2 (e)** are composed of many lamellar aggregates of the bacteriochlorophyll shown in **Table 4.2 (d)**. Microcavities containing these structures can be found in **Chapter 8** along with the first demonstration of strong coupling in a biological system.

The final class of materials covered within this thesis were carotenoids. These are naturally occurring pigments with strong absorption features that are used by cellular organisms to dissipate potentially damaging radiation as heat. β-carotene, neurosporene, and peridinin can be seen in **Table 4.2** parts **(f)**, **(g)**, and **(h)** respectively. β-carotene was purchased from Sigma Aldrich, neurosporene was extracted from the bacteria *Rhodobacter sphaeroides* by George Sutherland (University of Sheffield), and peridinin was cultivated in the dinoflagellate species *Amphidinium Carterae* with the assistance of Thomas Sydney (University of Sheffield). All three carotenoids displayed an affinity for tetrahydrofuran (**THF**) and were solution processed both neat and within polystyrene films. The photophysics of films and microcavities exploring the unusual inverted S2-S1 electronic symmetry of these carotenoids are covered in more detail in **Chapter 8**.

4.2. Mirror Deposition

4.2.1. Thermal Evaporation

Thermal evaporation is used to deposit thin films of metals for use as metallic mirrors or electrical contacts. Here, a small quantity of the desired metal is placed into a ceramic crucible or tungsten boat between two electrodes in a vacuum chamber. The crucible is warmed through resistive heating by passing a current between the two electrodes until the metal within reaches a high enough temperature to first melt, then boil. Once the metal reaches its boiling point, metallic vapour is deposited upon the substrates mounted in the chamber, **Figure 4.1**. It is important to maintain low pressures throughout the evaporation to prevent unwanted chemical reactions: if aluminium is deposited in the presence of oxygen it will form aluminium oxide. Higher pressures reduce the mean free path of the metal vapour, introducing the likelihood of collisions with other contaminants, and reducing the amount of vapour reaching the target substrate. Film quality can be improved by rotating the target substrates to account for any anisotropy in vapour deposition to ensure more even deposition.

The deposition rate can be adjusted by varying the current supplied to the crucible which in turn affects the properties of the film created. Higher currents result in faster deposition speeds and higher roughness surfaces[10]. In some circumstances it can be beneficial to evaporate an additional layer between the semiconducting and metallic layers. This can be useful in electrically driven devices as an intermediary to help match work functions of the metallic contact with the HOMO/LUMO level of the semiconductor. It also serves to limit metallic ion penetration into the underlying layer and thus reduce damage to the relatively fragile organic and provide a more uniform interface between the two layers. E.g. a calcium layer before an aluminium layer to aid electron injection/hole extraction or a LiF layer to reduce Al interdiffusion into lower layers[11-14]. This was particularly important when producing microcavities containing β-carotene (**Chapter 8**). As the substrates are neither heated nor in direct thermal contact with the evaporation source, it is possible to deposit metallic films upon relatively fragile organic materials with low melting points with this technique.
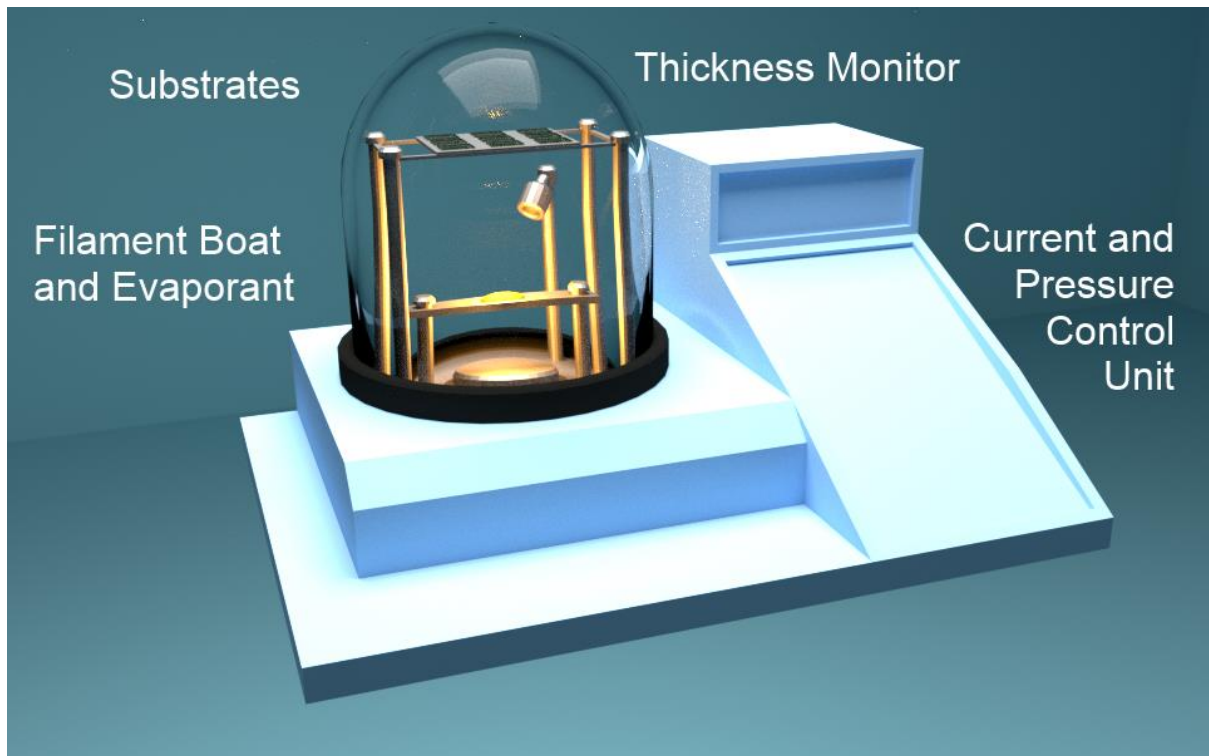
Figure 4.1. *Schematic of an Edwards 306 thermal evaporator.*

Many different metals can be deposited using thermal evaporation however gold, silver and aluminium have mainly been used in this body of research, the reflectivities of which are shown in **Figure 4.2**. Silver is very commonly used as it the most reflective metal across the widest range of wavelengths, having higher reflectivity than aluminium at all wavelengths >450nm. The reflectivity of Silver rapidly decreases at shorter wavelengths, falling close to zero as it approaches 310nm. When working at ultraviolet wavelengths, aluminium is used as it has a reflectivity of >90% even wavelengths as short as 200nm. For work at longer wavelengths, gold is typically used as it has a reflectivity of 98-99% throughout the infrared. The low reflectivity of gold at wavelengths <550nm (responsible for its distinctive colour), and high cost limit its use across other parts of the spectrum.
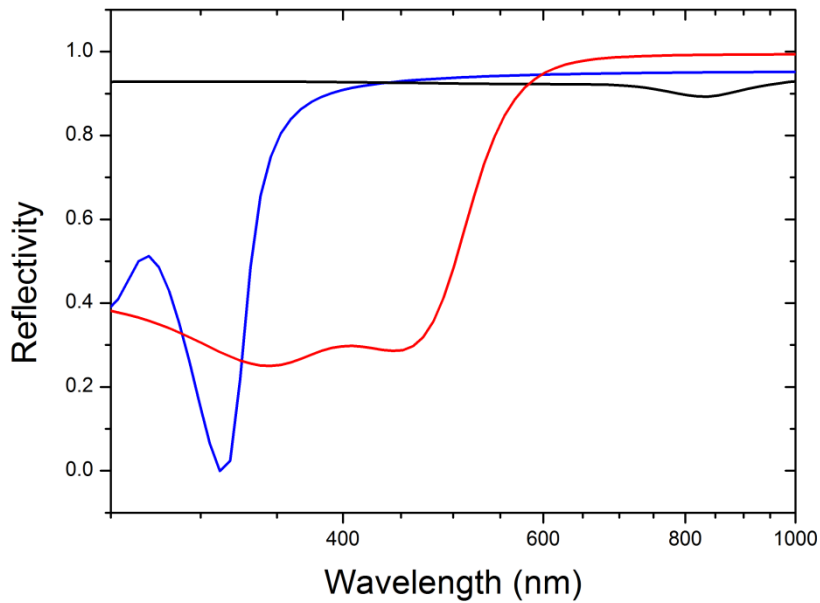
Figure 4.2. *Calculated reflectivity as a function of wavelength for a thin film of (black) aluminium, (red) gold and (blue) silver.*

An Edwards 306 evaporator was used to deposit the metallic mirrors in the microcavities described in **Chapters 6 & 8**.The thickness of the layers during deposition was monitored by observing how much the oscillations of a crystal are dampened, and later verified using surface profilometry.

4.2.2. Plasma-Enhanced Chemical Vapour Deposition

If higher Q-factor microcavities are desired, it is common to replace one or both of the mirrors with a DBR. As described in Section 3.2, DBRs are comprised of thin alternating layers of materials with contrasting refractive index (*n*) with thickness corresponding to *λ/4n* resulting in constructive interference over a certain band of wavelengths. Plasma-Enhanced Chemical Vapour Deposition (PECVD) is an extensively utilized technique in the semiconductor industry as it can deposit thin films or multilayer structures rapidly whilst maintaining (relatively) high film quality.
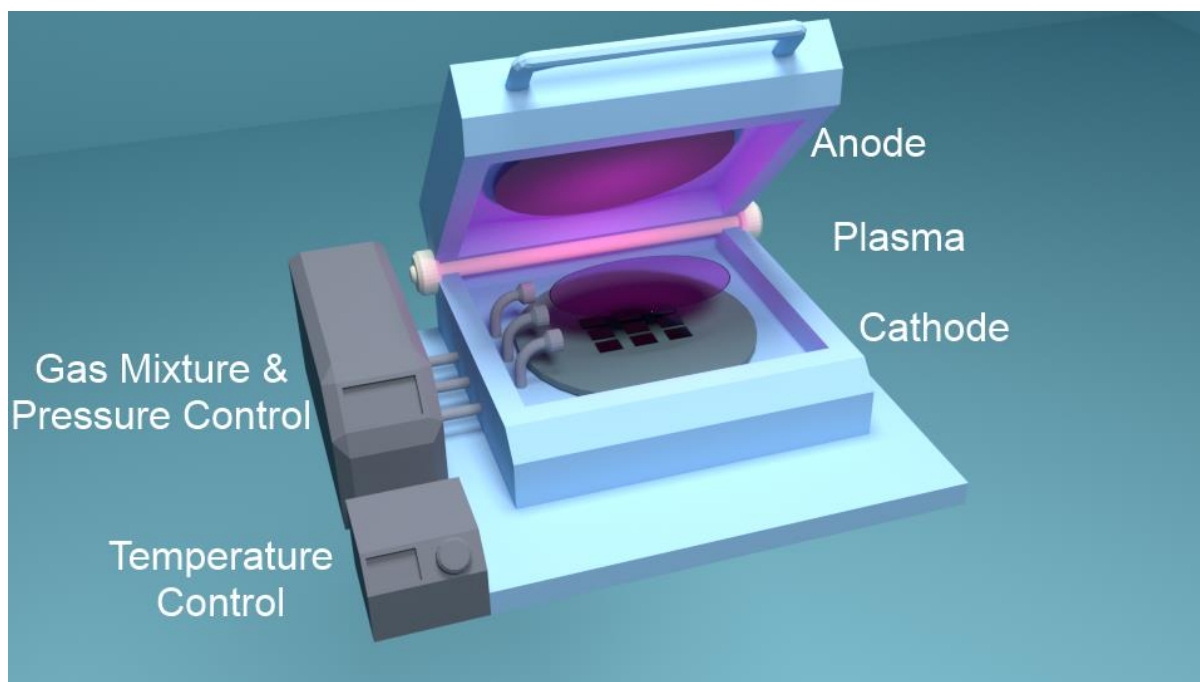
Figure 4.3. *Schematic of a plasma enhanced chemical vapour deposition system.*

As in traditional chemical vapour deposition, PECVD produces thin films on substrates by introducing volatile precursor gasses into a heated chamber (such as oxygen, silane, dichlorosilane and nitrous oxide). Precursor gasses undergo a series of chemical reactions until the desired material has been produced and deposited upon the substrates with any remaining by-products being evacuated from the system. For example, the production of a silicon dioxide film can be achieved via the following reactions:

$$SiH_4 + O_2 \rightarrow SiO_2 + 2H_2$$
$$SiCl_2H_2 + 2N_2O \rightarrow SiO_2 + 2N_2 + 2\ HCl$$
$$Si(OC_2H_5)_4 \rightarrow SiO_2 + By\text{-products}$$
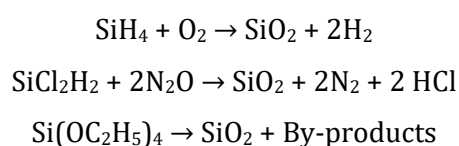
Though such systems can operate at atmospheric pressure, most systems tend to operate at lower pressures (typically $<10^{-6}$Pa); the lower pressure reduces the quantity of undesired gas (either excess reactant or outside contaminants) reducing the number of unwanted gas-phase reactions and resulting in a higher degree of uniformity across the deposited film.

PECVD differs from CVD, as the reactant gasses are passed between two parallel electrodes, resulting in the formation of a plasma. It is in this plasma that the chemical reactions take place. Electrons in a plasma are far more mobile than ions and this allows chemical reactions to be

used which would otherwise proceed very slowly. The benefit of this is that the chamber and substrate do not need to be held at such a high temperature (200°C vs 600-800°C). This reduces the risk of damage to the samples being produced and increases the range of materials that can be deposited. This is particularly important when working with organic materials as they typically have very low melting and boiling points and can easily be damaged by high temperature.

Silicon dioxide (SiO_2) and silicon nitride (Si_3N_x) are common used materials for DBRs as the difference between their refractive indices (1.46 and 2.02 respectively), allows for stopbands of ~100nm to be created when designing microcavities to work with materials in the visible region. Other silicon compounds are also common: silicon oxy-nitride (SiO_xN_y), silicon carbide (SiC), amorphous silicon (α-Si).

This technique is generally utilised for making DBR-metal microcavities, as the high-temperature nature of the process precludes its use on top of delicate semiconductors. A PECVD machine was used to deposit the DBRs utilized in **Chapter 6** and a schematic of the technique is depicted in **Figure 4.3**.

4.2.3. Ion-Assisted Physical Vapour Deposition

An alternative method to produce dielectric mirrors is to use Ion-Assisted Physical Vapour Deposition (**IAPVD**). In this technique, low-energy ions are fired a target anode causing it to eject material and convert from a solid to a vapour which is then deposited on desired substrates. Though there are some similarities between IAPVD and PECVD (namely the containment of the deposition within a vacuum chamber), the primary difference is that the reaction is physical rather than chemical, broadening the range or materials that can be deposited.

Figure 4.4. *Schematic of an ion-assisted physical vapour deposition system.*

Care must be taken with this technique not to use highly energetic ions as they can erode the semiconductor or substrate beneath. It is for this reason that low energy ions are used for the initial few nanometers despite the potential slight increase in dielectric absorption.

IAPVD is a low temperature technique that produces highly uniform films with low surface roughness. This means that microcavities with two DBR mirrors can be fabricated without risking damage to the organic semiconducting layer that might be cause by other deposition methods (morphological or chemical). The wider range of materials available permits the selection of materials with greater refractive indices such as Niobia (Nb_2O_5, $n\sim2.2$) or Titania (TiO_2, $n\sim2.5$). Design and fabrication of stopbands with even greater bandwidths is possible, allowing the study of excitonic materials with larger linewidths, Rabi splittings, or photon-mode detunings.

In this thesis, DBR deposition via IAPVD was performed by Caspar Clark at Helia Photonics, a company specialising in optical coatings for micro-optics. The microcavities described in **Chapters 6 & 7** employ mirrors created via this technique (Nb_2O_5 + SiO_2).

4.3. Light Harvesting Complex Growth and Extraction

The dinoflagellate *Amphidinium carterae* (*A. carterae*) was supplied by CCAP (Culture Collection of Algae and Protozoa) and grown in 250ml conical flasks in L1 medium (CCAP, As detailed in **Table 4.3**) approximately 10cm away from a 36W 1m fluorescent light source in a thermostatically temperature controlled box at 20°C. Cells were grown to an approximately density of 0.34 mg/ml, based on dry weight of a freeze dried sample. 13ml of culture was centrifuged (13000rpm) before freezing with liquid nitrogen and lyophilisation to obtain dry weight of cells in a pre-weighed Eppendorf.

Following growth, cells were harvested from 300ml of culture via centrifugation (8500 rpm) before extraction of peridinin and chlorophyll via addition of 25ml of methanol as outlined by Jiang et al[15]. The sample was then centrifuged again before collection of the supernatant containing the pigments. The remaining pellet was subjected to another solvent extraction with methanol twice before recombining all supernatants. Samples were kept below 4°C and away from light to slow pigment degradation. The recombined 75ml of methanol containing pigment underwent lyophilisation to obtain 32mg dry weight of pigment in a pre-weighed round bottom flask. This indicated a concentration of 120mg peridinin/chlorophyll extract per gram dry cell weight. Pigment was then stored in a freezer in a methanol solution to minimise degradation prior to experiments.

Cell growth media for *Chlorobium tepidum* was made up as described by **Table 4.3**, before being autoclaved and cooled under a N_2/CO_2 atmosphere (at a ratio of 9:1) before the addition of the stock solution described in **Table 4.4**;the final pH of the medium was then adjusted to 6.7-6.8. After this *C. tepidum* cells were incubated anaerobically at a temperature of 45° under low level illumination of (20 ± 2μmol^{-2}s^{-1}). The culture was periodically replenished with sterile neutralised sulphide solution to ensure that cell growth continued; care was taken to ensure oxygen did not pervade through the system, poisoning the cells.

Quantity	Compound	Stock Solution	Molar Concentration
3.15 g	$FeCl_3 - 6H_2O$	-	1.17×10^{-5} M
4.36 g	$Na_2EDTA - 2H_2O$	-	1.17×10^{-5} M
0.25 mL	$CuSO_4 - 5H_2O$	2.45 g/L dH_2O	1×10^{-8} M
3 mL	$Na_2MoO_4 - 2H_2O$	19.9 g/L dH_2O	9×10^{-8} M
1 mL	$ZnSO_4 - 7H_2O$	22 g/L dH_2O	8×10^{-8} M
1 mL	$CoCl_2 - 6H_2O$	10 g/L dH_2O	5×10^{-8} M
1 mL	$MnCl_2 - 4 H_2O$	180 g/L dH_2O	9×10^{-7} M
1 mL	H_2SeO_3	1.3 g/L dH_2O	1×10^{-8} M
1 mL	$NiSO_4 - 6H_2O$	2.7 g/L dH_2O	1×10^{-8} M
1 mL	Na_3VO_4	1.84 g/L dH_2O	1×10^{-8} M
1 mL	K_2CrO_4	1.94 g/L dH_2O	1×10^{-9} M
0.0005 g	Cyanocobalamin	-	-
0.1 g	Thiamine HCl	-	-
0.0005 g	Biotin	-	-
0.075 g	$NaNo_3$	-	-
0.00565 g	$NaH_2PO_4-2H_2O$	-	-

Table 4.3. *Contents of one litre of cell culture as made up using L1 Medium supplied by CCAP.*

Prior to the extraction of their chlorosomes, the green sulphur bacteria *Chlorobium tepidum* were cultured anaerobically and phototropically in low light conditions (20 ± 2 µmol m^{-2}s^{-1}) and incubated at a temperature of 45°C[16]. Chlorosomes were harvested once the bacteria had reached a steady state of growth with the addition of 2 M NaI. After this, the extract was purified by sucrose gradient separation via ultra-centrifugation at 135,000 x g for 16 h before finally being desalted and lyophilized. After extraction samples stored in low light conditions and refrigerated to minimize degradation

Medium Additive	Freshwater Strain	Marine Strain
KH_2PO_4	0.3 g	0.3 g
NHCl	0.34 g	0.34 g
KCl	0.34 g	0.34 g
$CaCl_2 \cdot 2H_2O$	0.15 g	0.15 g
NaCl	-	20.0 g
$MgSO_4 \cdot 7H_2O$	0.5 g	3.0 g

Table 4.4. *The defined medium composition for one litre of fresh, or salt water used to culture green sulphur bacteria.*[16]

Stock Solution	Volume Added per Litre of Medium
10% (w/w) $NaHCO_3$, saturated with CO_2	15 ml
1 M $Na_2S \cdot 9H_2O$ (autoclaved under N_2)	2.5 ml
2 mg of vitamin B_{12} in 100 ml H_2O	1 ml
Trace element solution SL 10*	1 ml

Table 4.5. *Stock solution added after autoclaving. *Trace element solution SL 10 contains per litre of distilled water: 25% HCl, 10 ml; FeSO4 · 7H2O, 2.0g; CoCl2 · 6H2O, 190 mg; MnCl2 · 4H2O, 100 mg; ZnCl2, 70 mg; Na2MoO4 · 2H2O, 36 mg; NiCl2 · 6H2O, 24 mg; H3BO3, 6 mg; and CuCl2 · 2H2O, 2 mg. The FeSO4 is dissolved in HCl, and distilled water is then added, followed by the other components.*[16]

4.4. Summary

The materials and techniques used to produce samples throughout this thesis are briefly outlined in this chapter. It is worth noting that although all of the semiconductors described in this thesis are solution-processed, not all organic semi-conductors are deposited through liquid-phase techniques. Small molecules lend themselves well to deposition via evaporation and are often used in applications where precision is prioritised over cost.

Likewise the deposition of mirrors need not come from high-temperature thermal, sputtering, or plasma based techniques and dielectric mirrors can be dip- or spin-coated. Though this technique was not employed in any complete cavities described within this thesis, a single DBR-structure comprised of 8 pairs of poly(9-vinylcarbazole) (**PVK**) and PS was produced to demonstrate the principle. This has also been reported in the literature using poly(methyl methacrylate) and Poly[1-[4-(3-carboxy-4-hydroxyphenylazo)benzenesulfonamido]-1,2-ethanediyl, sodium salt]) (**PAZO**)[17]. DBRs processed this way tend to have relatively low reflectivities and narrow stopbands as the refractive index contrast between organic materials tends to be quite small. In order to achieve high reflectivities, many layers must be deposited and with them come issues with surface wetting, roughness, and defects propagating through the DBR structures.

4.5. References

1. Bonn, D., Eggers, J., Indekeu, J., Meunier, J. & Rolley, E. Wetting and spreading. *Rev. Mod. Phys.* **81,** 739–805 (2009).

2. Louisville, U. of. Spin Coating Theory. *Micro/Nano Technol. Cent.* (2013). at <https://louisville.edu/micronano/users/standard-operating-procedures>

3. Hellstrom, S. L. *Basic Models of Spin Coating*. (2007).

4. Lidzey, Bradley, Armitage, Walker & Skolnick. Photon-mediated hybridization of frenkel excitons in organic semiconductor microcavities. *Science (80-.).* **288,** 1620–3 (2000).

5. Wenus, J. *et al.* Optical strong coupling in microcavities containing J-aggregates absorbing in near-infrared spectral range. *Org. Electron. physics, Mater. Appl.* **8,** 120–126 (2007).

6. Lidzey, D. G. *et al.* Observation of strong exciton–photon coupling in semiconductor microcavities containing organic dyes and J-aggregates. *Opt. Mater. (Amst).* **12,** 243–247 (1999).

7. Bradley, M. S. & Bulović, V. Intracavity optical pumping of J-aggregate microcavity exciton polaritons. *Phys. Rev. B* **82,** 033305 (2010).

8. Obara, Y., Saitoh, K., Oda, M. & Tani, T. Room-Temperature Fluorescence Lifetime of Pseudoisocyanine (PIC) J Excitons with Various Aggregate Morphologies in Relation to Microcavity Polariton Formation. *Int. J. Mol. Sci.* **13,** 5851–65 (2012).

9. Coles, D. M. *et al.* Strong coupling between chlorosomes of photosynthetic bacteria and a confined optical cavity mode. *Nat. Commun.* **5,** 5561 (2014).

10. Bordo, K. & Rubahn, H. G. Effect of deposition rate on structure and surface morphology of thin evaporated al films on Dielectrics and Semiconductors. *Medziagotyra* **18,** 313–317 (2012).

11. Kéna-Cohen, S., Maier, S. a. & Bradley, D. D. C. Ultrastrongly Coupled Exciton-Polaritons in Metal-Clad Organic Semiconductor Microcavities. *Adv. Opt. Mater.* **1,** 827–833 (2013).

12. Lee, J. H., Moon, D. W. & Yi, Y. The initial interface formation between Al and tris-(8-hydroquinoline) aluminum (Alq3) with LiF interlayer. *Org. Electron. physics, Mater. Appl.* **11,** 164–168 (2010).

13. Le, Q. T. *et al.* Photoemission study of aluminum/tris-(8-hydroxyquinoline) aluminum and aluminum/LiF/tris-(8-hydroxyquinoline) aluminum interfaces. *J. Appl. Phys.* **87,** 375 (2000).

14. Lee, J. H., Yi, Y. & Moon, D. W. Direct evidence of Al diffusion into tris-(8-hydroquinoline) aluminum layer: Medium energy ion scattering analysis. *Appl. Phys. Lett.* **93,** 1–4 (2008).

15. Jiang, J. *et al.* Characterization of the peridinin-chlorophyll a-protein complex in the dinoflagellate Symbiodinium. *Biochim. Biophys. Acta* **1817,** 983–9 (2012).

16. Dowrkin, M., Falkow, S., Rosenberg, E., Schleifer, K.-H. & Stackebrandt, E. *The Prokaryotes - A Handbook on the Biology of Bacteria: Proteobacteria: Delta and Epsilon Subclasses. Deeply Rooting Bacteria - Volume 7*. (2006). doi:10.1007/0-387-30741-9

17. Goldenberg, L. M., Lisinetskii, V. & Schrader, S. Fast and simple fabrication of organic Bragg mirrors—application to plastic microchip lasers. *Laser Phys. Lett.* **10,** 055808 (2013).

5.

Experimental Methods: Characterisation

This chapter outlines the methods used to characterise the samples produced by the techniques in **Chapter 4** and the underlying physical principles behind them. It is split into two sections, the first of which is based upon optical techniques, which covers both steady state and time resolved measurements. The second section describes the physical techniques used to investigate surface properties and film morphology.

5.1. Optical Characterisation

5.1.1. UV-Vis Spectroscopy
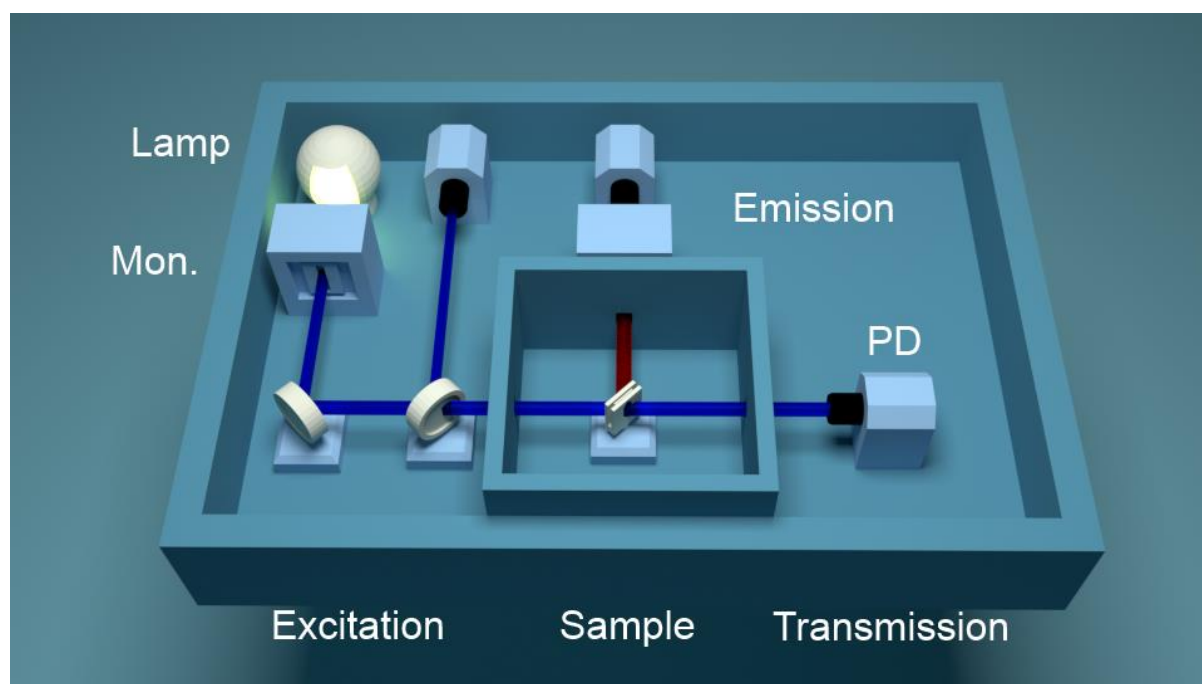
Figure 5.1. *Diagram of the Horiba fluoromax used for transmission measurements.*

Ultraviolet-visible spectroscopy is a technique used to probe electronic transitions between a ground and an excited state. A sample is illuminated by photons of varying wavelength; if the photon energy corresponds to that of an allowed electronic transition, the photon is absorbed and an electron is promoted to a higher energy level. By comparing the number of photons emitted by the source to the number collected after passing through a thin film of the material, the relative strength of the transition can be determined.

Three experimental set ups have been used for such measurements in this. The first of which is a Fluoromax 4 system produced by Horiba Scientific; a self-contained unit capable of absorption and photoluminescence measurements. It is comprised of a xenon lamp, an elliptical mirror, two monochromators, and three photodiode detectors (with identical response functions) as shown in **Figure 5.1**.

The xenon lamp provides light (from ~350 to 1000nm) which is collected and collimated by the elliptical mirror before illuminating the sample. After passing through the sample, the beam reaches the excitation monochromator which selects the desired wavelength (using a diffraction grating and stepper motor), before light is incident onto a silicon photodiode which records the intensity of the incident photons. Measurements are repeated with the sample absent in order to obtain a reference spectrum of the light source and absorption as a function of wavelength is obtained by comparing them with **Equations 5.1** and **5.2**.

$$Transmission(\lambda) = \frac{Sample(\lambda)}{Reference(\lambda)} \qquad \textbf{(5.1)}$$

$$A = -\log T = log\left(\frac{1}{T}\right) \qquad \textbf{(5.2)}$$

$$\tau = A \, ln \, 10 = \alpha l \qquad \textbf{(5.3)}$$

The Beer-Lambert law states that transmission of a material is related to both its overall absorption A and its optical depth τ given by **Equation 5.4**; it can also be expressed in terms of a material's attenuation coefficient α, and the path length l, that the beam travels through the medium. If the thickness of the material is known (either through AFM measurements of thin films, or by placing solution in a cuvette of known dimensions), the absorption coefficient per unit length or concentration can be determined; likewise, for a material with known absorption coefficient, the thickness can readily be ascertained from transmission measurements.

$$T = e^{-\tau} = 10^{-A} \qquad \textbf{(5.4)}$$

As power output of the xenon lamp is not consistent across all wavelengths of light, a beamsplitter is placed after the excitation monochromator which diverts a portion of the light onto a reference photodiode with an identical response function. By dividing the signal from the excitation detector by the reference (**Equation 5.5**), such differences can be corrected.

$$Corrected\ intensity = \frac{Excitation\ detector\ signal}{Reference\ detector\ signal} \qquad \textbf{(5.5)}$$

Whilst the Fluoromax is a very useful tool for absorption and photoluminescence measurements, it is limited by both the wavelength range of the xenon lamp and the sensitivity of the photodiode detectors used. For more sensitive measurements, or to cover a wider spectral range, an alternative system was employed. A fibre-coupled DH-2000-BAL Ocean Optics deuterium and halogen light source replaced the xenon lamp (allowing the UV and near-IR to be probed) with all wavelengths recorded simultaneously using an Andor Shamrock imaging spectrometer rather than using a series of monochromators and photodiodes.

5.1.2. Photoluminescence Spectroscopy

After the absorption of a photon and promotion of an electron to an excited state, the electron eventually relaxes to its ground state. It must do so by the emission of a photon or through a number of different non-radiative pathways (both of which processes have differing timescales depending on the material being studied), the former of which is known as photoluminescence (**PL**).

When samples are illuminated for long enough periods, i.e. under continuous wave (CW) excitation or when the length of excitation is much longer than that of the decay time (ms vs ns), the system can be considered to be in a quasi-stable equilibrium and such measurements are referred to as steady state. In many circumstances, the Fluoromax system described previously is a sufficiently sensitive tool for accurately measuring sample PL despite its incoherent (xenon) light source.

Unfortunately, the geometry of the Fluoromax precluded the measurement of sample PL or absorption as a function of angle; this rendered it unsuitable for characterising microcavities and limited its use to samples which did not carry an angular dependence, namely thin films and solutions. In order to overcome these limitations, the experimental set up as depicted in **Figure 5.2** was used. The sample is mounted in an Oxford Instruments nitrogen bath cryostat located at the rotation axis of two optical rails. The optical rails are connected to computer-controlled stepper motor via a rack and pinion linear actuator which allows precise movement of one or both arms.
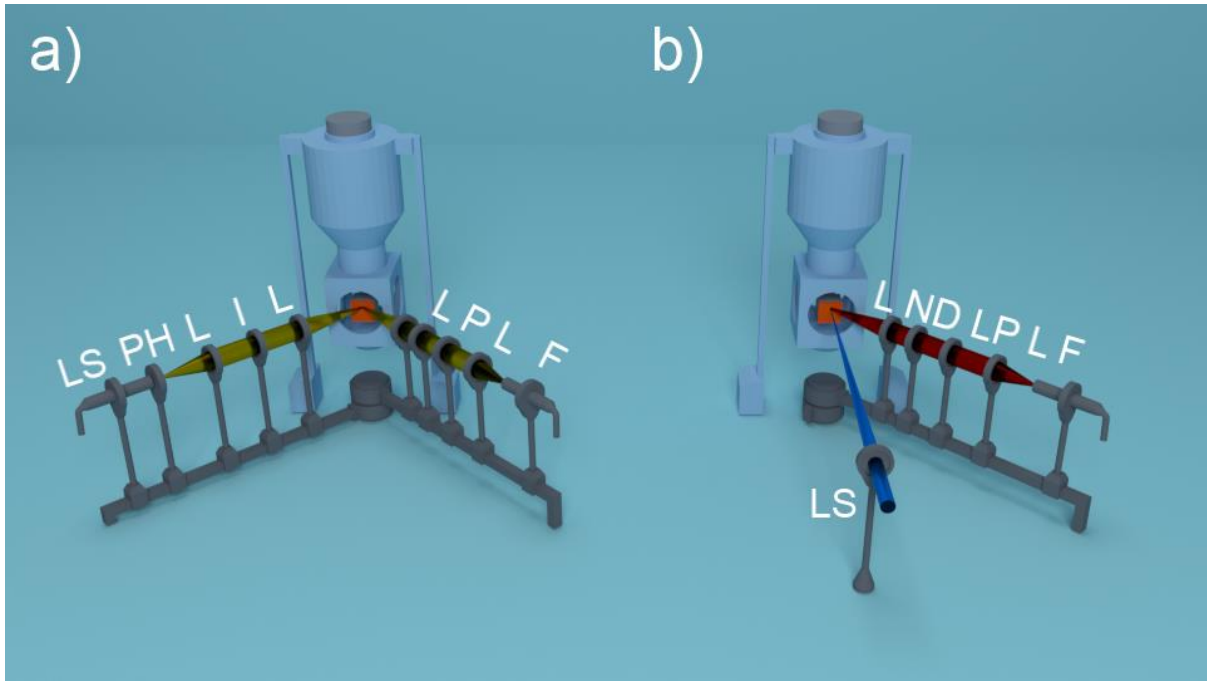
Figure 5.2. *The experimental set up configurations for **(a)** white-light reflectivity, and **(b)** angular dependent PL measurements. LS denotes light source, PH pinhole, L lens, I iris, ND neutral density filter, P polariser, LP long-pass filter, and F fibre coupling to a CCD.*

For reflectivity measurements: on the excitation arm was mounted a fibre coupled to an excitation lamp, a pinhole, a collimation lens, an iris (for adjusting light intensity), and a focusing lens. The collection arm contained a collimating lens, a long pass filter (to cut laser light), a polarizer (to ensure only TE light is collected), a focussing lens, and a fibre to the Andor Shamrock 303i spectrometer with air-cooled CCD camera. The primary light source used for such measurements is an Ocean Optics DH-2000-BAL balanced deuterium halogen lamp with a spectral range from 200nm to >1000nm.

Reflectivity measurements of microcavities are used to determine whether the system is in the strong coupling regime as it is not uncommon for the upper polariton branch to be weakly-or entirely non-emissive. In such systems, the upper and lower polariton branches can be observed as dips in the reflected lamp spectra.

For PL the laser was focussed on the surface at normal incidence upon the same spot used for reflectivity measurements (the central axis of rotation for the collection arm). This allowed both

reflectivity and PL measurements to be performed in rapid succession upon the same region of the sample (or in principle simultaneously).

Measured emission intensity from films is not uniform at all angles due to the Lambertian nature of the PL emission. "*the intensity observed from an ideally reflecting surface or diffuse radiator is directly proportional to the cosine of the angle θ between the direction of the incident light and the surface normal*"[1]. As the observation angle increases, the perceived area of the emitter decreases by *dAcosθ* as described by **Equation 5.6**. This can be compensated for by dividing the measured PL intensity by the cosine of the angle at which it has been collected.

$$I_0 = \frac{Id\Omega \, dA}{d\Omega_0 \, dA_0} = \frac{Icos(\theta)}{d\Omega_0 cos(\theta)dA_0} \tag{5.6}$$

The cryostat permits the role of temperature to be explored whilst preventing sample damage due to oxygen-induced photobleaching, though the geometry of the window limits the range of angles that are accessible from 0° to 55°.
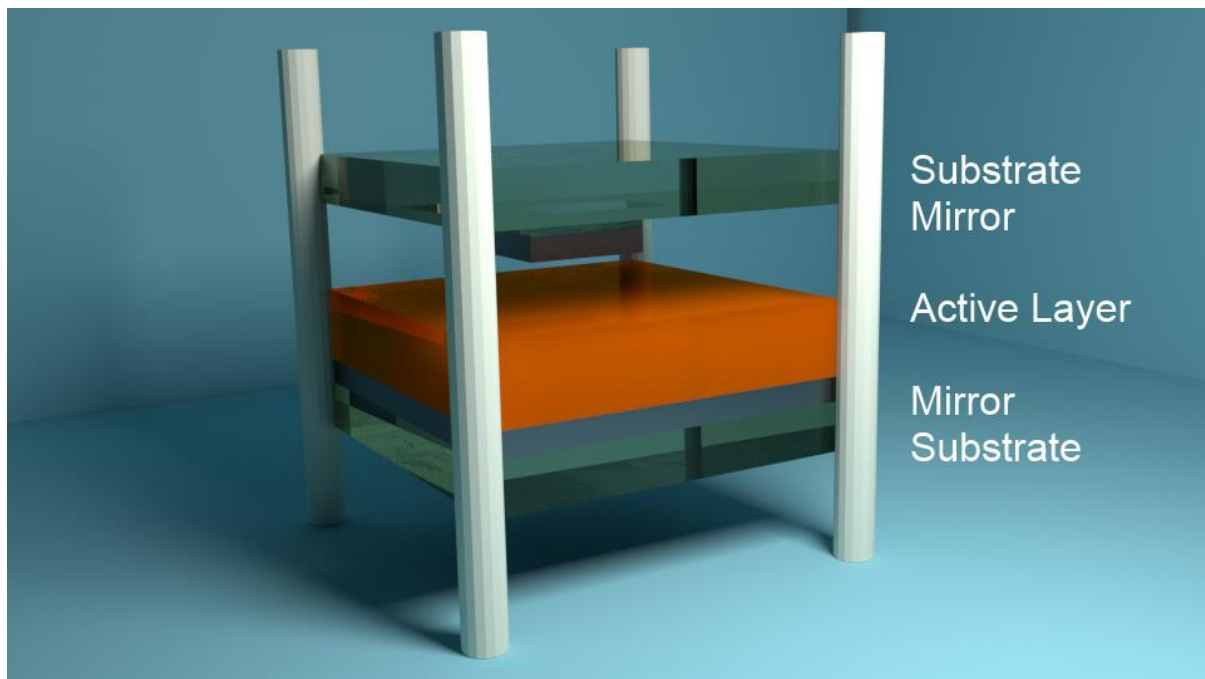
5.1.2.1. Open Cavities

Figure 5.3. *Experimental set up of an open cavity, a plinth is often employed to raise a section of the mirror above the rest of the surface. This reduces the chance of dust (or other surface contaminants) getting between the two mirrors and artificially limiting the smallest separation between the two mirrors.*

An alternative to angular-dependent reflectivity or PL measurements upon conventional planar microcavities is to use an open cavity. In this system, mirrors are deposited upon separate substrates that are mechanically by piezoelectric motors. As described in **Equation 3.1**, the allowed wavelengths of light within a cavity are defined by the separation between the two mirrors. A semiconducting layer is placed upon one mirror and by varying the cavity length, the photon mode within the cavity can be detuned as desired across a wide range of energies.

This technique is useful for fragile systems which cannot withstand the conditions required to place a mirror directly on top of the active layer. Q-factors are generally higher in open cavity systems too as the surface roughness of the mirror is not limited by the planarity of the semiconducting layer. Fitting to experimental results using the transfer matrix method described in **Chapter 3** requires only the energy term for the photon mode from a parabolic to a linear term. Transmission measurements made within an open cavity can be found in **Chapters 8** and **9**.
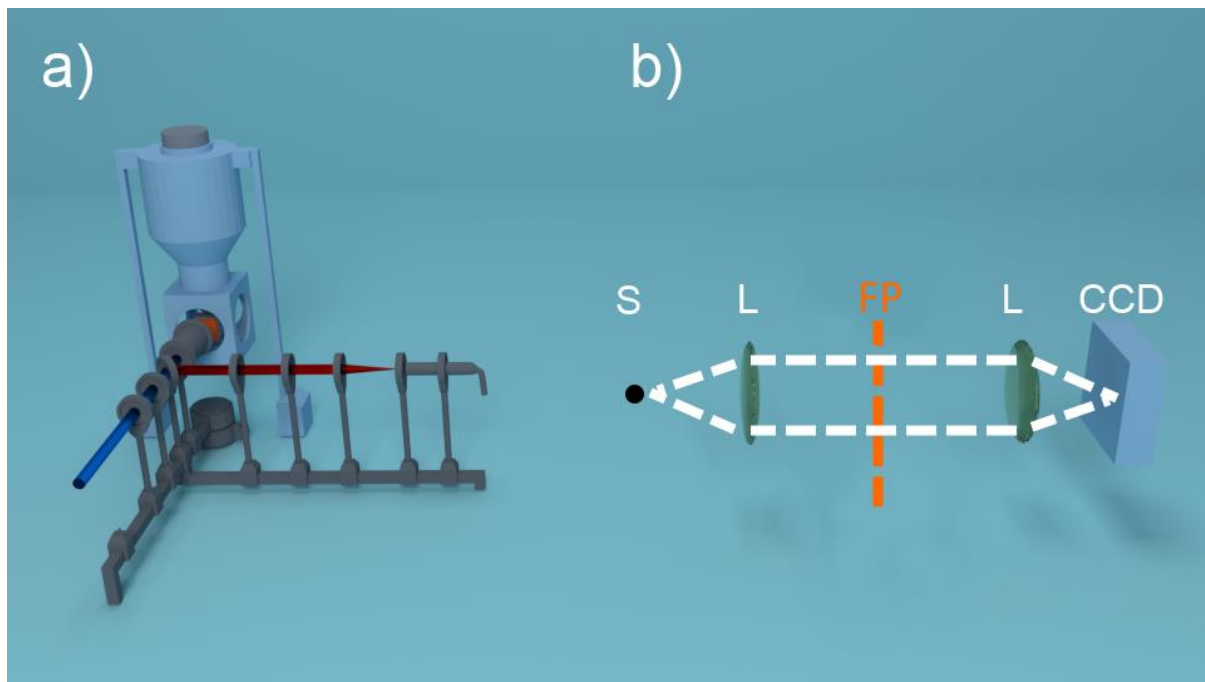
5.1.3. Fourier Plane Imaging

Figure 5.4. (a) *The experimental set up employed for Fourier plane imaging and **(b)** the Fourier plane as projected onto the back focal plane of the imaging lens. S denotes sample emission, L – lenses, and CCD – charge coupled device. Dashed (white) lines indicate the path of light propagation, the vertical dashed (orange) line denotes the Fourier plane FP.*

Rather than adjusting the excitation and collection arms multiple times for each individual angle, the entirety of the cavity emission dispersion can be imaged simultaneously. This can be done by using a microscope lens with a high numerical aperture placed very close to the sample to collect and collimate emission from a very small spot. A second lens is placed in the beam path one focal length from the back focal plane of the objective, projecting an image of the Fourier transform onto an imaging CCD camera as is depicted in **Figure 5.4**.

This is known as Fourier, or k-space, imaging and allows the angular distribution of photons emitted from a specific point in real space to be viewed in momentum space. These photons can be spectrally resolved, allowing a full dispersion curve to be created. In theory, the image projected onto the CCD of the camera is circular, though in practice it is slightly elliptical. As such, it is not uncommon to place a spatial filter between the second and third lenses in the intermediate real image plane.

For the smallest possible spot sizes, widest collection angles and highest resolutions, objectives with small focal lengths must be employed. Fine control of the sample's position relative to the lens is controlled by a series of piezo-electric motors; these allow thermal expansion/contraction to be accounted for when changing the temperature of the system (z-axis), or to scan across the sample surface (x- and y-axes), **Figure 5.4**. The range of angles that can be collected from is given by the numerical aperture, *NA*, of the objective which follows the relationship described by **Equation 5.7**.

$$NA = n\,sin\theta \qquad\qquad \textbf{(5.7)}$$

In order to achieve this degree of precision, the objective lens must be placed in close proximity with the sample being measured. In this case mounting the lens within the cryostat meant that angles as high as 45° could be observed.

Fourier space measurements made upon microcavities containing BODIPY-Br (**Chapter 6**) were performed at Université de Montréal, under the supervision of Carlos Silva with the assistance of Pascal Gregoire and Eleonora Vella.

5.1.4. Time-Resolved Photoluminescence

Whilst steady state measurements provide some information about radiative decay paths in films and microcavities, they do not reveal information regarding the emission timescales or other dynamics (such as energy transfer). The intensity *I* of PL emission from a population *N* of identical excited states decaying spontaneously falls exponentially with time. This is described by **Equation 5.8** below in which *t* is time, I_0 the intensity at time zero, and τ the time period for the number of excited states to fall to 36.8% of their original value.

$$I(t) = I_0 e^{-t/\tau} \qquad\qquad \textbf{(5.8)}$$

This means that the radiative decay lifetime of an excited state can be calculated simply by fitting an exponential decay to the measured PL intensity over time. Emission from a single species can be isolated by using a monochromator or band-pass filter to select emission from a narrow band of wavelengths. Alternatively, the emission from multiple species with different decay rates can be fitted using a series of exponentials as depicted in **Figure 5.6**. If the observed PL decay of a sample cannot be well fitted with a single, or at most two, exponential functions, this is indicative of other processes which are modifying the observed decay rate. These could be anything ranging from Forster resonance energy transfer (**FRET**), to the presence of additional populating mechanisms.
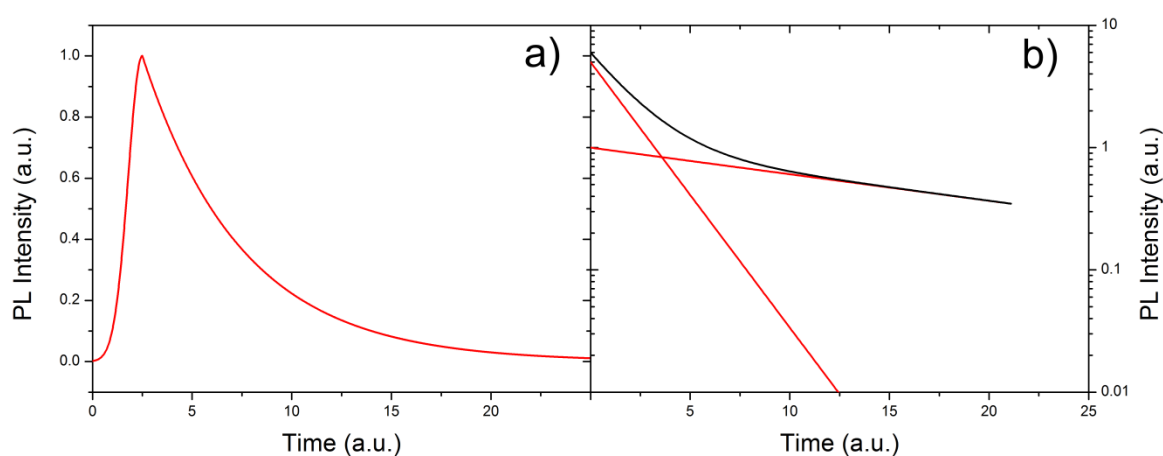
Figure 5.6. (a) *PL intensity decay vs time for a single transition.* ***(b)*** *Fitting of PL decay from two distinct species with different lifetimes using exponential fits described by* ***Equation 5.8****.*

Care must be taken to select an excitation source appropriate for the material being studied. If the laser has a fast repetition rate (or the material possesses a long excited state lifetime), it is possible that the excited state population created by the first laser pulse has not fully decayed before the next pulse arrives. In this case the observed background counts and decay profile can be distorted by remnant emission, increasing the difficulty of accurately fitting a decay profile; this is shown in **Figure 5.7**.
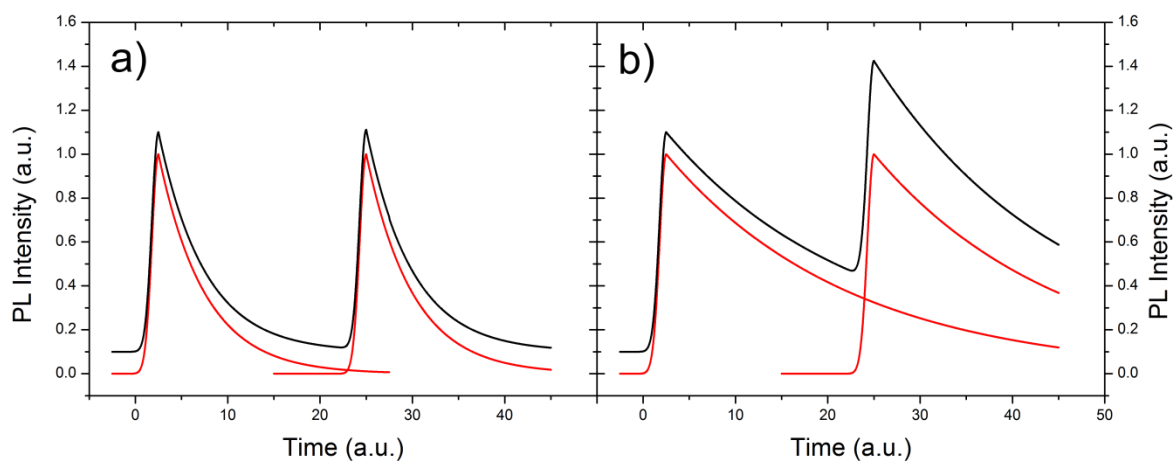
Figure 5.7. *Measured PL intensity as a function of time for (a) a material possessing an excited state lifetime shorter than the laser repetition time interval, and (b) an excited state lifetime longer than that of the time interval between pulses.*

In order to measure the emission dynamics of microcavities and films a number of time resolved PL techniques were used. Gated CCD Fourier space measurements were used to analyse microcavity PL dispersions on timescales of 200ps to ~10ns. Streak camera measurements were used to study aggregation dynamics of BODIPY-Br films on timescales ranging from ~5ps to 150ps. Finally time-correlated single-photon counting was used to study the dynamics of emissive films on timescales ranging from ~60ps to ~10ns.

5.1.4.1. Gated CCD Fourier Space Imaging

Though the read-out times from CCDs usually exceed practical timescales for time-resolved photoluminescence measurements of fast phenomena (100s of kilopixels/second), there exist a number of work arounds. One common solution is to mask half of the pixels on the CCD and use the unmasked region for imaging; this allows electrons to be transferred to the masked region and read out at leisure whilst the unmasked region acquires the next image, effectively halving the acquisition time. This technique is still fundamentally limited by the speed at which the pixels can be read out, which can be accelerated by increasing the voltage used to drive electrons out of their traps at the expense of slight loss of image integrity

An alternative (and often complementary) solution is to use a camera with a rapid shutter speed. The shutter restricts the temporal window in which photons can strike the CCD. By synchronising the shutter frequency with that of the laser pulse, the CCD can be left "acquiring" whilst only being exposed to photons from a narrow range of times; this is particularly beneficial when studying weakly emissive materials. Ultimately this means that the readout time of the CCD electronics is no longer the limiting factor and the temporal resolution of the system is determined by the shutter speed.

The Lavision Picostar gated camera and Acton SP-2300i imaging spectrometer described previously have a rapid shutter that permitted k-space images to be recorded with a nominal time resolution of 200 picoseconds. This allowed the decay dynamics of different states along the lower polariton branch to be studied simultaneously. For shorter temporal resolutions other techniques must be employed. Gated CCD Fourier-space measurements were performed at Université de Montréal, under the supervision of Carlos Silva with the assistance of Pascal Gregoire and Eleonora Vella.

5.1.4.2. Streak Camera Measurements

For measurements in the 200 femtosecond to picosecond scale, imaging using a streak camera is often the most desirable technique.

When a beam of light first enters a streak camera, it passes through a diffractive element. The degree to which light is diffracted is determined by the wavelength of the photon; this creates a horizontal dispersion ("fan") of photon energies which exit the slit at different angles. The diffracted light is then collimated by a lens, allowing photons of differing wavelength to propagate parallel to one another in a stripe-like fashion. After this, the photons are focussed by a secondary lens onto a photocathode which produces an electron when a photon is absorbed. These electrons are then accelerated in a cathode ray tube towards a phosphor screen placed directly in front of an imaging CCD. Before they can strike the phosphor screen however, they must first pass between two charged plates, the potential of which is swept rapidly at a known frequency. If the electrons pass between the two plates at time zero, the potential difference between the plates will be also zero, and it will continue to propagate along its original path towards the phosphor screen. If however the electron passes between the plates at some time after time zero, a potential will exist between the plates; this generates an electromagnetic field and causes the electron to be deflected vertically. The longer the delay before the electron arrives between the plates, the greater the field between the plates will be, as will the deflection that the electron experiences.

Thus from the vertical position on the phosphor screen we can calculate the time at which the photon arrived. Likewise from the horizontal position on the phosphor screen we can calculate the wavelength to the photon. In this way, photons registered by the CCD can be assigned spectral and temporal characteristics purely by the pixel coordinate at which they were recorded. It is worth noting that a micro-channel plate (**MCP**), is placed immediately before the phosphor screen; as electrons pass through the MCP, they are multiplied many thousands of times before striking the screen. From the measured intensity of the screen phosphorescence, the energy of the initial pulse can be determined. This is more clearly depicted in **Figure 5.8**.
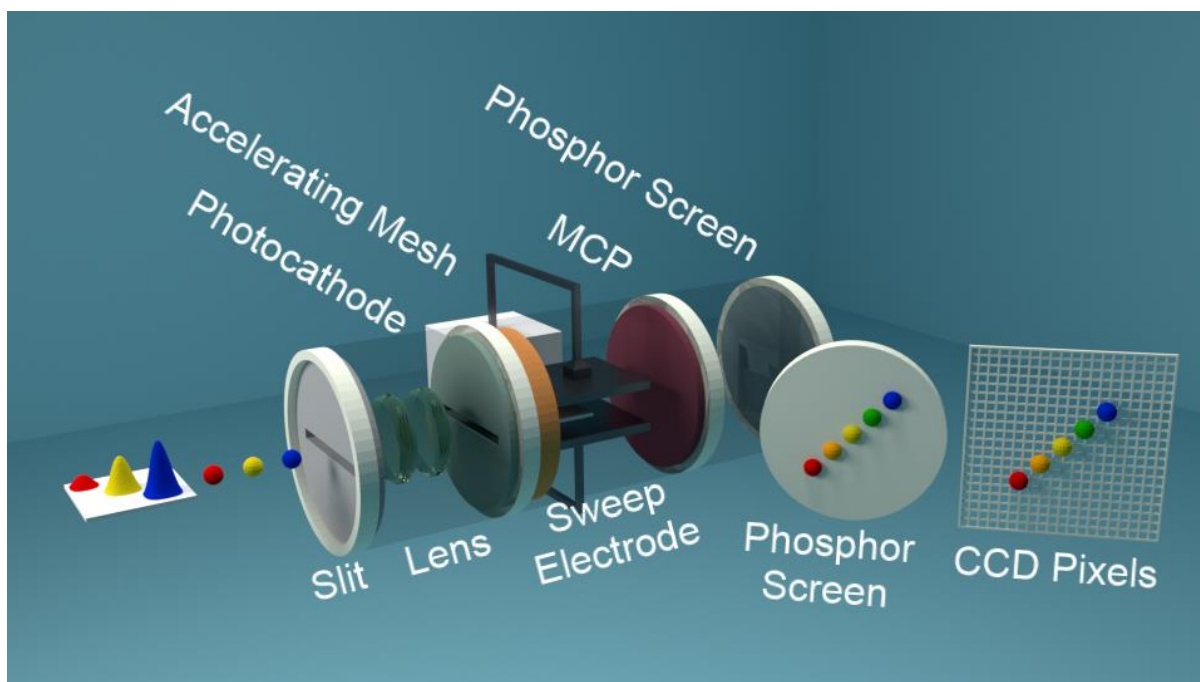
Figure 5.8. *The operating principle of a streak camera. Incident photons are separated spectrally along one axis and temporally along the other. The larger the delay, the higher the potential difference between the two sweep electrodes and the greater the horizontal/vertical deflection. The wavelength of the photon passing through the diffractive element determines its vertical/ horizontal coordinate.*

Though this is a very powerful technique as it allows multiple wavelengths of light to be measured simultaneously as well as the dynamics of a single excitation pulse, its widespread use is prohibited by both its substantial cost and lower sensitivity in comparison to other techniques. Thus to record the same emission intensity observed in other techniques, measurements are required to use large numbers of acquisitions or higher excitation power; this risks sample damage which can be hard to overcome in materials prone to photo-bleaching. The streak camera measurements in this thesis were performed at the University of St. Andrews with the assistance of Sai Kiran and Andrew Musser.

5.1.4.3. Time-Correlated Single Photon Counting

Time-correlated Single-Photon Counting (**TCSPC**) is a technique used for analysing decay lifetimes on the scales of ~100ps to nanoseconds. It does so via the detection of single photons and their arrival times with respect to reference signal. Through many repetitions of these measurements, a large number of data points can be gathered to plot an intensity vs time graph from which a decay lifetime can be extracted.

The pulse used to excite the material is passed through a beam splitter where it splits into two branches. In the first branch the light is passed through a delay line and a constant fraction discriminator (**CFD**, this eliminates timing jitter) before reaching a time-to-amplitude converter (TAC, a circuit that charges a capacitor). This stores the signal until the next electrical pulse arrives, "starting" the measurement. In the second branch, the excitation pulse continues on to the sample where it is absorbed and generates PL. This emission is then passed through a monochromator (or through a series of bandpass filters to select the appropriate wavelength of light) before reaching a photomultiplier tube or fast photodiode. The photodiode registers the arrival of the pulse and sends a signal to a second CFD to the TAC which "stops" the measurement. The greater the delay between the two pulses, the more the capacitor is allowed to charge. Once both pulses have arrived, the capacitor is discharged and passed through an analogue to digital converter where a histogram is built up and the decay profile can be studied; larger voltages correspond to longer time periods. See **Figure 5.9**.
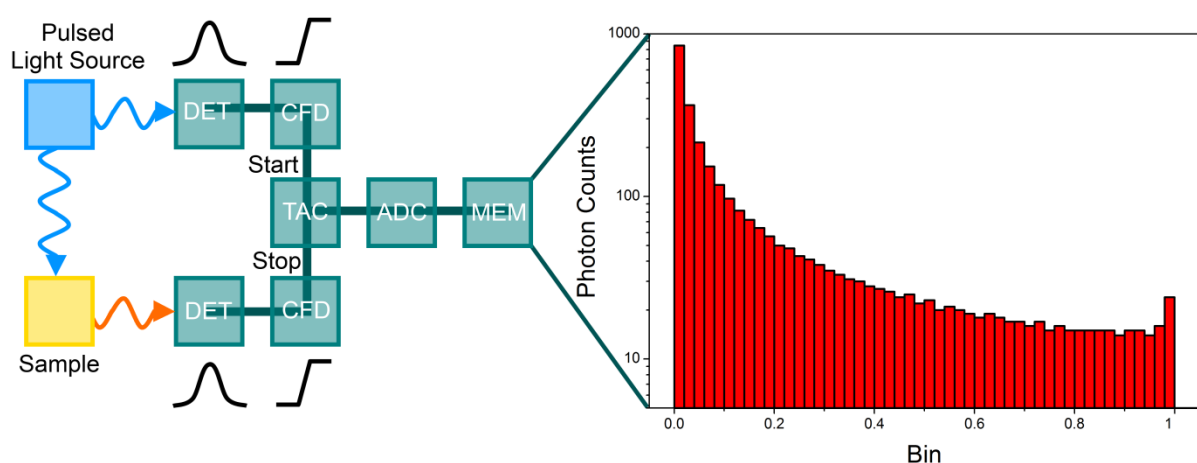

Figure 5.9. *(left)A schematic of the time-correlated single-photon counting experimental set up. (right) a histogram assembled from binned pulses.*

In theory TCSPC can be used to measure lifetimes from ~5ps to >50μs; the lower limit being determined by the jitter of the electronics within the system and the upper limit is given by the overall length of time spent acquiring. In practice however, resolutions as low as 5ps are rare and the system is generally limited by the response of the detector which in many cases is ~50ps.

As sample PL falls off exponentially with time, the number of acquisitions required to achieve a statistically significant signal to noise ratio from weak PL at very long time scales can be prohibitive. In practice, it is normally the light source and detectors used are the limiting factors with the instrument response function (given by **Equation 5.9**) determining the lower limit; this is measured by replacing the fluorescent sample with a scattering media and measuring the excitation pulse directly. The 1/10 factor represents the smallest decay that can be numerically separated from the instrument response function.

$$\tau_{min} = \frac{1}{10} \times \sqrt{FWHM^2_{Light\ Source} + FWHM^2_{Detector} + FWHM^2_{Jitter}} \qquad \textbf{(5.9)}$$

Generally, the dark current or repetition rate determines the upper time limit. If the sample emission does not have sufficient time to diminish to zero before the next excitation pulse arrives, then a background will build up; if sample decay is allowed to continue to <1/10000 of its peak counts than the longest measurable lifetime can be estimated by **Equation 5.10**.

$$\tau_{max} = \frac{1}{f_{Light\ Source}} \times \frac{1}{10} \qquad \textbf{(5.10)}$$

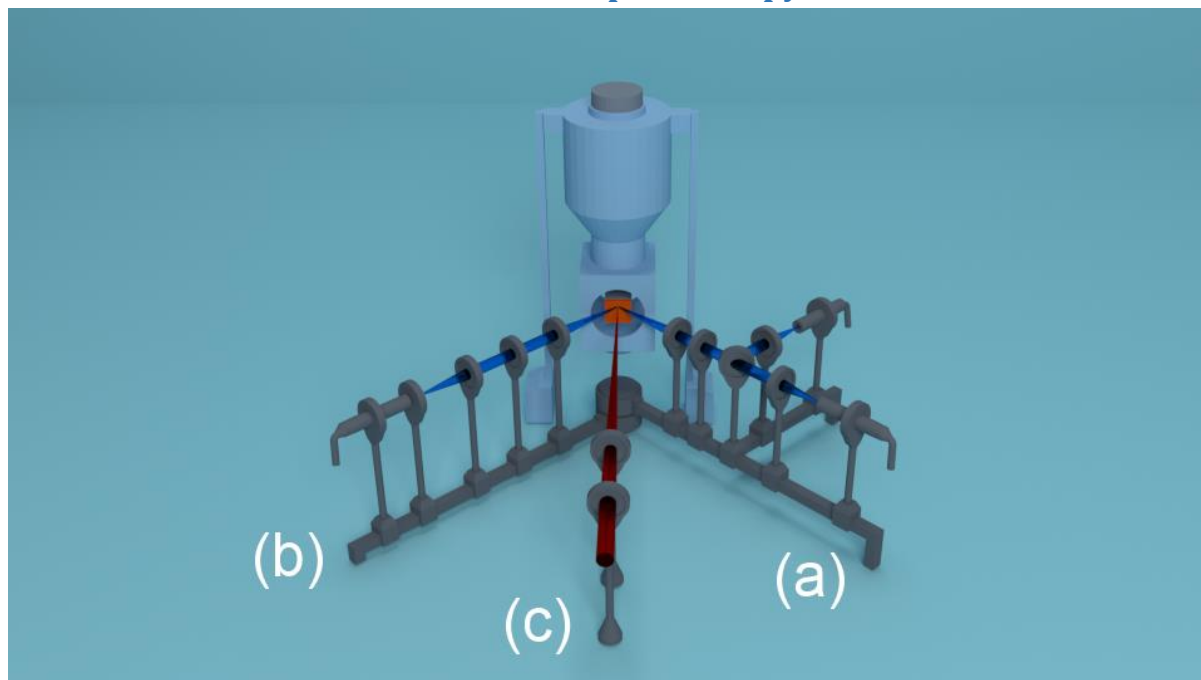## 5.1.5. Photoluminescence Excitation Spectroscopy

Figure 5.10. *Configuration of the PLE experimental set up. **(a)** Is the excitation arm – Spectrally broad light is passed through a monochromator, fibre coupled and focussed onto the sample. A small portion of the light is reflected using a beamsplitter onto a photodiode in order to measure the power of the light at a given wavelength. **(b)** Is the reflection arm – Light is collected and focussed onto a second photodiode with an identical response function to the one on the excitation arm. **(c)** Is the PL collection arm – Light is collimated and focussed into a fibre-coupled CCD to record sample emission.*

Photoluminescence Excitation Spectroscopy (**PLE**) is a method used for probing the energy levels within a system and how energy is transferred from one state to another. It operates by varying the excitation wavelength whilst observing the measured PL at a fixed wavelength. For simple systems e.g. a pure solution of a single fluorescent compound, the PLE spectrum will be identical to that of the absorption spectrum. Like (steady state) absorption, this technique only probes transitions between the ground and first excited state. Unlike absorption, which provides information about all allowed transitions from the ground state, PLE can be used to determine which of those features contribute to a specific peak in PL. For this reason, it is a powerful technique for determining the purity of a sample, and the presence of additional species.

A modification of the experimental set up shown in **Figure 5.2** was used, depicted in **Figure 5.10**. Light from a SC400 Fianium supercontinuum laser filtered by a SPEX 270M

monochromator replaces the Tungsten/Deuterium lamp on the excitation arm with a beamsplitter and photodiode to measure the intensity of the light source as a function of wavelength. The fibre to the CCD has been removed from the collection arm and in its place a second photodiode with an identical spectral response function has been placed; this collects reflected light from the cavity and indicates what fraction of the excitation light has been absorbed by the cavity. A fixed third arm has been placed at normal incidence to collect light from the bottom of the lower polariton branch, and fibre-couple it to the CCD. It is essential that the two photodiodes on the excitation and reflection arms have identical response functions, as this allows the absorption to be measured simultaneously.

If the sample contains a single fluorescent species, then the PLE and absorption spectra will be identical. If the sample contains a fluorescent species and a non-fluorescent impurity, then two peaks will be observed in the absorption spectrum but only one will be present in the PLE spectrum. If two distinct fluorescent species are present in the sample, two peaks will be observed in the absorption spectrum, but only one in the PLE spectrum depending on wavelength; if the measured PL wavelength is changed to correspond to that of the second species, a different single PLE peak will be observed. If a single non-fluorescent species is present this measurement proves to be impossible. This is shown more clearly in **Figure 5.11**.
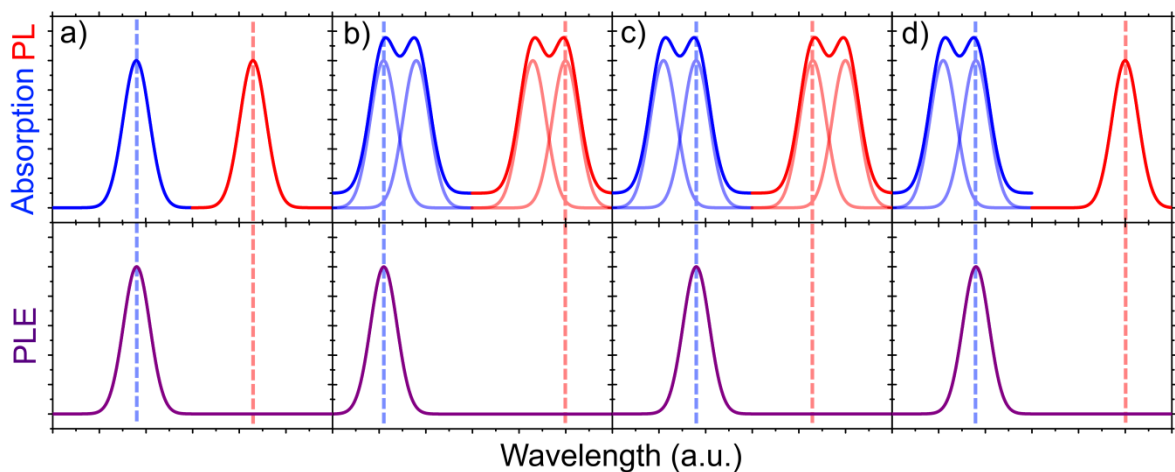
Figure 5.11. *Absorption and PL (top), and PLE (bottom) measurements of a thin film containing **(a)** a single fluorescent species, **(b)** and **(c)** a film containing two fluorescent species, **(d)** a film containing one fluorescent species and one non-emissive species. It can be seen that for a single fluorescent species (a), the PLE spectrum strongly resembles that of the absorption spectrum. For films containing two fluorescent species (b and c), individual contributions to a specific PL feature can be deconvoluted by varying the collection wavelength. In the case of one emissive and one non-emissive species (d), the non-radiative component can easily be identified by its absence in the measured PLE spectra regardless of which wavelength is being observed.*

The PLE experiment can be operated statically for the study of films, or dynamically to study microcavities. When studying strongly coupled microcavities, PLE measurements can be very useful for determining which energy transfer mechanisms are used to populate polariton states along the branches and whether the process is primarily radiative or non-radiative in nature[2,3].

5.1.6. Fluorescence Quantum Yield
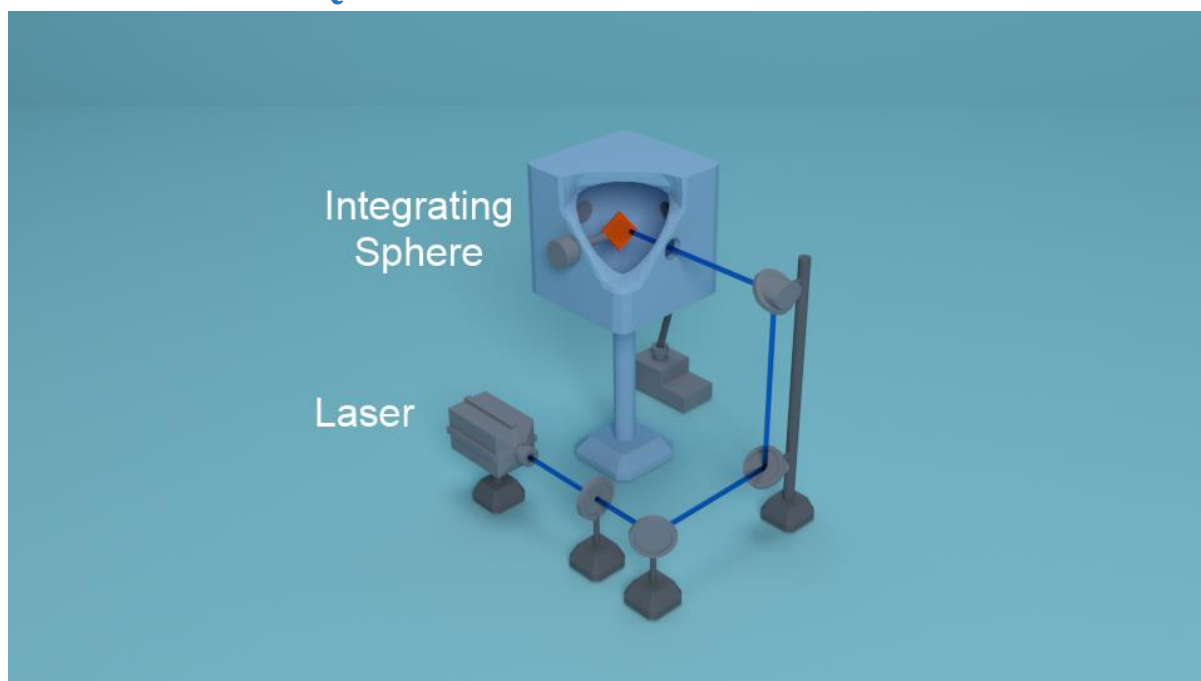
Figure 5.12. The experimental set up of fluorescence quantum yield measurements.

The Photoluminescence Quantum Yield (**PLQY**) of a material is a measure of the efficiency with which photons are emitted from photo-excited states[4]. The PLQY of a material can be expressed as the ratio of the number of photons emitted to the number of those absorbed as described by **Equation 5.11**.

Laser light is shone into an integrating sphere before being diffusely scattered off the white PTFE interior surface and into a fibre-coupled spectrometer. The number of photons produced by the laser is measured by integrating the measured laser intensity over a fixed range of wavelengths. Next the sample is mounted in the beam path within the integrating sphere and the number of photons from both the laser and sample PL are counted (separately) via

integration, **Figure 5.13**. The difference between the two recorded laser counts indicates the number of photons absorbed by the sample, from which the PLQY can be estimated.

$$\Phi = \frac{Photons\ emitted}{Photons\ absorbed} = \frac{k_f}{\sum_i k_i} \tag{5.11}$$

Alternatively PLQY can be described by **Equation 5.11** in which k_f is the rate constant of spontaneous emission and $\Sigma_i k_i$ is the sum of all rates of excited state decay. This non-radiative decay can be caused by a number of mechanisms including photochemical reactions which can result in the cleaving of a bond (photo-bleaching).
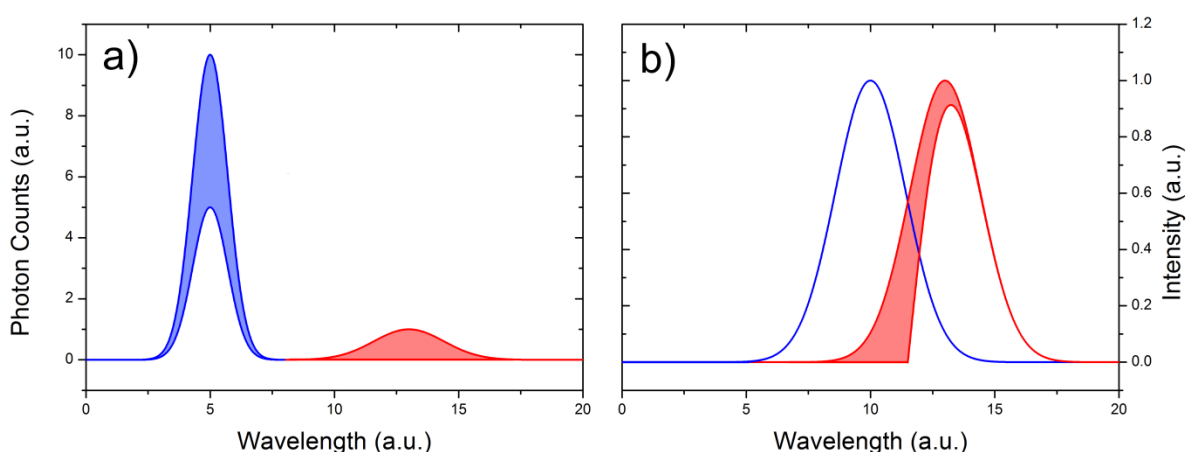

Figure 5.13. (a) *The number of laser photons measured in a fixed amount of time within an integrating sphere with and without the sample present, the number of photons produced by the sample in the same period of time is also counted.* ***(b)*** *Self-absorption correction for materials with significant overlap between absorption and PL.*

For materials lacking a significant Stokes shift between absorption and PL, a significant portion of the PL can be lost due to self-absorption, causing the PLQY to be underestimated as depicted in **Figure 5.13(b)**. This can be expressed with a self-absorption coefficient a, which is defined as the overlap of the absorption and emission spectra, **Equation 5.13** and diminishes the overall PLQY the longer the path length that a photon must travel through the sample before it escapes. A problem that can be exacerbated by the use of an integrating sphere as photons can undergo several cycles of self-absorption and reemission before they are collected. In order to correct for this, PL emission of a thinner version of the sample outside of the integrating sphere is

measured in which the path length is minimised. From the profile of this second measurement, the shape of the original can be adjusted and the total number of counts can be estimated[5].

$$a = \int_0^\infty F(\lambda)\left[1 - 10^{-A(\lambda)}\right]d\lambda = 1 - \int_0^\infty F(\lambda) \times 10^{-A(\lambda)}d\lambda \qquad \textbf{(5.12)}$$

$$QY_{obs} = \frac{QY(1-a)}{1-aQY} \qquad \textbf{(5.13)}$$

Whilst the intensity of light emitted from a sample can be recorded by collecting from a small range of angles using a single lens, and from this solid angle, the radiant flux can be calculated. This is not an accurate method. Any small inaccuracies or errors present in the initial measurement are compounded by multiplication when expanded to larger areas, if the sample emits anisotropically then the solid angle initially measured from may not provide an accurate estimate of sample emission. Furthermore, this geometry fails to account for photons from the laser source that were reflected or scattered, providing an inaccurate estimate for number of laser photons absorbed; it is for this reason an integrating sphere should be used for such measurements.
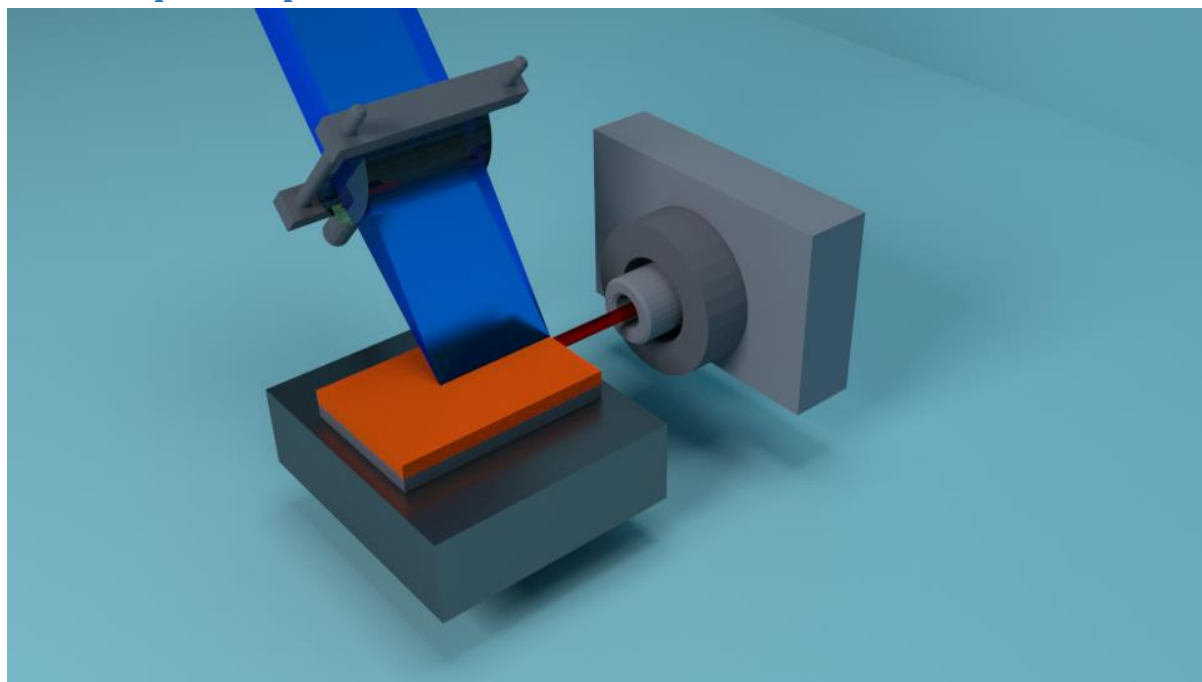
5.1.7. Amplified Spontaneous emission

Figure 5.14. *Stripe pumping (blue) of films (orange) to measure amplified spontaneous emission (red).*

Amplified Spontaneous emission (**ASE**), sometimes referred to as superluminescence, is the term given to the enhancement of emission from a material possessing large optical gain. Unlike conventional luminescence, which occurs with no preferential spatial orientation, ASE has a high degree of directionality and is often enhanced by waveguide effects. In many applications (notably lasers and high-gain amplifiers) ASE is an (often undesirable) side-effect of the structure used to confine light in a gain medium; it provides a competitive decay pathway which ultimately limits the maximum gain that can be achieved. It is however desirable in a number of scenarios, particularly for the generation of intense, spectrally broad emission. It is often an indicator of high fluorescence quantum yields that may make a material lend itself well to lasing in a confined structure.

A pulsed laser is focussed onto a film of organic materials using a cylindrical lens to create a horizontal excitation "stripe". The contrast in refractive index between the film and air above causes the film to act as a waveguide, collection occurs at an angle perpendicular to the surface of the film as is shown in **Figure 5.14**. The wavelength of emission can thus be tuned by varying the thickness of the film, and in the case of dyes dispersed within a host polymer, or the refractive index of the material to vary the energy of the confined mode. Amplified spontaneous

emission measurements were performed with the assistance of Sai Kiran at Politecnico Di Milano, the results of which can be found in **Chapter 7**.

5.2. Physical Characterisation

One of the most important aspects of the fabrication of photonic structures is ascertaining the roughness and thickness of thin films. This is because the roughness of an interface determines the planarity of the next layer to be deposited and the degree of optical scattering that will occur. In a DBR structure, the thickness of a layer determines which wavelengths experience a phase change (and hence destructive interference) a beam of photons would experience as they pass through, **Equation 3.11**. Likewise, the thickness of the layer separating the two mirrors within a microcavity structure determines the wavelength at which the confined photon mode will be located, **Equation 3.23**.

5.2.1. Surface Profilometry

The simplest and most commonly employed technique for measuring film thickness is contact profilometery. A diamond tipped stylus radius is lowered onto, then moved laterally across the surface with a set force over a set distance. On the opposing end of the stylus arm is a magnet mounted within the centre of a solenoid. As the stylus is moved across the surface of the film, any variations in the height of the surface deflect the tip vertically, inducing a current into the solenoid that is proportional to the magnitude of the displacement. This experimental set up is depicted in **Figure 5.15**.
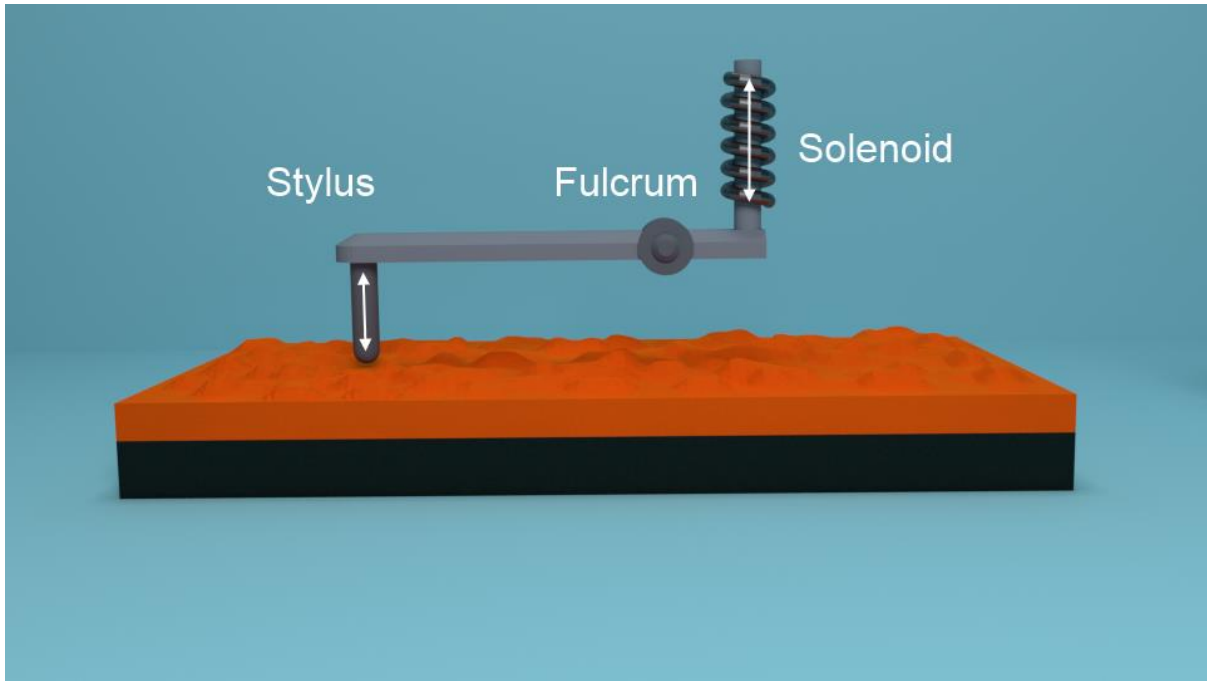
Figure 5.15. *Surface profilometry (Dektak) experimental set up.*

As this is a physical rather than an optical technique, the radius of the stylus tip limits lateral resolution, which can be as low as 20nm. The electronics used for measuring vertical deflection are very sensitive and sub-nanometre vertical resolutions are typical. To ascertain the thickness of a film, a region must be removed beforehand (either by physical scratching or chemical swabbing) to reveal the substrate below before the stylus is engaged. As the cantilever has a large range of travel, this is technique can be used to study surfaces with millimetre-scale features. Veeco 3ST-Dektak and Bruker XT stylus profilometer systems were used for thickness measurements of films in this thesis.

5.2.2. Atomic Force Microscopy

For higher resolution measurements of surface roughness, Atomic Force Microscopy (**AFM**) is typically preferred to surface profilometry as it is possible to build up a 3D map of the surface. Additional information can also be extracted (such as the hardness of the surface), and can be less damaging to the surface being measured. Though many variations of AFM exist, tapping mode was used exclusively in this thesis.

An AFM works by using a fine tip (2-10nm radius) upon the end of a piezoelectric cantilever that is located above the surface of the sample to be measured. The cantilever is non-harmonically driven to oscillate, causing it come into contact and "tap" the surface below. A laser is focussed onto the back of the tip and is reflected onto a quadrant photodiode, **Figure 5.16**.
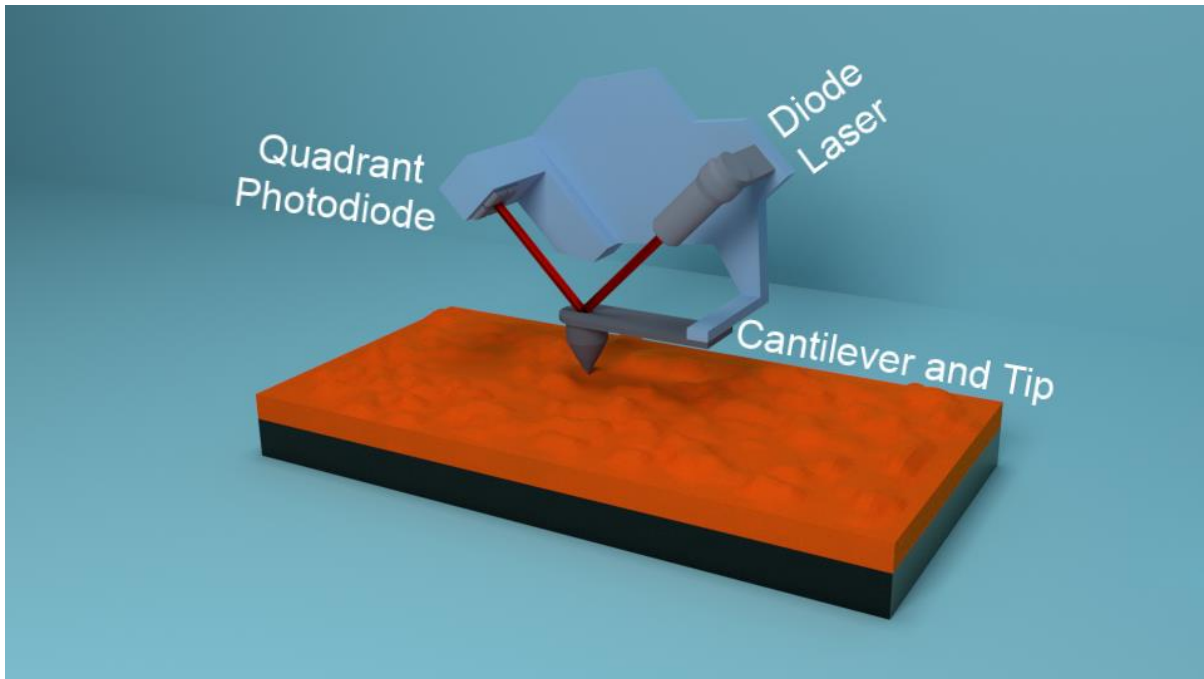
Figure 5.16. *Schematic of an atomic force microscope operating in tapping mode.*

The cantilever and tip are raster scanned across the surface of the material to build up a map of its topography. The cantilever is deflected as it passes over different surface features. This causes the position of laser spot focussed on the back of the tip to be reflected onto a different position on the quadrant photodiode; the magnitude of the deflection corresponds to the height of the feature.

Similarly, the extent to which the oscillation of the tip is damped with each tap provides information about the hardness of the surface. This can be useful when studying a film containing a blend of materials with varying degrees of hardness. Though the film may be uniform in height, domain structures may exist within the film which can be identified by looking at the phase map (**Figure 5.17**) produced by the AFM which plots the degree of dampening which the tip experiences when striking the surface.

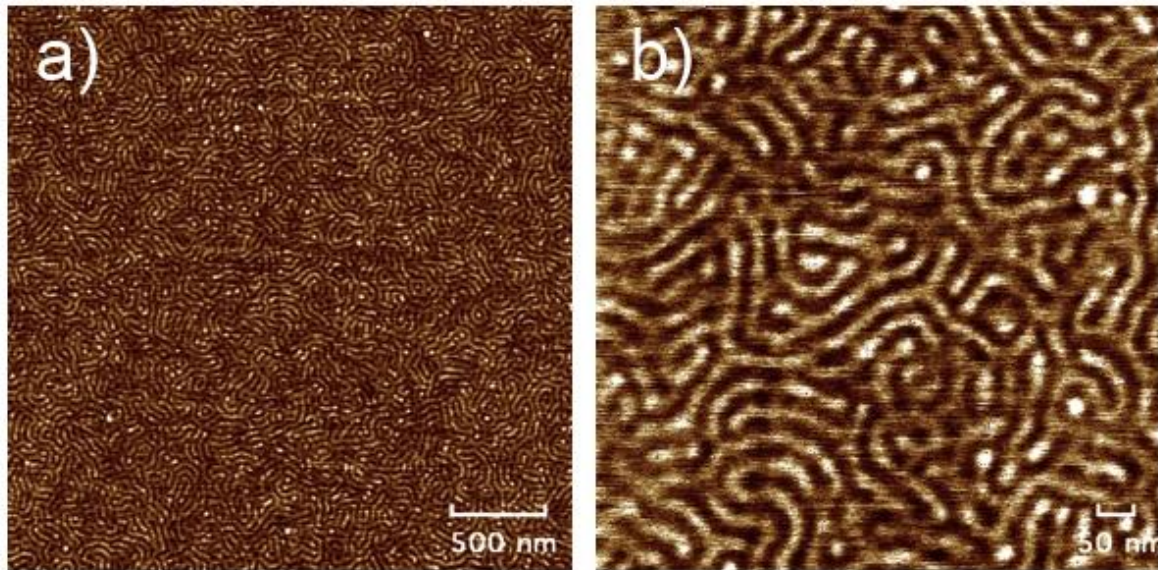**Figure 5.17.** *A phase map of a film of Kraton block co-polymer of polystyrene and polybutadiene on a scale of* **(a)** *3μm, and* **(b)** *850nm. Despite the uniform height, the morphology of individual domains can be observed by the degree of damping that the tip experiences when striking surfaces with different hardnesses. A Veeco Dimension 3100 AFM was used for the experiments shown in* **Chapter 9**.

5.3. Conclusions

The experimental techniques used to characterise materials and evaluate their candidacy for polariton formation, along with microcavities containing said materials, in the subsequent experimental chapters have been reviewed here.

5.4. References

1. Lambert, J. *Photometria*. *Astron. Nachrichten* (1760). doi:10.1002/asna.19182071002

2. Coles, D. M., Grant, R. T., Lidzey, D. G., Clark, C. & Lagoudakis, P. G. Imaging the polariton relaxation bottleneck in strongly coupled organic semiconductor microcavities. *Phys. Rev. B* **88,** 121303 (2013).

3. Coles, D. M. *et al.* Polariton-mediated energy transfer between organic dyes in a strongly coupled optical microcavity. *Nat. Mater.* **13,** 712–9 (2014).

4. Green, A. P. & Buckley, A. R. Application of gauge R&R to the rigorous measurement of quantum yield in fluorescent organic solid state systems. *Rev. Sci. Instrum.* **83,** 073108 (2012).

5. Ahn, T.-S., Al-Kaysi, R. O., Müller, A. M., Wentz, K. M. & Bardeen, C. J. Self-absorption correction for solid-state photoluminescence quantum yields obtained from integrating sphere measurements. *Rev. Sci. Instrum.* **78,** 086105 (2007).

6.

Efficient Pumping of Polariton States by a Highly Fluorescent Molecular Dye

A series of films and microcavities containing a bromine substituted variant of the BODIPY dye (shown in **Figure 6.1** and hereafter referred to as **BODIPY-Br**) are studied in this chapter. We have explored the optical properties of a series of strongly-coupled microcavities containing the fluorescent molecular dye BODIPY-Br dispersed into a transparent dielectric matrix with each cavity having a different exciton-photon detuning. Derivatives of the dye explored (BODIPY-Br) have previously been shown to undergo aggregation to form both H- and J-aggregates[1–3], and our results point towards a strong tendency to form excimers. Here, we couple the cavity-photon to a transition associated with the BODIPY-Br monomer species and thereby reach the strong-coupling regime. By varying the exciton-photon detuning, we were able to comprehensively explore the photoluminescence emission from the lower polariton branch as a function of its separation from the so-called "exciton reservoir". It was observed that at large exciton-photon mode detunings, the majority of polariton states in the lower branch could be

found at large viewing angles close to the exciton reservoir. However, as this detuning was reduced, the polariton population became increasingly concentrated around the bottom of the branch at normal incidence.

With the assistance of Paolo Michetti at the University of Würzburg, a simple fitting model based upon radiative pumping of polariton states through the decay of weakly coupled exciton reservoir was developed. By introducing a second radiative pumping term (corresponding to that of an excimer revealed during photoluminescence excitation measurements), excellent agreement between modelled and experimentally observed results was achieved even at low temperatures. Temperature- and time-resolved Fourier space images were recorded at the Université de Montréal with assistance of Pascal Gregoire and Eleonora Vella under the supervision of Carlos Silva. The BODIPY-Br dye was provided by Tersilla Virgili, Marco Cavazzini, and Francesco Galeotti at IFN, ISMAC and ISTM respectively.

6.1. Introduction to BODIPY-Br

The BODIPY, family of fluorescent dye fluorescent dyes is known for its remarkable versatility. Originally produced by Treibs and Kreuzer in 1968[4], it gained popularity in the 1980's[5] and has since seen use as everything from biological cell label[6] to tunable laser dye[7]. Its widespread use is due to its low propensity to form triplet states, high chemical- and thermal-stability as well as compatibility with a wide range of solvents[5]. In addition to this, BODIPY dyes are noted for their high fluorescence quantum yield, excited state lifetimes on the order of nanoseconds, and narrow spectral features. Perhaps most importantly, derivatives of BODIPY have been show to undergo π-π stacking to form dimers and larger aggregates at high concentrations and these aggregates can coexist within the monomers in both solution and the solid phase[1–3]. Such planar π systems can also be susceptible to the formation of stabilized, weakly emissive dimers, or excimers, through excited-state intermolecular relaxation. This made it an interesting candidate for the study of strong coupling as these excimers can contribute to the so called "electron reservoir" within the microcavity.

By "exciton reservoir" (**ER**), we mean the ensemble of excitonic states that remain uncoupled or weakly-coupled to light. This has been shown to play a crucial role in the photo-excitation dynamics of a strongly-coupled microcavity under non-resonant pumping[8,9], with intra-molecular scattering being the first relaxation step. We emphasize that the properties and the composition of the ER are strongly material (and possibly sample) dependent, as are the different scattering mechanisms that generate the final polariton population and that these are not fully understood.   Normally the ER contains uncoupled exciton states derived from molecular states[10], which are also responsible for strong-coupling (in our case, BODIPY monomer excitons) and have a maximum density of states near the bare 'uncoupled' exciton energy. Previous work has demonstrated the scattering to and from such states and the polariton branches is mediated by emission and absorption of molecular vibrations [8,9,11]. However this process can be more varied and complex. Indeed, in materials with intense vibronic replicas, a radiative scattering mechanism mediated by vibronic states has been observed[12] and described theoretically[13,14]. It is also possible, (as we show here) that the ER contains excitonic species that are different in nature than those that undergo strong coupling. This situation has been demonstrated in a strong-coupled microcavity containing a porphyrin dye by Lodden et al[15]. Here a second luminescent low-weight dye was also incorporated into the cavity that emitted light in a spectral range below the main exciton resonance line of the strong-coupled material. Here it was demonstrated that the spontaneous radiative emission of the luminescent dye was able to effectively populate the LPB through a radiative pumping process.

By exploring the dynamics of both cavity and film emission through a variety of techniques including fluorescence quantum yield measurements, angle-resolved PL (CW pump) and time-resolved k-space imaging (pulsed excitation), we conclude that polariton states in this system are most effectively populated via optical pumping by photons emitted from weakly-coupled states within the so-called exciton reservoir. Our work extends the understanding of the mechanisms by which polariton states are populated[16]; a process of key importance in generating a macroscopic occupancy around $k_{\parallel}$ = 0, and thus our results are likely to aid the design and construction of low-threshold organic-exciton polariton laser devices.
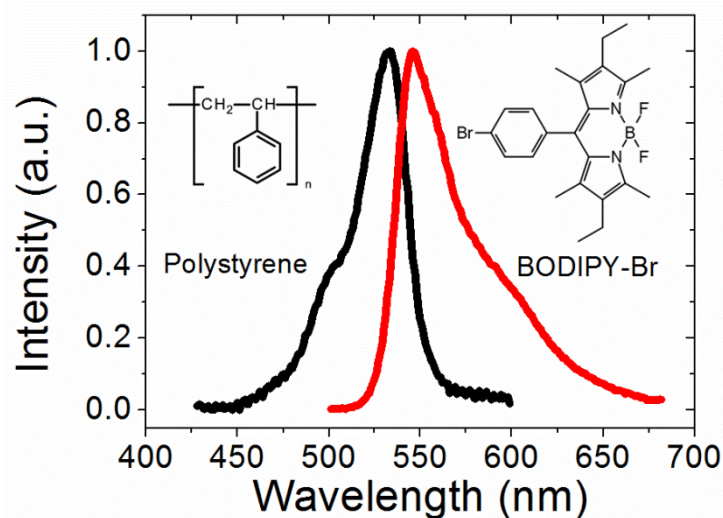
Figure 6.1. *Absorption and PL emission of BODIPY-Br (inset right) doped into a polystyrene* ***(PS)*** *(inset left) film (at a 1% concentration of dye by mass). BODIPY-Br was provided by Marco Cavazzini and Francesco Galeotti at CNR.*

When doped into a PS matrix at low concentration (1% by mass) BODIPY-Br has a relatively narrow absorption (0-0) transition at 530 nm (2.33 eV) having a FWHM of 15 nm (66 meV), with a (0-1) vibronic replica observed at 500 nm (as shown in **Figure 6.1**). The PL emission from 1% BODIPY-Br films is characterized by a peak at 542 nm (2.288 eV) having a FWHM of 25 nm (104 meV). The relatively narrow absorption and emission linewidths of BODIPY-Br together with its high PL quantum yield made it an interesting material to study light-matter interactions in strongly-coupled microcavities.

6.2. Aggregation and Excimers

Before the properties of BODIPY-Br within a microcavity can be evaluated, it is first necessary to explore the properties of an unconfined "bare" film of dye. This section outlines an extensive series of optical measurements used to characterize thin films of BODIPY-Br-doped PS matrices at varying concentrations and temperatures; this understanding was then carried through to cavity design and study in the following sections.

The absorption and emission spectra of a low concentration BODIPY-Br/PS control film (1% by mass) is shown in **Figure 6.1**. At higher relative concentrations of BODIPY-Br in PS, we see a broadening in absorption and PL and a reduction in PLQY as shown in **Figures 6.2(a)** and **(b)** respectively. Previous work on other BODIPY-derivatives has similarly seen red-shifts and broadening of absorption and have attributed this to the formation of both H- and J-aggregates that co-exist (at lower concentration) with un-aggregated monomers[1]. Critically, we find the PLQY is strongly concentration dependent, ranging from 55% in a film containing 0.1% BODIPY-Br (by mass) to ~5% in films in which the dye concentration is increased to 20%. A significant reduction in PLQY at increased dye concentration has been observed in other BODIPY derivatives, and has been attributed to an increased fraction of molecules forming weakly-emissive or non-fluorescent H-aggregates[1]. On the basis of previous work[1] therefore, we identify the strong absorption at 530 nm with the uncoupled monomeric form of BODIPY-Br, and the broadening at shorter wavelengths with a population of H-aggregates.

However, we found no evidence for the presence of J-aggregates in these films, and instead propose that the red-shifted emission be attributed to excimers. To evidence such states, we have performed temperature-dependent PL spectroscopy (following C.W. excitation at 405 nm) on films having a high concentration (20%) of BODIPY-Br in polystyrene. Typical spectra are shown in **Figure 6.2(c)** recorded at 298, 150, 50 and 4K. At room temperature, the emission peaks at 555 nm (2.24 eV) [attributed to monomer emission], with a shoulder evident at 588 nm (2.11 eV). As the film is cooled to 4K, we saw a significant evolution in the film spectra, with a peak at 570 nm (2.18 eV) emerging from the low-energy shoulder that was observed at room temperature. Previous work has also identified J-aggregates in BODIPY-derivatives around this wavelength[3,17]. However, there is no corresponding red-shifted absorption for this species, and indeed our measurements at all temperatures demonstrate excitation of the same monomer-like species.

To verify the absence of these species, PLE measurements were made upon dilute and concentrated films of BODIPY-Br across a broad range of temperatures, these measurements are shown in **Figure 6.3**). In the dilute (1%) film, **Figure 6.3(a)**, only a slight red-shift (~6 nm) was observed at low temperatures, with no change in spectral shape. In the concentrated 20% film, **Figure 6.3(b)**, we observed a growth of the redder emission feature as the temperature is reduced. This feature undergoes a progressive blue-shift as temperature is reduced, and at low

temperature it merges with and then dominates the short-wavelength monomeric emission peak around 550nm (compare peak positions at 150 K and 100 K). However, no corresponding changes in the apparent absorption of the film can be detected (vertical axis). For both films, the temperature series was measured in the order 295-250-200-150-100-175-225-295 K to ensure no permanent changes to the film were induced by the measurements. Both maps are all normalized to the same colour scale.
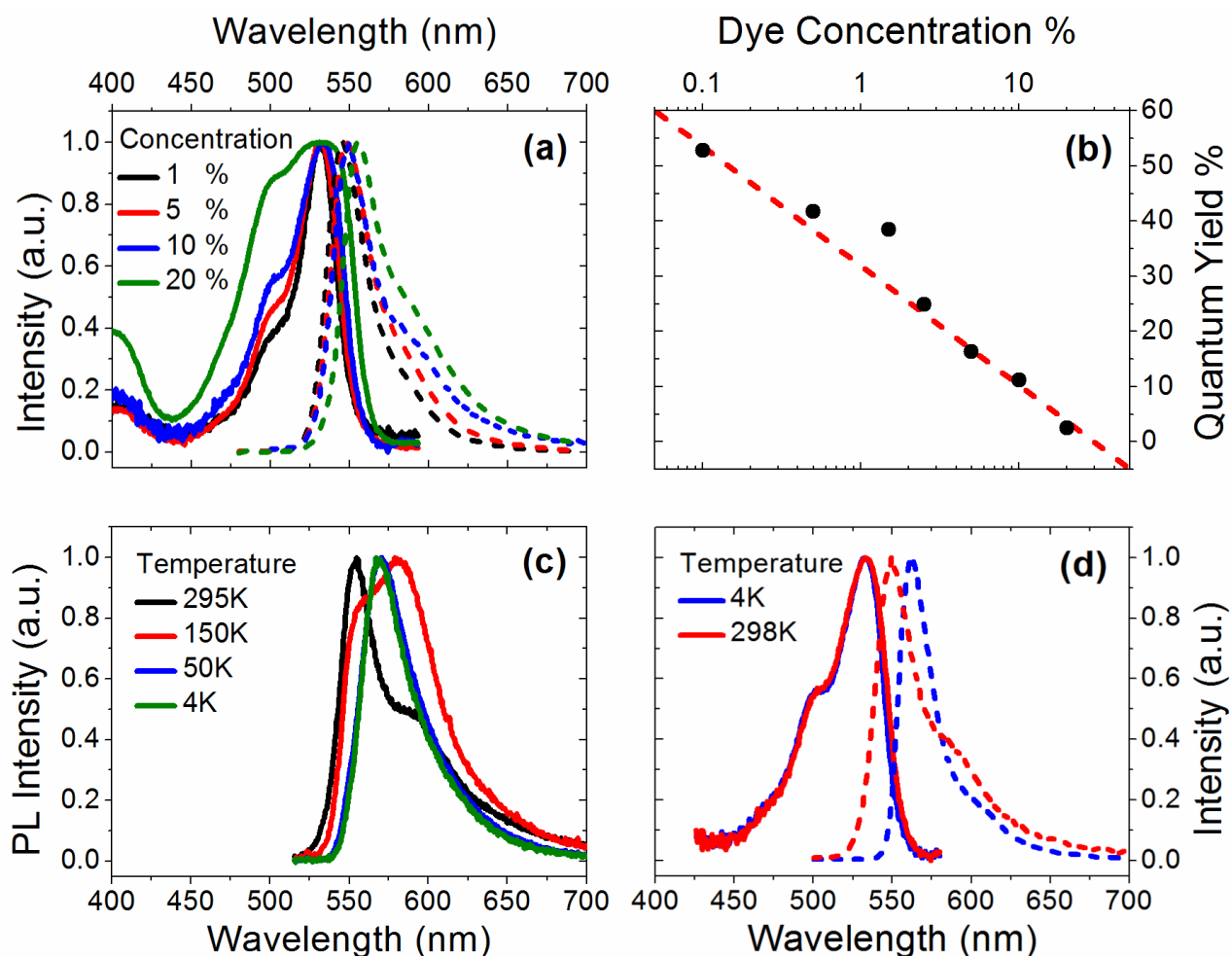
Figure 6.2. *Part **(a)** shows optical absorption (solid lines) and PL emission (dashed lines) of BODIPY-Br as a percentage concentration in a film of polystyrene. Part **(b)** shows the PLQY of BODIPY-Br films as a function of concentration. Part **(c)** depicts PL emission of a film containing BODIPY-Br dispersed in a polystyrene matrix (20% dye by mass) as a function of temperature. In part **(d)**, we plot absorption and PL emission of BODIPY-Br films dispersed in a polystyrene matrix (10% dye by mass) at 4K and 300K.*

Figure 6.3. (a) *PLE maps of BODIPY-Br in polystyrene (1% dye by mass), taken over a series of temperatures ranging from 295K to 100K.*
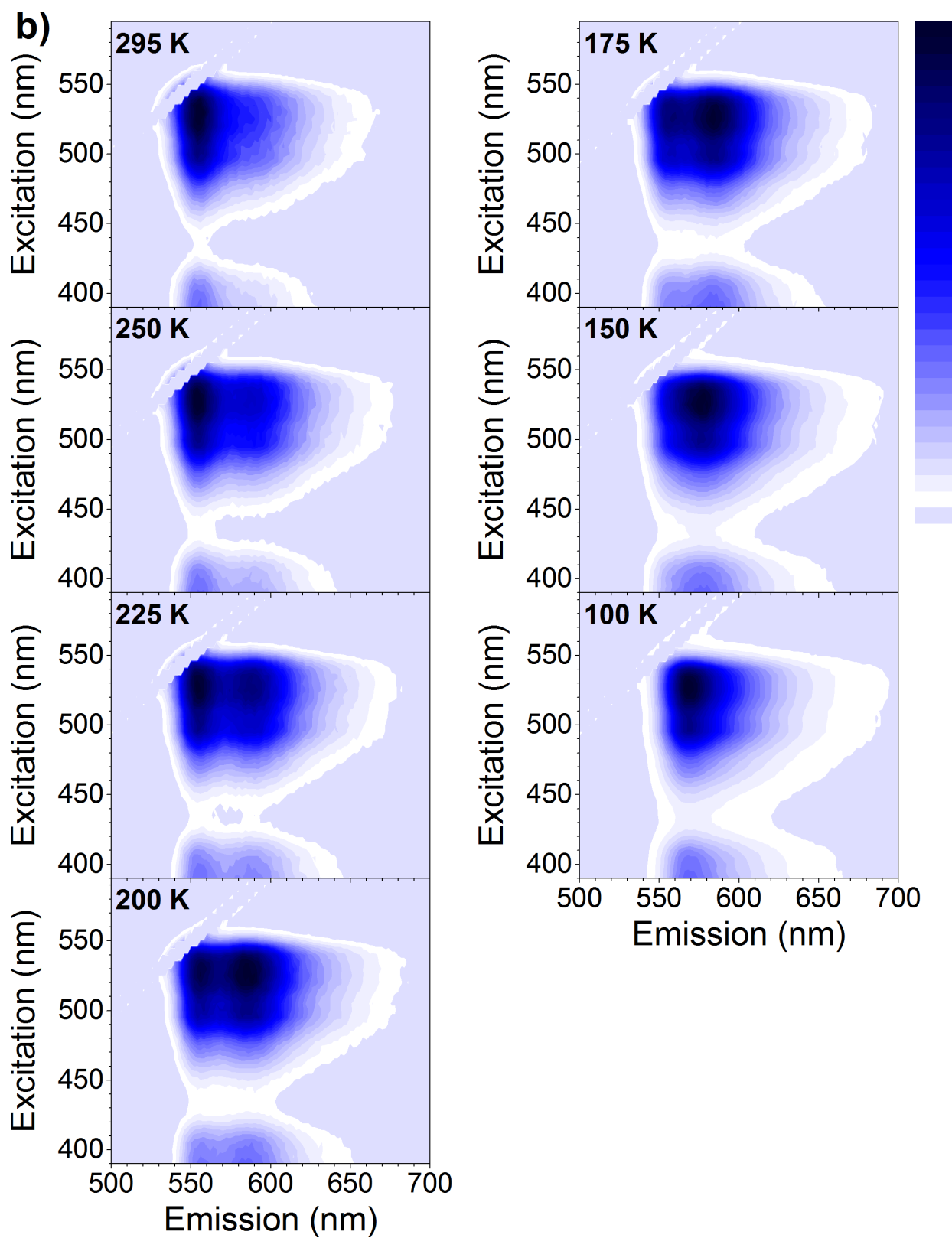
Figure 6.3. (b) *PLE maps of BODIPY-Br in polystyrene (20% dye by mass), taken over a series of temperatures ranging from 295K to 100K.*

In the dilute film, the only spectral changes observed were a slight narrowing and redshift at low temperature: at this concentration the molecule behaves as a well-isolated chromophore. In concentrated films, PL excitation revealed an invariant absorption lineshape at every temperature. Similarly, at any one fixed temperature, we do not observe changes in the PL spectrum as a function of excitation wavelength. In all cases, the same initial population (resembling monomeric BODIPY-Br) is photo-excited. However, the overall red-shift is twice that observed in dilute films (~12 nm) and is accompanied by new long-wavelength PL features (~585 nm) and a significant thermally-activated increase in relative PL efficiency (see **Figure 6.5**). These effects cannot be explained from intramolecular properties and must arise from intermolecular interactions. Unlike in previous studies of BODIPY aggregates, there is no evidence in excitation spectra of distinct 'sub-gap' aggregate absorption. These effects are thus most consistent with an intermolecular quenching pathway active only in the excited state, namely excimer formation. PL excitation spectra are shown in 4 nm steps of emission wavelength. PL emission spectra are shown in 10 nm steps of excitation wavelength. These effects can be more clearly seen in **Figure 6.4** which plots individual slices of the PLE spectra as a function of both temperature and excitation/emission wavelength.

Figure 6.4. (a) *Normalized spectral cuts of the PLE maps above along each emission wavelength (left) or excitation wavelength (right), for a dilute BODIPY-Br film (1% dye by mass). Excitation/emission pump/collection wavelength is plotted from low to high using a blue-red colour gradient.*
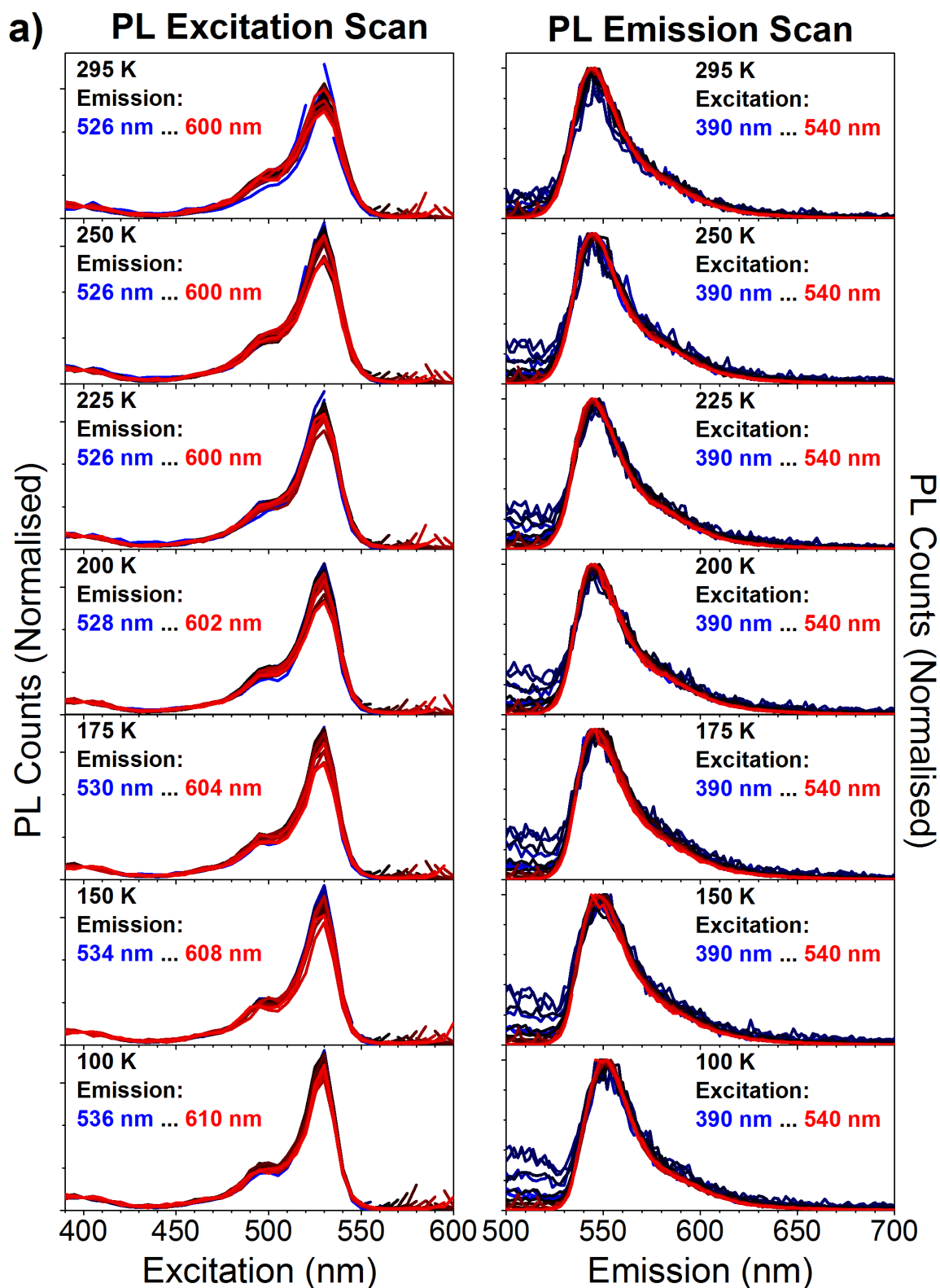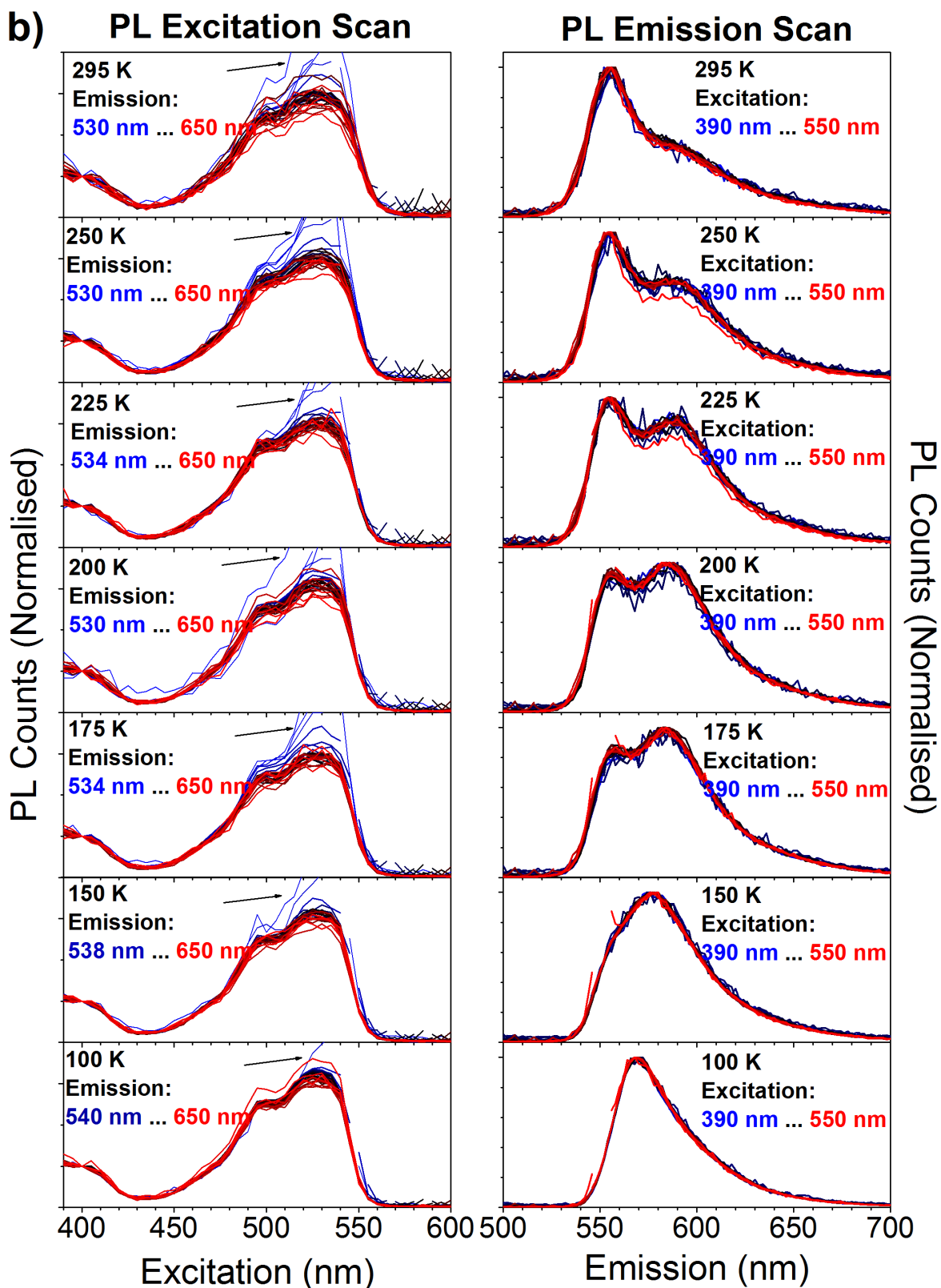
Figure 6.4.(b) *Normalized spectral cuts of the PLE maps above along each emission wavelength (left) or excitation wavelength (right), for a concentrated BODIPY-Br/PS film (20% dye by mass). Excitation/emission pump/collection wavelength is plotted from low to high using a blue-red colour gradient.*

The absolute intensities of the absorption and PL emission profiles at different temperatures can be compared in order to both identify aggregate species and gain an estimate of the increase in fluorescence quantum yield. It can be seen in **Figure 6.5(a)** that PL intensity increased by a factor of ~3.8x from 295 K to 100 K for high concentration films, versus ~1.3x for low concentration films, indicating an increase in PL quantum yield as the temperature is reduced for both concentrations. It can also be seen that as the temperature is reduced, the 20% BODIPY-Br absorption spectrum sharpens and slightly blue-shifts at the band edge, and additional absorption can be detected in the high-energy region previously attributed to non-emissive H-aggregates. It is evident from the significant overlap of absorption and 1% film emission, and the high optical density of the concentrated films, that the large shift of PL spectral edge between 1% and 20% films can be largely attributed to self-absorption. To distinguish the effects of aggregate- and monomer-type emission, we have scaled the PL of the 1% film (dotted) by the absorption spectrum of the concentrated film at each wavelength; from this, **Figure 6.5(b)** gives an approximation of self-absorption effects. The agreement of peak positions and PL edge is excellent at all temperatures. Note the size of the monomer contribution signified by the scaled 1% spectra does not vary significantly through the temperature series.
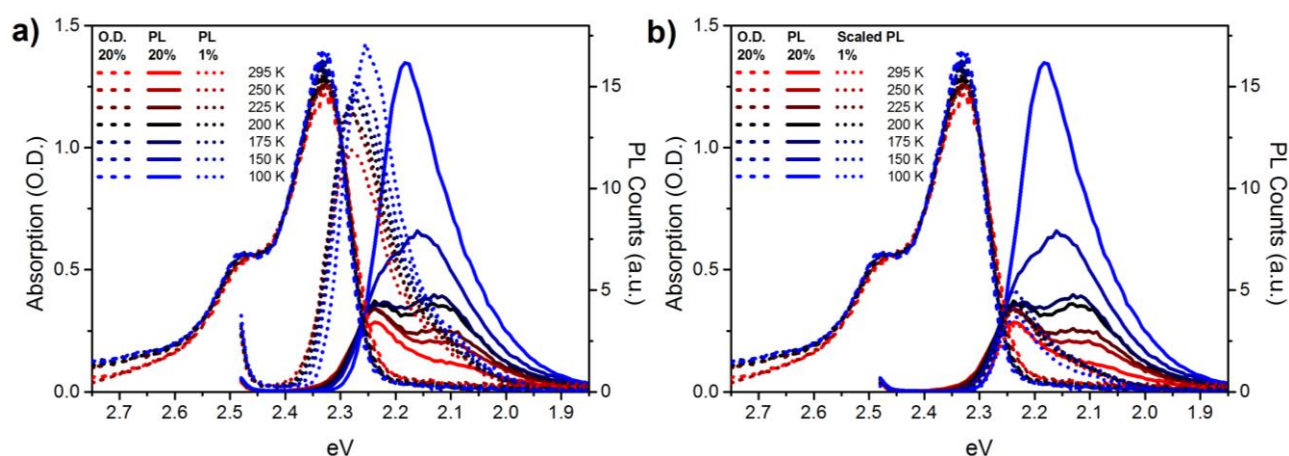

Figure 6.5. (a) *Temperature-dependent absorption (dashed) and PL (solid) of 20% BODIPY-Br/PS films, and PL of 1% BODIPY-Br/PS films (dotted). PL spectra were collected with excitation at 495 nm (2.51 eV).* ***(b)*** *PL of the dilute 1% film scaled (by a factor varying between 1 and 2) to match the intensity of the concentrated 20% film.*

Interestingly, we find that as temperature is further reduced, the low-energy emission feature becomes progressively stronger, undergoes a continuous blue-shift, and completely dominates the spectrum by 100K. Throughout the course of this blue-shift, the spectral shape of the low-energy component remains essentially constant. This behavior is incompatible with H- or J-type aggregation. In light of this and the invariably monomer-like PL excitation spectra, we attribute the low-energy emission in these films to excimers (excited-state molecular dimers). We speculate that the observed blue-shift of the emission reflects a reduction of excited-state conformational freedom as the intermolecular packing becomes denser at low temperature, while the increase in intensity is expected to arise from a reduction in non-radiative decay rates.

Monomer emission can be separated using a deconvolution of spectra as shown in **Figure 6.6**. Following subtraction of the self-absorption-corrected monomer (i.e. 1% film) contribution (**Figure 6.5**), we are left with the PL spectrum of the red-shifted species. The emission of this species progressively blue-shifts and increases in intensity as the temperature decreases. Such an increase in intensity is consistent with a reduction in the rates of non-radiative decay, (**Figure 6.6(a)**). Upon normalisation, the gradual shift of the entire spectrum with temperature is strong evidence that no new species appear. Rather, the low-energy species responsible for radiative pumping at room temperature gradually increases in energy (and PL yield) as the temperature is decreased. Thus the 'same' population is responsible for radiative pumping at both temperature extremes (**Figure 6.6(b)**). Manually shifting the red-shifted spectrum at each temperature to overlap with that at 100 K, we find no variation in the spectral shape within the noise of the measurement, except for at most a slight narrowing at low temperature, (**Figure 6.6(c)**). The degree of spectral shift appears to vary linearly with temperature. This behaviour would not be expected of any type of aggregate (any change in J- or H-type character would result in a change in relative vibronic peak ratios). Given the stability of the spectral shape over the temperature range, the lack of vibronic structure and the absence of any signatures in PL excitation or ground-state absorption of a distinct red-emitting species, we assign this emission to an excimer.
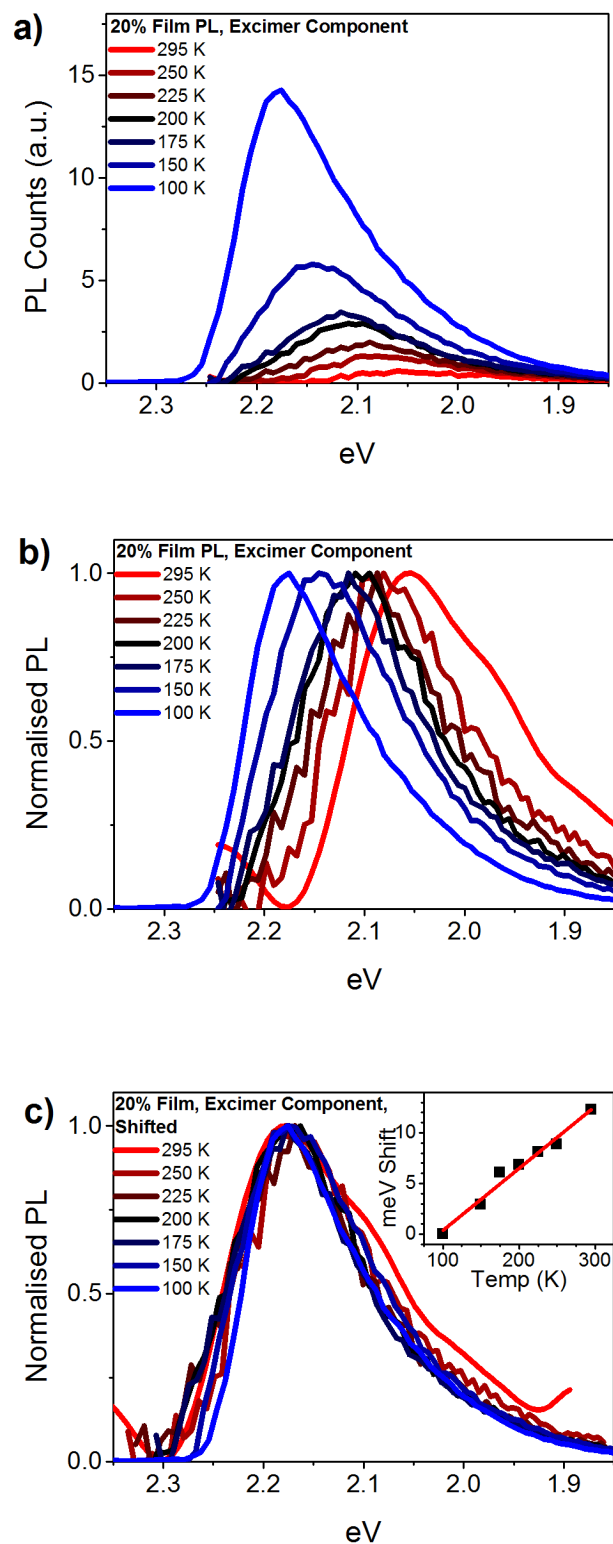
Figure 6.6. *(a) Isolated excimer emission following subtraction of the self-absorption-corrected monomer profile as a function of temperature. (b) Normalisation of excimer emission (c) Manual spectral correction of excimer emission to investigate changes in profile shape. (Inset) Peak excimer emission wavelength/energy as a function of temperature.*

Finally any possible sub-gap absorbing species were proven to be absent by directly comparing the absorption and PLE spectra for both 1% and 20% films as shown in **Figure 6.7**. All spectra showed the same lineshape at each temperature, apart from slight broadening in the 20% film spectra. At the band edge, there is no evidence of additional sub-gap absorbing species in the concentrated film (dotted, solid). In particular, at 100 K where the red-shifted emission is most pronounced, the low- and high-concentration PLE spectra overlap completely. This indicates that the red-emitting species is only accessed through excitation of the monomer, as in an excimer. Spectra are scaled to have comparable magnitude.
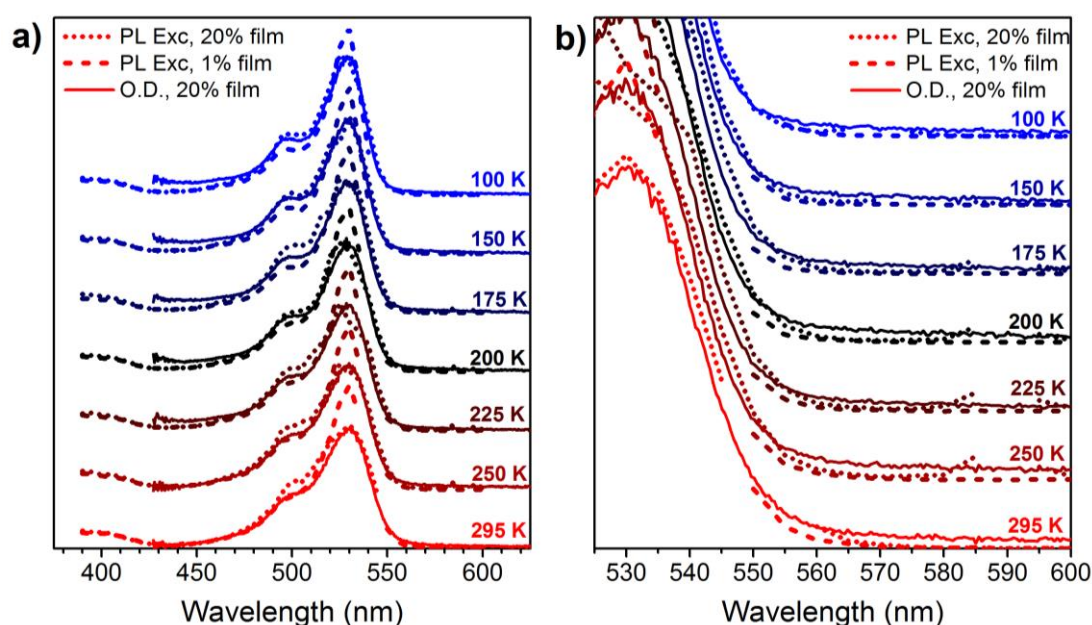

Figure 6.7. *(a)* *Temperature-dependent PLE spectra for 20% (dotted) and 1% (dashed) BODIPY-Br films, taken at the emission maximum wavelength, and converted into optical density scale for comparison with the film absorption (solid).* *(b)* *A plot of the same data over a narrower spectral range, more clearly showing the band edge.*

6.3. Microcavity Fabrication and Strong Coupling

A necessary condition to reach the strong-coupling regime in a microcavity is that the Rabi splitting energy is larger than the excitonic absorption linewidth. In organic semiconductors, such transitions are inhomogeneously broadened and can have linewidths of 100s of meV, however by using organic films containing a high concentration of chromophores, very large values of Rabi-splitting can be achieved (~ 1 eV) as a result of the large oscillator strength (f) of many Frenkel excitons ($\hbar\Omega_{Rabi} \propto \sqrt{f}$). In order to simultaneously reach the strong-coupling regime and to generate efficient luminescence from the BODIPY-Br we have fabricated microcavities containing thin films containing BODIPY-Br at a concentration of 10% by mass (corresponding to a PLQY of $\sim 15\%$). For completeness, we plot the absorption and PL of a film composed of 10% BODIPY-Br in PS at 298K and 4K as shown in **Figure 6.2(d)**. It can be seen that the absorption of BOIDIPY-Br has negligible temperature dependence.
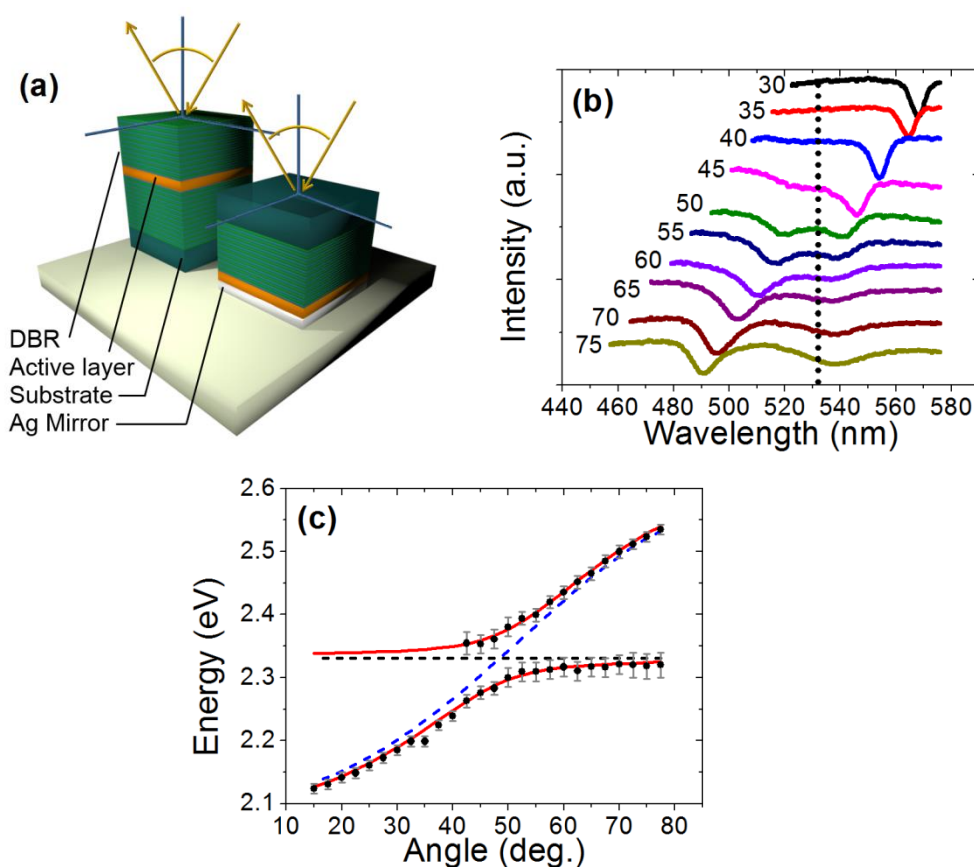

Figure 6.8. *Part **(a)** shows a schematic of a DBR-DBR (left) and DBR-Metal (right) microcavity structure. Part **(b)** plots white light reflectivity as a function of external viewing angle of a DBR-Metal microcavity, with part **(c)** showing a fit of upper and lower polariton branches to measured reflectivity dips shown in part (b).*

The microcavities fabricated are shown in **Figure 6.8(a)** and are designed such that the cavity photon mode undergoes strong-coupling to the main BODIPY-Br absorption transition (corresponding to uncoupled monomers) at ~530 nm. The structures were composed of a 12 pair Distributed Bragg Reflector (DBR) consisting of alternate Nb_2O_5 and SiO_2 layers deposited by ion assisted electron beam and reactive sublimation respectively and were centred at 540 nm. An active BODIPY-Br/PS film was then spin-cast onto the DBR. A second dielectric mirror consisting of 10 mirror pairs was then deposited onto the organic film by the same method. Such microcavities had a Q-factor of ~200 as measured by comparing linewidths of the (almost entirely photon-like) LPB at θ=0°. Here all measurements (reflectivity, excitation and emission) were made through the 10 pair DBR as indicated in **Figure 6.8(a)**. For comparative purposes, a second series of microcavities were also fabricated between a SiO_2 / Si_3N_4 dielectric mirror (deposited by Plasma Enhanced Chemical Vapour Deposition) and a 200 nm silver mirror. Here all measurements (reflectivity, excitation and emission) were made through the DBR. We found that the DBR-Metal cavities had a similar Q-factor of ~150 and thus we feel justified in directly comparing experiments made on either type of structure.

To tune the relative energy-separation of the exciton (E_x) and photon (E_p), the thickness of the BODIPY-Br / PS thin film was tuned between 185 and 290 nm, permitting the exciton-photon detuning (Γ) to be varied between $Γ = E_x – E_p$ = 80 and 400 meV. To evidence strong coupling in the microcavities, white light reflectance spectroscopy was performed as a function of external viewing angle as shown in **Figure 6.8(b)** (data shown for a metal-DBR cavity).

It can be seen that at an angle of θ = 30°, the reflectivity spectrum is characterized by a broad background (originating from the combined reflectivity of the DBR and the metallic mirror) on which a dip at 568 nm (2.183 eV) is superimposed. At increasing viewing angles, this photon-like mode moves closer in energy to the exciton energy (2.33 eV, marked by a dashed line in **Figure 6.8(b)**) and a second dip emerges at higher energies. At resonance (θ = 50°) the two dips in the spectrum are located either side of the exciton energy. We plot the energy of these features on the dispersion plot shown in **Figure 6.8(c)** and identify the upper and lower polariton branches (UPB and LPB). It can be seen that as expected, the polariton branches undergo anticrossing around the peak absorption energy of the BODIPY-Br (marked by a horizontal dashed line).

Such behavior can be described using a model of two coupled classical oscillators as described by **Equation 6.1**. Here Λ is the interaction potential ($\Lambda = \hbar\Omega_{Rabi} / 2$), $E_p(\theta)$ is the angular dependent photon energy, E_x is the exciton energy and α and β are the Hopfield coefficients corresponding to the relative fraction of photon and exciton mixed into the polariton modes respectively. To account for the dispersion of the cavity photon, we use a standard transfer matrix that includes the average refractive index of the cavity and the energy of the photon-mode at normal incidence (E_p).

$$\begin{pmatrix} E_p(\theta) & \Lambda \\ \Lambda & E_X \end{pmatrix} \begin{pmatrix} \alpha \\ \beta \end{pmatrix} = E \begin{pmatrix} \alpha \\ \beta \end{pmatrix} \qquad \textbf{(6.1)}$$

This equation is solved by diagonalization and then fitted to the measured dispersion curves to extract the Rabi-splitting energy and Hopfield coefficients. For example, from the best fit to the reflectivity dispersion shown in **Figure 6.8(c)** we determine values of $\hbar\Omega_{Rabi}$ = 79 meV, E_p = 2.11 eV and E_x = 2.33 eV, corresponding to a detuning of 180 meV. The DBR-Metal microcavities studied had values of $\hbar\Omega_{Rabi}$ ranging from 90 to 190 meV and Γ between 80 and 400 meV, while the DBR-DBR microcavities had values of $\hbar\Omega_{Rabi}$ from 65 to 100 meV and Γ between 106 and 345 meV.

To study the emission from DBR-DBR microcavities, they were mounted in a cryostat permitting the role of temperature to be explored. Cavities were excited non-resonantly with k-space imaging used to record the entire polariton dispersion in a single shot. Typical data is shown in **Figure 6.9**, where we plot the PL emission dispersion for two cavities having different detunings (Γ= 106 and 290 meV) recorded at 4K and 298K. To exclude the possibility of surface-plasmons contributing to the effects seen here, a series of 'empty' microcavities were fabricated containing a thin film of non-luminescent PS deposited between a DBR and a silver mirror. Reflectivity measurements indicated that such structures were weakly-coupled with the cavity photon mode undergoing a near parabolic dispersion as a function of angle, with no anti-crossing observed. Furthermore we find that following laser excitation at 473nm, no luminescence was detected from such 'empty-cavity' structures. This indicates plasmon-exciton coupling does not contribute to strong coupling and that any plasmon-emission generated is below the noise floor of our detector.
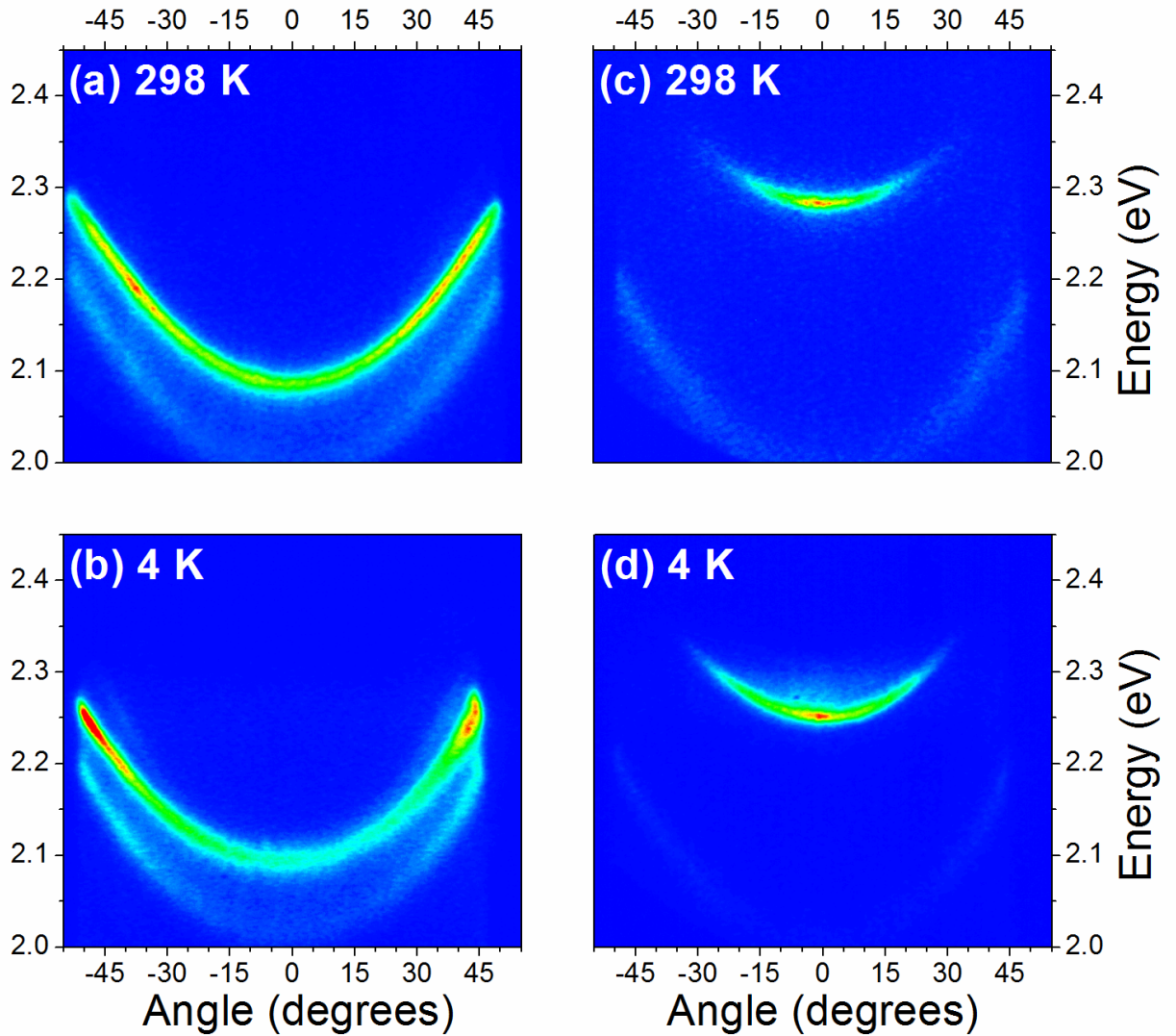
Figure 6.9. *Fluorescence emission from microcavities having a detuning of 290 meV (parts (a) and (b)), and 106 meV (parts (c) and (d)) at cryogenic (4K) and room temperature (298K). Here emission was generated using with a pulsed pump laser and recorded using a k-space imaging setup. All four dispersions plots have been individually normalized to clearly depict overall population distribution.*

Typical emission from two cavities having different detunings (Γ= 106 and 290 meV) recorded at 4K and 298K is shown in **Figure 6.9**. We find that for both cavities, no PL emission is detected from the UPB, with the intense luminescence detected in all cases corresponding to the energy of the LPB as detected in reflectivity measurements. Note, a weak emission feature with a near parabolic dispersion located at an energy ~100 meV below that of the LPB is detected. This emission corresponds to light escaping the cavity through the first minima of the DBR stopband which also has a strong angular dependence.

In **Figure 6.9**, it can be seen that strong PL emission is observed from the LPB (a finding that is also observed in cavities that also incorporate metallic mirrors). In particular, it can be seen that at 298 K, emission from the cavity having the smaller detuning (**Figure 6.9(c)**) is strongly concentrated towards the bottom of the LPB (i.e. around $\Gamma = 0°$). In the cavity having the much larger detuning (**Figure 6.9(a)**), the emission pattern is qualitatively different, with emission apparently distributed evenly along the LPB. When the temperature is reduced to 4K, we find that emission from the cavity having the smaller detuning (**Figure 6.9(d)**) is still concentrated towards the bottom of the LPB, however a significant change is observed in the cavity having the larger detuning (**Figure 6.9(b)**), with emission now concentrated around points on the LPB ($\Gamma > 30°$), corresponding to states close in energy to the exciton reservoir. Our measurements therefore indicate that thermalization of the excitation is incomplete and that relaxation to large detunings is ineffective. The mechanism of population of the polariton branches appears to be both energy- and temperature-dependent, being more effective in the spectral region near the exciton reservoir. This is consistent with the observed change in the photoluminescence emission as can be seen in **Figure 6.2(d)**.

To further explore emission from the cavity structures, the fluorescence decay lifetime from cavities was recorded as a function of time following a pump pulse, with measurements performed at 4K and 298K. It was found that the PL emission decay dynamics of both BODIPY-Br control films and the microcavities can be described by the sum of two exponentials (see **Figure 6.10**), having fast and slow time constants of ≤ 300 ps and $2 - 5$ ns with lifetime and amplitudes dependent on detection wavelength and temperature (see data summary in **Table 6.1**). Previous work has similarly evidenced a multi-exponential decay from BODIPY-Br films, and has interpreted this on the basis of dipole-dipole energy transfer between monomeric and aggregated forms of the molecule.[1] Here, we associate the longer-lifetime decay components observed with excimer states that have reduced radiative rates[18], and believe that the combination of fast and slow decay kinetics to be consistent with dipole-dipole energy transfer between isolated monomers and sites where excimers can form. Significantly however, we find that the decay lifetimes recorded from the cavities and the control films are in most cases similar (within a factor of two).
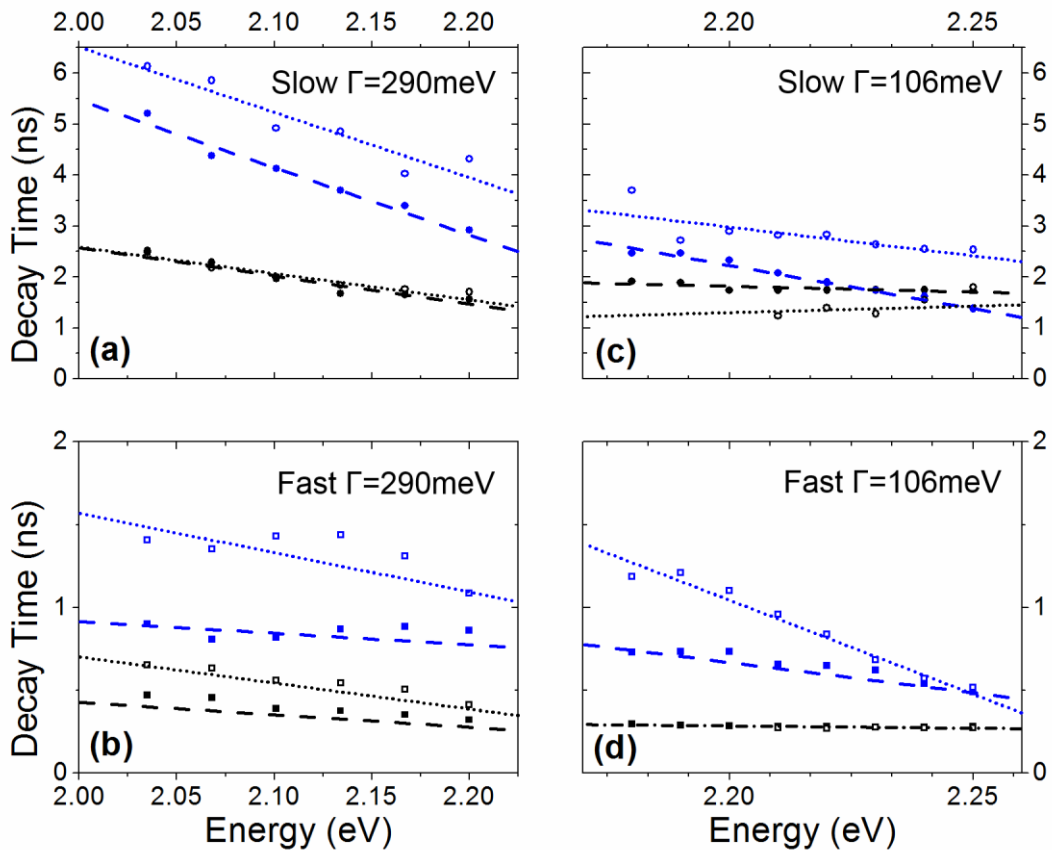
Figure 6.10. *PL decay time constants of control films (solid markers) and microcavities (open markers) at 298K (black) and 4K (blue) for detunings of Γ = 290 meV (left, parts **(a)** and **(b)**) and Γ = 106 meV (right, parts **(c)** and **(d)**) as a function of detection energy. The top panels (parts (a) and (c)) summarize the slow decay components whilst the bottom panels (parts (b) and (d)) plot the fast decay components which coincide with the temporal resolution of the detector (~250 ps). These measurements were taken from a series of k-space lifetime images, a subset of which were shown in Figure 6.9.*

	τ_1 4K	τ_1 298K	τ_2 4K	τ_2 298K	A:B 4K	A:B 298K
Units	(ns)	(ns)	(ns)	(ns)	(ratio)	(ratio)
Cavity-small detuning	0.57-1.2	0.27	2.5-2.9	1.6-2	180-340	165-250
Film-small detuning range	0.5-0.75	0.27-0.29	1.3-2.4	1.7-1.9	5-15	270-290
Cavity large detuning	1.1-1.4	0.41-0.65	4.3-6.1	1.7-2.2	15-25	7-90
Film-large detuning range	0.8-0.9	0.32-0.47	3-5.2	1-1.7	7-9	35-70

Table 6.1. *PL decay time constants for **Figure 6.10**. Decay constants for different points along the LPB are compared to the decay times for the corresponding energies of a control film of the same concentration (10% by mass), at 4K and at 298K. The components correspond to the formula: $I = Ae^{-\tau_1/t} + Be^{-\tau_2/t} + C$ where I represents measured PL intensity, τ_1 and τ_2 represent decay constants for the fast and slow components, and A and B represent their relative amplitudes.*

The similarity between cavity and control film decay rates (at least in a low pump-density regime) has been observed in a number of systems[19–21], and indicates that polariton states along the LPB are populated relatively slowly from the exciton reservoir, and do not significantly change the overall emission dynamics of the BODIPY-Br. To gain a more quantitative understanding of the population of polariton states, the PLQY from the microcavities was measured using an integrating sphere using previously reported methods as given by Green et al.[22] This measurement was performed for a large number of metal-DBR cavities having a range of detunings, and is shown in **Figure 6.11(a)**.
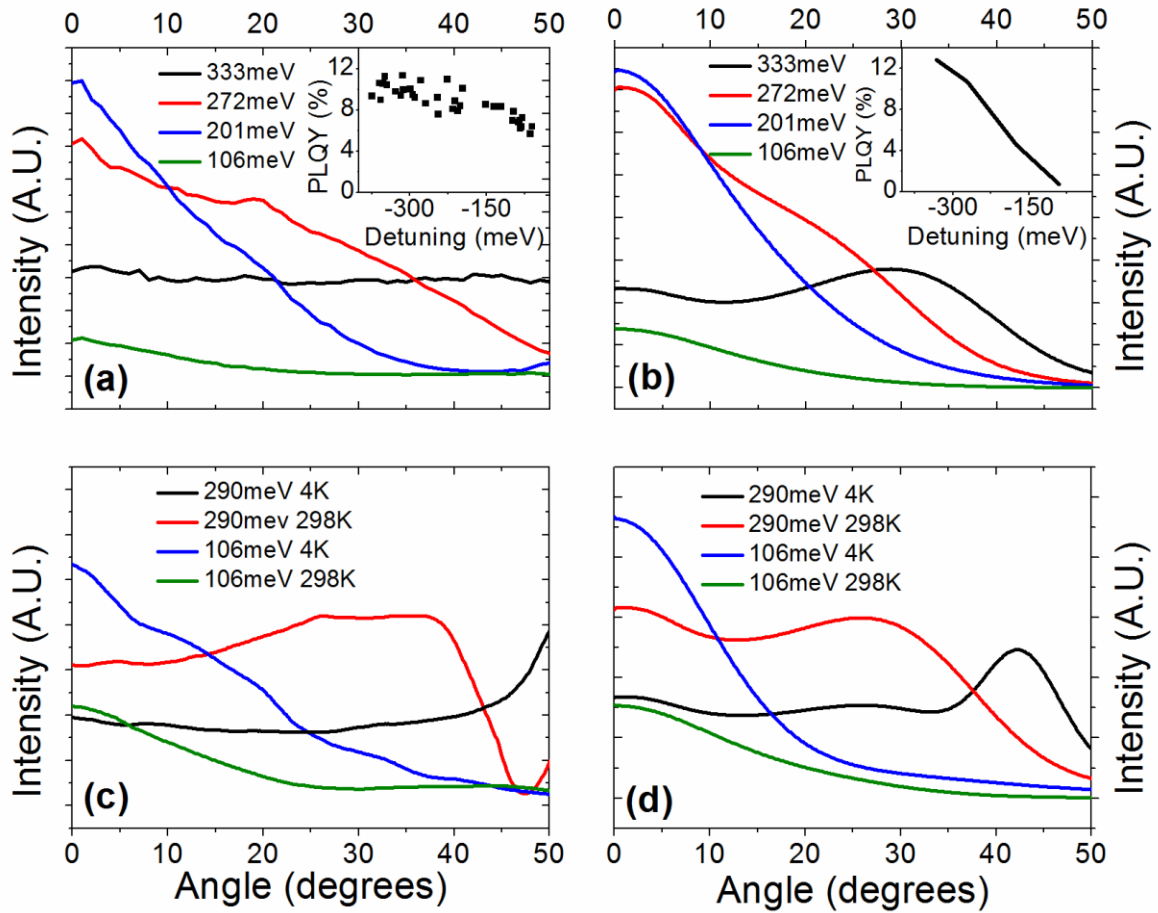
Figure 6.11. *Part **(a)** plots the measured PL intensity at 298K as a function of angle for four DBR-DBR microcavities having detunings of Γ = 333, 272, 201 and 106 meV. Part **(b)** plots the simulated PL intensity as a function of angle for the same four detunings. In part **(c)** we plot the PL emission intensity measured at 298K and 4K for cavities having a detuning of Γ = 290 and 106 meV. Part **(d)** plots the calculated PL intensity for the cavity emission shown in part (c). Inset: (left) is the measured PLQY of a series of DBR-Metal microcavities having detunings ranging from Γ= 80 to 400 meV. Inset (right) simulated PLQY as a function of detuning provided by Paolo Michetti.*

6.4. Radiative Pumping of Polariton States

Despite some scatter in the data, it is clear that microcavities possessing larger negative exciton-photon detuning generally emit luminescence with greater efficiency than do cavities having a smaller detuning; specifically cavities having the greatest (smallest) detuning have a PLQY of 11% (6%), with the efficiency of emission of the control film being 15%. The similarity between the PLQY of the control film of BODIPY-Br and that of the most negatively detuned cavities suggests the following polariton-population scenario: following optical excitation of an exciton, rapid relaxation inside the BODIPY-Br molecular film populates a reservoir of uncoupled states positioned at lower energies than the main absorption transition. These weakly coupled excitons are able to decay by emission of a photon that radiatively-pumps a strongly-coupled polariton state. The similarity in the PLQY of emission from cavities having a large detuning and that of the control film confirms that this process can be quite efficient.

To confirm this hypothesis, a phenomenological model describing the mechanisms of polariton population from the exciton reservoir that lead to polariton emission under continuous non-resonant excitation was developed with Paolo Michetti. Photoexcitation relaxation is taken into account using a series of rate equations describing the particle exchange between the exciton reservoir (ER) states and the UPB and LPB. The polariton branches are divided into annular regions, labelled by the modulus of the wave vector k, of energy $E_{k,U}$ and $E_{k,L}$ for UPB and LPB, containing N_k states. The division of the polariton density of states in homogeneously populated annular regions is supported by the isotropy of the microcavity emission. The inhomogeneously broadened ER is described in the model by a single state having an effective FWHM of 30 meV. We assume that non-resonant pumping directly populates the ER. It is also assumed that the ER is composed of monomeric dye molecules that are each described as a two-level-system that undergoes strong-coupling. In this idealized picture, a polariton state is described by **Equation (6.2)** as a superposition of a photon mode $|\vec{k}\rangle_{ph}$ and an exciton component delocalized over the whole film, with equal weight distributed between N dye monomers ($|j\rangle$):

$$|\vec{k}\rangle = \alpha(k)|\vec{k}\rangle_{ph} + \beta(k) \sum_{j}^{N} \frac{e^{i\vec{k}\vec{r}_j}}{\sqrt{N}}|j\rangle \qquad (6.2)$$

Following the model developed for J-aggregate films and J-aggregate microcavities[8,9,23], we initially tried to describe the exciton-polariton scattering process mediated by the emission/absorption of a molecular vibration, localized on each monomer dye molecule or in the host matrix. Here we explored a scattering process summarized by Equation (6.3), where W_0 and p are fitting parameters, with $n(E)$ being the Bose-Einstein distribution.

$$W_{k \leftarrow X} = W_0 |E_k - E_X|^p \frac{|\beta(k)|^2}{N} [1 + n(E_k - E_X)] \qquad \textbf{(6.3)}$$

We find that this approach can explain the relative suppression of UPB PL (but not its complete absence) via a rapid depletion of the UPB states through the effective scattering of polaritons back to the ER accompanied with the emission of a vibrational quanta. However to explain the variation of the LPB emission intensity observed in the experiments, we needed to invoke unrealistic changes in the parameters W_0 and p as a function of the detuning of the microcavity. A second process is therefore needed. Considering the fluorescent nature of the dye monomer, we postulate a mechanism whereby excitons in the ER radiatively pump polariton states as described by **Equation (6.4)**, where E_1 and σ are fitting parameters that describe the energy and linewidth of the weakly-coupled exciton states involved in the pump-process.

$$W_{k \leftarrow x} = W_1 e^{\frac{-(E_k - E_1)^2}{2\sigma^2}} |\alpha(k)|^2 \qquad \textbf{(6.4)}$$

This model assumes that ER states possess at least two electronic transitions; a high oscillator strength 0-0 transition being responsible for strong-coupling together with a population of weakly coupled states that are able to undergo spontaneous emission and 'pump' states along the LPB. A similar process was first invoked to explain the optical population of polaritons in crystalline anthracene; microcavities in which the 0-0 transition was strongly-coupled and emission from the weakly-coupled 0-1 transition pumped states at the bottom of the LPB[13,14]. We note that in other work, microcavities have been constructed that contain both strongly- and weakly-coupled components, with a polariton population being generated via weakly-coupled radiative emission[24]. In the present case we pragmatically adopt a simple Gaussian emission profile to describe the shape of the weakly-coupled emission pumping the LPB. We will later discuss the issue of the exact nature of such weakly-coupled emission in the present system,

which seems temperature activated. Surprisingly, we find that a single pump-reservoir described by parameters E_1 = 2.086 eV (593 nm) and σ = 58 meV (16 nm) results in a quite reasonable fit describing the polariton PL emission as a function of emission angle at all microcavity detuning values explored. This can be seen in **Figure 6.11**, where we plot the photoluminescence emission intensity following non-resonant CW excitation recorded at 298K as a function of angle for 4 different cavities having a detuning of Γ = 333, 272, 201 and 106 meV in part **(a)**, with the modelled emission intensity shown in part **(b)**.

Interestingly the best fit to the data suggests that this radiative relaxation mechanism is the dominant process that populates the LPB, with exciton to polariton scattering following the emission/absorption of a vibrational quanta being a rather ineffective channel. We can also fix the absolute value of the scattering rate W_1, by means of the PLQY. We determine a PLQY from a control film of BODIPY-Br (10% in PS by mass) of the order of 15%, and using a PL decay time of the order of 3 ns, a non-radiative exciton quenching time of τ_x = 3.5 ns is determined. This then suggests that ER excitations have a non-radiative depletion rate of $1/\tau_x$. By using a value of W_1 ($\approx$ 3 x 10^3 s^{-1} in **Equation (6.4)**), we can provide a quite reasonable description of the PLQY of the microcavities as a function of their detuning value as shown in **Figure 6.11**. By integrating the radiative pumping process along the LPB ($K = \sum_{LPB} W_{k \leftarrow X}$), a physically meaningful life-time ($\tau = K^{-1}$) for each cavity can be calculated, with times determined between 20 ns for the microcavity having the most significant negative detuning, to 1 ns for cavities having much smaller detunings. Our model allows us to understand the dependence of PLQY as a function of cavity detuning; cavities having a greater detuning have a larger fraction of more photon-like states that exist at larger viewing angles. These states are more efficiently pumped by the reservoir, and their subsequent radiation increases the relative photon yield from the lower polariton branch. It is clear however that for microcavities that possess small detunings, the present model fails to completely reproduce the measured PLQY, although it provides a reasonable qualitative description of the measured PL emission along the LPB.

To further explore the validity of the model, we have used it to simulate the PL emission from cavities having a detuning of Γ = 290 and 106 meV at 4K and 298K. Here, experimental data is plotted in **Figure 6.11(c)**, with the results of the calculation plotted in **6.11(d)**. Again it can be seen that good qualitative agreement is obtained between measured and modelled results. Importantly however, it is necessary to modify the radiative term at 4K to include a second pump emission peak at 2.18 eV (567 nm), with the peak at 2.086 eV (593 nm) being relatively diminished in amplitude but remaining present. The parameters used in the radiative pumping terms are summarized in **Table 6.2**.

Table 6.2. *Parameters used to fit the angular-dependent cavity population. E denotes the energy of each emission peak included, A the amplitude, and D the width of each peak.*

Temp.	E_1	E_2	A_1	A_2	D_1	D_2
K	meV	meV	-	-	meV	meV
300	2086	-	1	-	82	-
4	2086	2180	0.5	1	82	30

We now discuss the nature of the weakly-coupled states that pump the LPB polaritons. We interpret our results on the basis of the thin-film emission spectra, in which we observed photoluminescence from two distinct BODIPY-Br species: monomers and excimers. As shown in **Table 6.2**, a single pump term at E_1 = 2.086 eV (593 nm) appears to be sufficient to describe the polariton emission at 298K. As can be seen in **Figure 6.2(c)** and **Figure 6.6**, this wavelength seems close in energy to the excimer emission at 2.06 eV (602 nm). At 4K, the additional pump term at E_2 = 2.18 eV (567nm) that is necessary to describe the cavity population appears to coincide with intense, blue-shifted excimer emission observed in the neat films at 2.202 eV (563 nm) (see **Figure 6.2(d)**). In the microcavity, the excimer states are weak-coupled and can therefore radiatively pump the polariton states at all temperatures. We can thus identify emission from excimers with both the E_1 and E_2 pump terms: the former is sufficient to describe the high-temperature excimer spectrum, while at low temperatures the emission is better described as a combination of the two.

This picture is able to explain the temperature-dependant behaviour of the control film PL and identify the presence and relative importance of E_1 and E_2 pumping terms in the model at low- and room-temperature. At room temperature, a significant fraction of the exciton population is quenched in the weakly emissive excimer state, which corresponds to the E_1 pumping term, with some contribution from the emission of the degenerate 0-1 vibronic monomer transition also being possible. Note that the migration of 0-0 exciton population into various states at lower energy that are unable to undergo vibrationally-assisted scattering to or from the polariton branches is consistent with the absence of UPB luminescence. At low temperature, energy relaxation in the film follows the same pathway as before, but the nature of the weakly coupled state partially changes, enabling even more efficient optical pumping of states along the LPB (the E_2 term) from enhanced excimer luminescence. However weaker pumping from the E_1 term is still observed. We note that the relative reduction in the amplitude (A_1) of the lower-energy (E_1) pump-term required to describe cavity emission at 4K is consistent with the lineshape of the excimer emission observed at that temperature (See **Figure 6.2(c)**). Our model thus suggests the apparent redistribution of polariton population that occurs along the LPB as a function of temperature observed in microcavities having a large energetic detuning appears to originate from changes in the energetic excitation distribution within the ER, rather than some type of polariton thermalisation process.

It is instructive to compare our work with other recent work on strong-coupled organic microcavities. Ballarini et al[25] fabricated a series of strongly coupled microcavities using a squaraine dye having a low PLQY of < 0.01%, and observed large enhancements in PLQY from the cavity (up to an order of magnitude for resonant pumping); a result in direct contrast with the small reduction in PLQY observed here. The difference between such findings can be understood on the basis of the relative magnitudes of radiative decay of uncoupled reservoir excitons and the exciton to polariton scattering rate. Here, our model indicates that direct radiative pumping of polaritons by weak-coupled excimer decay is a much more efficient process than phonon-assisted exciton-polariton scattering process, and thus the net yield of photons emitted from the cavity is largely unchanged in the strong-coupling regime. In contrast, in cavities containing materials having a low radiative rate (or reduced PLQY)[25], the exciton to polariton scattering rate can be comparable to radiative decay and thus the additional generation of additional highly-radiative polaritons can increase the overall photon yield substantially.

6.5. Conclusions:

In conclusion, we have demonstrated strong coupling in a series of microcavities containing the fluorescent molecular dye BODIPY-Br and have investigated the change in polariton distribution along the lower polariton branch as a function of detuning and temperature. It was found that as the exciton-photon detuning is reduced, the polariton population is increasingly concentrated around the bottom of the lower polariton branch. Measurements of photoluminescence quantum efficiency indicated that the overall yield of photons from the cavity is similar to that of a non-cavity control film, and that the photoluminescence decay lifetime of cavity and control films are quite similar. To understand such observations, a fitting model was used that describes the population of polaritons following weakly-coupled radiative decay of reservoir excitons. Surprisingly, it was found that this radiative pumping process provided an adequate description of the cavity emission over a large range of detunings at room temperature and at 4K, with the model indicating that phonon-mediated exciton-to-polariton scattering does not contribute substantially to the polariton population mechanism. Indeed, it appeared to be similar to cavities containing crystalline anthracene[12], though in such systems no change in the energy of the radiative pumping term was observed as a function of temperature. Here, π-π interactions between BODIPY-Br molecules are likely to give rise to co-existing spectral signatures of well-isolated monomers and excimers. Using a phenomenological fitting model, we suggest the population along the lower polariton branch to be the result of the optically pumping due to emission from the weakly-coupled vibronic 0-1 monomer transition and a stabilized, temperature-dependent excimer state.

The relatively high photoluminescence emission quantum yield of BODIPY-Br, together with the high efficiency by which lower polariton branch states are populated make the cavities studied here a strong candidate in which to observe polariton condensation and lasing. The importance of the radiative pumping mechanism identified here suggests that polariton condensation thresholds in organic-semiconductor microcavities can most likely be reduced by using molecular materials having high photoluminescence quantum efficiency and a high radiative rate.

A peer-reviewed copy of this work can be found in Advanced Optical Materials, 2016, vol. 5 under the title "*Efficient Radiative Pumping of Polaritons in a Strongly Coupled Microcavity by a Fluorescent Molecular Dye*" by Grant et al.

6.6. References

1. Vu, T. T. *et al.* Understanding the Spectroscopic Properties and Aggregation Process of a New Emitting Boron Dipyrromethene (BODIPY). *J. Phys. Chem.* **117,** 5373–5385 (2013).

2. Choi, S., Bouffard, J. & Kim, Y. Aggregation-induced emission enhancement of a meso-trifluoromethyl BODIPY via J-aggregation. *Chem. Sci.* **5,** 751 (2014).

3. Mikhalyov, I., Gretskaya, N., Bergström, F. & Johansson, L. B.-A. Electronic ground and excited state properties of dipyrrometheneboron difluoride (BODIPY): Dimers with application to biosciences. *Phys. Chem. Chem. Phys.* **4,** 5663–5670 (2002).

4. Treibs, A. & Kreuzer, F.-H. Difluorboryl-Komplexe von Di- und Tripyrrylmethenen. *Justus Liebigs Ann. Chem.* **718,** 208–223 (1968).

5. Ulrich, G., Ziessel, R. & Harriman, A. The chemistry of fluorescent bodipy dyes: versatility unsurpassed. *Angew. Chem. Int. Ed. Engl.* **47,** 1184–201 (2008).

6. Ariano, M. A. *et al.* Direct visualization and cellular localization of D1 and D2 dopamine receptors in rat forebrain by use of fluorescent ligands. in *Proc. Natl. Acad. Sci. U. S. A.* **86,** 8570–8574 (1989).

7. Shah, M., Thangaraj, K., Soong, M.-L., Wolford, L. T. & Boyer, J. H. Pyrromethene-BF2 Complexes as Laser Dyes: 1. *Heteroat. Chem.* **1,** 389–399 (1990).

8. Michetti, P. & La Rocca, G. C. Simulation of J-aggregate microcavity photoluminescence. *Phys. Rev. B* **77,** 195301 (2008).

9. Michetti, P. & La Rocca, G. C. Exciton-phonon scattering and photoexcitation dynamics in J -aggregate microcavities. *Phys. Rev. B* **79,** 035325 (2009).

10. Michetti, P. & La Rocca, G. C. Polariton states in disordered organic microcavities. *Phys. Rev. B* **71,** 115320 (2005).

11. Litinskaya, M., Reineker, P. & Agranovich, V. M. Fast polariton relaxation in strongly coupled organic microcavities. *J. Lumin.* **110,** 364–372 (2004).

12. Kena-Cohen, S. & Forrest, S. R. Room-temperature polariton lasing in an organic single-crystal microcavity. *Nat. Photonics* **08,** 1–5 (2010).

13. Mazza, L., Fontanesi, L. & La Rocca, G. C. Organic-based microcavities with vibronic progressions: Photoluminescence. *Phys. Rev. B* **80,** 235314 (2009).

14. Mazza, L., Kéna-Cohen, S., Michetti, P. & La Rocca, G. C. Microscopic theory of polariton lasing via vibronically assisted scattering. *Phys. Rev. B* **88,** 075321 (2013).

15. Lodden, G. H. & Holmes, R. J. Electrical excitation of microcavity polaritons by radiative pumping from a weakly coupled organic semiconductor. *Phys. Rev. B - Condens. Matter Mater. Phys.* **82,** 1–5 (2010).

16. Michetti, P., Mazza, L. & La Rocca, G. C. in *Org. Nanophotonics* (ed. Zhao, Y. S.) 39–68 (Springer, 2015).

17. Kim, S., Bouffard, J. & Kim, Y. Tailoring the Solid-State Fluorescence Emission of BODIPY Dyes by meso Substitution. *Chem. - A Eur. J.* **21,** 17459–17465 (2015).

18. Jenekhe, S. A. & Osaheni, J. A. Excimers and Exciplexes of Conjugated Polymers. *Science (80-.).* **265,** (1994).

19. Schwartz, T. *et al.* Polariton dynamics under strong light-molecule coupling.

ChemPhysChem **14,** 125–31 (2013).

20. Tassone, F., Piermarocchi, C., Savona, V., Quattropani, A. & Schwendimann, P. Photoluminescence decay times in strong-coupling semiconductor microcavities. *Phys. Rev. B* **53,** 7642–7645 (1996).

21. Lidzey, D. G. *et al.* Experimental study of light emission from strongly coupled organic semiconductor microcavities following nonresonant laser excitation. *Phys. Rev. B* **65,** 195312 (2002).

22. Green, A. P. & Buckley, A. R. Application of gauge R&R to the rigorous measurement of quantum yield in fluorescent organic solid state systems. *Rev. Sci. Instrum.* **83,** 073108 (2012).

23. Heijs, D. J., Malyshev, V. A. & Knoester, J. Decoherence of Excitons in Multichromophore Systems: Thermal Line Broadening and Destruction of Superradiant Emission. *Phys. Rev. Lett.* **95,** 177402 (2005).

24. Akselrod, G. M., Young, E. R., Bradley, M. S. & Bulovic, V. Lasing through a strongly-coupled mode by intra-cavity pumping. *Opt. Express* **21,** 3691–3696 (2013).

25. Ballarini, D. *et al.* Polariton-Induced Enhanced Emission from an Organic Dye under the Strong Coupling Regime. *Adv. Opt. Mater.* **2,** 1076–1081 (2014).

7.

Lasing in Strongly Coupled Microcavities Containing Fluorescent Molecular Dyes

Following the successful demonstration of strong coupling in a series of microcavities containing the fluorescent molecular dye BODIPY-Br, this chapter explores the steps taken to identify fluorescent molecular dyes and evaluate their likelihood of lasing. This is a necessary step required before fabrication of microcavities containing said dyes to create coherent emission. Key parameters that indicate whether a material is a promising candidate for polariton lasing are high-quantum yield, a tendency to undergo amplified spontaneous emission, narrow electronic transitions, and sufficient oscillator strength to enter the strong coupling regime.

7.1. Spectral Characterisation of Fluorescent Molecular Films

Four materials were identified as promising candidates: BODIPY-Br, LFO, meso-TFBOD and meso-QFBOD. This section describes characterisation of these dyes outside of a microcavity via steady state absorption, photoluminescence spectroscopy, photoluminescence quantum yield (**PLQY**), and amplified spontaneous emission measurements (**ASE**). Unless otherwise stated, all measurements were performed using the same experimental parameters. Concentration dependent absorption and PL measurements were made using a Xenon lamp and a 473nm CW diode laser respectively. PLQY measurements were made using Coherent Mira 900 laser operating at 80MHz in conjunction with a second harmonic generator.
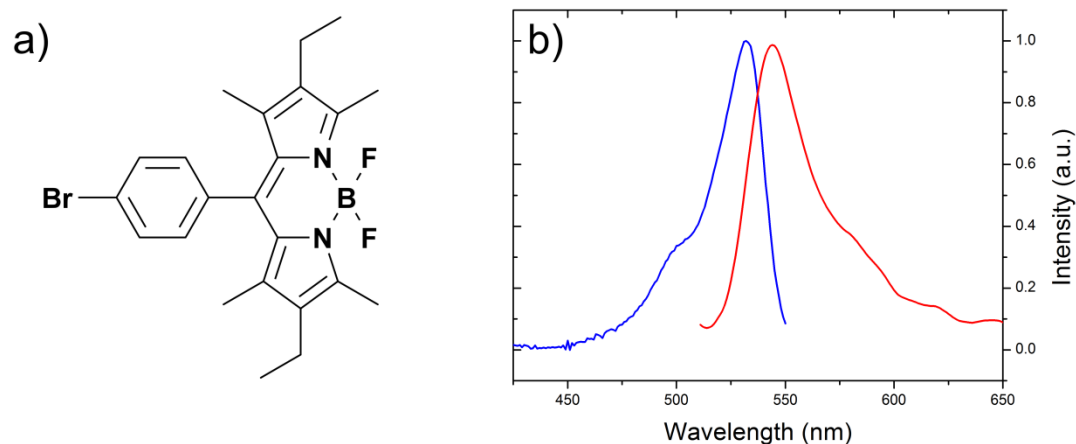
7.1.1. BODIPY-Br

Figure 7.1. (a) *The chemical structure of BODIPY-Br.* ***(b)*** *The absorption (blue) and photoluminescence (red) of a BODIPY-Br doped polystyrene film at a concentration of 1% by mass.*

The first of these materials is a bromine-substituted variant upon boron-dipyrromethene, **BODIPY-Br**. A more thorough description of this dye (and microcavities containing it) is covered in significant detail in **Chapter 6**, but will be briefly recapped here. It is a member of a family of dyes known for their versatility and widespread use in a variety of applications[1–6], and is typically characterised by narrow spectral features and high quantum yields. **Figure 7.1** depicts the chemical structure of the BODIPY-Br fluorophore and absorption and photoluminescence measurements of a low dye concentration film. From measurements made in chapter 6, we can ascertain that there is unlikely to be enough dye in a 1% film to create a microcavity capable of entering into the strong coupling regime; hence it is necessary to explore the spectral characteristics of the dye at higher concentrations.
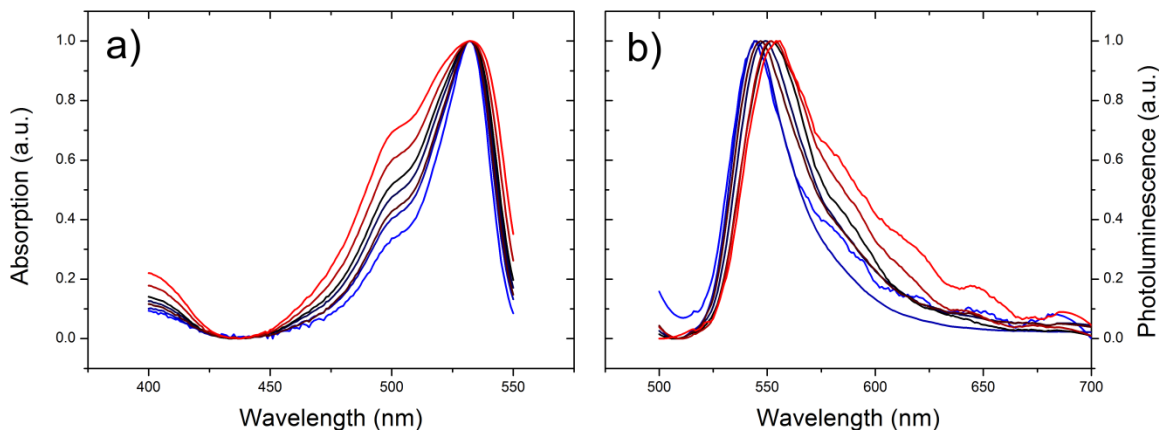
Figure 7.2. (a) *Absorption and **(b)** PL of a series of BODIPY-Br films dispersed within a polystyrene matrix as a function of dye concentration by mass from 0.1% (blue) to 10% (red).*

It can be seen in **Figure 7.2** that as the concentration of the dye increases, both the absorption and emission profiles of the film undergo significant broadening. At a 1% concentration, the (0-0) absorption transition located at 530nm is ~2.8x stronger than the blue-shifted shoulder at 500nm corresponding to the (0-1) vibronic replica. At a concentration of 10%, the (0-0) transition is only ~1.3x stronger than the (0-1) transition. The emergence of the blue-shifted shoulder in the absorption spectrum is indicative of the formation of H-aggregates; this is confirmed by both the PLE measurements shown in chapter 6, and the reduction in PLQY as concentration is increased as is shown in **Figure 7.3**.
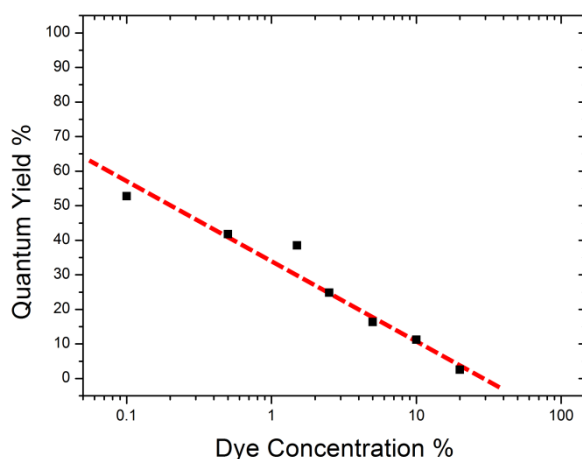

Figure 7.3. *Fluorescence quantum yield measurements of a series of BODIPY-Br-doped polystyrene film as a function of dye concentration.*
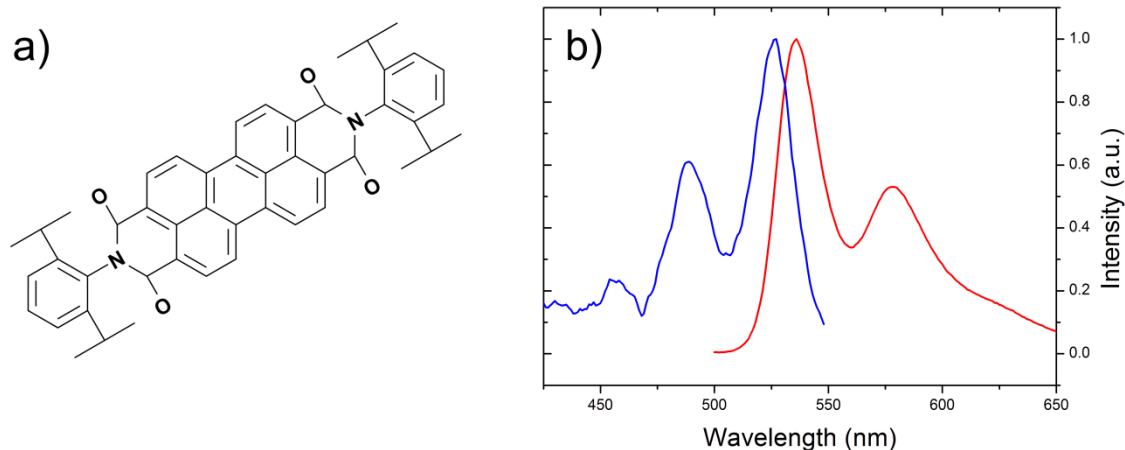
7.1.2. LFO

Figure 7.4. (a) *The chemical structure of LFO.* ***(b)*** *The absorption (blue) and photoluminescence (red) of a LFO doped polystyrene film at a concentration of 1% by mass.*

The second material to be investigated was Lumogen F Orange 240, a derivative of the perylene family of dyes purchased from BASF noted for their thermal and photo stability hereafter referred to as **LFO**. The chemical structure of LFO and the spectral properties of a dilute (1% dye by mass) film can be seen in **Figure 7.4**. The (0-0) transition along with its vibronic replicas, (0-1) and (0-2), are well defined and clearly observed in both the absorption and PL spectra.
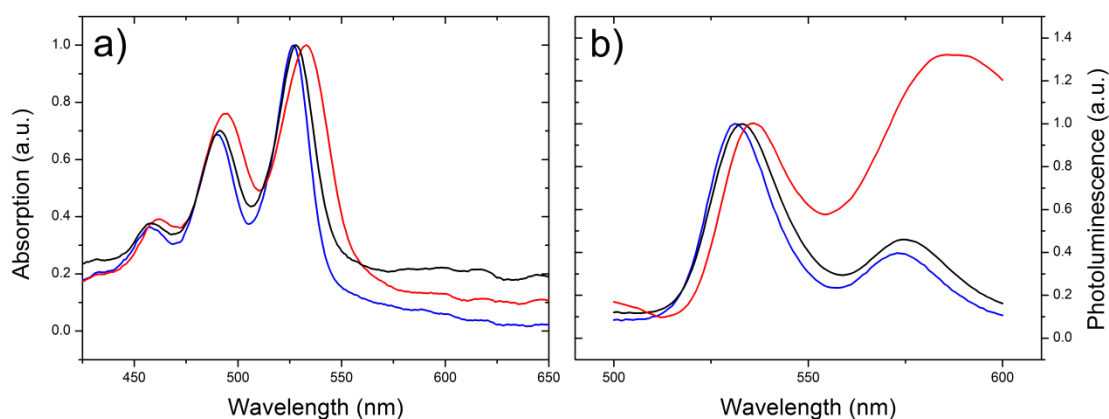

Figure 7.5. (a) *Absorption of LFO-doped polystyrene films at concentrations of 1% (blue), 10% (black), and 100% (red).* ***(b)*** *Photoluminescence of LFO-doped polystyrene films at concentrations of 0.1% (blue), 1% (black), and 10% (red) dye by mass.*

At higher concentrations (**Figure 7.5**), it can be seen that despite a small shift (4nm) in the peak positions and slight broadening of transitions, the absorption spectrum of LFO remains virtually unchanged even in neat films. The same cannot be said for the PL spectrum however. The primary emission peak at 530nm shifts by 4nm, but diminishes in strength relative to the secondary PL peak which experiences a 14nm shift from 573nm to 587nm. Interestingly despite the large change in PL shape, the PLQY of LFO films do not diminish as rapidly as BODIPY-Br as the concentration is increased. **Figure 7.6** reveals a PLQY of 0.84 at a concentration of 0.5%, falling to 0.23 at a concentration of 10% dye by mass. As with BODIPY-BR, we attribute the emergence of the red-shifted feature in PL measurements to the formation of weakly emissive H-aggregates, a statement corroborated by the observed reduction of PLQY with concentration. The photophysics of the two dyes are very similar and changes in polariton population distribution as a function of photon mode detuning have been observed in LFO similar to those shown in **Chapter 6**.
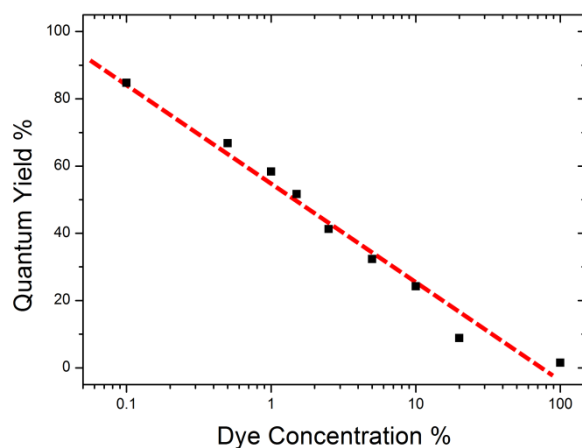

Figure 7.6. *Fluorescence quantum yield measurements of a series of LFO-doped polystyrene films as a function of dye concentration.*
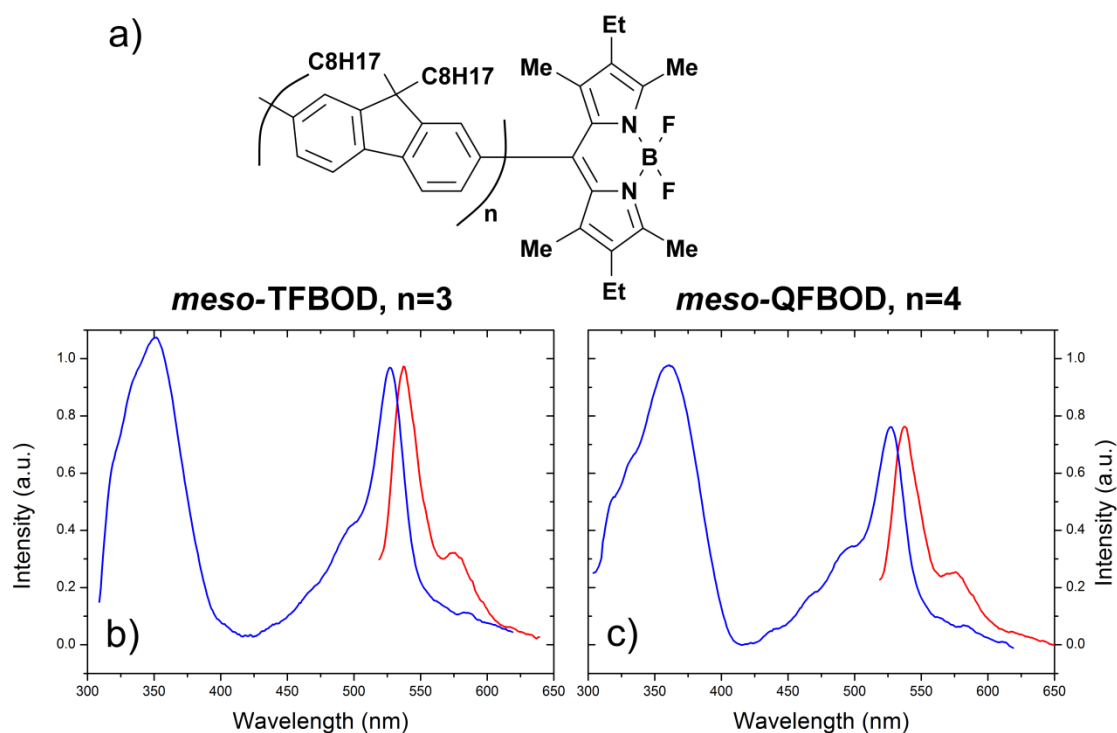
7.1.3. Meso-TFBOD and meso-QFBOD

Figure 7.7. (a) *The chemical structure of both meso-TFBOD and meso-QFBOD.* **(b)** *The absorption (blue) and photoluminescence (red) of a meso-TFBOD.* **(c)** *The absorption (blue) and photoluminescence (red) of a meso-QFBOD. Both dyes are dispersed within a polystyrene matrix at a concentration of 1% dye by mass.*

Two variations upon the BODIPY molecule were also studied in which oligofluorene side chains of varying length were substituted onto the "meso" position of the BODIPY chromophore, these are shown in **Figure 7.7**. Meso-TFBOD and meso-QFBOD were synthesised and supplied by Neil Findlay at the University of Strathclyde. Originally developed for use in conjunction with a blue LED to produce spectrally broad white light LEDs[7], these dyes lend themselves to study within microcavities. The addition of oligofluorene side chains introduces a strong absorption feature in the ultraviolet region which efficiently transfers energy from the side-chains to the BODIPY core from which it emits. The side chains have the added benefit of reducing aggregation effects through steric hindrance in both absorption and PL measurements as can be seen in **Figure 7.8**. As (virtually) all emission comes from the same BODIPY core, the fluorescence profiles for both dyes are identical and undergo a red-shift of ~9nm as the concentration increases from 0.5% to 100% dye by mass (when dispersed in a polystyrene matrix). The shape of the absorption profile is almost invariant with concentration for both dyes (though the peak absorption of TFBOD is blue shifted from that of QFBOD by 10nm).
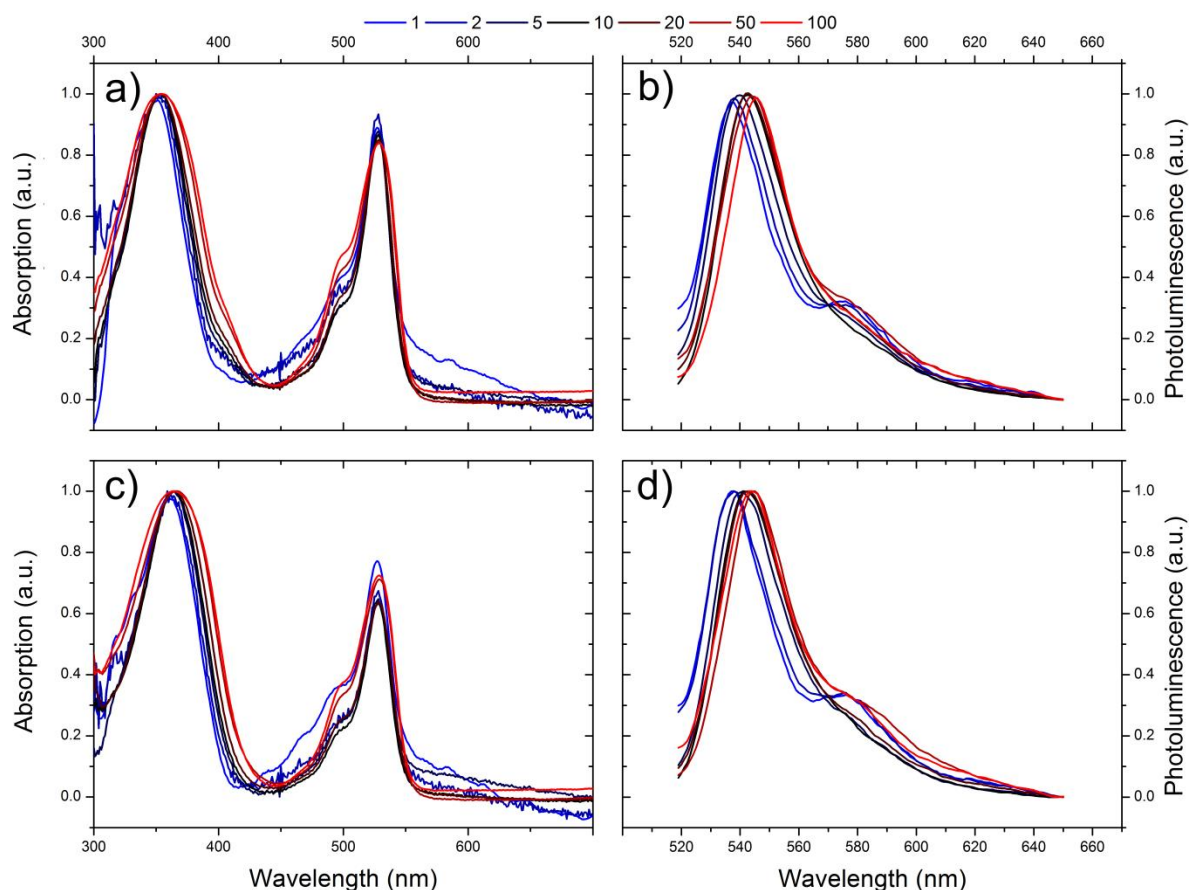
Figure 7.8. (a) *Absorption and **(b)** PL as a function of concentration for a film of meso-TFBOD dispersed within a polystyrene matrix. **(c)** Absorption and **(d)** PL as a function of concentration for a film of meso-QFBOD dispersed within a polystyrene matrix. Dye concentrations range from 1% (blue) to 100% (red) as indicated at the top of this figure.*

Peak PL position for meso-TFBOD (QFBOD) shifts from 535 nm (537nm) at a concentration of 0.5% to 543nm (545nm) at a concentration of 100%. As the concentration increases, the PLQY of both materials diminishes from 0.9 at a concentration of 0.5% to 0.6 at a 10% dye by mass, but remains higher than that of the unmodified molecule. This is due primarily to the oligofluorene side chains which reduce both aggregation and the quenching that can be caused by adjacent chromophores. Interestingly it was found that the PLQY of both materials was highest when the absorption feature corresponding to said side chains was excited, suggesting efficient energy transfer. This is shown in **Figure 7.9**. Exciting at the absorption minima (448nm) resulted in a reduction of PLQY, indicating non-resonant pumping was an inefficient process.
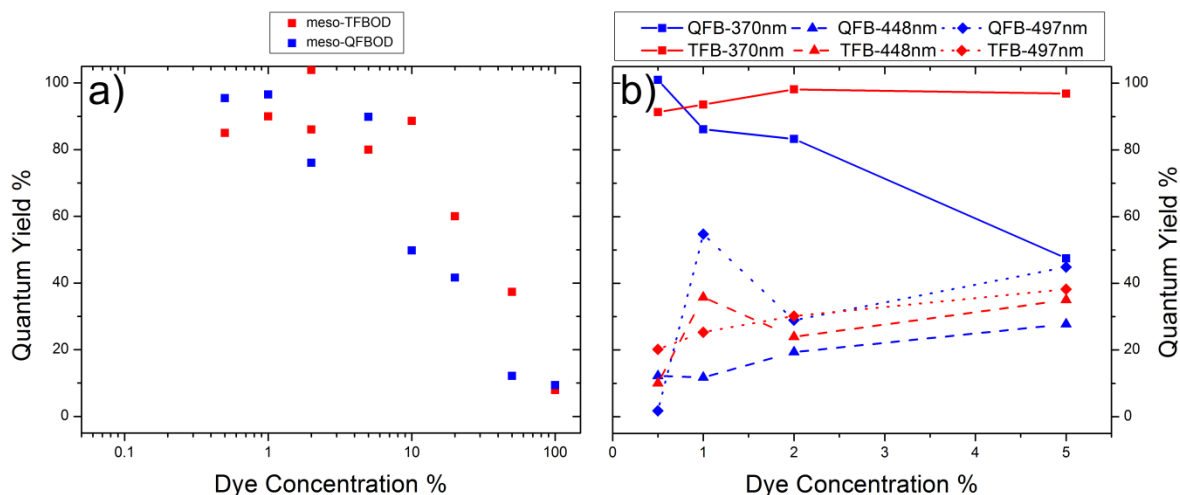
Figure 7.9. (a) *Quantum yield measurements upon a series of meso- TFBOD (red) and QFBOD (blue) films across a wider range of concentrations using a 370nm excitation source to coincide with peak absorption wavelength. **(b)** Fluorescence quantum yield measurements as a function of both dye concentration and excitation wavelength for films of meso-TFBOD and -QFBOD dispersed within a polystyrene matrix. Solid lines indicate excitation at 370 nm, dashed at 448 nm, and dotted at 497 nm.*

7.2. Amplified Spontaneous Emission Thresholds

Amplified spontaneous emission (**ASE**) measurements are a good indication as to whether materials possessing high quantum yields are able to act as good gain media and produce non-linear behaviour. ASE measurements were performed with the assistance of Sai Kiran Rajendran and Kyriacos Georgiou at Politecnico di Milano. Unless otherwise mentioned, a 500nm pulsed laser operating at a repetition rate of 1 kHz and cylindrical lens were used to create an excitation stripe upon the surface of sample films with the approximate dimensions of 650µm x 35µm, corresponding to an area of $2.275 \times 10^{-5} cm^2$. Emission was collected at an angle perpendicular to the excitation path, in plane with the film. More details about ASE can be found in **Chapter 5**.

7.2.1. BODIPY-Br

Following PLQY measurements, ASE measurements were performed upon a series of BODIPY-Br films of identical thickness (300nm) but different concentrations in order to determine whether or not they would undergo ASE, and if so, at what wavelengths this would occur. By keeping film thickness consistent from sample to sample, this allowed the thresholds to be directly compared. Peak ASE wavelength red shifted from 580.5nm at a concentration of 4% in PS to 591nm at a concentration of 15%. Note that concentrations below 4% dye by mass did not exhibit ASE. ASE thresholds could be reduced by changing the excitation wavelength to one closer in wavelength to peak absorption as can be seen in **Figure 7.10**. ASE thresholds were over an order of magnitude smaller when pumping at 500nm than at 400nm.
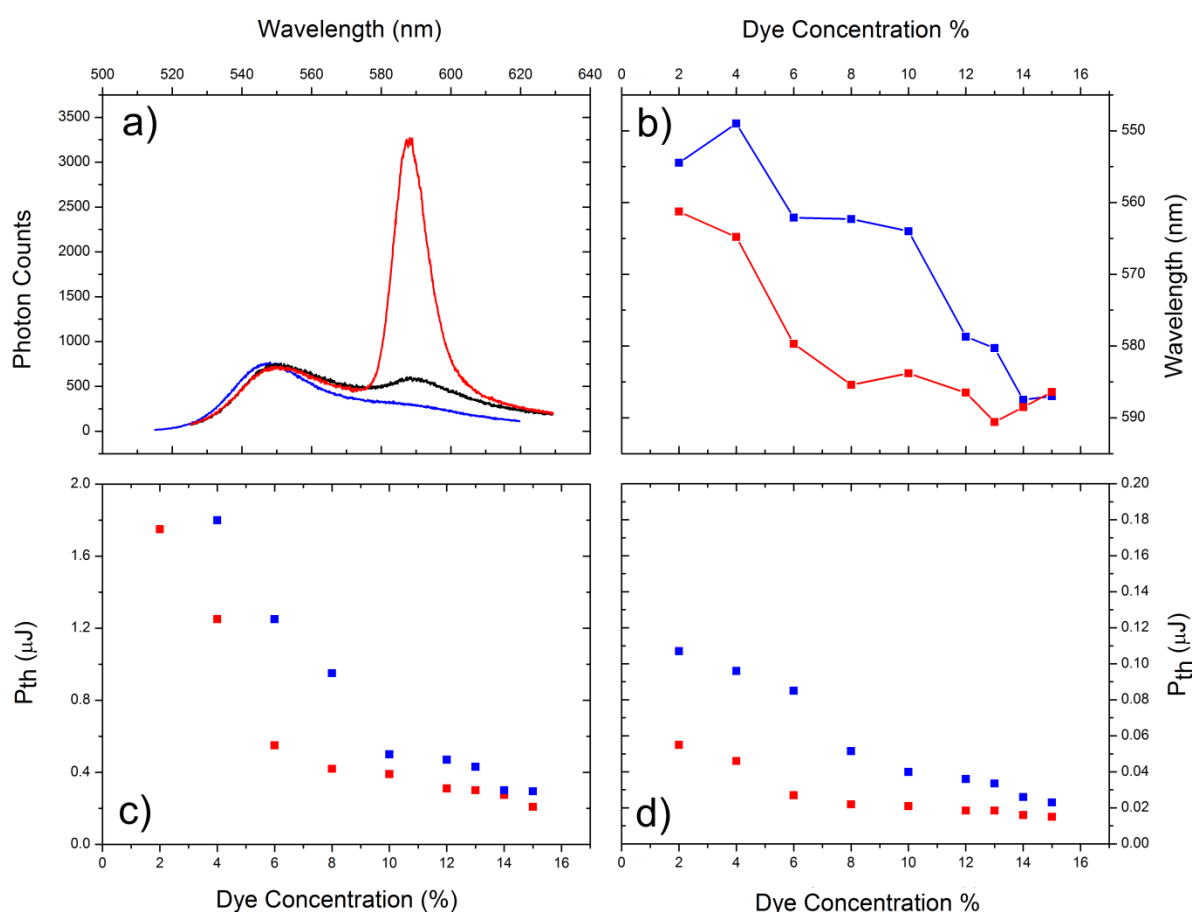

Figure 7.10. *(a)* *ASE stripe measurements of a BODIPY-Br doped polystyrene film at a concentration of 10% dye by mass below (blue), at (black), and above (red) threshold.* *(b)* *Peak ASE wavelengths of 200nm (blue) and 300nm (red) thick BODIPY-Br films as a function of concentration following 500nm excitation. ASE thresholds for 200nm (blue) and 300nm (blue) films of BODIPY-Br as a function of concentration following excitation from a* *(c)* *400nm pump source and,* *(d)* *a 500nm pump source.*

7.2.2. LFO

ASE measurements performed upon a series of LFO films of identical thickness (200nm and 300nm) revealed that ASE occurred in all samples except for one 200nm thick film with a dye concentration of 2%. As seen previously in the BODIPY-Br films, the threshold for ASE lowered with both increased film thickness and dye concentration. A shift in peak ASE emission was also observed from 578 nm at a 2% concentration to 582 nm at 9%. Changing from a 500nm to a 400nm pump shifts peak ASE wavelength for a 10% film from ~580nm to ~591nm and increases lasing thresholds by an order of magnitude at lower concentrations.
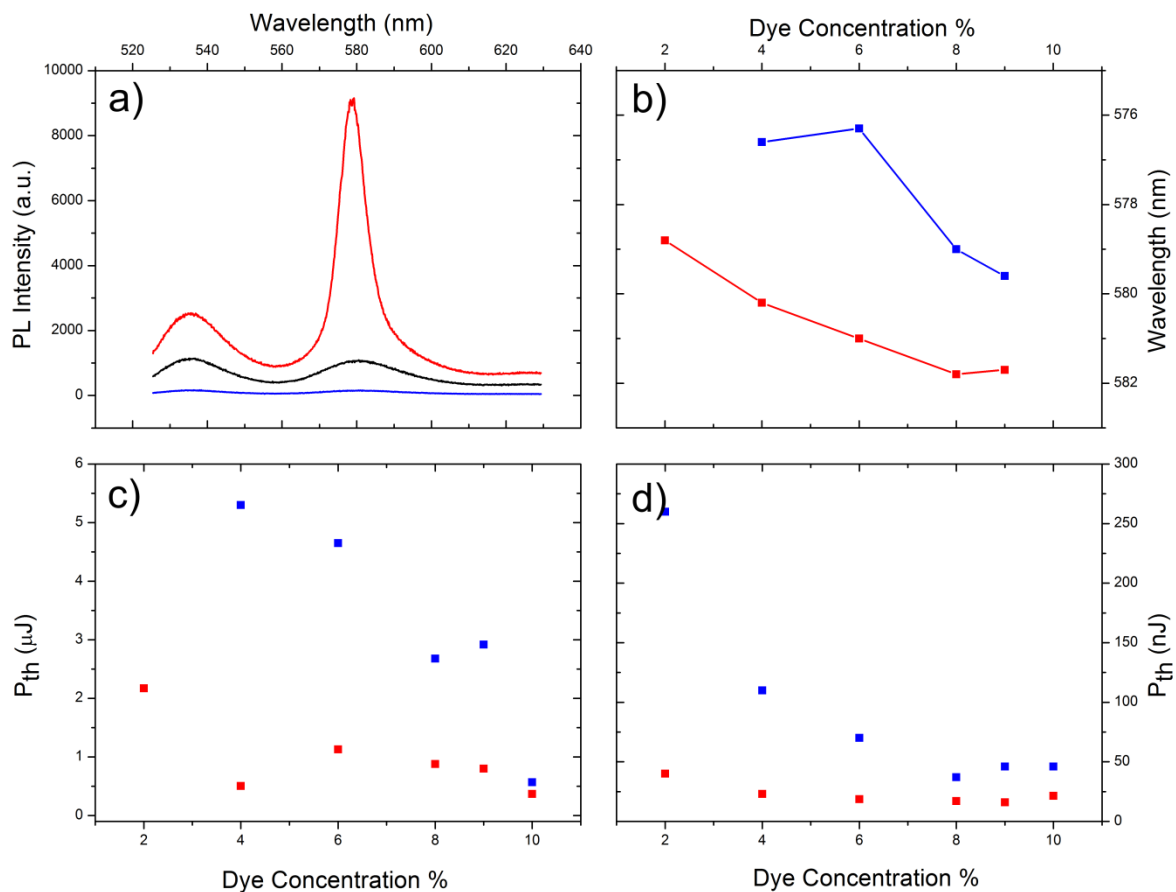

Figure 7.11. (a) *ASE stripe measurements of a LFO-doped polystyrene 300nm film at a ratio of 2% dye by mass below (blue), at (black), and above (red) threshold. **(b)** Peak ASE wavelength of 300nm thick LFO films as a function of concentration following 500nm excitation. ASE thresholds for 200nm (blue) and 300nm (red) films of LFO as a function of concentration following excitation from a **(c)** 400nm pump source and, **(d)** a 500nm pump source.*

7.2.3. meso-TFBOD and meso-QFBOD

Due to the presence of a strong absorption feature in the near-UV region of the EM spectrum, ASE measurements were performed with 100fs pulses from a 400nm laser operating at repetition rate of 1kHz. Stripe dimensions were approximately 650μm x 35μm. **Figure 7.12** depicts the PL spectra of meso-TFBOD below, at, and above its ASE threshold. It can also be seen that peak ASE PL wavelength shifts from 551nm at low concentration for both dyes to ~560nm at a concentration of 5%. No ASE was found in QFBOD films at dye concentrations below 1%. Time constraints and equipment difficulties prohibited further measurements at higher concentrations.
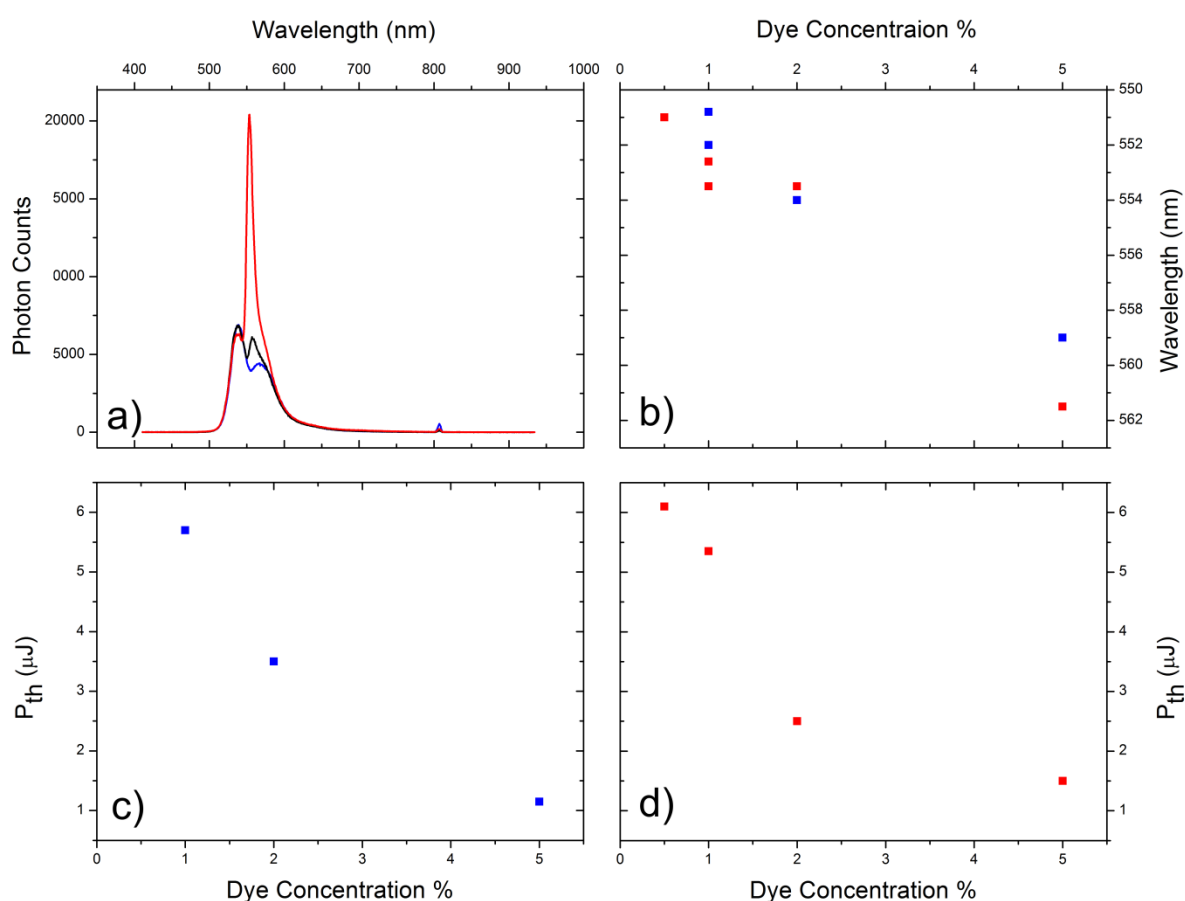

Figure 7.12. (a) *ASE stripe measurements of a meso-TFBOD doped polystyrene film at a ratio of 2% dye by mass below (blue), at (black), and above (red) threshold.* ***(b)*** *Peak ASE wavelength of 250nm thick meso-TFBOD films as a function of concentration. ASE thresholds for 250nm films of* ***(c)*** *meso-QFBOD and* ***(d)*** *meso-TFBOD as a function of dye concentration following excitation from a 400nm pump source.*

7.3. Strong-Coupling in Microcavities

Once films had been analysed and been shown to exhibit an enhancement of spontaneous emission through stripe pumping, it became necessary to determine if these materials could enter the strong coupling regime, and if so at what concentration. A series of microcavities were prepared that comprised of DBR-metal (12 pairs produced by PECVD and thermal evaporation) and DBR-DBR (12 and 10 pairs produced by IAPVD, courtesy of Helia Photonics).

Microcavities were designed in such a way that the energies at which ASE occurred were resonant with the bottom of the LPB. As this wavelength varies with film thickness, dye concentration, and excitation wavelength, it was necessary to produce a series of microcavities with slight variations in cavity length for each dye. Unless otherwise stated all measurements shown are of DBR-DBR microcavities. For the sake of brevity, only one microcavity is depicted per dye.
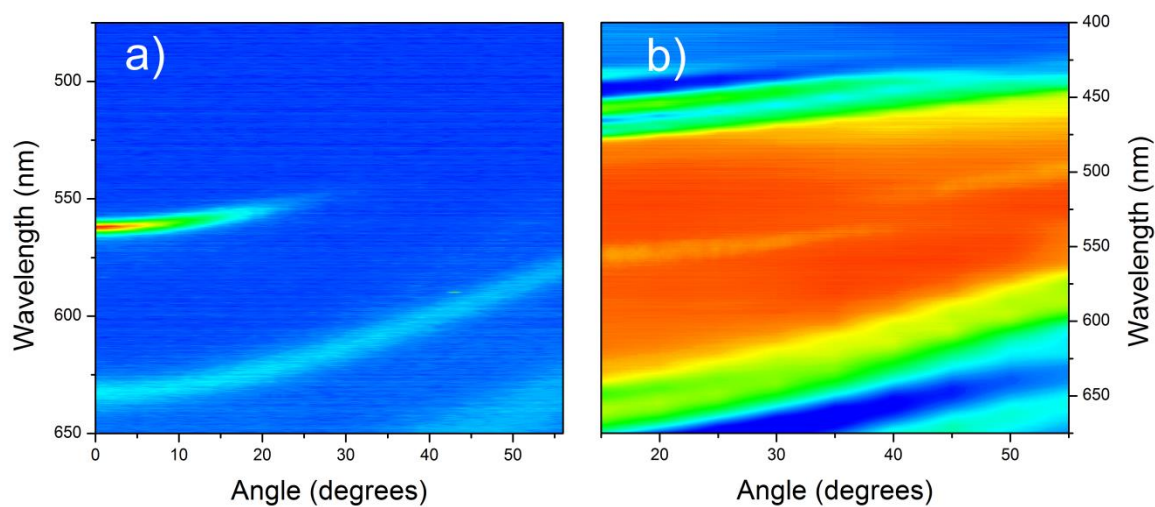
7.3.1. BODIPY-Br

Figure 7.13. *Angular dependent **(a)** photoluminescence and **(b)** reflectivity measurements of a DBR-DBR microcavity containing BODIPY-Br doped into a polystyrene matrix at a concentration of 10% by mass. The microcavity shown here has Rabi splitting of 155meV and a negative photon mode detuning of 60meV as calculated using the transfer matrix method.*

BODIPY-Br was found to enter the strong coupling regime at all concentrations tested >2% dye by mass. **Figure 7.13** plots photoluminescence and reflectivity measurements made upon a microcavity containing an active layer of BODIPY-Br-doped polystyrene at a 10% concentration. A Rabi-splitting of 155meV and photon-mode detuning of 60meV were calculated via the TMM.
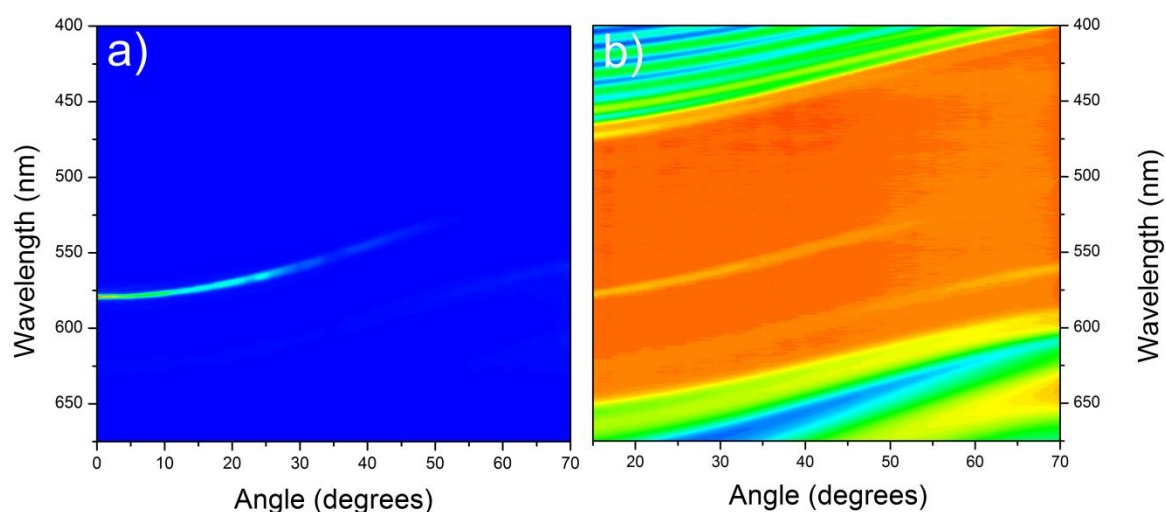
7.3.2. LFO

Figure 7.14. *Angular dependent **(a)** photoluminescence and **(b)** reflectivity measurements of a DBR-DBR microcavity containing LFO doped into a polystyrene matrix at a concentration of 2.5% by mass. The microcavity shown here has Rabi splitting of ~45meV and a negative photon mode detuning of 210meV as calculated using the transfer matrix method.*

The lowest concentration of LFO dye that would undergo strong coupling was 1% though the visibility of modes at this concentration was very small. **Figure 7.14** depicts photoluminescence and reflectivity measurements made upon a microcavity containing LFO at a concentration of 2.5% dye by mass. At higher concentrations, the dips in reflectivity measurements become more pronounced and the middle polariton branch becomes visible between the (0-0) and (0-1) vibronic modes. The small quantity of dye within the cavity in conjunction with the high reflectivity of the dielectric mirrors, significantly reduce the visibility of the upper polariton branch.

7.3.3. Meso-TFBOD and meso-QFBOD

Figure 7.15. Angular dependent (a) photoluminescence and (b) reflectivity measurements of a DBR-DBR microcavity containing meso-TFBOD doped into a polystyrene matrix at a concentration of 10% by mass. Angular dependent (c) photoluminescence and (d) reflectivity measurements of a DBR-DBR microcavity containing meso-QFBOD doped into a polystyrene matrix at a concentration of 10% by mass.

Unfortunately, the addition of oligofluorene sidechains to the BODIPY molecule meant that there were significantly fewer chromophores per unit mass of dye. This reduced the total number of interacting particles within the cavity so the Rabi splitting was not large enough to overcome the linewidths of the cavity modes. **Figure 7.15** shows data recorded for cavities containing dye a concentration of 10% by mass. Despite the broadening of the features observed in both **Figure 7.15 (b)** and **(d)** as the reflectivity dip approaches the exciton energy, the system cannot be definitively said to be in the strong coupling regime.
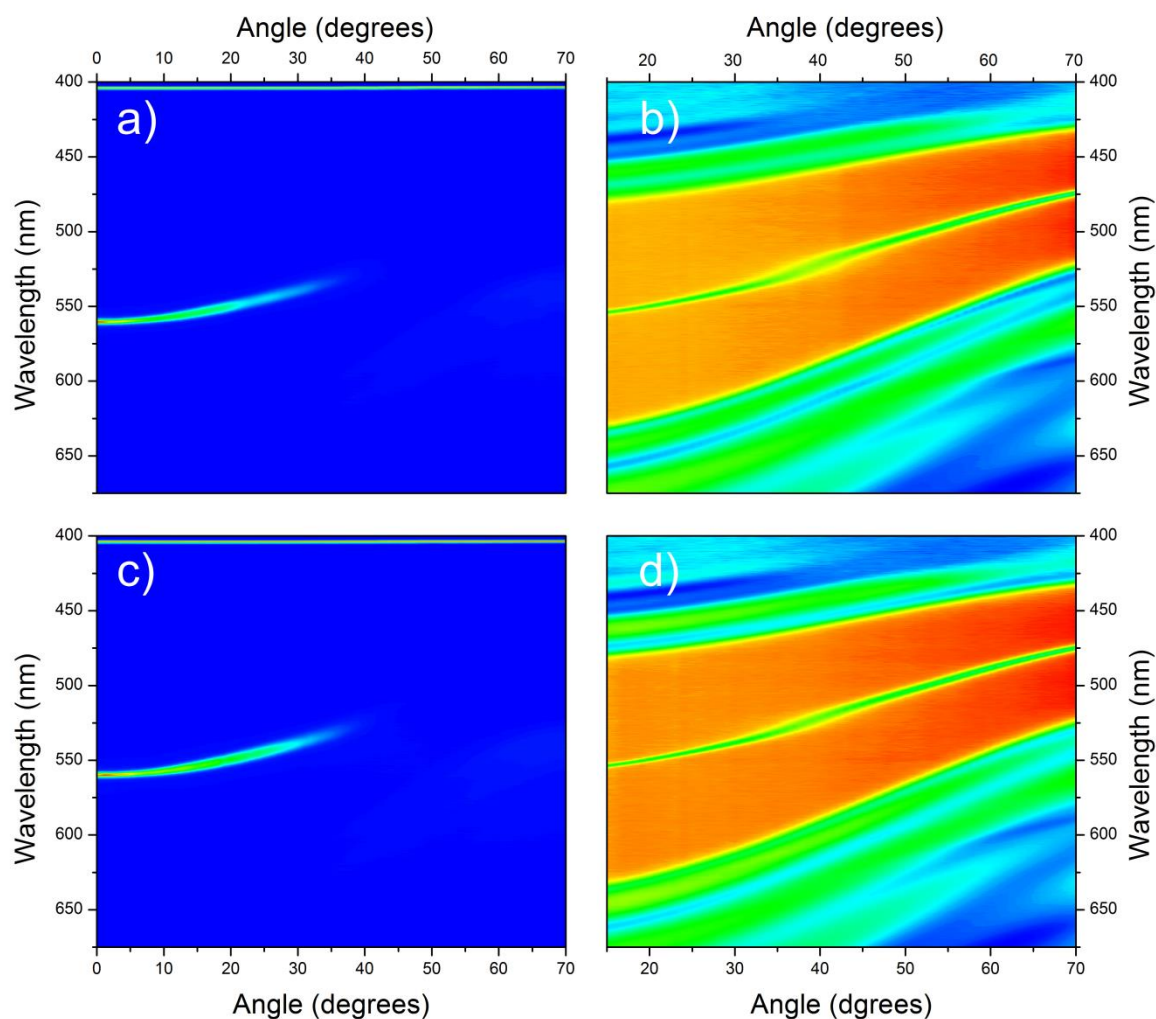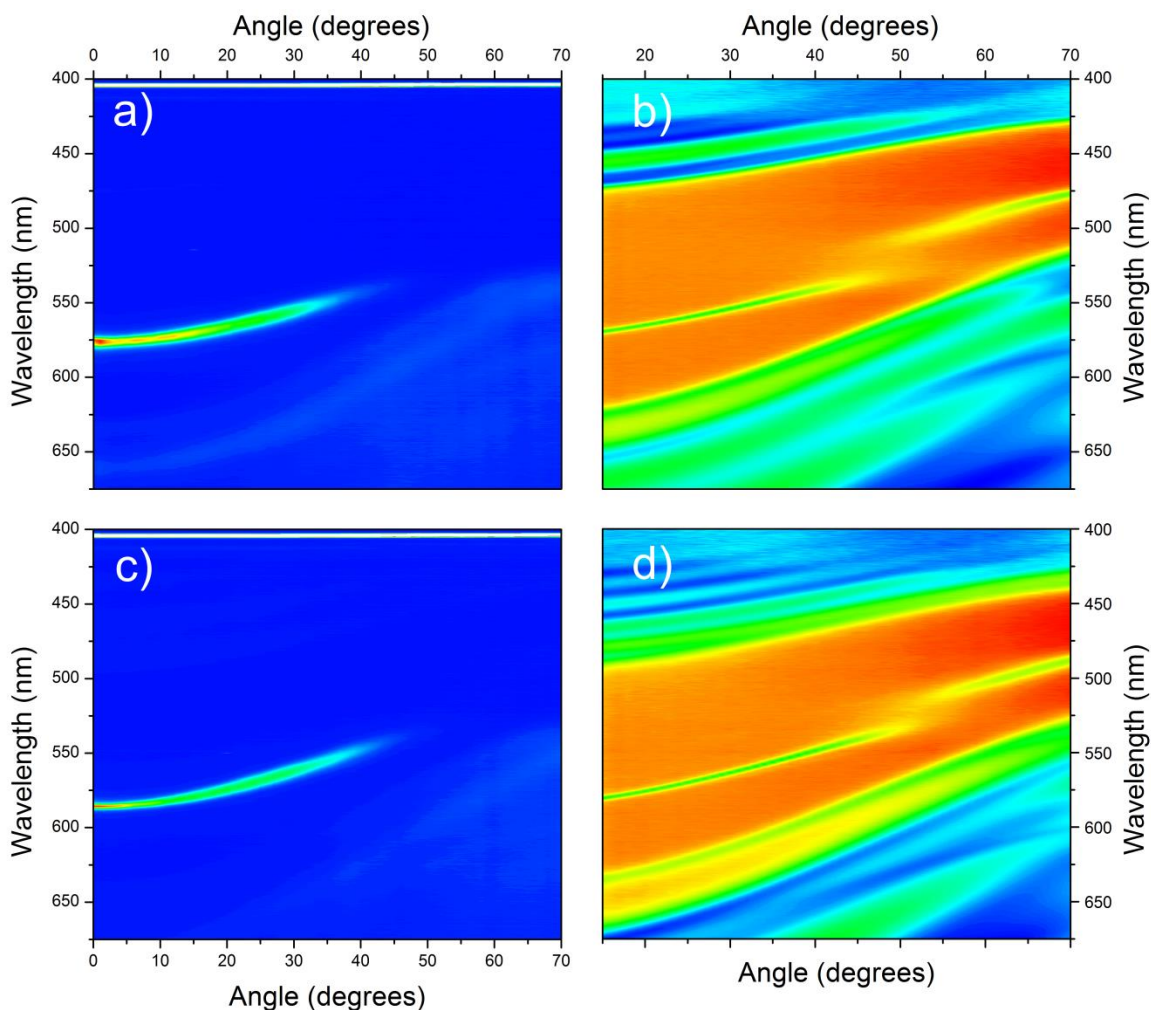
Figure 7.16. *Angular dependent **(a)** photoluminescence and **(b)** reflectivity measurements of a DBR-DBR microcavity containing meso-TFBOD doped into a polystyrene matrix at a concentration of 50% by mass. Angular dependent **(c)** photoluminescence and **(d)** reflectivity measurements of a DBR-DBR microcavity containing meso-QFBOD doped into a polystyrene matrix at a concentration of 50% by mass.*

To demonstrate that both dyes were capable of strongly coupling, a second set of cavities containing dye at a concentration of 50% by mass were fabricated (**Figure 7.16**). Both meso-TFBOD and meso-QFBOD were found to strongly couple with Rabi splittings of 110 and 64 meV respectively. PL Linewidths of 10 and 6.7 meV (for meso –TFBOD and –QFBOD respectively) were measured at normal incidence which increased in width at higher angles as they approached the exciton energy. At resonance, reflectivity linewidths of 68 and 60 meV were measured for meso -TFBOD and -QFBOD respectively. As Rabi splitting scales with the square root of the number of interacting particles, we calculate that the lowest concentration of dye required to enter the strong coupling for a microcavity of equivalent dimensions to be 16% for meso-TFBOD and 45% for meso-QFBOD.

7.4. Polariton Lasing

After the demonstration of both ASE and strong coupling in all dyes, cavities were tested to see if lasing could be observed from the lower polariton branch. Cavities were pumped at 400nm from an angle of 30°. Emission from the LPB was collected at normal incidence in a reflective geometry. Despite having shown that a 500nm pump source produced lower ASE thresholds in **Figure 7.10**, a 400nm source was chosen for the excitation of cavities to minimise losses caused by reflection from the DBR stopband. Whilst none of the DBR-metal cavities exhibited lasing, a few of the DBR-DBR cavities containing BODIPY-Br at concentrations of 5% and 10% dye did. **Figure 7.17** plots the spectral characteristics of one such cavity above and below threshold.
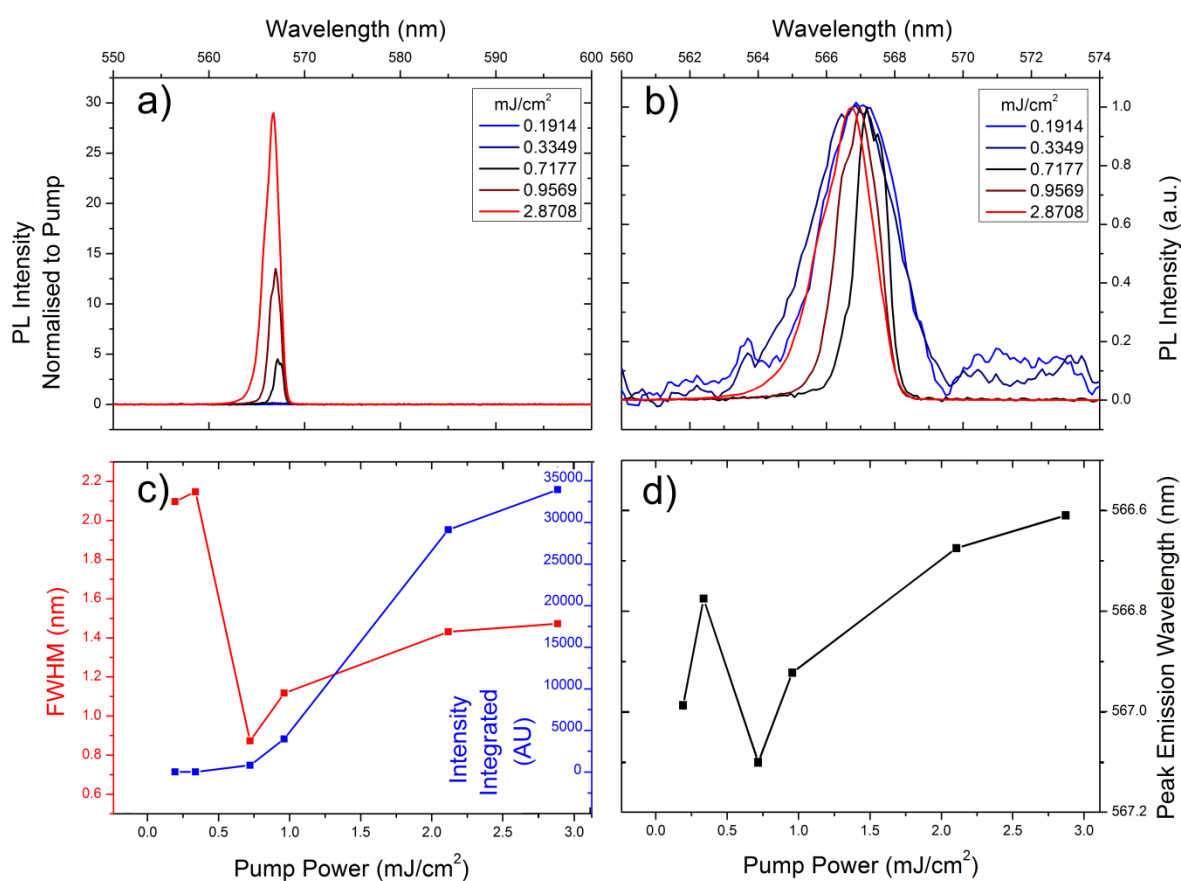
Figure 7.17. (a) *Integrated cavity emission intensity corrected for pump power. **(b)** Integrated cavity emission normalised to peak emission intensity to demonstrate narrowing of features at higher pump powers above threshold. **(c)** Integrated emission intensity (blue) and FWHM of said emission (red) as a function of pump power for a DBR-DBR microcavity containing a BODIPY-Br-doped PS film at a concentration of 10% dye by mass. **(d)** Peak emission wavelength as a function of pump power.*

A threshold of ~150nJ was observed when pumping with a spot size diameter of 0.0209mm^2 (or 2.09x10^{-4} cm^2, this corresponded to a power density of 0.7212mJ/cm^2. This was considerably lower threshold value than the ASE threshold observed in control films: 390nJ (17.14mJ/cm^2) or 500nJ (219.8mJ/cm^2) for films thicknesses of 300nm and 200nm respectively when pumping with a 400 nm source. Despite correcting for the disparity in excitation areas, it remains hard to directly compare the two, as a significant portion of the light incident upon the cavity is reflected by the DBR (~30% of 400nm light at 30°, further lowering threshold power to 0.505mJ/cm^2), and the active layer has a thickness of 150nm which would suggest an even higher ASE threshold. Upon crossing the lasing threshold, peak PL blue-shifted from 567.1nm to by ~ΔE=1.9meV to 566.6nm, and the FWHM of emission fell from 2.1nm to 0.8nm. This is 80meV greater in energy than the ASE wavelength (588nm) measured for a 10% film of BODIPY-Br using a 400nm pump, and approximately 15 times narrower (ASE FWHM = 12.48nm = 45meV); thus it is clear that the system is undergoing a non-linear transition, lasing emission.

Though it is clear that the cavity operates in the strong coupling regime and that it is lasing, some questions remain as to whether this lasing is polaritonic or photonic in nature. Variations in pump power were achieved by placing a series of neutral density filters in the beam path; unfortunately as only six pump powers were measured, two below, one at, and three above threshold, it is difficult to draw any concrete conclusions without combining data-sets from different spots. The point measured at 600nJ which deviates from the linear above threshold behaviour, could either be caused by bleaching of the dye or the beginnings of an S-type curve which has been observed in other systems[8]. This result is however thought to be genuine as a more comprehensive series of measurements have been performed upon otherwise identical cavities containing equal quantities of BODIPY-Br dye by a colleague of the author (Kyriacos Georgiou). Had the measurements continued to higher powers, it may have been possible to see two S-curves in the power-dependent measurements: one corresponding to a polaritonic lasing threshold, and a secondary (higher energy) transition corresponding to a stimulated emission (photonic) threshold[9] once population inversion had been achieved; an example of which is shown in **Figure 7.19**.

Several cavities containing lower concentrations of BODIPY Br (5%) also exhibited lasing in a transmission geometry (excitation continued to occur at an angle of 30°). **Figure 7.18** displays one such cavity below, at, and above threshold demonstrating narrowing of linewidths, increased emission from the cavity, and a blue shift of features, albeit to a lesser extent than the 10% cavity. Here variations in excitation power were achieved by using a motorized filter wheel to provide a constant increase in pump power in regular increments. The onset of non-linear behaviour occurred at a threshold of 650nJ (3.11mJ/cm^2, or 2.18mJ/cm^2 accounting for the 30% reflectivity of the dielectric mirror), approximately four times greater than that displayed in **Figure 7.17**.Upon reaching the polariton lasing threshold, the emission linewidth decreased from 6nm (23meV) to 2nm (8meV), peak emission blue-shifted from 562nm to 560.4nm (ΔE = 6meV), and the intensity of cavity light output increased markedly. At high enough pump powers (>800nJ) the sample begins to degrade, and the intensity of cavity emission falls; despite this linewidths remain narrow.
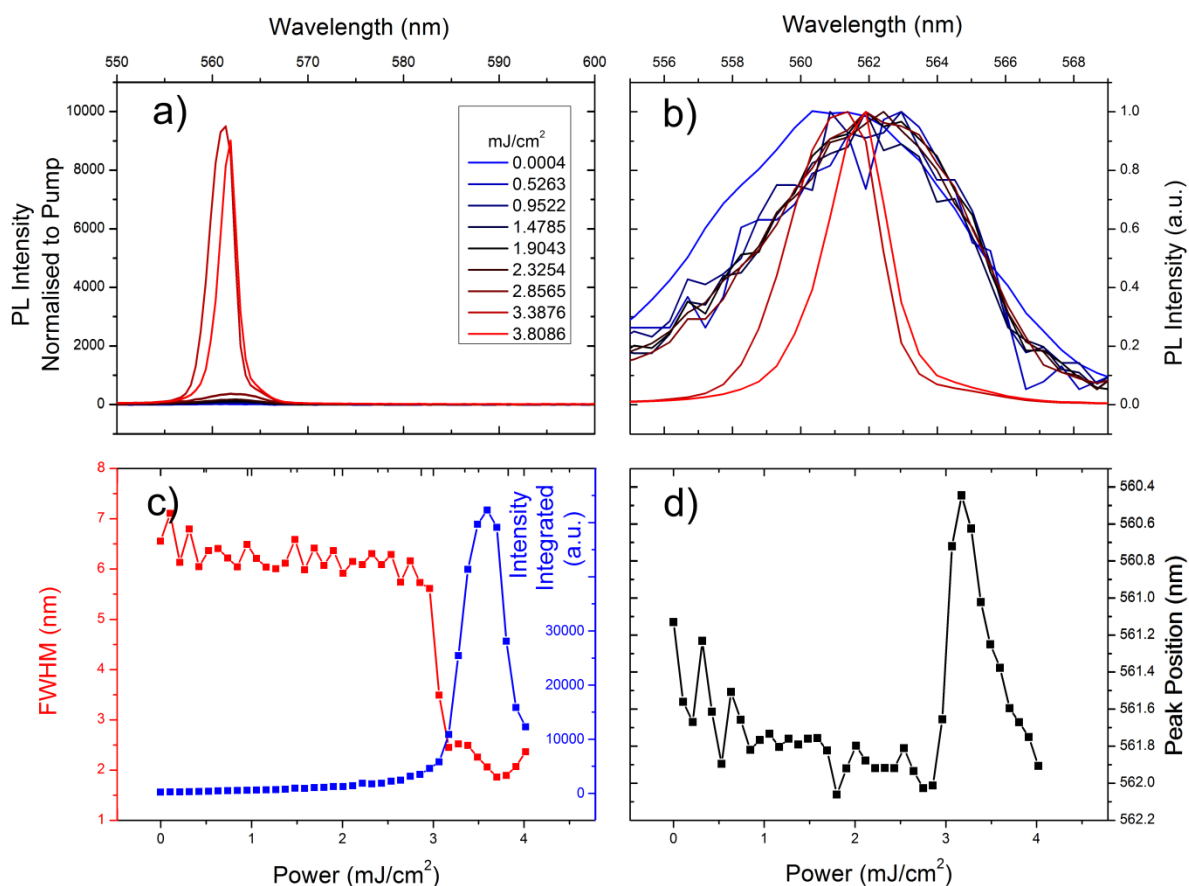
Figure 7.18. (a) *Integrated cavity emission intensity corrected for pump power.* ***(b)*** *Integrated cavity emission normalised to peak emission intensity to demonstrate narrowing of features at higher pump powers above threshold.* ***(c)*** *Integrated emission intensity (blue) and FWHM of said emission (red) as a function of pump power for a DBR-DBR microcavity containing a BODIPY-Br-doped PS film at a concentration of 5% dye by mass.* ***(d)*** *Peak emission wavelength as a function of pump power.*

As stated previously, it is hard to state definitively the portion of light absorbed by the sample and thus the true polariton lasing threshold. By changing the wavelength of the excitation source in ASE measurements from 400nm to 500nm, thresholds could be lowered by greater than an order of magnitude (**Figure 7.10**). Though a 500nm excitation source could not be used for cavity measurements in the experiment's current form (DBR reflectivity exceeded 95% at an angle of 30°), the pump wavelength (or angle) could be varied in order to resonantly pump the upper polariton branch. While this may alter the excitation spot size (due to Lambertian solid angle considerations[10]), this may not significantly alter the threshold power or cavity emission output. This is because polariton states in the LPB of microcavities containing BODIPY-Br (particularly at low concentrations) are predominantly populated by radiative means rather than scattering (**Chapter 6**).
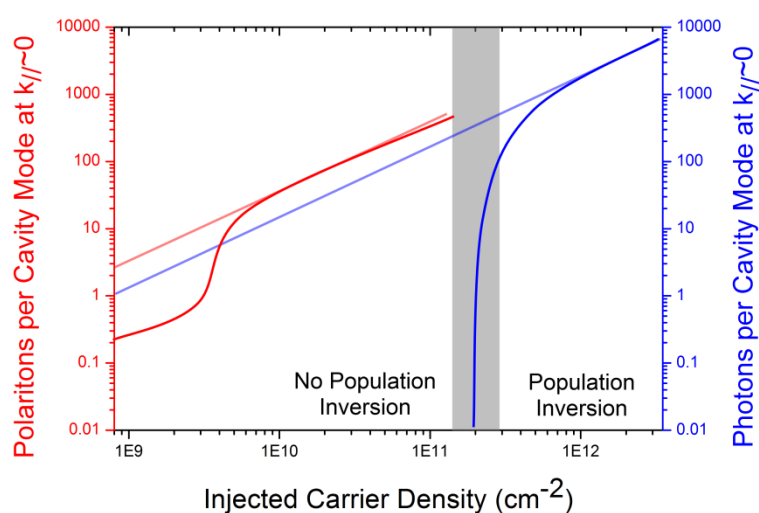
Figure 7.19. *The population of states within a cavity as a function of pump power or injected carrier density. At low pump powers, the majority of atoms/molecules are in the ground state and polariton (red) lasing can be observed above a certain threshold. At higher excitation powers, the majority of the atoms/molecules are in excited states and a population inversion (grey box) is achieved. Once population inversion has been achieved, stimulated emission of photons (blue) can be achieved. From such an experiment, the threshold excitation powers for both polaritonic and photonic emission can be measured.*

Polaritonic lasing has previously been observed in other organic semiconductor systems by other research groups who report varying degrees of blue-shift in emission, ranging from <1meV in crystalline anthracene[11], to ~10meV in amorphous ladder polymers(MeLPP)[12]. There remains considerable debate in the field as to what constitutes a polariton laser or Bose-Einstein condensate; in any case, if this system did undergo condensation, it would be a non-equilibrium BEC. If certain properties of the system such as the exciton binding energy, Bohr radius, and number of (participating) excitons within the mode volume are known, the expected degree of blue shift can be calculated[13]. This can be compared to the observed blue-shift to provide quantitative information about the nature of non-linear emission that was observed. Unfortunately without making a large number of assumptions, such calculations are beyond the scope of this thesis.

7.5. Conclusions

To conclude, we investigated the optical properties of four fluorescent molecular dyes. Above a certain dye concentration, all four dyes exhibited both amplified spontaneous emission in control films and underwent strong coupling when confined within a microcavity. Only one dye however, BODIPY-Br, also showed lasing from the lower polariton branch at 10% and 5% concentrations of dye by mass. Though the cavity was been verified to be in the strong coupling regime through angular dependent white light reflectivity measurements, there is some question as to nature of the non-linear emission observed. This is because emission was only collected at normal incidence (k=0) and dispersion of the entirety of the LPB could not be observed. A tentative argument may however be made for polaritonic lasing as the blue-shift of emission observed above threshold pump powers is characteristic of polaritonic lasing, and not predicted for stimulated-emission. The magnitude of this blue-shift is proportional to (amongst other things) the number of participating excitons within the cavity[13], as such we would expect smaller blue-shifts than those observed in single material, monolithic cavities.

If experiments were to be repeated, Fourier-space measurements over a wider range of powers using smaller increments would be made to observe the collapse (if any), or redistribution, of the LPB dispersion as a function of pump power. Interferometry measurements would also be employed to see if any coherence effects or long range order were present. In addition, a polarization dependent series of measurements could be made upon the LPB. By changing the

orientation of the polarizer in the collection path, two distinct species should exist which exhibit different behaviour upon reaching lasing threshold. In one polarization, super-linear threshold behaviour should be observed as all laser light will be in line with coherence. In a second polarization, orthogonal to the previous orientation, emission (if any) will increase linearly with pump power. Whilst this alone may not distinguish between stimulated emission and polaritonic lasing, it will reveal whether or not this is simply an enhancement of spontaneous emission. As ASE in control films occurred at significantly different wavelengths to the observed non-linear behaviour from the LPB, spontaneous emission is not thought to be likely. Time-resolved Fourier-space images are being planned by a colleague of the author (Kyriacos Georgiou) in collaboration with the University of Southampton to in order to view the collapse (if any) of the LPB dispersion.

Addendum: After the submission of this thesis, a more comprehensive series of experiments upon microcavities containing Bodipy-Br revealed that polariton condensation was occurring was performed in collaboration with the University of Southampton. A publication titled "*A yellow polariton condensate in a dye filled microcavity*" has been submitted to Advanced Optical Materials.

7.6. References

1. Ulrich, G., Ziessel, R. & Harriman, A. The chemistry of fluorescent bodipy dyes: versatility unsurpassed. *Angew. Chem. Int. Ed. Engl.* **47,** 1184–201 (2008).

2. Ariano, M. A. *et al.* Direct visualization and cellular localization of D1 and D2 dopamine receptors in rat forebrain by use of fluorescent ligands. in *Proc. Natl. Acad. Sci. U. S. A.* **86,** 8570–8574 (1989).

3. Shah, M., Thangaraj, K., Soong, M.-L., Wolford, L. T. & Boyer, J. H. Pyrromethene-BF2 Complexes as Laser Dyes: 1. *Heteroat. Chem.* **1,** 389–399 (1990).

4. Vu, T. T. *et al.* Understanding the Spectroscopic Properties and Aggregation Process of a New Emitting Boron Dipyrromethene (BODIPY). *J. Phys. Chem.* **117,** 5373–5385 (2013).

5. Choi, S., Bouffard, J. & Kim, Y. Aggregation-induced emission enhancement of a meso-trifluoromethyl BODIPY via J-aggregation. *Chem. Sci.* **5,** 751 (2014).

6. Mikhalyov, I., Gretskaya, N., Bergström, F. & Johansson, L. B.-A. Electronic ground and excited state properties of dipyrrometheneboron difluoride (BODIPY): Dimers with application to biosciences. *Phys. Chem. Chem. Phys.* **4,** 5663–5670 (2002).

7. Findlay, N. J. *et al.* Linear oligofluorene-BODIPY structures for fluorescence applications. *J. Mater. Chem. C* **1,** 2249 (2013).

8. Deng, H., Weihs, G., Snoke, D., Bloch, J. & Yamamoto, Y. Polariton lasing vs. photon lasing in a semiconductor microcavity. *Proc. Natl. Acad. Sci. U. S. A.* **100,** 15318–23 (2003).

9. La Rocca, G. C. Organic photonics: Polariton lasing. *Nat. Photonics* **4,** 343–345 (2010).

10. Lambert, J. *Photometria*. *Astron. Nachrichten* (1760). doi:10.1002/asna.19182071002

11. Kena-Cohen, S. & Forrest, S. R. Room-temperature polariton lasing in an organic single-crystal microcavity. *Nat. Photonics* **08,** 1–5 (2010).

12. Plumhof, J. D., Stöferle, T., Mai, L., Scherf, U. & Mahrt, R. F. Room-temperature Bose – Einstein condensation of cavity exciton – polaritons in a polymer. *Nat. Mater.* **13,** 1–6 (2013).

13. Christopoulos, S. *et al.* Room-Temperature Polariton Lasing in Semiconductor Microcavities. *Phys. Rev. Lett.* **98,** 126405 (2007).

8.

Strong-Coupling in Biological Systems

The first part of this chapter describes a series of microcavities containing a component of the light-harvesting complexes, chlorosomes, of the green sulphur bacteria *Chlorobaculum tepidum*. In these cavities we report the first demonstration of strong-coupling in a biological system[1]. Though other pigments which may have originated in cellular organisms have been shown to strongly couple[2], the electronic structure of an isolated pigment is not representative of the energy of biological structures as a whole. Chlorosomes possess molecular excitons with significantly different energies from those of the single-pigment excited states and are not confined to the energy of an individual component of the complex.

The second part of this chapter describes microcavities containing carotenoids, a class of materials widely considered to be non-emissive as electronic transitions between the ground and first excited states are symmetry forbidden. By coupling to the second excited state, we hoped to achieve sufficiently large Rabi splitting to place the lower polariton branch below that of the first excited state. This would mean that radiative decay to the ground state would be allowed, and fluorescence could be induced through purely optical means. Here we describe preliminary efforts to produce such a microcavity as a proof of concept, and simulations of other cavities in order to estimate the conditions required to achieve this phenomena in a range of other materials. The work in this chapter would not have been possible without the assistance of David Coles, Thomas Sydney and Rahul Jayaprakash.

8.1. Chlorobaculum tepidum

The green sulphur bacteria *Chlorobaculum tepidum* was first discovered in the late 1980s by R.W. Castenholz in microbial mats located in highly sulfidic and acidic hot springs in New Zealand[3]. *C. tepidum* grow anaerobically in the photic zone of sulphur-rich bodies of water. The photic zone is defined as the depth at which incident light falls to one percent of its intensity at the surface and can range from a depth of only a few centimetres in highly turbid eutrophic lakes to around 200 metres in the open ocean. As photosynthetic organisms, *C. tepidum* have evolved extremely efficient light-harvesting complexes (**LHC**s) in order to make the most of the low light conditions they live in, some sources suggest they may only receive a few hundred photons per second per bacterium[1]. An image of a cell and its contents are shown in **Figure 8.1**.
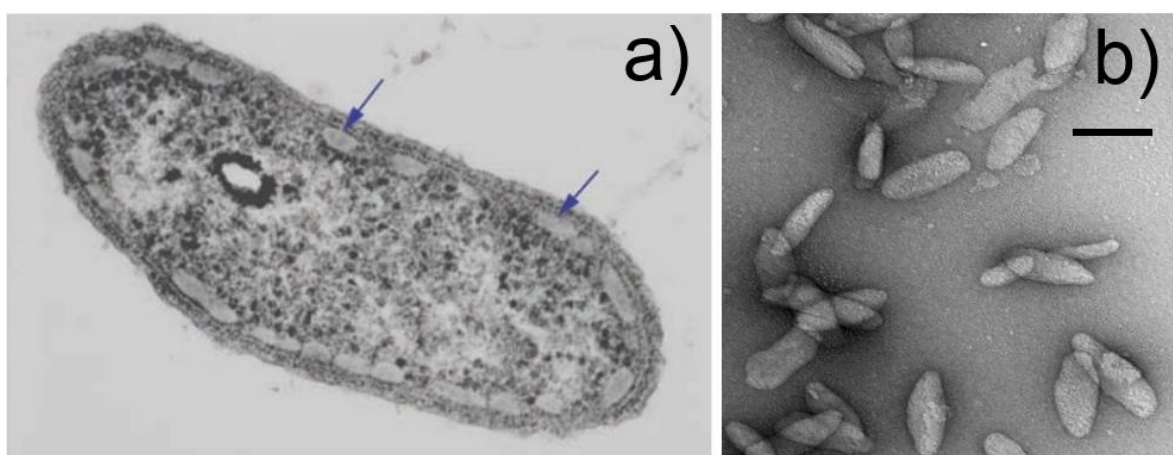

Figure 8.1. (a) *Thin cross-section of a cell of C. tepidum strain TLS (courtesy of Wahlund et al. 1991[4]), arrows demote chlorosomes located in the periphery of the cell.* ***(b)*** *Transmission electron microscope image of the chlorosome; the scale bar represents 100nm.*

In nature it can be difficult to find the correct conditions in which *C. tepidum* can flourish: There must be sufficiently high levels of sulphide present (milimolar concentrations) in order to prevent growth of competing cyanobacteria and the medium must be sufficiently acidic to prevent growth of purple bacteria (as low as pH4). In a controlled lab environment however *C. tepidum* does not need to directly compete with other organisms and can be grown with a pH of 6.8 at 48°C. [5]

The primary optical antenna structures in *C. tepidum* (and green sulphur bacteria in general) are chlorosomes. They differ from the antenna complexes used in other photosynthetic organisms in both size and their lack of protein matrix used to bind them in place[6]. The organelles take the shape of oblate spheroids ~100-200nm in length, 30-70nm in width and 30-40nm in depth. An individual chlorosome is comprised of up to 250,000 bacteriochlorophyll c/d/e (**BChl** c/d/e) molecules that self-assemble to form two dimensional lamellae structures which roll to take a tubular shape. These large aggregates are enclosed within a protein-lipid monolayer. Chlorosomes produced by *C. tepidum* differ from those in other bacteria in that their protein content is an order of magnitude lower than other bacteria[7,8] and does not act as a scaffold. This is important as it means that both the function and structure of chlorosomes is determined not by pigment-protein interactions, but by pigment-pigment interactions. The differences between BChl c/d/e can be found in **Table 8.1**, and the structure of a LHC is shown in **Figure 8.2**.
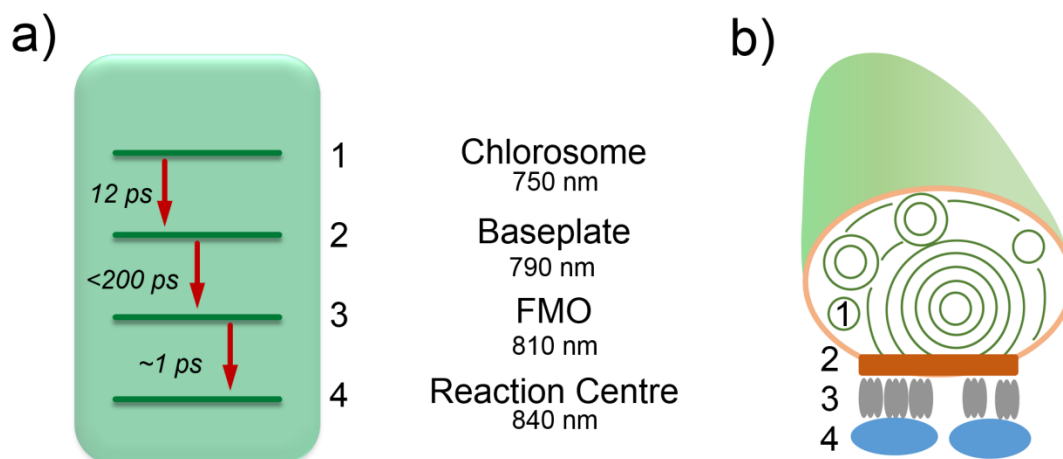

Figure 8.2. (a) *Structure of a single LHC.* **(b)** *The timescales for energy to transfer from the excited state of one component to another and their corresponding wavelengths. Note that the chlorosome aggregates are primarily composed of BChl c. Often the FMO acts as a rate limiting step to stop the system being saturated.*

When the LHC absorbs a photon, a molecular exciton is formed. In order for this energy to be put to use by the cell, the exciton must make its way to the lowest energy state, the reaction centre, where it is used to produce various chemical compounds that the cell requires. The keys to efficient light harvesting (and photosynthesis) are strong absorption features and fast energy relaxation. This occurs in several distinct steps each with a different associated timescale. It is important that the transfer rates for each of these steps are significantly faster than the excited state lifetime of each isolated component; this minimises the chances of photon reemission and non-radiative recombination. Firstly the molecular exciton present in the chlorosomes is transferred to the baseplate, a process that takes <12 ps[9]. Next the exciton is transferred to the Fenna-Matthews-Olson (**FMO**) complex in <200 ps[7]; the FMO complex is a trimeric protein complex containing BChl a which exists purely to facilitate energy transfer to the reaction centre. Finally a rapid transfer from the FMO complex to the reaction centre occurs within approximately 1 ps[10].

Pigment	Absorption Maximum Wavelength
Bacteriochlorophyll a	805, 830-890 nm
Bacteriochlorophyll b	835-850, 1020-1040 nm
Bacteriochlorophyll c	745-755 nm
Bacteriochlorophyll d	705-740 nm
Bacteriochlorophyll e	719-726 nm

Table 8.1. *Peak bacteriochlorophyll absorption features found in green sulphur bacteria. Types c, d, and e are chlorins and possess 20 π-bond electrons; types a and b are bacteriochlorins and possess 18 π-bond electrons. Bacteriochlorophyll b is included for the sake of completeness and is found primarily in purple bacteria.[11,12]*
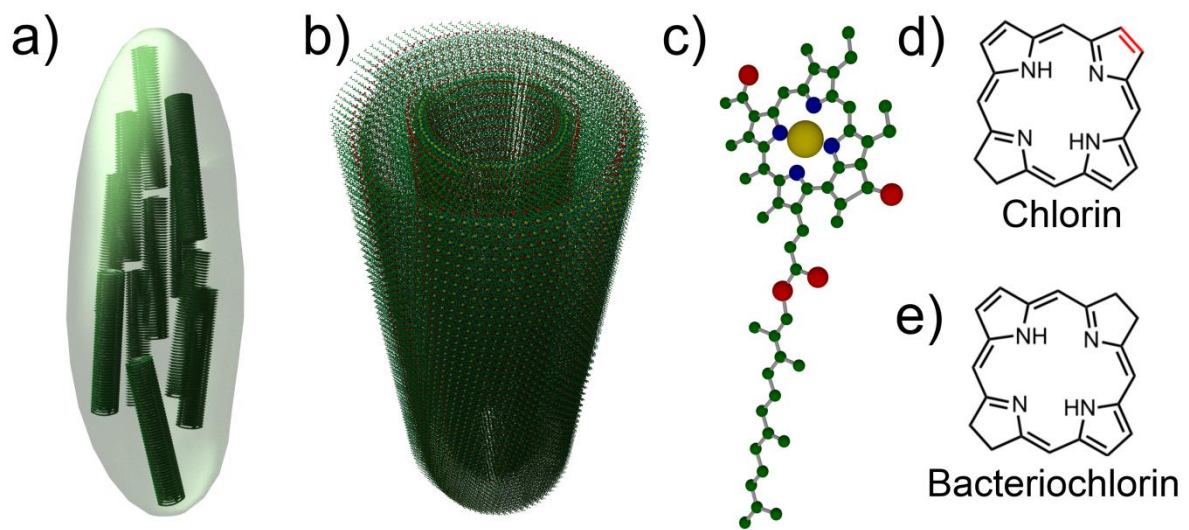
Figure 8.3. (a) Structure of a chlorosome composed of many *(b)* lamellar aggregates of *(c)* Bacteriochlorophyll. *(d)* and *(e)* Structural differences between the chromophores in different BChl variations, the absorption band of bacteriochlorins typically occurs at longer wavelengths. Types c, d, and e are chlorins and possess 20 π-bond electrons, these are the primary components of chlorosomes. Types a and b are bacteriochlorins and possess 18 π-bond electrons; the FMO complex is primarily composed of BChl a.

From a biological perspective, the fact that cells can double their number in a 2-hour period under optimal conditions[4], a rate far faster than any other species of mesophilic green sulphur bacteria, made it a simple task to grow sufficient quantities. From a polaritonics perspective, the high absorption coefficient (and relatively narrow absorption linewidth) of the chlorosome made *C. tepidum* a promising candidate for strong-coupling. In this chapter we describe our successful attempts to create the first reported strongly-coupled biological system, the modification of exciton energy transfer timescales within said system, and the potential to create "living polariton" systems.

8.2. Chlorosome Cultivation, Extraction and Sample Preparation

Cell growth media was made up as described by **Table 8.2**, before being autoclaved and cooled under a N_2/CO_2 atmosphere (at a ratio of 9:1) before the addition of the stock solution described in **Table 8.3**; the final pH of the medium was then adjusted to 6.7-6.8. After this *C. tepidum* cells were incubated anaerobically at a temperature of 45° under low level illumination of (20 ± 2µmol^{-2}s^{-1}). The culture was periodically replenished with sterile neutralised sulphide solution to ensure that cell growth continued; care was taken to ensure oxygen did not pervade through the system poisoning the cells.

Medium Additive	Freshwater Strain	Marine Strain
KH_2PO_4	0.3 g	0.3 g
NHCl	0.34 g	0.34 g
KCl	0.34 g	0.34 g
$CaCl_2 \cdot 2H_2O$	0.15 g	0.15 g
NaCl	-	20.0 g
$MgSO_4 \cdot 7H_2O$	0.5 g	3.0 g

Table 8.2. *The defined medium composition for one litre of fresh, or salt water used to culture green sulphur bacteria[13].*

Stock Solution	Volume Added per Litre of Medium
10% (w/w) $NaHCO_3$, saturated with CO_2	15 ml
1 M $Na_2S \cdot 9H_2O$ (autoclaved under N_2)	2.5 ml
2 mg of vitamin B_{12} in 100 ml H_2O	1 ml
Trace element solution SL 10*	1 ml

Table 8.3. *Stock solution added after autoclaving. *Trace element solution SL 10 contains per litre of distilled water: 25% HCl, 10 ml; FeSO4 · 7H2O, 2.0g; CoCl2 · 6H2O, 190 mg; MnCl2 · 4H2O, 100 mg; ZnCl2, 70 mg; Na2MoO4 · 2H2O, 36 mg; NiCl2 · 6H2O, 24 mg; H3BO3, 6 mg; and CuCl2 · 2H2O, 2 mg. The FeSO4 is dissolved in HCl, and distilled water is then added, followed by the other components.[13]*

After the bacterial cells had grown to a sufficient density, a portion of the culture was separated for extraction and the missing volume was replaced with an equal quantity of media. Chlorosomes were extracted from the membrane fraction with the addition of 2 M NaI. Following this a sucrose gradient separation (using an ultracentrifuge operating at 135,000 x g for 16h) was used to isolate the chlorosomes from other cell waste products. The resulting extract was then desalted and lyophilized (freeze-dried).

Once extracted from their host cells, chlorosomes were dispersed in a PVA matrix (m_w = 31K-50K, 87-89% hydrolysed, Sigma Aldrich) at a concentration of 25% by mass, and spin-coated upon fused-quartz substrates for optical and physical characterisation. The absorption (and hence extinction coefficient) of a film as a function of wavelength was measured through transmission measurements using the experimental set up described in **Chapter 5** and is shown in **Figure 8.4**. It can be seen that there is a strong absorption feature at 750nm corresponding to BChl c which chlorosomes are predominantly composed of.
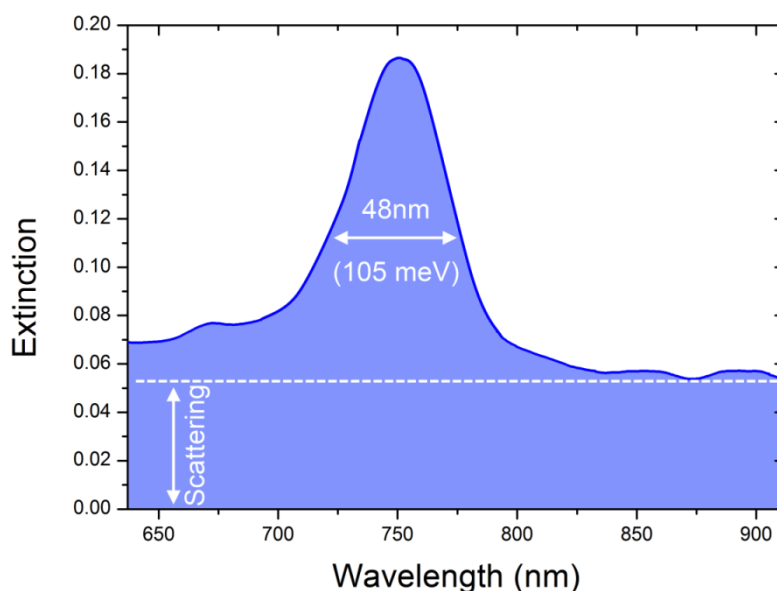

Figure 8.4. *Extinction coefficient (sum of scattering and absorption components) as a function of wavelength for a 205 nm thick film of chlorosomes dispersed into a PVA matrix at a concentration of 25% by mass. An absorption beak corresponding to that of chlorosomes can be seen at 750 nm above a wavelength-independent scattering contribution of ~0.06.*

AFM was used to study the morphology of this film at resolutions of 10 μm x 10 μm and 1 μm x 1 μm. Features ranging from 50-250nm, similar dimensions to those of chlorosomes, were observed. The root mean square surface roughness (**RMS-Sq**) of the film containing chlorosomes was ~10nm and the largest feature to protrude from the surface of the film had a height of 100nm. To confirm that these features did indeed corresponded to chlorosomes and were not caused by the PVA matrix wetting poorly to the surface, an otherwise identical PVA film was produced without chlorosomes and the AFM measurements were repeated. In contrast to the first film, the film containing no chlorosomes had a RMS roughness of only 1nm with no large features visible at all. AFM images of both films are shown in **Figure 8.5**. The high roughness of the chlorosome-doped PVA was significant as this meant that scattering losses in any microcavity containing such a film would be high; this would have a negative impact on the cavity Q-factor.
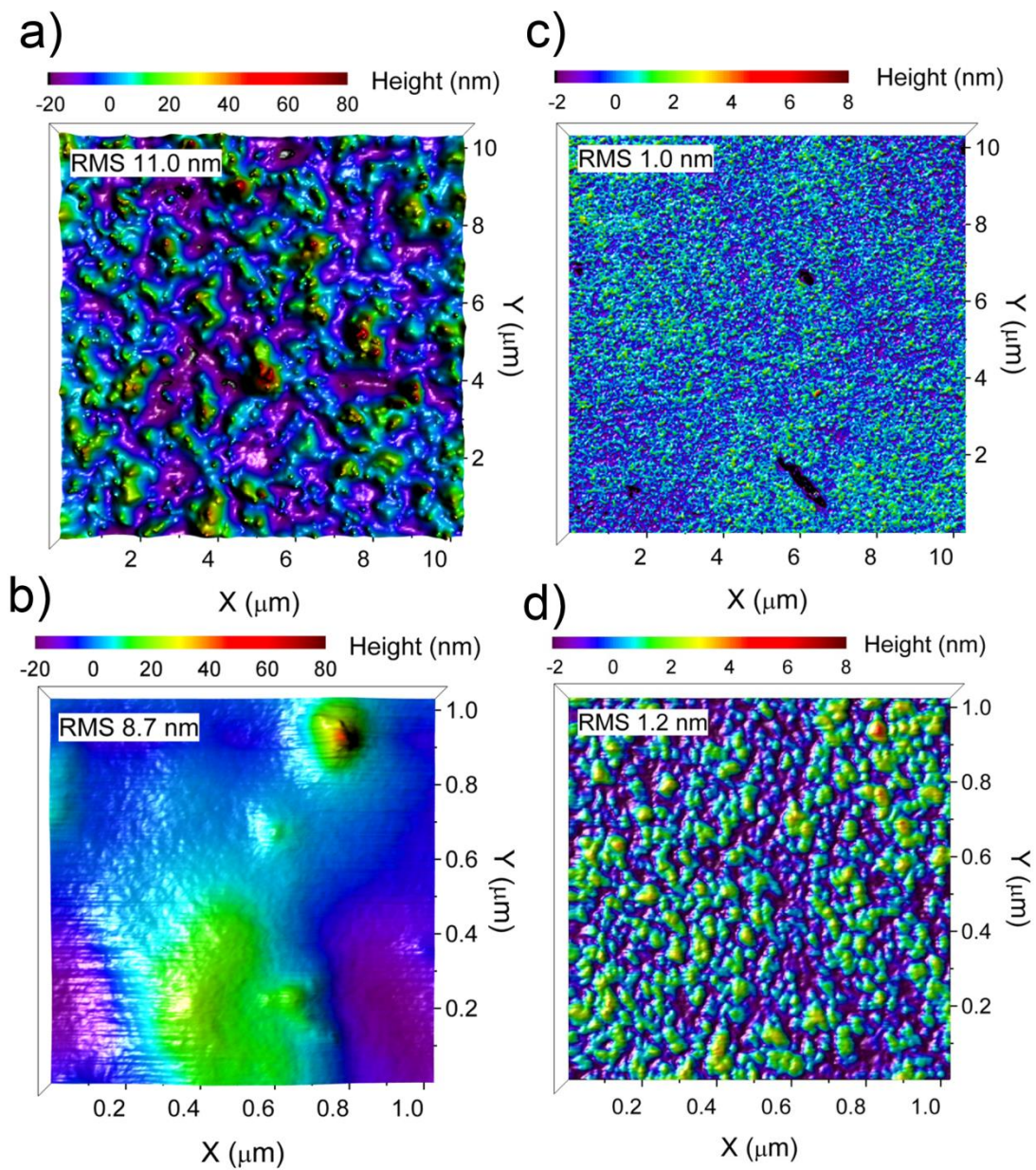
Figure 8.5. *Surface height contour maps produced by AFM of a PVA film containing chlorosomes at a concentration of 25% by mass at **(a)** 10 μm x 10 μm and **(b)** 1 μm x 1 μm resolution. For comparative purposes a PVA film of identical thickness without chlorosomes was also measured at **(c)** 10 μm x 10 μm and **(d)** 1 μm x 1 μm resolution.*

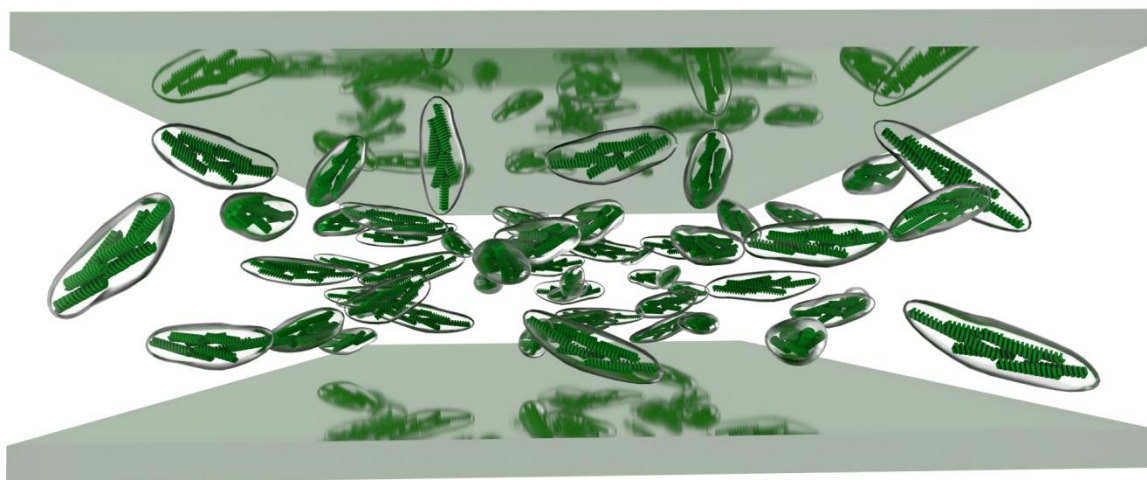## 8.3. Strong Coupling and Transfer Matrix Modelling

Figure 8.6. *A microcavity produced composed of two 40nm thick semi-transparent silver mirrors either side of a 205nm PVA film containing chlorosomes dispersed at a concentration of 25% by mass.*

Microcavities were produced by depositing a 40 nm thick thermally-evaporated silver mirror either side of a 205nm thick spin-coated film of chlorosome-doped PVA (at a 25% concentration by mass) on a fused-quartz substrate. A second, otherwise identical, microcavity was produced lacking chlorosomes was produced for comparative purposes. Both microcavities were measured using white-light reflectance and transmission spectroscopy as described in **Chapter 5**, and modelled using the transfer matrix method (**TMM**) described in **Chapter 3** and is shown in **Figure 8.6**. The measured absorption and transmission of this "blank" PVA microcavity are shown in **Figure 8.7**.
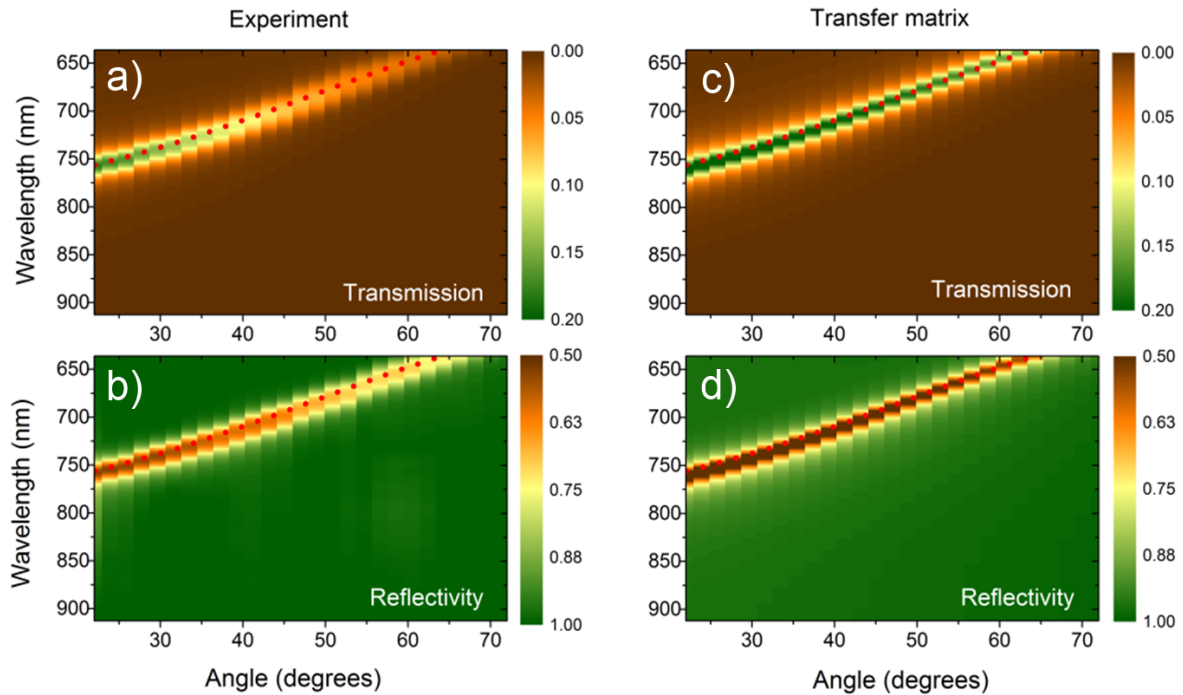
***Figure 8.7. (a)** & **(c)** Transmission and **(b)** & **(d)** Reflectivity measurements of a "blank" microcavity containing only a 205nm thick PVA layer as **(a)** & **(b)** measured experimentally and **(c)** & **(d)** modelled using the transfer matrix method.*

It can be seen in **Figure 8.7** that there is a single feature corresponding to the confined photon mode that starts at a wavelength of 760nm and increases in energy as a function of angle. From the measured linewidth of this feature (~20nm at an angle of 16 °) and by using **Equation 3.9**, we calculate a Q-factor of 40 which corresponds to a photon confinement time of 15 fs. The low roughness of the PVA films (~1nm RMS-Sq) means that scattering terms can be neglected from this model, and the confined photon mode can be accurately fitted using **Equation 3.8**. Using a constant refractive index of 1.53 for the PVA layer for the TMM we achieve good agreement between experimentally measured data and the TMM model in linewidth and visibility (depth/height of feature) of the photon mode. All measurements and modelling were done using the TE-polarisation of light.
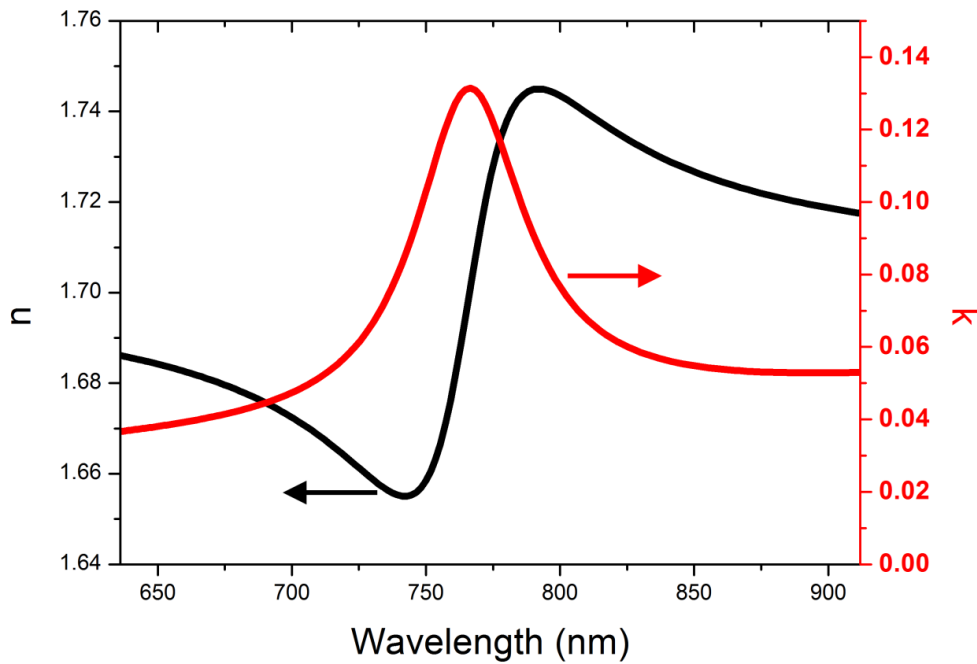
Figure 8.8. *The real (n) and imaginary (κ) components of the complex refractive index of a chlorosome-doped PVA film at a concentration of 25% by mass used for TMM modelling. κ accounts for both absorption and scattering contributions of the thin film.*

The PVA layer with constant refractive index and no scattering contributions previously used in the TMM model was replaced by the complex refractive index profile for a chlorosome-doped film as shown in **Figure 8.8**. The increased scattering caused by the high surface roughness is accounted for in the imaginary component of the refractive index by including an offset of ∼0.04 independent of wavelength. Reflection and transmission measurements were repeated under the same conditions used for the blank cavities; these are shown in **Figure 8.9**.
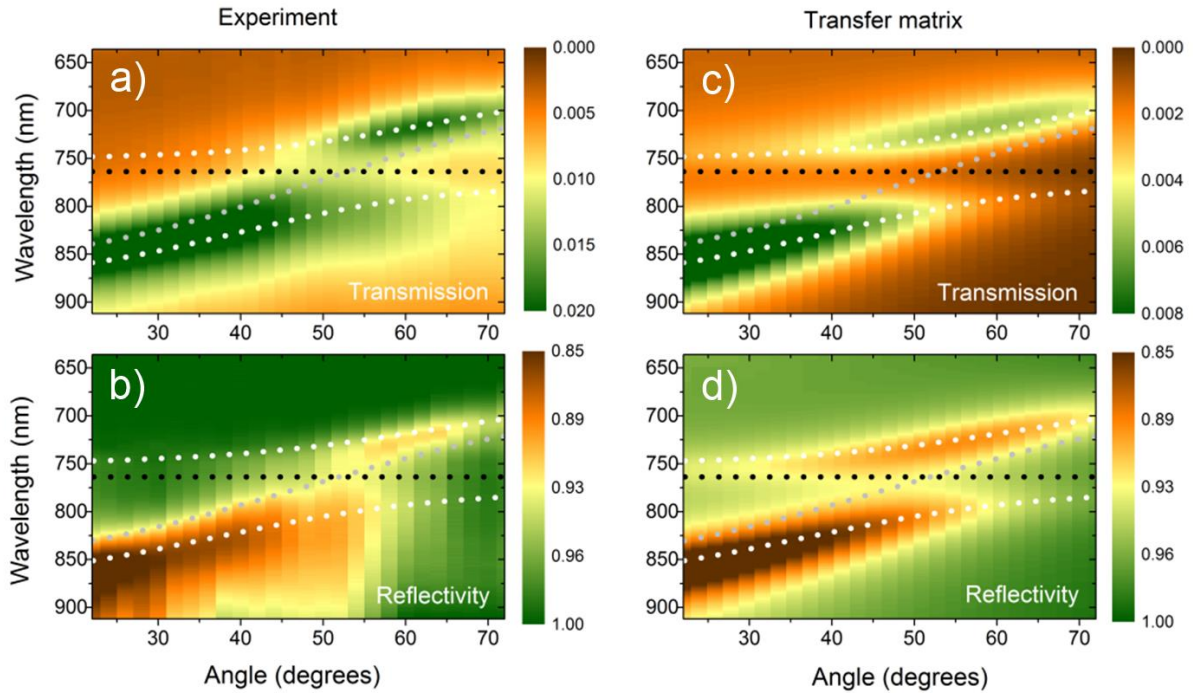
Figure 8.9. *(a) & (c) Transmission and (b) & (d) Reflectivity measurements of a microcavity containing a 205nm thick chlorosome-doped PVA layer (25% concentration by mass) as (a) & (b) measured experimentally and (c) & (d) modelled using the transfer matrix method. The wavelength corresponding to the energy of the molecular exciton is marked with a dotted black line, the confined photon mode is marked with a dotted grey line, and the polariton branch wavelengths as calculated using the TMM are marked with a dotted white line.*

Two distinct features corresponding to the UPB and LPB could be seen in both transmission and reflectivity measurements which exhibited the characteristic anti-crossing about the exciton energy indicative of strong-coupling. Due to the increased scattering caused by the large film roughness (~10 nm RMS-Sq), the linewidth of the LPB broadened to ~70 nm. This corresponds to a lower Q-factor of 12 and a threefold reduction of photon confinement time to 5fs compared to the "blank" cavity. It is worth noting that the photon-mode from the TMM fit has been shifted to longer wavelengths. This is caused by the addition of chlorosomes which have a higher refractive index than pure PVA, this changes the refractive index from 1.53 to ~1.7 and increases the effective cavity length.

Interestingly, it was found that the exciton energy E_X as calculated by the TMM fitting model was red-shifted ~12nm from that corresponding to BCHl c observed in a film chlorosomes outside of the cavity. Similar effects have been observed in strongly coupled microcavities containing J-

aggregates of cyanine dyes which exhibited a blue-shift of the exciton energy compared to that of its absorption peak in a control film[14,15]. Here this shift was attributed to the asymmetric shape of the absorption profile which meant that there was a small portion of the oscillator strength lying at shorter wavelengths than the central peak, causing it to shift slightly. We believe that a comparable phenomenon may be occurring in these microcavities and that there may be a residual component of oscillator strength at longer wavelengths that causes the exciton energy to red-shift.

At normal incidence, the photon mode is negatively detuned from the exciton mode by 164meV. At 54° the photon and exciton energies are resonant and the UPB and LPB are separated by 75nm which corresponds to a Rabi-splitting ($\hbar\Omega$) of 156meV. Using the coupled oscillator model[16] described in **Chapter 3** (**Equations 3.34** and **3.36**), the polariton branch energies as well as their the photonic and excitonic mixing coefficients can be calculated; these along with a transmission cross-section at 54° are shown in **Figure 8.10**.
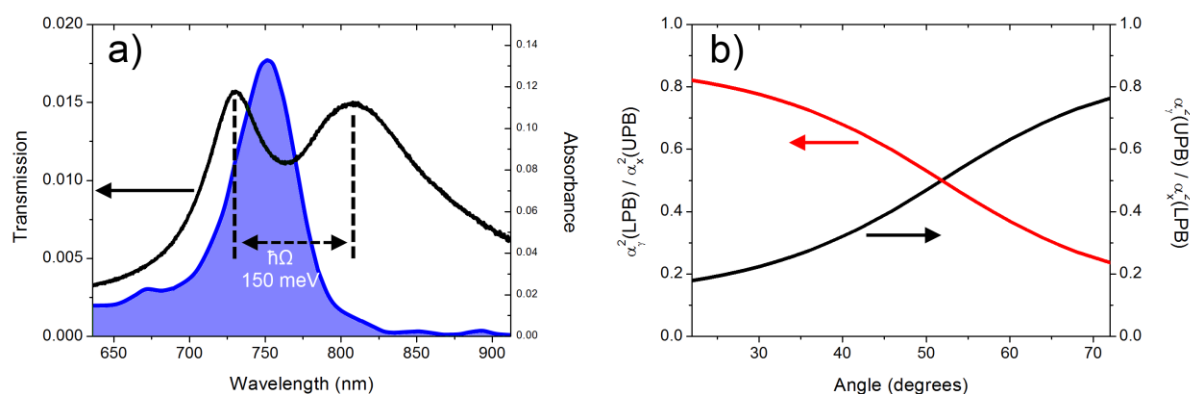

Figure 8.10. (a) *Transmission spectra of the strongly-coupled microcavity containing chlorosomes at an angle of 54°; this is superimposed over an absorption spectrum of a control film depicting the red-shift of the cavity exciton.* ***(b)*** *Photonic and excitonic fractions of the upper and lower polariton branches as a function of angle calculated using* ***Equation 3.42***.

Crucially, despite the line width broadening caused by inhomogeneous scattering[17], the Rabi splitting remains sufficiently large that the two peaks satisfy the Rayleigh criterion and can be individually resolved. The broad nature of the cavity mode linewidth is not as problematic as it might seem as the coupling strength is increased when the linewidths of the photon and exciton modes are of comparable magnitudes[17,18].

8.4. Further Work and Implications for Living Polaritons

As the Rabi-splitting scales proportionally with the number of interacting particles N, this can be used to give a very rough estimate of the number of chlorosomes that participate in the formation of polaritons. This relationship is described by **Equation 8.1**, in which μ is the dipole moment of the participating lorentzian oscillators, $\hat{E}$ the unit vector parallel to the electric field polarization, V the volume of the cavity mode, ϵ_0 the permittivity of free space, and n_{eff} the effective cavity length[19].

$$\hbar\Omega = 2(\mu \cdot \hat{E})\sqrt{N}\left(\frac{\pi\hbar\Omega}{n_{eff}^2\lambda\epsilon_0 V}\right)^{1/2} \qquad (8.1)$$

The mode volume for a short path length microcavity (~λ/2 nm) was estimated using **Equation 8.2**[20]. From the TMM modelling we calculated an effective refractive index (n_{eff}) of ~1.8, which corresponded to a mode volume of 15.7 cubic wavelengths (or ~850μm³). Note that actual mode volume was smaller than this as **Equation 8.2**, does not take into account in-plane scattering and other mechanisms which serve to reduce the mode volume.

$$V = L_X L_Y L_Z = \left(\frac{\lambda}{n_{eff}}\right)^3 \qquad (8.2)$$

Each chlorosome contains an average of ~200,000 BChl c monomers[21] with an average deviation of 28° between the axis of the transition dipole monomer and the central axis of the chlorosome[22]. The square of the monomer transition dipole |μ|² is given by **Equation 8.3**[23], where D is Debeys.

$$|\mu|^2 = 30D^2 \qquad (8.3)$$

Due to the nature of the spin-coating process, we assumed that there was some slight degree of spatial alignment amongst the chlorosomes. From this we estimated that there were [~2,500,000 BChl c which corresponds to] ~1000 chlorosomes with an orientation parallel to confined electric field coherently coupled at any given time within the cavity.

Importantly, despite the intermolecular coupling that occurs in large aggregates of BChls, the oscillator strength of electronic transitions can only be exchanged or redistributed amongst transitions which share the same of product $|\mu|^2N$ as given by **Equation 8.3**. This means that all of the interacting particles (N) expressed by **Equation 8.1** can be assumed to be BChl c monomers. This is subject to the conditions that the linewidth of the confined photon mode is sufficiently broad to interact resonantly with all optically allowed electronic transitions, and that the energetic shift of 26 meV (or ~12 nm) the peak absorption feature shown in **Figure 8.10** is applied.

Our work is the first reported instance of a strongly coupled biological system rather than simply an organic dye or pigment which has shown strong coupling. It is interesting to consider whether the strong coupling regime can affect the timescales of energy transfer and whether a reduction in exciton transfer time would translate to increased photosynthetic efficiency. Whilst it is conceivable that other components of the LHC could individually couple to the cavity photon mode (the FMO complex in particular), the vast majority of the oscillator strength for the LHC is concentrated in the chlorosome electronic transition. This fact is reflected clearly in the absorption spectra shown in **Figures 8.4** and **8.10**, and so we consider the case in which only the chlorosome possesses enough oscillator strength to enter the strong coupling regime.
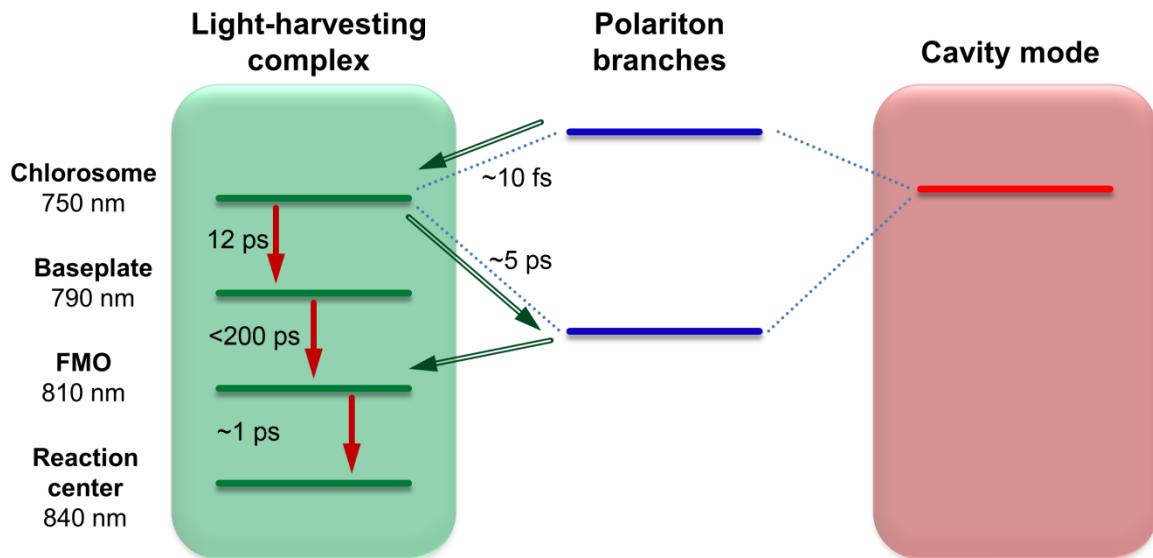
Figure 8.11. *Energy levels of individual components of the unmodified C. tepidum LHC and the time taken for a molecular exciton to transfer from one level to another. Also shown here are the energies of the cavity mode and polariton branches for a strongly coupled microcavity with a Rabi splitting of 156 meV. Red arrows denote transitions that occur normally in an unmodified LHC, green arrows denote potential alternative energy pathways utilising the polariton branches in a strongly coupled system.*

Upon entering the strong coupling regime, two new energy levels are created $\hbar\Omega/2$ meV above and below that of the cavity (chlorosome) exciton energy. The microcavity described above possessed a Rabi splitting of 156 meV, this allows the LPB to range in energy from ~840 to ~780nm, overlapping the energies of both the baseplate (~790nm) and FMO complex(~810nm); this presents several possible scenarios for excitation and energy transfer depending on the energy of an incident photon.

In the first scenario, incident photons are highly energetic and possess considerably shorter wavelengths than that of the chlorosome absorption band (750nm). In this case, the exciton created will have an excess of energy which is rapidly dissipated through thermal interactions before arriving at the exciton band of the chlorosome. Here the exciton can either progress as usual to the baseplate if the system is weakly- or un-coupled, or to an available state on the LPB if strongly coupled. Though there exists no time-resolved measurement for this transition for BChl, this transfer from the exciton to a polariton state occurs on a timescale of ~ 1ps in J-aggregate systems[24]. These are one of the most directly comparable systems in the literature as

both form aggregates which change their spectroscopic properties with respect to the monomer. Once occupying a position on the LPB, the polariton may transfer energy to either the baseplate or the FMO complex on a similar timescale.

The second scenario occurs when the incident photon has a wavelength of light corresponding to that of an UPB state. Relaxation to the exciton reservoir can occur very rapidly over a period of tens of femtoseconds[24] from which it can progress via either route in the first scenario. It is also possible that the UPB state may scatter directly to the baseplate; this is exceptionally unlikely however owing to the speed of relaxation. The final scenario occurs when the incident photon is of lower energy than the exciton and is instead directly absorbed into a LPB state, from which it can take one of the relaxation routes described previously.

The microcavity is a very flexible system which allows us to change the position and nature of the energy states within it. It can be designed in such a way to change the energetic position of the lower polariton branch by either varying the Rabi-splitting (increasing numbers of chlorosomes), the photon mode detuning (changing cavity length), or simply by changing the external viewing angle. As the photon mode detuning is varied, so too are the photonic and excitonic mixing coefficients that make up each state and the LPB and their relaxation kinetics. The lifetime of a state in the LPB is determined (in part) by the lifetime of the confined photon mode. One of these polariton-assisted transfer paths is shown in **Figure 8.11**.

From our previous calculations using **Equation 8.1**, we calculated that there needed to be $\sim$1000 coupled chlorosomes within a mode volume of 0.850μm^3 in order to achieve strong coupling and a Rabi splitting of $\sim$156 meV. As there are $\sim$200-250 chlorosomes within each *C. tepidum* bacterial cell[25], it is predicted that if $\sim$4 cells can be placed within the microcavity, the oscillator strength should be sufficiently large to enter into the strong coupling regime. As each cell is $\sim$0.6-0.8μm long[26], it is conceivable that it may be possible to fit 4 of these cells within the mode volume. This could create a strongly coupled biological system, a living expression of quantum mechanical phenomena.

If a strongly-coupled biological system such as this were fabricated, it could provide valuable insight into the efficiency of energy transfer within the LHC. It may become apparent that positioning the LPB at different energies allows us to bypass certain steps altogether and could have an effect upon the efficiency with which light is harvested and thus cell growth rates. A microcavity designed to contain living cells could not be fabricated using the methods used for a cavity containing only chlorosomes as the cells would not survive the vacuum exposure that is required for the deposition of the silver mirror, instead an open cavity (**Chapter 5**) must be constructed.

The total number of cells and their growth within the cavity could be monitored in a number of ways. Firstly the number of cells within the cavity region could be directly counted using the microscope itself; this unfortunately would not differentiate between cells that were dead or alive. Secondly, a quantity of Trypan blue could be introduced to the cell culture medium; Trypan blue is a cell stain which is only able to label cells with a compromised membrane (i.e. dead and decomposing cells) and from this we could examine whether or not cells were alive. Finally, we could continue to make reflectivity or transmission measurements over a prolonged period of time. If there is an enhancement in chlorosome production or an increase in the number of cells within the cavity region, there would be more BChl c monomers interacting with the confined photon mode and we should observe an increase in the Rabi splitting over time.

8.5. Energy Levels of Carotenoid Excited States

The second portion of this chapter describes efforts to produce strongly-coupled microcavities containing carotenoids. Due to a unique quirk of sufficiently long chain polyenes and carotenoids, the ground (S_0) and first excited state (S_1) are of the same symmetry ("A_g") and transitions between the two are forbidden by selection rules. Instead optical absorption occurs between the ground and second excited state (S_2) which has the opposing symmetry ("B_u"). From this second state, the electron undergoes an extremely rapid relaxation to the S_1 state on a timescale of $\sim$100 fs[27]. Once in the S_1 state, decay to the ground state is forbidden and the electron must remain there until it can decay through non-radiative means. This renders a lot of carotenoids effectively non-emissive; a property covered in more detail in **Chapter 2**.
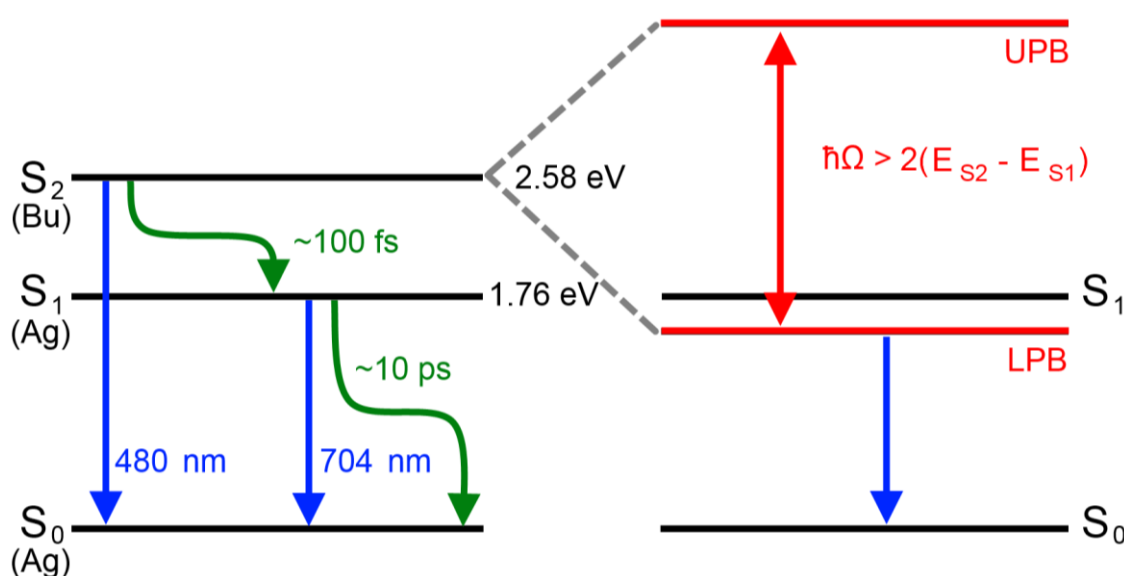

Figure 8.12. *Energy levels of the first three singlet states, the transitions between them, and their associated timescales for β-carotene*[27].

By placing a carotenoid film within a microcavity we explore the effect of strong coupling to the S_2 state. In particular, we speculate that if a sufficiently large Rabi splitting ($\hbar\Omega$) could be achieved it may be possible to move the lower polariton branch below that of the S_1 state (0.82 eV[27] or 0.84 eV[28] in the case of β-carotene). If this were possible, then the lowest lying excited state would have "B_u" symmetry and transitions between it and the ground state would be permitted. This would mean that a non-emissive material could be made to fluoresce by purely optical engineering. As a phototypical material β-carotene was chosen as it is one of the few commercially available carotenoids that can be purchased in significant quantities.

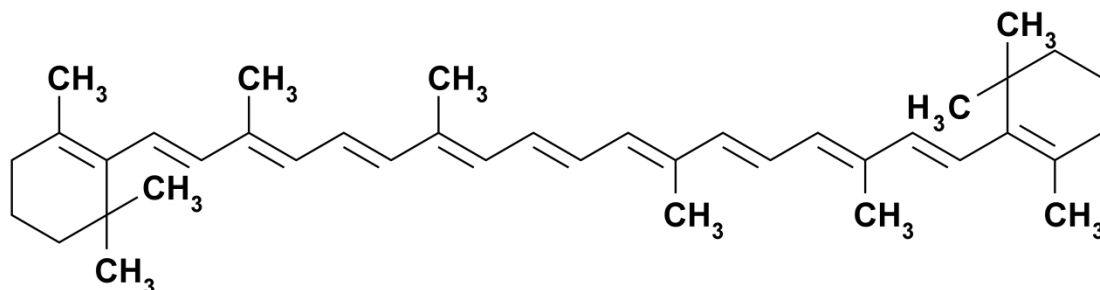## 8.6. Characterisation of β-Carotene Films and Transfer Matrix Modelling

Figure 8.13. *The chemical structure of β-carotene.*

In order to achieve both large Rabi-splittings in microcavities and appropriate photon-mode detunings, a suitable solvent had to be chosen from which to spin-coat β-carotene. The key considerations were the use of solvents which would not cause β-carotene to form aggregates at the high concentrations required to spin sufficiently thick films, either while in solution or on evaporation and conversion to a solid phase. **Figure 8.13** shows the chemical structure of β-carotene (and carotenoids in general) and highlights its hydrophobic nature. By contrast xanthophylls, a virtually identical subcategory of polyenes, contain a number of oxygen atoms which render them significantly less hydrophobic.

In a "good" solvent such as acetone, β-carotene retains its monomeric properties. The addition of a bad solvent such as water however causes it form aggregates which undergo hypsochromic and bathochromic shifts. It is thought that the achiral nature of β-carotene means that it does not preferentially form H- or J-aggregates, but rather a messy "haystack" of aggregates that continue to increase in volume with time[29]. This is evidenced in **Figure 8.14 (a)** by the emergence of both blue- and red- shifted features in the absorption spectrum and a reduction in intensity peaks corresponding to those of the monomer. After investigating a range of solvents tetrahydrofuran was settled upon, as β-carotene solubility of >40mg/ml was achieved with the absorption profile of the film closely resembling that of the monomer in solution as is shown in **Figure 8.14 (b)**.
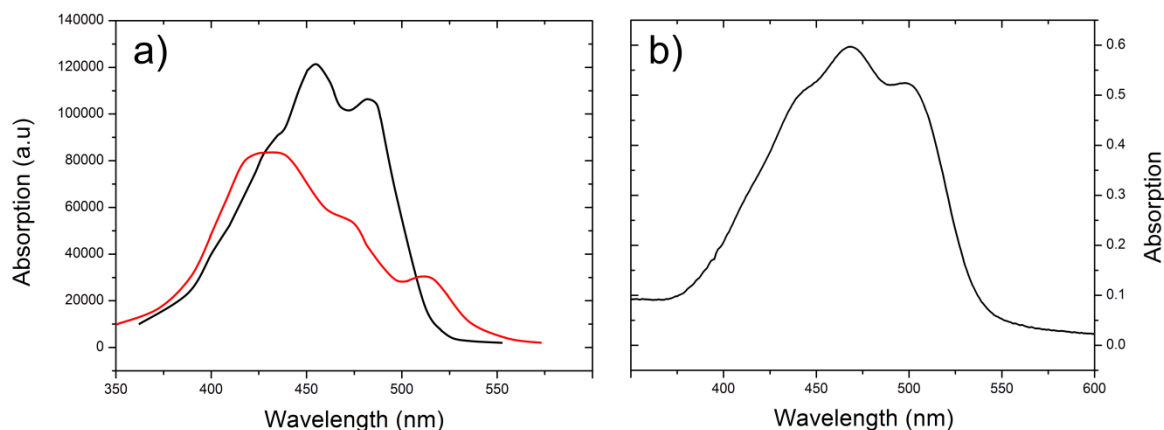
Figure 8.14. (a) *Absorption spectra of β-carotene dispersed into a "good" solvent (acetone, black line), and a "bad" solvent (acetone and water at a ratio of 3:1, red line) to demonstrate how aggregation can be induced.* ***(b)*** *Absorption spectrum of a 210 nm thick film of β-carotene doped into a polystyrene matrix at a concentration of 50% by mass as cast from a tetra-hydrofuran solution and a three peak fit corresponding to the three features.*

For the sake of comparison, we plot the absorption coefficients of a series of β-carotene films in **Figure 8.15(a)**, and normalised to peak absorption in **Figure 8.15(b)**. This was useful as it allowed us to investigate the role that concentration played upon the absorption profile of the pigment and identify the formation of any aggregate states. Here it can be seen that below a concentration of 80% pigment, the shape of the absorption spectrum does not significantly vary and we can conclude that little to no aggregation is occurring.

The broad absorption feature observed between 400-550 nm in the pure film was deconvoluted to reveal four separate absorption features at 504, 468, 440, and 410 nm with FWHMs of 47, 48, 35, and 69 nm; the first three of which correspond to the 0-0, 0-1, and 0-2 vibronic transitions from the ground state (S_0) to the second excited state (S_2) respectively and have comparable FWHMs. The fourth peak at 410 nm is a combination of the 0-3 and 0-4 transitions which cannot readily be resolved and as such has a much broader FWHM.
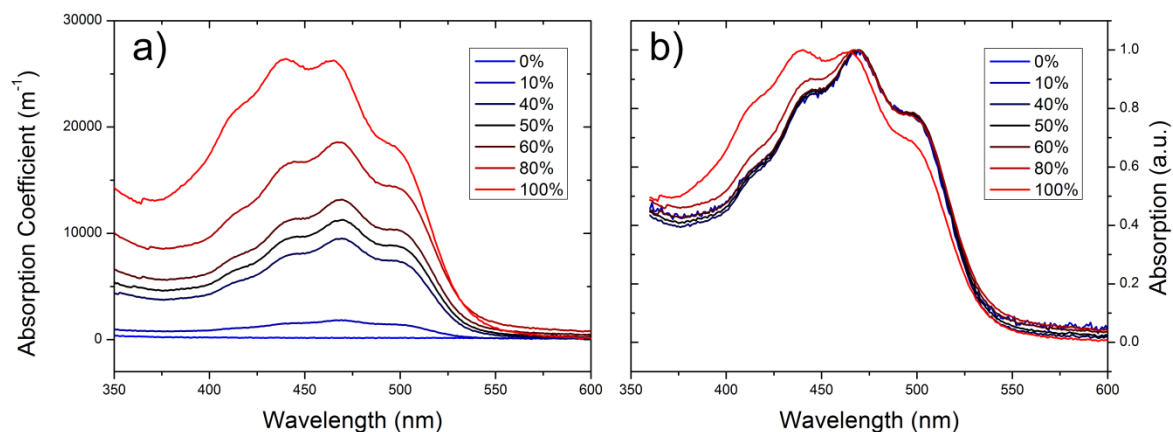
Figure 8.15. (a) *The absorption coefficients of a series of β-carotene-doped polystyrene films across a from a concentration of 0% (polystyrene control film, blue) to 100% (β-carotene control film, red).* ***(b)*** *Normalisation of extinction coefficients to that of the 0-1 vibronic transition.*

At a concentration of 80% or more pigment, it can be seen that compared to the unaggregated monomer, the optical density has increased, vibronic transitions have undergone a degree of broadening, peak absorption has shifted to shorter wavelengths and the absorption feature at 350nm corresponding to photoisomerisation[30] has increased; attributes consistent with the formation of H-aggregates.

From these fits, it was possible to build a complex refractive index profile for β-carotene across a range of concentrations and simulate the optical properties of microcavities using the transfer matrix method approach (**TMM**) as shown in **Figure 8.16**. As the absorption profile for the 60% concentration film was identical to that of all of the lower concentrations it was possible to adapt the model for any lower concentration by reducing the oscillator strength by the appropriate amount. From these simulations we predicted that, despite the broad nature of the transitions, the coupling strength was large enough to enter the strong coupling regime at concentrations of 80% or higher. Furthermore individual peaks corresponding to those of the polariton branches were sufficiently separated from one another to be discretely resolved.

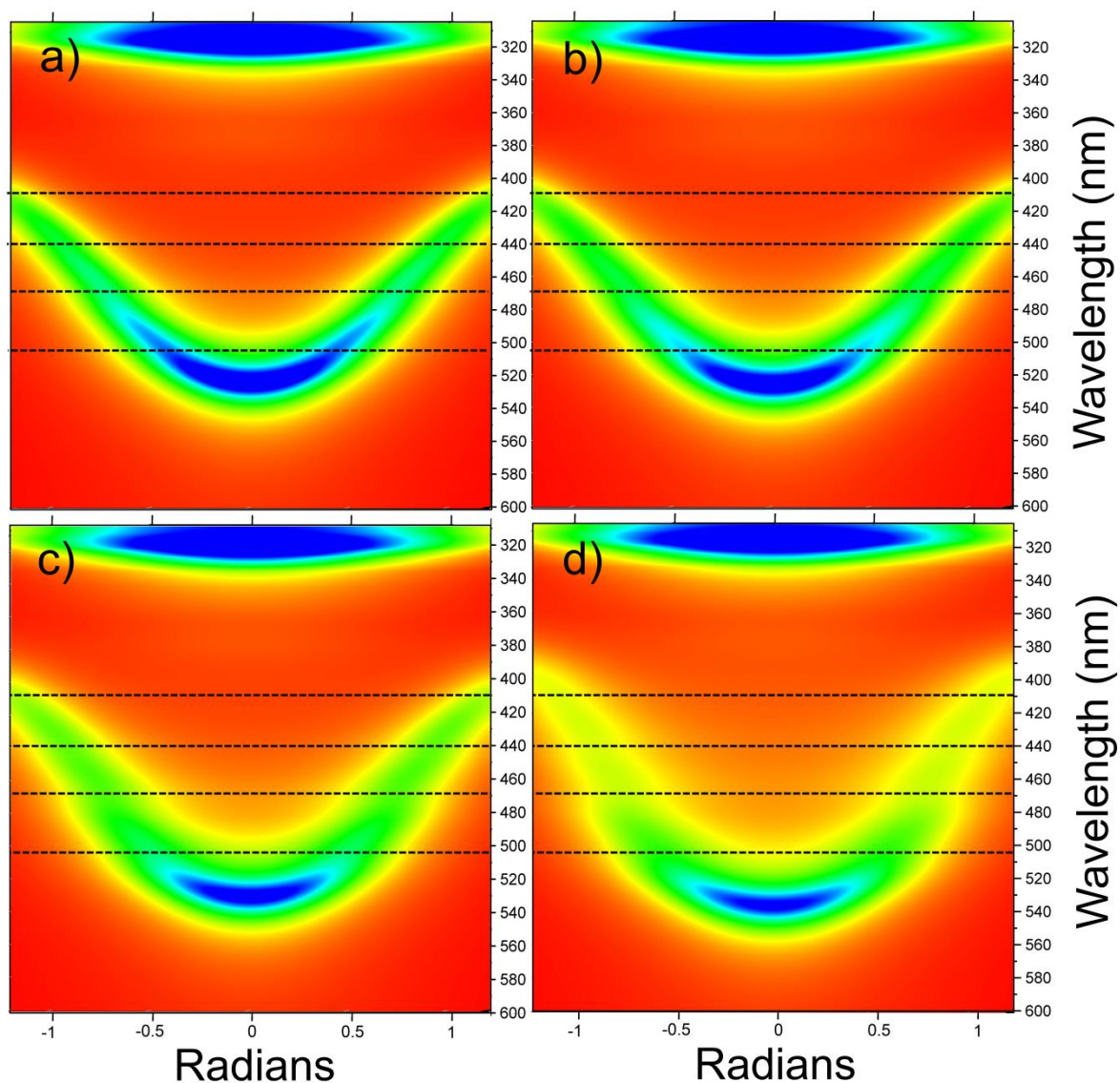**Figure 8.16.** *Transfer matrix reflectivity simulations of a (metallic) microcavity containing a 110nm thick film of β-carotene dispersed within a polystyrene matrix at a concentration of (a) 50%, (b) 60%, (c) 80%, and (d) 100% pigment bye mass. The first four vibrational sublevels of the S₂ excited state are marked by black dashed lines. Simulations were performed with the assistance of Rahul Jayaprakash.*

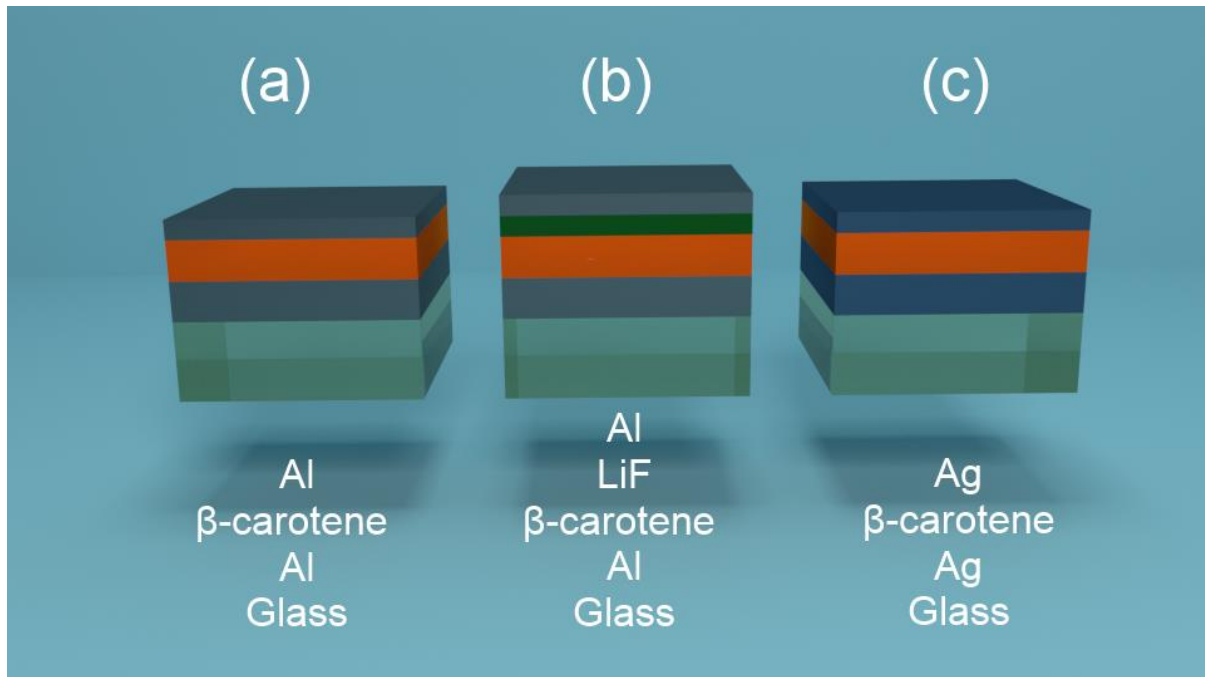## 8.7. Planar Microcavities and Degradation issues.

Figure 8.17. *Planar β-carotene microcavities comprised of: **(a)** 150nm Al bottom and 15nm Al top mirrors, **(b)** 150nm Al bottom and 15nm Al bottom mirrors with the addition of a protective 2nm LiF layer to prevent Al ions embedding into the β-carotene film, and **(c)** 200nm Ag bottom and 40nm Ag top mirrors. Individual layers are not drawn to scale.*

Based upon the TMM simulations shown in **Figure 8.16**, several series of planar microcavities were constructed according to the design in **Figure 8.17**. Metallic mirrors were selected over dielectric alternatives for their higher EM field confinement, reflectivity over larger ranges, and lower deposition temperatures. Initially Aluminium mirrors were chosen with the intention of exploring the upper polariton branch at ultraviolet wavelengths. When constructing "blank" microcavities containing only a spacer layer of polystyrene between the two mirrors for comparative purposes, relatively narrow linewidths could be seen in reflectivity measurements and Q-factors of <10 were typical.

When preparing samples containing the active layer of pure β-carotene however, much broader features were observed in reflectivity measurements. It was found that this could be mitigated by sacrificing some oscillator strength and dispersing the pigment within a high molecular weight matrix such as polystyrene or poly-lactic acid (resulting in a reduced number of interacting dipoles for an identically thick film). This suggested some degree of aluminium interdiffusion into the active layer was responsible for significant variations in the cavity length over small length scales, broad spectral features, and changes to refractive index. A secondary benefit of dispersing the pigment within a matrix was a reduction in the surface roughness.

To overcome this, an additional series of β-carotene microcavities were produced with an intermediate 1nm thick layer of LiF deposited between the organic layer and semi-transparent aluminium mirror. This protective method has been used extensively in the literature to prevent damage to fragile organic layers from reactive aluminium ions[31–34]. Whilst the addition of a LiF layer appeared to reduce aluminium embedding and interdiffusion as evidenced by both (slightly) narrower reflectivity dips and increased separation between modes (an indicator of increased cavity length and reduced aluminium penetration).Finally a series of microcavities employing silver mirrors were produced to see if the larger ion size of silver would penetrate less into the film; while this proved to further narrow cavity linewidths, it was still not possible to observe strong coupling in these systems, though some features with ambiguous broadening were observed when the reflectivity dispersion approached the exciton energy. As measurements progressed it rapidly became apparent that increased interfacial roughness between the active layer and mirror was not the only problem and that a significant degree of bleaching was occurring.

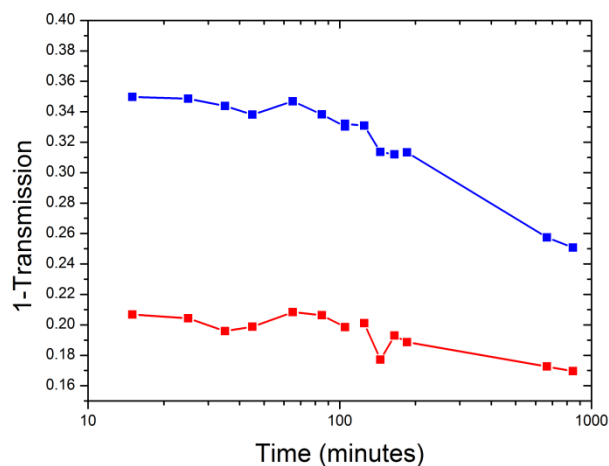## 8.7.1. Photodegradation and Oxidization of β-Carotene Films

Figure 8.18. The reduction in absorption intensity for the 0-1 vibronic transition as a function of time for films of pure β-carotene(blue) and β-carotene dispersed into a polystyrene matrix at a ratio of 20% by mass (red).

The reduction in absorption intensity of a control film of pure β-carotene left in ambient conditions is depicted in **Figure 8.18**. Over a three hour period the strength of the 0-1 transition fell by 11%; over a 14 hour period, the same transition reduced by 30%. To see if the matrix used could mitigate this decay, the experiment was repeated for a film of β-carotene dispersed into a PS matrix at a ratio of 20% by mass. This film showed a reduction of 10% after 3 hours, and a reduction of 19% over a 14 hour period. To determine the nature of this decay, a series of control films were produced and stored under different conditions. From a series of transmission measurements over a 72 hour period (shown in **Figure 8.19**), it was revealed that atmospheric oxygen and water were the primary culprits, though the presence of light accelerated the decay. Samples stored under a nitrogen atmosphere remained virtually unchanged, with absorption reducing at most 5% over three days. In solution it was found that aggregate growth continued unchecked over a period of days until individual β-carotene aggregates grew too large and dropped out of solution.
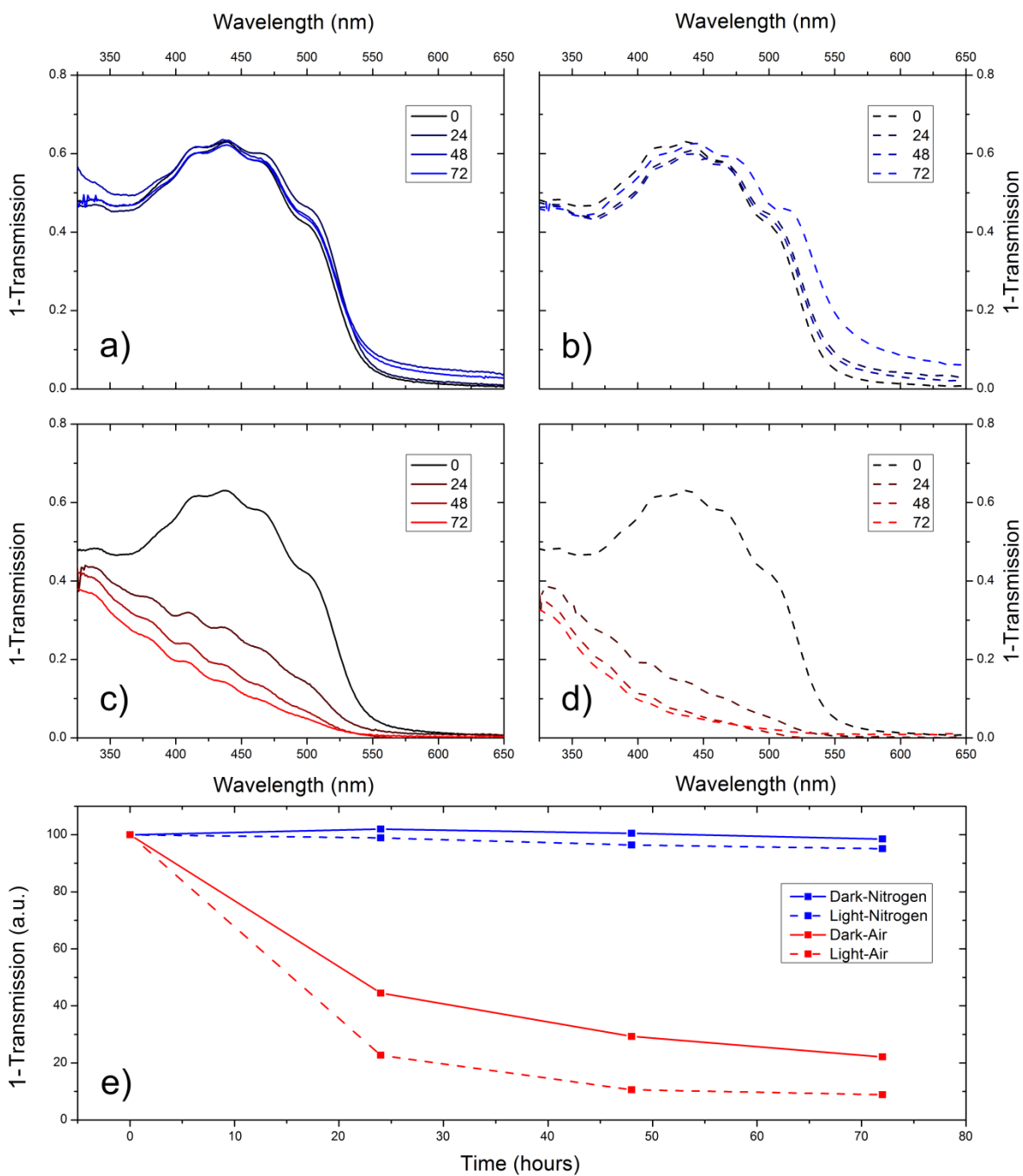
Figure 8.19. *The diminishment of the absorption profile of pure 185nm thick β-carotene films stored in various environments over a 72 hour period as measured through transmission spectra. Samples were stored under **(a)**&**(b)** nitrogen (blue lines) and **(c)**&**(d)** atmosphere (red lines) in both **(a)**&**(c)** dark (solid lines) and **(b)**&**(d)** light (dashed lines) conditions to ascertain the nature of the degradation. Part **(e)** plots the strength of the 0-1 vibronic transition relative to its initial value at time zero.*

8.7.2. Open Microcavities and Strong Coupling

From the photo-degradation measurements in the previous section, it was concluded that planar microcavities were not the best system for observing strong coupling in β-carotene films. Using an open microcavity solved many of the problems associated with planar microcavities. Higher Q-factor cavities were possible as the planarity of the top mirror was not limited by the film beneath it, there was no risk of penetration into the active layer, and degradation could be minimised by preparing the film seconds or minutes before measurements.
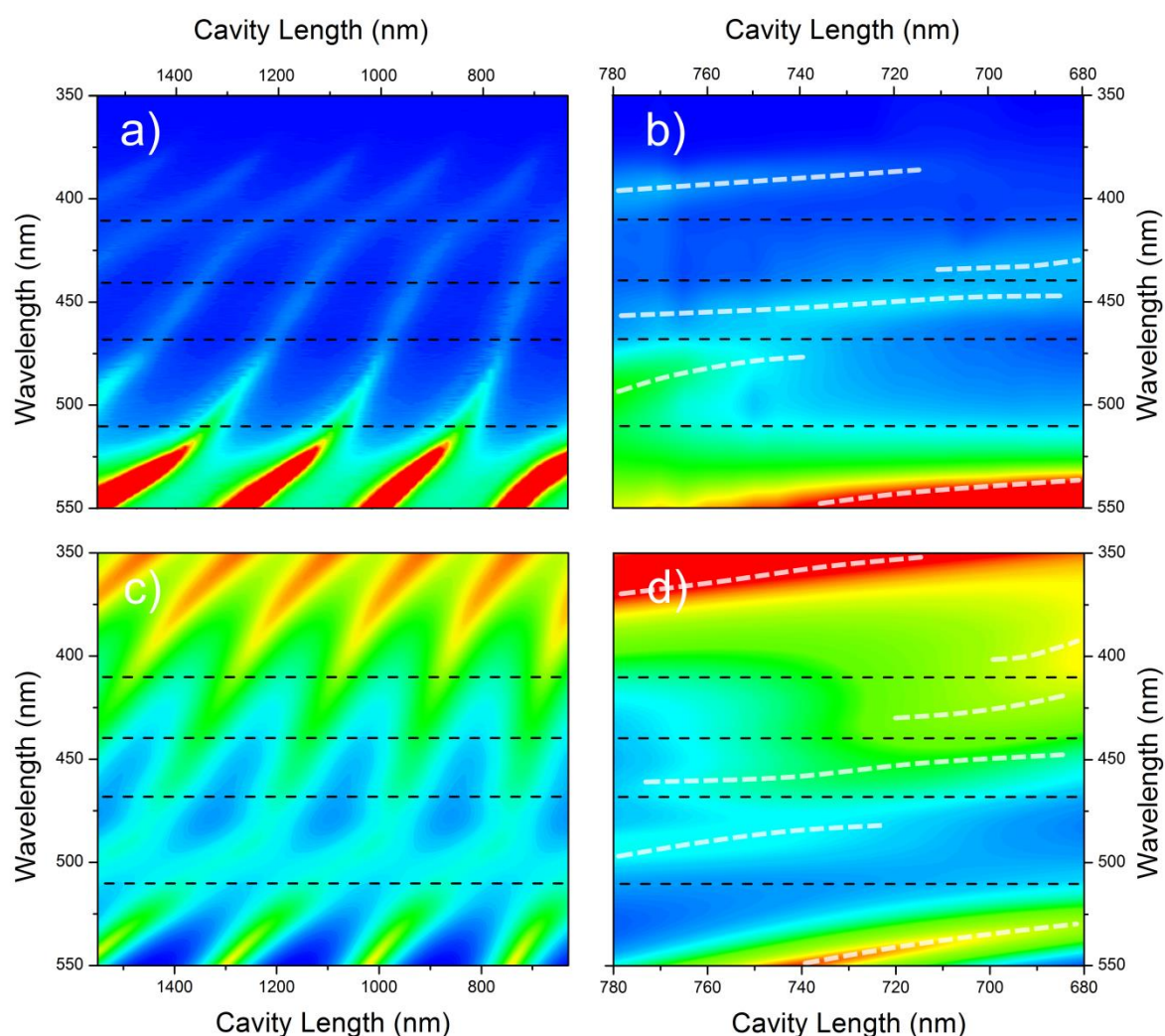
Figure 8.20. (a) *Transmission measurements of an open microcavity as a function of mirror separation. **(b)** A smaller subset of cavity separations shown in part (a) to more clearly highlight individual anticrossings. Part **(c)** plots a TMM model of the same cavity employing a 510nm β-carotene film. Part **(d)** plots a smaller subset of the TMM model to match the range of cavity lengths shown in part (b). The first four vibronic transitions are marked by dashed black lines and polariton branches are marked by dashed white lines.*

To prepare an open cavity, 40nm silver mirrors were thermally deposited upon a fused quartz substrate and (100 x 100 μm) plinth and a ~510nm film of β-carotene was spun at 500RPM from a 40 mg/ml THF solution. Transmission measurements were made periodically as the separation between the two mirrors was reduced by applying a voltage to a piezo-electric stack. The results of these transmission measurements are plotted in **Figure 8.20**.

From these transmission measurements, two peaks could be observed anticrossing the 0-0 vibronic transition at 504nm, secondary and tertiary anticrossings can be seen around the 0-1 and 0-2 vibronic transition at 440 and 468nm. It also appears that there may be an anticrossing occurring around the 410nm 0-3 transition, but the low photon counts of the halogen lamp in this spectral region make it difficult to be certain. A "waterfall" plot of individual slices of the transmission data is shown in **Figure 8.21**. The energy difference between transmission peaks indicated a Rabi splittings ($\hbar\Omega_{Rabi}$) from 103meV for the 0-0 transition to 200meV for the 0-3 transition. Spectral separation between adjacent modes suggested a cavity length of varying from ~780 to 680nm. As Rabi splittings of ~130meV were calculated from TMM modelling of transmission measurements, we can conclude that we have not managed to place the S_2 level with "B$_u$" symmetry below the S_1 level with "A$_g$" symmetry.
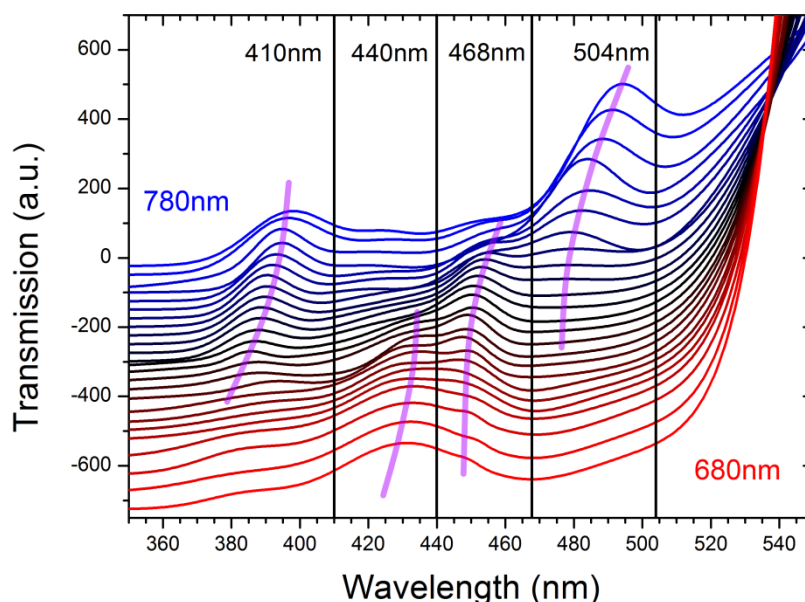

Figure 8.21. A "waterfall" plot displaying a small subset of the transmission measurements shown in Figure 9.11(b). Several anticrossings around vibronic transition energies (marked by vertical black lines) can be observed. Visible polariton branches are marked by purple lines.

8.8. Alternative Carotenoid Systems

Despite the small Rabi splittings observed in the open β-carotene cavity (100-200meV), strong coupling was still observed. This remains an encouraging result as it demonstrates that despite exceptionally broad absorption features, carotenoids are capable of entering the strong-coupling regime. This suggests that inverted excited state symmetry may be possible in other carotenoid systems possessing smaller energy separations between the first and second excited states. Here we explore a number of possible alternatives.

There exists a host of other carotenoids and polyenes with smaller energy separations between their S_1 and S_2 excited states than β-carotene. Many of these energy levels can be estimated using an energy gap relationship which is proportional to the number of conjugated double bonds along their backbone as is given in **Chapter 2**, by **Equation 2.12**. Two carotenoids of interest which have been studied briefly are neurosporene and peridinin.

Neurosporene and peridinin have similar electronic properties to β-carotene and are discussed briefly here. The limited commercial availability of these pigments meant that they had to be cultured on small scales here at the University of Sheffield and limited the number of experiments that could be performed.
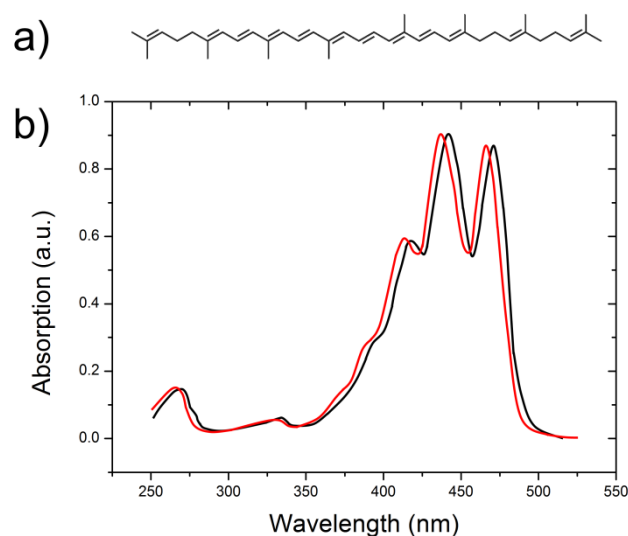
8.8.1. Neurosporene

Figure 8.22. (a) *The chemical structure of neurosporene.* **(b)** *The absorption profile of neurosporene in a AcCN/MeOH/THF blend (black line) and methanol (red line).* **(b)** *The energy levels of the S_0, S_1, and S_2 states and the transitions between them.*

Based upon the formation of polariton states using β-carotene, the possibility of other carotenoids (neurosporene and peridinin) entering the strong coupling regime was investigated. It can be seen in **Figure 8.22** that like β-carotene, the absorption profile is dominated by vibronic transitions. Unlike β-carotene however, they are significantly narrower which would make the presence of any middle polariton between the transitions easier to distinguish. Neurosporene experiences a degree of solvatochromism with peak absorption features shifting between 5 and 8nm depending on the polarity of the solvent. The lack of phenyl rings at the ends of the conjugated backbones make neurosporene moderately more stable than β-carotene. Neurosporene was chosen for its electronic similarities with β-carotene but slightly smaller energetic separation between the S_2 and S_1 excited states, with estimates of ΔE ranging from 715[35] to 760 meV[36]. This would mean that a considerably smaller Rabi-splitting be required to sufficiently split the S_2 state below that of the S_1, ensuring that the lowest lying excited state would have "B$_u$" symmetry. The FWHM of the 0-0 transition in neurosporene is half that of β-carotene, yet has a 25% greater extinction coefficient[37]. From this we could expect an oscillator strength ~2.5 times greater than that of β-carotene.
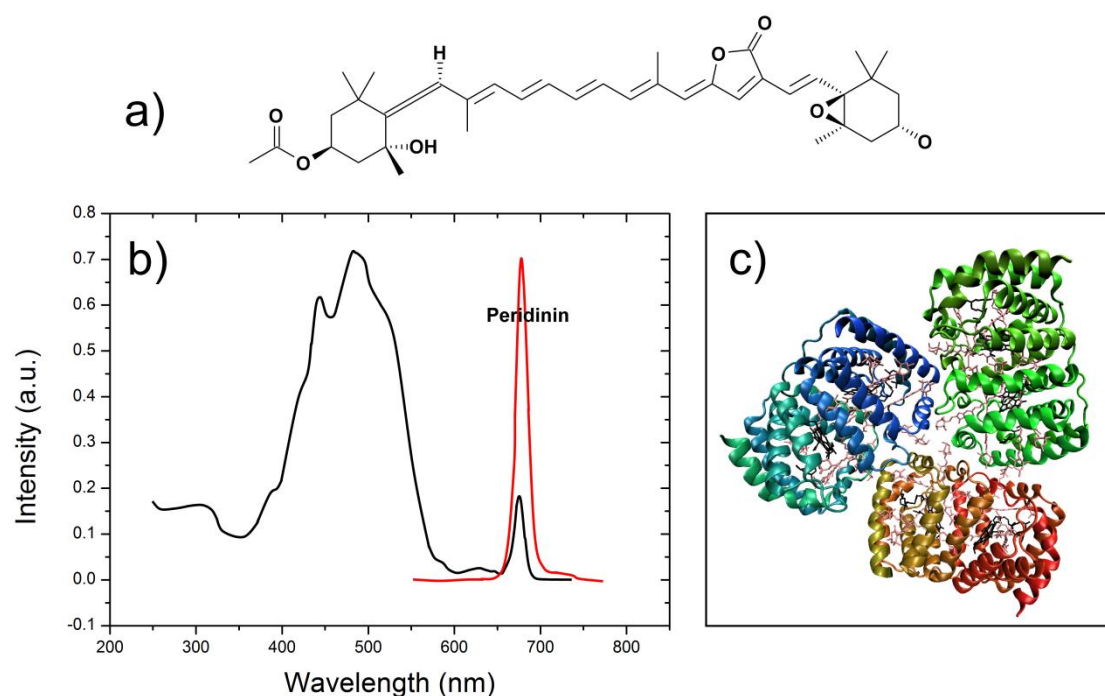
8.8.2. Peridinin

Figure 8.23. (a) *The chemical structure of peridinin.* ***(b)*** *The absorption profile of peridinin as part of a larger protein trimer complex* ***(c)*** *The peridinin-chlorophyll protein light harvesting complex found within the dinoflaggelate Amphidinium carterae, image courtesy of Opabinia regalis[38].*

A third carotenoid named peridinin was studied in detail with a conjugation length, N, of 8. As the number of double bonds along the carotenoid "backbone" increases, so too does the energy of the S_1 excited state. The energy of the S_2 state also increases with conjugation, but at a significantly smaller rate. As the carotenoid grows in length, internal conversion from the S_2 to the S_1 state also slows. In practice means that for carotenoids in which N>9 fluorescence (if any) occurs primarily from the S_2 state and for carotenoids in which N<7, emission occurs from the S_1 state. Intermediate length carotenoids 7≤N≤9 generally show fluorescence from both the S_2 and S_1 states. Peridinin is unusual for an intermediate length carotenoid in that the S_2 and S_1 have inverted A/B and g/u symmetry but it emits solely from its S_1 state[39]. This is a property which has led many to suggest that the S_1 state may lie at higher energies than initially expected, placing it close to that of the S_2 state (internal conversion rates are higher between states close in energy, and slow when this energy separation increases) and that additional intermediate energy transfer states may exist between the two[40].

Peridinin is generally found in the light harvesting complexes of the dinoflagellates *Amphidinium carterae* as part of a larger protein trimer (**PCP**) in which eight peridinin molecules are bound to two chlorophylls. Energy transfer between the two occurs at a remarkable efficiency of ~88%[41-43], most of which occurs through the S_1 state (as verified through two-photon excitation[39]) and strong fluorescence features can be seen from the chlorophyll. Preliminary work placing extracted peridinin and chlorophyll as separate entities within a polyvinylpyrrolidone matrix and performing photoluminescence excitation measurements has revealed changes to energy transfer pathways. Placing this extract within an open cavity indicated that (at least at low concentrations) peridinin was not capable of strongly-coupling but isolated chlorophyll was. An anticrossing around the exciton wavelength (665nm) was observed and a Rabi-splitting of ~80meV measured.

8.9. Conclusions

To conclude we present the first reported strongly-coupled biological system reported in the literature and propose a series of experiments to study the first living systems in the strong coupling regime. In these experiments we hope to modify energy transfer within the light harvesting complexes by reducing the time between, or bypassing altogether, different steps; this could potentially reduce losses and result in more efficient light harvesting and faster cell reproduction.

Films and microcavities containing a component of the light harvesting complexes from the *Chlorobaculum tepidum* bacteria known as chlorosomes have been characterised using physical and optical techniques. From measurements of the film, a description of the complex refractive index of a film containing chlorosomes was developed. This was used in a transfer matrix fitting model to describe the transmission and reflectivity measurements made upon cavities containing chlorosomes dispersed within a PVA matrix at a ratio of 25% mass.

A Rabi splitting of 156meV was observed and using the TMM, a 164meV negative detuning between the confined photon mode and cavity exciton was calculated. We note that the exciton being coupled to is not that of individual (isolated) BChl c, but a molecular exciton of the chlorosome in its entirety. These molecular excitons have significantly different energies from

those of the single-pigment excited states and are not confined to the energy of an individual component of the complex. By studying linewidths of features in the lower polariton branch a Q-factor and cavity lifetime was calculated and compared to the transition time between states in the light harvesting complex.

A peer-reviewed publication describing this work can be found in Nature Communications volume 5, 2014, under the title "*Strong coupling between chlorosomes of photosynthetic bacteria and a confined optical cavity mode*"[1].

The author also presents a strongly coupled microcavity containing β-carotene as proof of concept for carotenoid coupling. From this we speculate that it may be possible, given the correct pigment, to create other strongly coupled carotenoid systems with sufficient Rabi splitting to exceed the energy difference between the S_2 and S_1 excited states. For carotenoids with a long enough conjugation length to experience S_2/S_1 symmetry inversion, this could change the symmetry of the lowest lying excited state and allow direct radiative decay to the ground state. Neurosporene is sufficiently long carotenoid to experience S_2/S_1 symmetry inversion but an energy separation of only 715meV compared to ~820meV for β-carotene; this coupled with its narrower linewidths and greater photostability make it a more likely candidate for displaying this phenomena. Besides these two there exist a wealth of other carotenoids

Ultimately, the restricted commercial availability of all but a select few carotenoids limits further work on an otherwise very interesting class of materials. Further work would require a significant investment of time to both culture cells and extract the desired pigment.

8.10. References

1. Coles, D. M. *et al.* Strong coupling between chlorosomes of photosynthetic bacteria and a confined optical cavity mode. *Nat. Commun.* **5,** 5561 (2014).

2. Baieva, S., Ihalainen, J. a & Toppari, J. J. Strong coupling between surface plasmon polaritons and β-carotene in nanolayered system. *J. Chem. Phys.* **138,** 44707 (2013).

3. Castenholz, R. W., Bauld, J. & Jørgensen, B. B. Anoxygenic microbial mats of hot springs: thermophilic Chlorobium sp. *FEMS Microbiol. Lett.* **74,** 325–336 (1990).

4. Wahlund, T. M., Woese, C. R., Castenholz, R. W. & Madigan, M. T. A thermophilic green sulfur bacterium from New Zealand hot springs, Chlorobium tepidum sp. nov. *Arch. Microbiol.* **156,** 81–90 (1991).

5. Madigan, M. T. *et al.* Diversity of Anoxygenic Phototrophs in Contrasting Extreme Environments. *Geotherm. Biol. Geochemistry YNP* **1,** 203–220 (2005).

6. Olson, J. M. Chlorophyll Organization and Function in Green Photosynthetic Bacteria. *Photochem. Photobiol.* **67,** 61–75 (1998).

7. Orf, G. S. & Blankenship, R. E. Chlorosome antenna complexes from green photosynthetic bacteria. *Photosynth. Res.* **116,** 315–331 (2013).

8. Blankenship, R. E., Olson, J. M. & Miller, M. in *Anoxygenic Photosynthetic Bacteria* 339–435 (Kluwer Academic Publishers, 1995).

9. Martiskainen, J., Linnanto, J., Aumanen, V., Myllyperkiö, P. & Korppi-Tommola, J. Excitation energy transfer in isolated chlorosomes from Chlorobaculum tepidum and Prosthecochloris aestuarii. *Photochem. Photobiol.* **88,** 675–683 (2012).

10. Mohseni, M., Rebentrost, P., Lloyd, S. & Aspuru-Guzik, A. Environment-assisted quantum walks in photosynthetic energy transfer. *J. Chem. Phys.* **129,** (2008).

11. Goedheer, J. C. Temperature dependence of absorption and fluorescence spectra of bacteriochlorophylls in vivo and in vitro. *Biochim. Biophys. Acta* **275,** 169–176 (1972).

12. Sistrom, W. R. The spectrum of bacteriochlorophyll in vivo: observations on mutants of Rhodopseudomonas spheroides unable to grow photosynthetically. *Photochem. Photobiol.* **5,** 845–856 (1966).

13. Dowrkin, M., Falkow, S., Rosenberg, E., Schleifer, K.-H. & Stackebrandt, E. *The Prokaryotes - A Handbook on the Biology of Bacteria: Proteobacteria: Delta and Epsilon Subclasses. Deeply Rooting Bacteria - Volume 7.* (2006). doi:10.1007/0-387-30741-9

14. Armitage, a *et al.* Modelling of asymmetric excitons in organic microcavities. *Synth. Met.* **111–112,** 377–379 (2000).

15. Coles, D. M. *et al.* Vibrationally Assisted Polariton-Relaxation Processes in Strongly Coupled Organic-Semiconductor Microcavities. *Adv. Funct. Mater.* **21,** 3691–3696 (2011).

16. Skolnick, M. S., Fisher, T. A. & Whittaker, D. M. Strong coupling phenomena in quantum microcavity structures. *Semicond. Sci. Technol.* **13,** 645–669 (1998).

17. Houdré, R., Stanley, R. P., Oesterle, U., Ilegems, M. & Weisbuch, C. Room-Temperature Cavity Polaritons in a Semiconductor Microcavity. *Phys. Rev. B* **49,** 761–764 (1994).

18. Kelkar, P. *et al.* Stimulated emission, gain, and coherent oscillations in II-VI

semiconductor microcavities. *Phys. Rev. B* **56,** 7564–7573 (1997).

19.   Fox, M. Quantum Optics. *Univ. Oxford* **53,** 1689–1699 (2013).

20.   Ujihara, K. Spontaneous emission and the concept of effective area in a very short optical cavity with plane-parallel dielectric mirrors. *Jpn. J. Appl. Phys.* **30,** L 901-L 903 (1991).

21.   Montano, G. *et al.* Determination of the number of bacteriochlorophyll molecules per chlorosome light-harvesting complex in Chlorobium tepidum. *PS2001 Proc. 12th Int. Congr. Photosynth. Artic. S* **1,** 3–6 (2001).

22.   Furumaki, S. *et al.* Absorption linear dichroism measured directly on a single light-harvesting system: The role of disorder in chlorosomes of green photosynthetic bacteria. *J. Am. Chem. Soc.* **133,** 6703–6710 (2011).

23.   Prokhorenko, V. I., Steensgaard, D. B. & Holzwarth, A. R. Exciton dynamics in the chlorosomal antennae of the green bacteria Chloroflexus aurantiacus and Chlorobium tepidum. *Biophys. J.* **79,** 2105–20 (2000).

24.   Virgili, T. *et al.* Ultrafast polariton relaxation dynamics in an organic semiconductor microcavity. *Phys. Rev. B* **83,** 2–7 (2011).

25.   *Encyclopedia of Microbiology: Third Edition*. (Academic Press/Elsevier, 2009).

26.   Imhoff, J. F. Phylogenetic taxonomy of the family Chlorobiaceae on the basis of 16S rRNA and fmo (Fenna-Matthews-Olson protein) gene sequences. *Int. J. Syst. Evol. Microbiol.* **53,** 941–951 (2003).

27.   Andersson, P. O. *et al.* Solvent and Temperature Effects on Dual Fluorescence in a Series of Carotenes. Energy Gap Dependence of the Internal Conversion Rate. *J. Phys. Chem.* **99,** 16199–16209 (1995).

28.   Takaya, T. & Iwata, K. Relaxation mechanism of β-carotene from S2 (1B u +) state to S1 (2Ag -) state: Femtosecond time-resolved near-ir absorption and stimulated resonance raman studies in 900-1550 nm region. *J. Phys. Chem. A* **118,** 4071–4078 (2014).

29.   Zsila, F., Bik??di, Z., Deli, J. & Simonyi, M. Configuration of a single centre determines chirality of supramolecular carotenoid self-assembly. *Tetrahedron Lett.* **42,** 2561–2563 (2001).

30.   Khoo, H. E., Prasad, K. N., Kong, K. W., Jiang, Y. & Ismail, A. Carotenoids and their isomers: Color pigments in fruits and vegetables. *Molecules* **16,** 1710–1738 (2011).

31.   Kéna-Cohen, S., Maier, S. a. & Bradley, D. D. C. Ultrastrongly Coupled Exciton-Polaritons in Metal-Clad Organic Semiconductor Microcavities. *Adv. Opt. Mater.* **1,** 827–833 (2013).

32.   Lee, J. H., Moon, D. W. & Yi, Y. The initial interface formation between Al and tris-(8-hydroquinoline) aluminum (Alq3) with LiF interlayer. *Org. Electron. physics, Mater. Appl.* **11,** 164–168 (2010).

33.   Le, Q. T. *et al.* Photoemission study of aluminum/tris-(8-hydroxyquinoline) aluminum and aluminum/LiF/tris-(8-hydroxyquinoline) aluminum interfaces. *J. Appl. Phys.* **87,** 375 (2000).

34.   Lee, J. H., Yi, Y. & Moon, D. W. Direct evidence of Al diffusion into tris-(8-hydroquinoline) aluminum layer: Medium energy ion scattering analysis. *Appl. Phys. Lett.* **93,** 1–4 (2008).

35. Zhang, J.-P. *et al.* Mechanism of the carotenoid-to-bacteriochlorophyll energy transfer via the S1 state in the LH2 complexes from purple bacteria. *J. Phys. Chem. B* **104,** 3683–3691 (2000).

36. Niedzwiedzki, D. M. *et al.* Ultrafast Time-Resolved Absorption Spectroscopy of Geometric Isomers of Carotenoids. *Chem. Phys.* **357,** 54–56 (2009).

37. Bramley, P. M., Davies, B. H., Rees, A. F., Crook, M. A. & Johnson, P. Colour Quenching by Carotenoids. in *Proceedings of a Symposium on Liquid Scintillation Counting organised by the Society for Analytical Chemistry* **3,** 306 (1973).

38. Regalis, O. Peridinin-Chlorophyll-Complex. (2006).

39. Zimmermann, J., Linden, P. A., Vaswani, H. M., Hiller, R. G. & Fleming, G. R. Two-photon excitation study of peridinin in benzene and in the peridinin chlorophyll a-protein (PCP). *J. Phys. Chem. B* **106,** 9418–9423 (2002).

40. Knecht, S., Marian, C. M., Kongsted, J. & Mennucci, B. On the photophysics of carotenoids: A multireference DFT study of peridinin. *J. Phys. Chem. B* **117,** 13808–13815 (2013).

41. Akimoto, S. *et al.* Excitation energy transfer in carotenoid-chlorophyll protein complexes probed by femtosecond fluorescence decays. *Chem. Phys. Lett.* **260,** 147–152 (1996).

42. Krueger, B. P. *et al.* Energy transfer in the peridinin chlorophyll-a protein of Amphidinium carterae studied by polarized transient absorption and target analysis. *Biophys. J.* **80,** 2843–55 (2001).

43. Bautista, J. A. *et al.* Singlet and triplet transfer in the Peridinin-Chlorophyll a- protein from Amphidinium carterae. *J. Phys. Chem. A* **103,** 2267–2273 (1999).

9.

Conclusions and Suggestions for Further Work

In this thesis, a brief historical overview of strong coupling and polaritons in organic semiconductors has been outlined, together with a timeline of major developments in the field. Though the inorganic field has been established for a considerably longer period of time, the first demonstration of polaritons in organic semiconductors coming in 1998[1] compared to the first observed inorganic polaritons in 1992[2], the field is rapidly advancing. Well understood non-linear phenomena once thought exclusive to inorganic semiconductors, Wannier-Mott excitons, and low temperatures are now being observed in organic systems, with Frenkel excitons, at room temperatures.

Chapter 2 describes the optical and electronic properties of organic materials in terms of atomic bonding between single atoms before expanding this to larger molecules through the hybridization of carbon atom orbitals. Finally it goes on to describe how individual molecules or monomers can form larger (aggregate) structures and how this further alters their spectral

properties. **Chapter 3**, outlines how light behaves as it passes through a single medium, the interface between two media, or complex multilayer structures and how they can be modelled using a transfer matrix method. By introducing a complex component to the refractive index of one or more materials within a structure, absorption and attenuation of light can be accounted for. The application of semiconductors in both the weak- and strong-coupling regimes is described. **Chapters 4 & 5** discuss the techniques used throughout this thesis to fabricate and characterise samples in the subsequent experimental chapters, in addition to the fundamental principles behind these methods and the merits and limitations of said techniques. Throughout **Chapters 6-9**, seven different materials were shown to enter the strong coupling regime.

In **Chapter 6**, we investigated the role that photon mode detuning plays upon the distribution of polariton states in the lower polariton branch of a series of strongly-coupled microcavities containing the fluorescent molecular dye BODIPY-Br. It was found that at large exciton-photon mode detunings, the majority of polariton states in the lower branch could be found at large viewing angles close to the exciton reservoir. However as the exciton-photon detuning was reduced, the polariton population was increasingly concentrated around the bottom of the branch at normal incidence. To better understand and explain these observations, a simple fitting model was developed based upon radiative pumping of polariton states through the decay of weakly-coupled reservoir excitons. Excellent agreement was found between the predicted and experimentally measured polariton population distribution. A secondary set of measurements were performed to investigate the role that temperature played upon these distributions. Photoluminescence excitation measurements revealed the presence of a weakly coupled excimer, and by introducing a secondary radiative pumping term corresponding to the energy of the excimer the observed changes in distribution could be well fitted even at low temperature. The model showed that the dominant process for populating polariton states in these microcavities is primarily radiative in nature; it also predicted that polariton states which are more photon-like are more readily pumped than states with a higher excitonic fraction. This was verified by measuring the overall fluorescence quantum yield of cavities and comparing them to a control film; it was found that microcavities with larger exciton-photon detunings (and thus higher photonic fractions) had larger quantum yields than their less significantly detuned counterparts, with no cavity exceeding the fluorescence quantum yield of the control film. Subsequent work has suggested that the model can be expanded to fit lower polariton branch populations in microcavities containing other fluorescent dyes (LFO).

Buoyed by the successful production of strongly-coupled microcavities containing BODIPY-Br, in **Chapter 7** we explored the possibility of producing microcavities capable of exhibiting polariton lasing. Through an extensive series of concentration-dependent absorption, photoluminescence, and fluorescence quantum yield measurements, four materials were selected for microcavity production. All four materials possessed high fluorescence quantum yields and strong-narrow absorption features. BODIPY-Br – covered extensively in **Chapter 6**; LFO – a perylene derivative purchased from BASF; meso-QFBOD and meso-TFBOD – two derivatives of the BODIPY fluorophore with oligofluorene side chains synthesised by Neil Findlay at the University of Strathclyde. Stripe pumping of control films revealed that all four materials demonstrated amplified spontaneous emission measurements across a range of film thicknesses and dye concentrations. Though ASE thresholds and peak wavelength positions varied from sample to sample, general trends such as the lowering of thresholds for higher concentration samples and thicker films were common for all four materials was observed. Following this a series of microcavities over a range of concentrations and detunings were fabricated for all four dyes to determine the minimum quantity of dye needed to enter the strong coupling regime. Following the successful demonstration of strong coupling in all four dyes, lasing measurements were performed at Politecnico di Milano with the assistance of Sai Rajendran. Despite the higher quantum yield of LFO and lower aggregate formation in both meso-QFBOD and -TFBOD, only microcavities containing BODIPY-Br were shown to demonstrate coherent (polaritonic) emission from the lower polariton branch at low excitation power densities. As collection was limited to normal incidence rather than imaging the entirety of the lower polariton branch, it was difficult to infer more information about the polariton dispersion at higher angles. Further efforts in this field are being continued by my colleague Kyriacos Georgiou and collaborators at the University of Southampton; A paper building upon this work titled "*A yellow polariton condensate in a dye filled microcavity*" has recently been submitted to Advanced Optical Materials.

From here, attention turned to the production and study of microcavities containing materials of biological origin. **Chapter 8** describes the cultivation and extraction of light-harvesting complexes from the bacteria *Chlorobaculum tepidum*. *C. tepidium* are a species of photosynthetic bacteria which inhabit the photic zone of sulphur-rich bodies of water and as such have evolved highly efficient light-harvesting complexes in order to effectively use the few photons they receive; a result of which is the remarkable oscillator strength of a component of the complex

known as a chlorosome. By producing a series of metallic microcavities containing these chlorosomes, the first strongly-coupled biological system was demonstrated. It was speculated that the splitting of energy levels caused by entry into the strong coupling regime, in conjunction with the ability to tune the energy of the lower polariton branch either by changing the angle of observation or cavity length, would allow us to change the temporal dynamics of energy transfer within the complex as a whole. Relaxation to the lower polariton branch is a rapid process and by designing a cavity with long enough polariton lifetimes, it may be possible to by-pass certain steps in exciton transfer altogether, and potentially increase the efficiency of the light-harvesting complex as a whole. From calculations based upon the number of participating chlorosomes within the cavity, we estimated that it would be possible to enter the strong coupling regime with living cells if ~4 could be placed within the mode volume of the cavity. This would be the first demonstration of "living" polaritons, and could open up a vast range of questions as to whether cellular processes could be enhanced (or hindered) purely by physical means. A very recent series of measurements by my colleague David Coles have successfully demonstrated strongly coupling across multiple cells (3-6 depending on their orientations). Not only are they able to form polariton states, but they are able to survive the process. An extensive series of measurements are currently being planned to further probe the dynamics of such a system.

Continuing the theme of the modification of energy levels in biological systems, the second part of **Chapter 8** describes preliminary attempts to enter the strong coupling regime with the carotenoids β-carotene, neurosporene, and peridinin. Carotenoids, polyenes, and certain other sufficiently long-chain conjugated systems possess unusual spectroscopic properties caused by electron-electron correlations which only become significant for materials possessing high degrees of spatial and rotational symmetry. In such systems, the ground and first excited singlet states (S_0 and S_1) have the same "A_g" symmetry and (single photon) electronic transitions are therefore forbidden between the two. Instead absorption must occur between the ground and second singlet excited state (S_2) which possesses "B_u" symmetry. From the S_2 state, the exciton undergoes a rapid relaxation to the S_1 state where it remains until it decays through non-radiative means; because of this longer carotenoids typically have quantum yields of $<10^{-5}$ and are considered to be non-emissive. By placing these carotenoids within a cavity, we hoped to couple to the S_2 state and achieve a Rabi splitting larger than the energy separation between the S_2 and S_1 states. In theory this would then cause the lowest lying excited state to have an opposing symmetry to the ground state; transitions between the two states would be dipole allowed, and fluorescence could be observed. Though strong coupling of β-carotene was

achieved (with great difficulty) using an open cavity system, the Rabi-splitting ($\sim$150meV) was not great enough to place the S_2 level below that of the S_1 (ΔE=820meV). Neurosporene was a promising alternative to β-carotene which possessed the same inverted excited state symmetry as β-carotene, but an energy separation of $\sim$715meV. Unfortunately not enough pigment was available to enter the strong coupling regime. Finally the peridinin-chlorophyll-protein trimer from the dinoflagellate *Amphidinium carterae*, and its individual components chlorophyll and peridinin were studied. Peridinin is an unusual carotenoid in that is of intermediate conjugation length so the S_1 and S_2 states are very close in energy and though it possesses the same A/B symmetry inversion as β-carotene and neurosporene, relatively strong $S_1 \rightarrow S_0$ fluorescence is observed. Energy transfer within the protein complex from the broad ultraviolet absorption feature to the narrow red absorption and emission features occurs at an efficiency of $\sim$88%. This could allow both the construction of microcavities with very high reflectivity Bragg mirrors, and efficient low-power pumping of the semiconductor outside of the stopband.

From these experiments it is clear that there remains a rich vein of research yet to be explored in the fields of strong-coupling, lasing, biological systems, and varying degrees of overlap between the three. It is the author's sincere hope that the work contained within this thesis has provided both an engaging read and piqued an interest in unconventional photonic structures and systems.

10.1. References

1. Lidzey, D. G. *et al.* Strong exciton-photon coupling in an organic semiconductor microcavity. *Nature* **395,** 53–55 (1998).

2. Weisbuch, C., Nishioka, M., Ishikawa, A. & Arakawa, Y. Observation of the Coupled Exciton-Photon Mode Spliting in a Semiconductor Quantum Microcavity. *Phys. Rev. Lett.* **69,** 3314–3317 (1992).

10.

Appendix

11. Roughness Propagation Through DBR Stacks

In order to produce cavities with the highest possible Q-factors, it was necessary to find out how "noisy" the deposition process was, and whether over time the roughness would increase as more dielectric layers were deposited or whether it would serve as a planarizing layer. Figure 11.1 plots the changes in surface roughness for 6 different substrates at various stages of DBR deposition via PECVD.
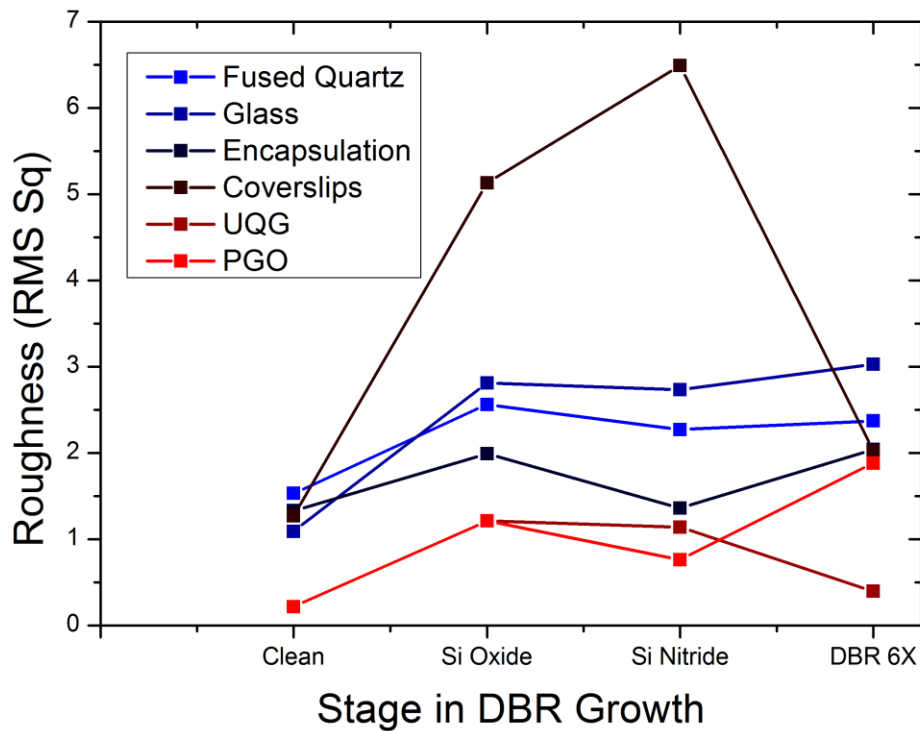
Figure 11.1. *The roughness of substrates through various stages of DBR growth as measured through atomic force microscopy.*

It appears that the roughness of mirrors does not increase markedly over the course of several layers for substrates which start with low RMS. The presence of dirt or other raised regions with higher roughness (such as the coverslip) serve to act as nucleation points when depositing new layers and roughness increases; over time however this tends back towards the mean. This can be seen more clearly in the AFM images of coverslips **Figure 11.2**, and substrates from UQG in **Figure 11.3**.
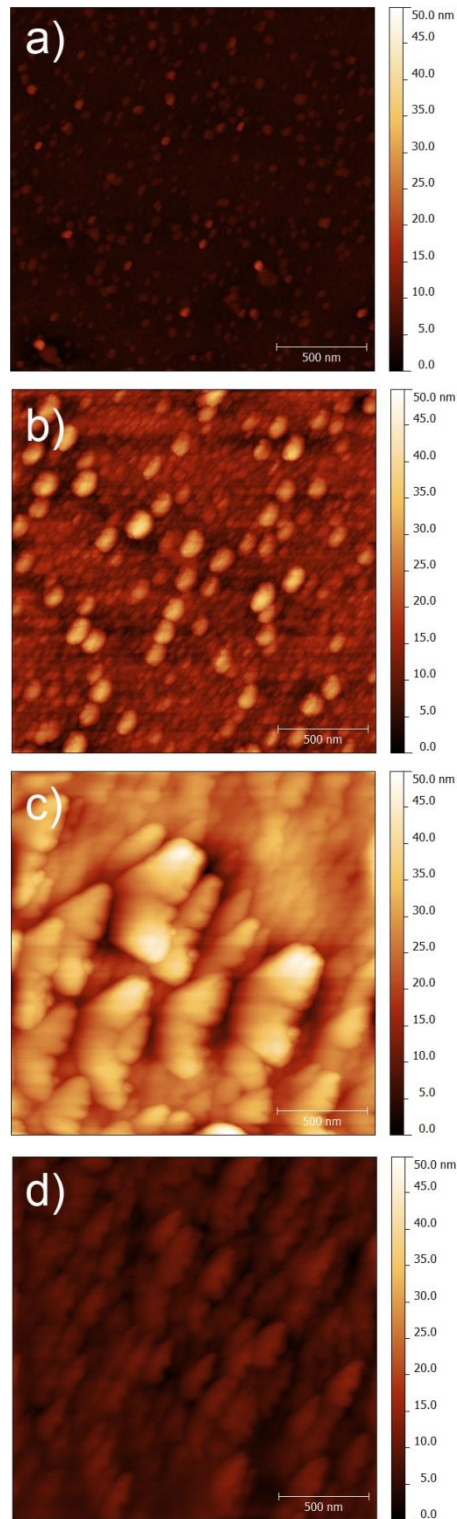
Figure 11.2. AFM images of a coverslip during various stages of deposition. *(a)* clean substrate, *(b)* with a single layer of SiO$_2$, *(c)* with the addition of a Si$_3$N$_4$ layer, and *(d)* 6 pairs of mirrors. Axes are scaled to 50nm, the scale bar represents 500nm. The colour scale indicates roughness in RMS nm.
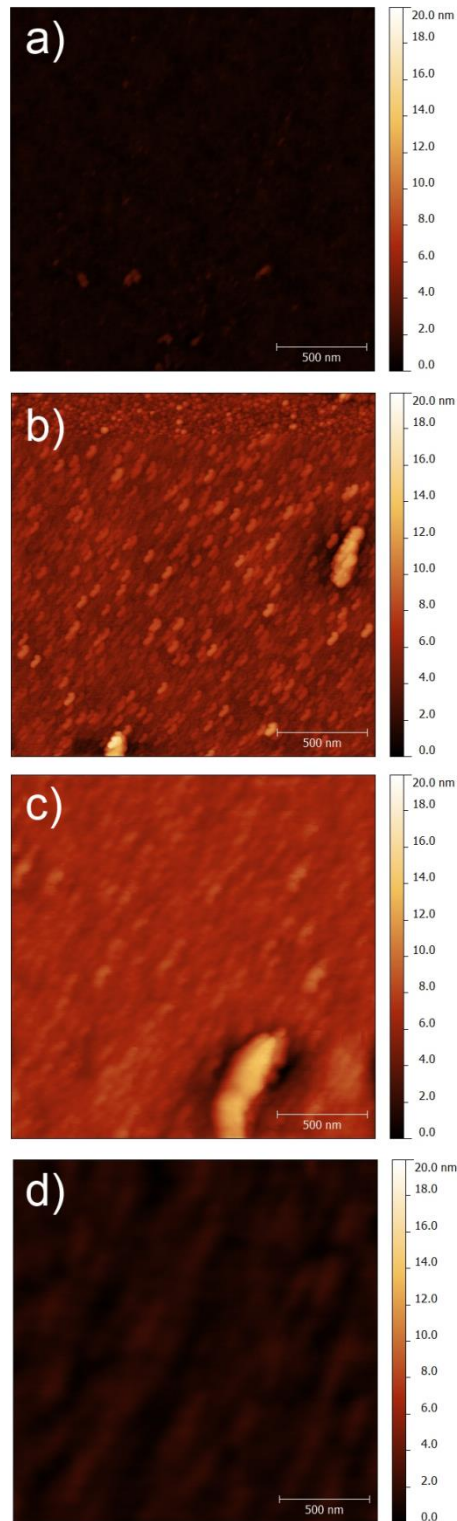
Figure 11.3. *AFM images of a PGO substrate during various stages of deposition.* **(a)** *clean substrate,* **(b)** *with a single layer of SiO₂,* **(c)** *with the addition of a Si₃N₄ layer, and* **(d)** *6 pairs of mirrors. Axes are scaled to 20nm, the scale bar represents 500nm. The colour scale indicates roughness in RMS nm.*

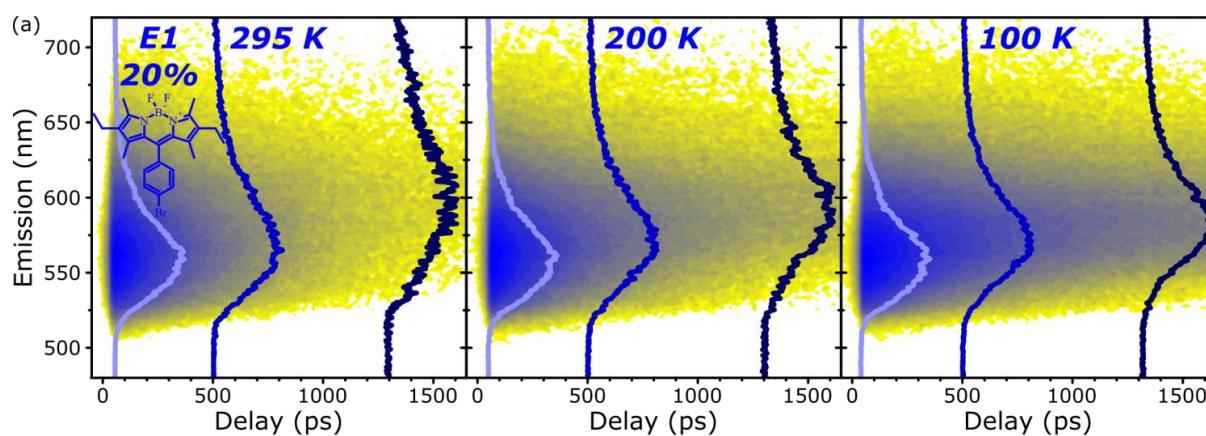## 11.2. Streak Camera Images of BODIPY-Br

Figure 11.4. *Fast PL dynamics. Temperature-dependent streak-camera measurements of high-concentration BODIPY-Br films, from 295 K (left) to 100 K (right). Normalised spectral cuts (lines; light blue: 50 ps, blue: 200 ps, dark blue: 1500 ps) highlight the evolution of emissive species. The initial spectrum corresponds to monomer emission detected in dilute films. The final spectrum matches the excimer component identified above, and similarly blue-shifts upon cooling Spectral maps are presented with logarithmic intensity scale to highlight the contribution of weak, long-lived features.*
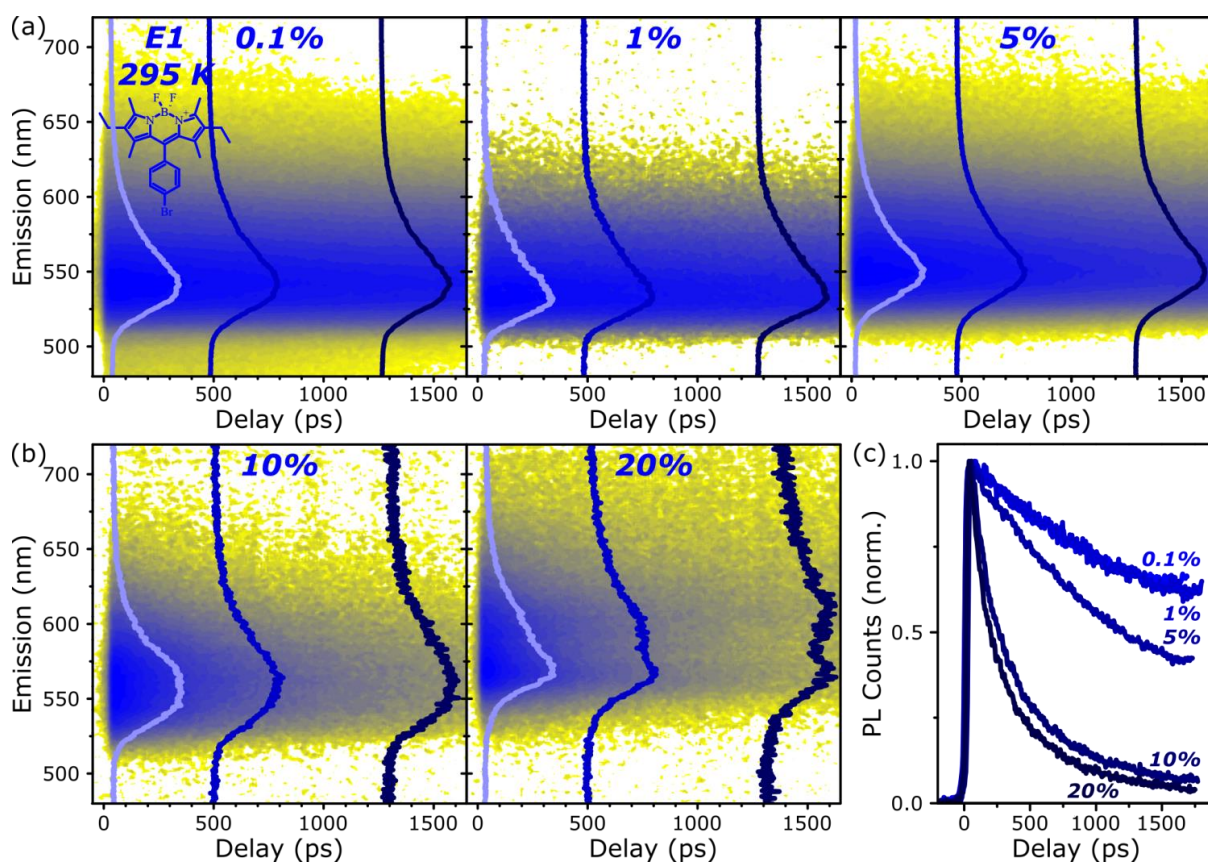
Figure S8. *Concentration dependence of PL dynamics in E1 films. **(a)** In the dilute regime, only monomer emission can be detected, though very slight changes in spectral shape can be observed at 5% on long timescales. **(b)** In the concentrated regime, there is a distinct red-shift and broadening on long timescales, due to efficient excimer formation. **(c)** The PL decay kinetic taken at the emission peak reflects this behaviour: isolated monomer decay at 0.1% and 1%, slight quenching at 5% to form a small population of excimers, and very rapid quenching at 10% and 20% by excimer formation.*